Efficient and Robust Uncertainty Quantification for Computational Fluid Dynamics and Fluid-Structure Interaction

Jeroen A.S. Witteveen

Efficient and Robust Uncertainty Quantification for Computational Fluid Dynamics and Fluid-Structure Interaction

Copyright © 2009 J.A.S. Witteveen

All rights reserved. No part of the material protected by this copyright notice may be reproduced or utilized in any form or by any means, electronic or mechanical, including photocopying, recording or by any other information storage and retrieval system, without written permission from the publisher.

Front cover photo: Jet airplane landing at sunset. Copyright © Stephen Strathdee. Used with permission.

Printed by Ipskamp Drukkers B.V. in The Netherlands.

ISBN 978-90-9024167-8

Efficient and Robust Uncertainty Quantification for Computational Fluid Dynamics and Fluid-Structure Interaction

PROEFSCHRIFT

ter verkrijging van de graad van doctor
aan de Technische Universiteit Delft,
op gezag van de Rector Magnificus prof.dr.ir. J.T. Fokkema,
voorzitter van het College voor Promoties
in het openbaar te verdedigen op dinsdag 7 april 2009 om 12:30 uur

door

Jeroen Adrianus Simon WITTEVEEN

ingenieur Luchtvaart- en Ruimtevaarttechniek
geboren te Tilburg

Dit proefschrift is goedgekeurd door de promotor:

Prof.dr.ir.drs. H. Bijl

Samenstelling promotiecommissie:

Rector Magnificus,	voorzitter
Prof.dr.ir.drs. H. Bijl,	Technische Universiteit Delft, promotor
Prof.dr.ir. A. van Keulen,	Technische Universiteit Delft
Prof.dr.ir. C.W. Oosterlee,	Centrum Wiskunde & Informatica, Technische Universiteit Delft
Prof.dr.ir. B. Koren,	Centrum Wiskunde & Informatica, Universiteit Leiden
Prof.dr.ir. C. Lacor,	Vrije Universiteit Brussel
Dr. G. Rogé,	Dassault Aviation
Dr. G. Iaccarino,	Stanford University

This research was supported by the Technology Foundation STW, applied science division of NWO and the technology programme of the Ministry of Economic Affairs.

Contents

1 Introduction 1

1.1 Uncertainty quantification 1
  1.1.1 Physical uncertainty 1
  1.1.2 Probabilistic description 3
  1.1.3 Mathematical formulation 3
1.2 Uncertainty quantification methods for CFD and FSI 4
  1.2.1 Efficiency 5
    1.2.1.1 Monte Carlo simulation 5
    1.2.1.2 Galerkin Polynomial Chaos 5
    1.2.1.3 Gram-Schmidt Polynomial Chaos 6
    1.2.1.4 Monomial Chaos 6
  1.2.2 Intrusivity 7
  1.2.3 Robustness 7
    1.2.3.1 Adaptive Stochastic Finite Elements 7
    1.2.3.2 Newton-Cotes quadrature in simplex elements . . . 8
  1.2.4 Unsteady problems 9
    1.2.4.1 Probabilistic Collocation for Limit Cycle Oscillations 9
    1.2.4.2 Unsteady Adaptive Stochastic Finite Elements . . . 10
    1.2.4.3 Unsteady Adaptive Stochastic Finite Elements with interpolation at constant phase 10
    1.2.4.4 Unsteady Adaptive Stochastic Finite Elements for multi-frequency aeroelastic responses 11
  1.2.5 High-dimensional probability spaces 11

2 Gram-Schmidt Polynomial Chaos 13

2.1 Introduction 14
2.2 Polynomial Chaos formulation for multiple uncertain parameters . . . 15

2.2.1 Polynomial Chaos applied to a differential equation with uncertainty 15
2.2.2 Construction of the polynomial basis 16
2.2.3 Efficient strategies for multiple uncertain parameters 18
2.3 Results for one-dimensional advection-diffusion 20
2.3.1 One-dimensional advection-diffusion equation 20
2.3.2 Standard two-dimensional Polynomial Chaos approach 22
2.3.3 Reduction of the dimensionality of probability space 24
2.3.4 Estimation of the combined effect of the uncertain parameters 27
2.4 Uncertainty analysis of heat transfer in a two-dimensional channel flow 28
2.4.1 Heat transfer in a two dimensional channel flow 29
2.4.2 Influence of the uncertain parameters separately 31
2.4.3 Combined effect of the four most important parameters 38
2.4.4 Estimation of the additional effect of the other parameters . . 39
2.5 Summary 41

3 Monomial Chaos 43
3.1 Introduction 43
3.2 The Monomial Chaos approach 45
3.2.1 The Monomial Chaos formulation 45
3.2.2 Error estimates 48
3.3 Application of Monomial Chaos 53
3.3.1 Burgers' equation 53
3.3.2 Results for Burgers' equation 55
3.3.2.1 Results for the uniform input distribution 56
3.3.2.2 Results for the lognormal input distribution 57
3.4 Comparison with other methods 58
3.4.1 Comparison with the perturbation method 59
3.4.2 Comparison with the Galerkin Polynomial Chaos method . . 59
3.4.3 Comparison with a non-intrusive Polynomial Chaos method . 60
3.5 Application to two-dimensional boundary layer flow 61
3.6 Summary 66

4 Adaptive Stochastic Finite Elements with Newton-Cotes quadrature in simplex elements 67
4.1 Introduction 68
4.2 Adaptive Stochastic Finite Elements 69
4.2.1 Newton-Cotes quadrature in simplex elements 69
4.2.2 Stochastic adaptive grid refinement 72

4.3 Numerical results 77
    4.3.1 Piston problem 77
        4.3.1.1 Problem description 78
        4.3.1.2 Uncertain piston velocity 79
    4.3.2 Stall flutter model 95
    4.3.3 Transonic flow over a NACA0012 airfoil 101
4.4 Summary 107

5 Probabilistic Collocation for Limit Cycle Oscillations 109
5.1 Introduction 110
5.2 Probabilistic Collocation for limit cycle oscillations 111
    5.2.1 Probabilistic Collocation method 111
    5.2.2 Time-independent parameterization of limit cycle oscillations 112
5.3 Numerical results 115
    5.3.1 Harmonic oscillator 115
    5.3.2 2 DOF flutter model 122
    5.3.3 Flow past an elastically-mounted cylinder 128
5.4 Summary 132

6 Unsteady Adaptive Stochastic Finite Elements 133
6.1 Introduction 134
6.2 Unsteady Adaptive Stochastic Finite Elements 135
    6.2.1 Adaptive Stochastic Finite Elements 135
    6.2.2 Adaptive Stochastic Finite Elements for unsteady problems . . 136
6.3 Results 141
    6.3.1 Mass-spring-damper system 141
        6.3.1.1 Governing mass-spring-damper equation 141
        6.3.1.2 Random spring stiffness parameter $K(\omega)$ 142
        6.3.1.3 Random damping parameter $C(\omega)$ 148
        6.3.1.4 Random $K(\omega)$ and $C(\omega)$ 149
    6.3.2 Duffing equation 150
        6.3.2.1 Duffing system of differential equations 152
        6.3.2.2 Random $x_0(\omega)$ 153
        6.3.2.3 Random $x_0(\omega)$ and $y_0(\omega)$ 156
    6.3.3 Rigid-airfoil fluid-structure interaction 158
        6.3.3.1 Two-degree-of-freedom airfoil model with Euler flow 160
        6.3.3.2 Effect of a random center of mass location 163
6.4 Summary 166

7 Unsteady Adaptive Stochastic Finite Elements with interpolation at constant phase 167
7.1 Introduction 168
7.2 Unsteady Adaptive Stochastic Finite Elements based on interpolation at constant phase 169
7.2.1 Interpolation at constant phase 169
7.2.2 Adaptive Stochastic Finite Elements interpolation 170
7.2.3 UASFE-cp algorithm summary 171
7.3 Results 172
7.3.1 Mass-spring-damper system 172
7.3.1.1 Governing mass-spring-damper equation 172
7.3.1.2 Parameterization error eliminated 173
7.3.2 Damped nonlinear Duffing oscillator 177
7.3.2.1 Duffing equation 180
7.3.2.2 Time-dependent functionals resolved 181
7.3.2.3 Combined randomness in initial condition $x_0(\omega)$ and damping $\delta(\omega)$ 182
7.3.3 Stochastic bifurcation behavior of an elastically mounted airfoil 184
7.3.3.1 Governing equations 185
7.3.3.2 Transient behavior captured 186
7.3.3.3 Stochastic bifurcation behavior 188
7.4 Summary 192

8 Unsteady Adaptive Stochastic Finite Elements for multi-frequency aeroelastic responses 195
8.1 Introduction 196
8.2 Unsteady Adaptive Stochastic Finite Elements for multi-frequency responses 196
8.2.1 Wavelet decomposition of multi-frequency signals 197
8.2.2 Treatment of continuous structures 198
8.2.3 Unsteady Adaptive Stochastic Finite Elements sampling interpolation 199
8.2.4 Algorithm summary 200
8.3 Results 201
8.3.1 Harmonically forced oscillator 201
8.3.1.1 Forced mass-spring system 201
8.3.1.2 Multi-frequency response resolved 202
8.3.1.3 Combination of randomness in structure and forcing 205
8.3.2 Flutter panel 206

8.3.2.1 Panel problem 207
8.3.2.2 Continuous structure analyzed 208
8.3.2.3 Random field for modulus of elasticity 211
8.3.3 Three-dimensional transonic wing 212
8.3.3.1 AGARD 445.6 wing benchmark problem 212
8.3.3.2 Randomness causes non-zero flutter probability . . 214
8.4 Summary 217

9 Derivation of total variation diminishing, extrema diminishing, and bounded error properties 219
9.1 Introduction 219
9.2 Adaptive Stochastic Finite Elements 220
9.2.1 Newton-Cotes quadrature in simplex elements 220
9.2.2 Total variation diminishing 222
9.2.2.1 One-dimensional probability space 222
9.2.2.2 Multi-dimensional probability space 226
9.2.3 Extrema diminishing 227
9.3 Unsteady Adaptive Stochastic Finite Elements 230
9.3.1 Interpolation at constant phase 230
9.3.2 Bounded error 231
9.4 Numerical results 235
9.4.1 Steady transonic airfoil flow 235
9.4.2 Transonic airfoil flutter 240
9.5 Summary 244

10 Conclusions and recommendations 247
10.1 Conclusions 247
10.1.1 Developed uncertainty quantification methods 247
10.1.1.1 Gram-Schmidt Polynomial Chaos 248
10.1.1.2 Monomial Chaos 248
10.1.1.3 Adaptive Stochastic Finite Elements with Newton-Cotes quadrature in simplex elements 249
10.1.1.4 Probabilistic Collocation for Limit Cycle Oscillations 249
10.1.1.5 Unsteady Adaptive Stochastic Finite Elements . . . 250
10.1.1.6 Unsteady Adaptive Stochastic Finite Elements with interpolation at constant phase 250
10.1.1.7 Unsteady Adaptive Stochastic Finite Elements for multi-frequency aero-elastic responses 250
10.1.2 Physical observations 251

10.2 Recommendations 252
    10.2.1 Uncertainty quantification methods 253
        10.2.1.1 Monomial Chaos 253
        10.2.1.2 Adaptive Stochastic Finite Elements 253
        10.2.1.3 Unsteady Adaptive Stochastic Finite Elements . . . 253
    10.2.2 Applications 253

A Standard uncertainty quantification methods 255
A.1 The Monte Carlo method 255
A.2 The perturbation method 256
A.3 The Galerkin Polynomial Chaos method 256
A.4 A non-intrusive Polynomial Chaos method 257

Bibliography 259

List of publications 271

Summary 275

Samenvatting 279

Acknowledgments 283

Curriculum Vitae 285

Chapter 1

Introduction

In this thesis, efficient and robust methods are developed for resolving the effect of physical uncertainties on the solution of numerical flow and fluid-structure simulations reliably and at low computational costs. This chapter starts with a general introduction into the topic of uncertainty quantification in section 1.1. In section 1.2 recent advances in the development of uncertainty quantification methods for computational fluid dynamics (CFD) and fluid-structure interaction (FSI) are sketched. In parallel an outline of this thesis is given.

1.1 Uncertainty quantification

The nature of the physical uncertainties present in practically all engineering problems is discussed in section 1.1.1. In section 1.1.2 a probabilistic framework is selected to describe the physical variations. The resulting mathematical formulation of the uncertainty quantification problem is given in section 1.1.3.

1.1.1 Physical uncertainty

Analytical solutions of the Navier-Stokes equations of fluid mechanics have so far been found only for a limited number of relatively simple cases. Engineering flow problems are usually solved numerically, which gives rise to discretization and iteration errors. In contrast with analytical solutions, these numerical approximations contain no information about the influence of parameter variations on the solution. The increasing availability of computational resources and fast algorithms has until now, however, mainly been invested into reducing the numerical errors in computational predictions. As a result, numerical errors in industrial simulations nowadays start to reach acceptable engineering accuracy levels. The effect of variations in physical parameters is usually not quantified in a systematic way. Instead, computations are performed for a set of fixed input parameter values only.

Physical uncertainties are, however, present in virtually all engineering applications. These uncertainties originate from, for example, varying atmospheric conditions (free stream velocity, angle of attack), wear and tear, and production tolerances affecting material properties (mass, stiffness, internal damping distributions) and the geometry (shape, surface roughness). They enter the computational problem through physical input parameters, and initial and boundary conditions. These inherent physical variations in the system and its environment are known as aleatoric uncertainties [71]. Other uncertainties are caused by a lack of knowledge or insufficient available experimental data to characterize input values. This second type of uncertainty is called epistemic uncertainty.

If the system is sensitive to changes in the input data, even small variations can have a significant effect on the solution. This can result in substantial performance degeneration of deterministically optimized designs. Especially discontinuous solutions of nonlinear problems and unsteady behavior of dynamical systems can be highly sensitive to input variability. Discontinuities are encountered in fluid dynamics and fluid-structure interaction as, for example, shock waves in transonic flows and bifurcation phenomena of structural responses. Dynamic fluid-structure interaction systems are also known to amplify input variations with time [78]. Since the asymptotic behavior of aeroelastic systems is usually of practical interest in post-flutter analysis, the effect of small input variations can be important. Flutter refers here to the onset of an unstable oscillatory aeroelastic response, which can lead to fatigue damage and structural failure [25].

As a consequence, the effect of physical uncertainties can be larger than numerical and modeling errors in computational predictions of engineering flow and fluid-structure interaction problems. It is then vital to quantify the effect of physical input variations in order to obtain reliable computational predictions. These can be used in robust design optimization and reducing design safety factors, which eventually contributes to the development of aerodynamically more efficient and environmentally friendly transportation and renewable energy technologies. Results for the effect of epistemic uncertainties can be used to reduce the most important sources of this type of uncertainty.

1.1.2 Probabilistic description

Physical variability can be described in a number of ways with different degrees of detail. The description of physical variations has to be sufficiently quantitative, in order for the uncertainty analysis to significantly improve the reliability of simulation results. Sensitivity derivatives give limited first-order results on the amount of amplification of input variation to the output of interest [83, 99]. Uncertainty intervals do not lead to quantitative information within the interval and they are sensitive to the often difficult to define extreme values of uncertain input [47, 68]. A fuzzy set description in terms of a membership function within an interval is more suitable for vague epistemic uncertainties [67, 121]. Low-order moment approximations of perturbation techniques are often not reliable in case of large input variations [45, 103].

In this thesis, a probabilistic description of physical variations is selected. Input variability is described in terms of probability distributions and covariance functions for random input parameters and random fields of spatially correlated data. This results in quantitative and detailed information on the effect of physical uncertainties. Second-order random processes with finite variance are considered, which includes most practical cases [40].

In most applications the required probability distributions for the random input parameters are available from measurements or expert opinion. Methods for fitting probability distributions through available experimental data are well established [41]. Otherwise an educated guess of the input statistical moments and the type of probability distribution by a senior engineer is a good starting point.

This thesis focuses on the quantification of the effect of input randomness on the probability distribution and the statistical moments of an output of interest such as aerodynamic drag or total structural energy. In contrast, in structural reliability analysis input randomness is propagated to compute the probability of failure [13]. Failure probabilities are often small such that in reliability analysis the tails of the distribution are pursued instead of the central moments.

1.1.3 Mathematical formulation

The resulting mathematical formulation of the uncertainty quantification problem for a flow or fluid-structure interaction system with random input and output of interest $u(\mathbf{x}, t, \omega)$ is given by

$$\mathcal{L}(\mathbf{x}, t, \omega; u(\mathbf{x}, t, \omega)) = \mathcal{S}(\mathbf{x}, t, \omega), \tag{1.1}$$

with appropriate initial and boundary conditions. Operator $\mathcal{L}$ and source term $\mathcal{S}$ are defined on domain $D \times T \times \Omega$, where $\mathbf{x} \in D$ and $t \in T$ are the spatial and temporal dimensions with $D \subset \mathbb{R}^d$, $d = \{1, 2, 3\}$, and $T = \mathbb{R}$. The argument ω emphasizes that $u(\mathbf{x}, t, \omega)$ is a random event with the set of outcomes Ω of the probability space (Ω, $\mathcal{F}$, P) with $\mathcal{F} \subset 2^\Omega$ the σ-algebra of events and P a probability measure. The probability space originates from n uncorrelated second-order random parameters $\mathbf{a}(\omega) = \{a_1(\omega), \dots, a_n(\omega)\} \in A$ with probability density $f_\mathbf{a}(\mathbf{a})$ in equation (1.1) and its initial and boundary conditions, with parameter space $A \subset \mathbb{R}^n$. Random fields are expressed in a countable set of uncorrelated random parameters using the mean-square error minimizing Karhunen-Loève expansion of the covariance function $C(\mathbf{x}_1, \mathbf{x}_2)$ [52]. Random fields and stochastic processes with sufficiently high correlation are considered here, otherwise Markov chain Monte Carlo can be a more suitable discretization [85].

For a single realization $\omega = \tilde{\omega}$, $u(\mathbf{x}, t, \omega)$ reduces to the deterministic function $\tilde{u}(\mathbf{x}, t) = u(\mathbf{x}, t, \tilde{\omega})$ in terms of the spatial coordinates $\mathbf{x}$ and time t. The numerical approximation of $\tilde{u}(\mathbf{x}, t)$ can be obtained using standard spatial discretization methods and time marching schemes. An increasing number of realizations $\tilde{u}(\mathbf{x}, t)$ for randomly varying $\tilde{\omega}$ approaches the probability distribution function F_u of $u(\mathbf{x}, t, \omega)$

$$u(\omega) = F_\mathrm{u}^{-1}(\omega), \qquad F_\mathrm{u}(u) = \omega, \tag{1.2}$$

where the arguments $\mathbf{x}$ and t are omitted for simplicity of the notation. Since the randomness ω is introduced into (1.1) by the random parameters $\mathbf{a}(\omega)$, the uncertainty quantification problem is to find the response surface $u^*(\mathbf{x}, t, \mathbf{a})$ of the output of interest u as function of the parameters $\mathbf{a}$ in parameter space A. Sorting (1.2) and integration of $u^*(\mathbf{x}, t, \mathbf{a})$ then results in the distribution function $F_\mathrm{u}(u, \mathbf{x}, t)$ and the statistical moments $\mu_{\mathrm{u}_i}(\mathbf{x}, t)$

$$\mu_{\mathrm{u}_i}(\mathbf{x}, t) = \int_A u^*(\mathbf{x}, t, \mathbf{a})^i f_\mathbf{a}(\mathbf{a}) \mathrm{d}\mathbf{a} = \int_\Omega u(\mathbf{x}, t, \omega)^i \mathrm{d}\omega, \tag{1.3}$$

which is an integral weighted by the probability density $f_\mathbf{a}(\mathbf{a})$ of the random input. Therefore, a weighted integrable approximation of the response surface $u^*(\mathbf{x}, t, \mathbf{a})$ in parameter space A is considered the solution of uncertainty quantification problem (1.1).

1.2 Uncertainty quantification methods for CFD and FSI

The main recent advances in the development of uncertainty quantification methods for computational fluid dynamics and fluid-structure interaction are described below. In parallel the contribution of this thesis to these developments is outlined as treated in the succeeding chapters. The developments are sketched roughly in chronological order following the changing focus of the uncertainty quantification community over the last decades from method efficiency, intrusivity, and robustness, to unsteady problems and high-dimensional probability spaces, respectively.

1.2.1 Efficiency

Initially the renewed attention for uncertainty quantification method development in structural mechanics in the early 1990s [27, 91] and in fluid mechanics a decade later [57, 104, 115] was primarily motivated by reducing the computational burden of an uncertainty analysis based on Monte Carlo simulation. The resulting additional computational costs for uncertainty quantification equivalent to many deterministic solves, is significant for deterministically already computationally intensive flow and fluid-structure simulations. Polynomial Chaos methods have, therefore, been proposed as more efficient alternatives for Monte Carlo simulation.

1.2.1.1 Monte Carlo simulation

A classical approach to determine the effect of random parameters is Monte Carlo simulation [65], in which deterministic problems are solved for randomly sampled parameter values, see Appendix A.1. However, the relatively low convergence rate of $\mathcal{O}(N_\mathrm{s}^{1/2})$ leads to a large number of required samples N_s. Monte Carlo simulation results, therefore, in impractically high computational costs for problems which are already computationally intensive in the deterministic case. More sophisticated sampling strategies and variance reduction techniques improve the efficiency to some extent [32, 64].

1.2.1.2 Galerkin Polynomial Chaos

The Galerkin Polynomial Chaos method was pioneered by Ghanem and Spanos [27] in the context of structural mechanics as a more efficient alternative to Monte Carlo simulation. Later applications of Polynomial Chaos in computational fluid dynamics problems can be found in [58, 59, 69, 119]. Galerkin Polynomial Chaos, based on the Homogeneous Chaos theory of Wiener [110], is a spectral method in probability space that approximates the response surface by a global polynomial function, see Appendix A.3. The approximation is constructed using a weighted Galerkin projection of an expansion of orthogonal polynomials. This results in a coupled set of deterministic equations, each of which is similar to the original deterministic problem. The efficiency of the homogeneous Galerkin Polynomial Chaos formulation with classical Hermite polynomials is based on its spectral convergence for Gaussian input randomness [10]. The spectral convergence was generalized to a number of other standard distributions, such as the beta distribution, by Xiu and Karniadakis [114] using classical polynomials of the Askey scheme [90].

1.2.1.3 Gram-Schmidt Polynomial Chaos

In practice often other input probability distributions are encountered than those which correspond to classical polynomials, for example, the lognormal distribution. Due to the limited convergence of Galerkin Polynomial Chaos for these input distributions, its extension to arbitrary probability distributions is essential. In Chapter 2 a Gram-Schmidt Polynomial Chaos formulation for arbitrary input distributions is developed. Gram-Schmidt orthogonalization is employed to construct a suitable set of basis polynomials orthogonal with respect to any given input distribution instead of using classical polynomials. The Gram-Schmidt algorithm has the advantage that the polynomials can be constructed analytically based on the moments of the random input. The spectral convergence of Gram-Schmidt Polynomial Chaos is illustrated in Chapter 2 for advection-diffusion problems of heat transfer in one-dimensional and two-dimensional pipe flows. Other extensions to arbitrary input distributions can be found in [92, 108].

1.2.1.4 Monomial Chaos

An important characteristic of flow problems is that they are governed by nonlinear partial differential equations in contrast to the often linear modeling in structural mechanics. The originally in the context of structural mechanics developed Galerkin Polynomial Chaos results for flow problems in a computationally intensive system of coupled nonlinear equations. It is, therefore, important for efficient uncertainty quantification in flow applications to develop methods which can deal with the nonlinearities in a more efficient way. In Chapter 3 a Monomial Chaos approach is proposed which results in an uncoupled set of linear equations for problems involving polynomial nonlinearities. In Monomial Chaos the coefficients of the Polynomial Chaos expansion with monomials as basis functions are solved for using differentiation of the governing equations, instead of a Galerkin projection. The computational work per additional Polynomial Chaos order of the equivalence of a single linear Newton iteration results in faster error convergence compared to other Polynomial Chaos methods for sufficiently small input variations. Results for the Burgers equation and a two-dimensional boundary layer flow in Chapter 3 demonstrate that the additional computational costs for a Monomial Chaos uncertainty quantification can be smaller than a single deterministic solve.

1.2.2 Intrusivity

The subsequent application of efficient Polynomial Chaos methods to more advanced practical applications, for example in [88, 113], revealed that also the intrusivity of the implementation of uncertainty quantification methods is of practical importance. Solving the coupled Polynomial Chaos equations requires significant alterations to existing deterministically optimized computer codes. This elaborate process may not even be possible when the source code of a commercial software package is unavailable or when the deterministic equations are highly nonlinear [112]. The attention has, therefore, shifted to non-intrusive Polynomial Chaos methodologies [36, 84], which construct the global polynomial approximation of the response by interpolating Monte Carlo samples, see Appendix A.4. Lagrange interpolation of samples located in suitable Gauss quadrature points employed in Probabilistic Collocation or Stochastic Collocation approaches [54, 62, 96] can under moderate assumptions also result in spectral convergence [5]. In these non-intrusive methods an existing deterministic solver is reused as a black-box, while significantly reducing the number of deterministic solves compared to Monte Carlo simulation. The computational costs for performing the uncertainty quantification interpolation of the samples are usually negligible compared to the computationally intensive deterministic solves.

1.2.3 Robustness

The global polynomial spectral approximation of intrusive and non-intrusive Polynomial Chaos methods can for more challenging problems with discontinuous solutions give unreliable results. Oscillatory approximations resulting from the stochastic Gibbs phenomenon [14, 114] can even lead to unphysical realizations. Since the principal motivation for uncertainty quantification is to assure more reliable computational predictions, much attention has been devoted to further develop Polynomial Chaos towards a more robust multi-element formulation.

1.2.3.1 Adaptive Stochastic Finite Elements

Several finite elements discretizations of probability space with a piecewise polynomial approximation of the response have been proposed. One such Stochastic Finite Elements method is the Wiener-Haar expansion introduced by Le Maître et al. [60], which results in a piecewise constant approximation based on a multi-resolution Haar wavelet discretization. Higher-order piecewise polynomial approximations in hypercube elements are developed by Deb et al. [19], Le Maître et al. [61], and Wan and Karniadakis [105]. These methods include adaptive refinement strategies in probability space [63] to limit the additional computational costs associated with multi-element discretizations.

Higher-order multi-element approximations can, however, still result locally in unphysical oscillations in elements which contain the, in general, a priori unknown discontinuity location. The adaptation is usually also performed by completely recomputing the solution in the refined domains. After several successive refinement steps the intermediate solutions in the refined domains represent a significant part of the computational efforts, even though they are not directly reflected in the final approximation. The computational costs of Adaptive Stochastic Finite Elements (ASFE) methods are, therefore, equivalent to solving a large number of uncoupled single-element problems on the different refinement levels.

1.2.3.2 Newton-Cotes quadrature in simplex elements

An alternative Adaptive Stochastic Finite Elements (ASFE) method based on Newton-Cotes quadrature in simplex elements is developed in Chapter 4. The piecewise polynomial approximation of the response is constructed by performing deterministic solves for parameter values corresponding to Newton-Cotes quadrature points in simplex elements. The stochastic grid is adaptively refined using a refinement measure based on the curvature of the response surface approximation weighted by the probability contained in the elements. The required number of deterministic solves is relatively low, since the samples are used in approximating the response in multiple elements and reused after refinements. Results for a piston problem, a stall flutter model, and transonic flow over a NACA0012 airfoil in Chapter 4 illustrate that these highly sensitive problems with discontinuous solutions lead to amplification of the input randomness.

In the field of deterministic finite volume methods there has been much attention for the robust approximation of discontinuities in physical space, which has resulted in the introduction of the total variation diminishing (TVD) [33] and extrema diminishing (ED) [42] concepts. In that context these properties ascertain that no unphysical solutions are predicted due to overshoots and undershoots near, for example, shock waves. The total variation diminishing and extrema diminishing properties are extended to probability space in Chapter 9 as basis for the development of robust uncertainty quantification methods. In probability space the extrema diminishing property assures that an uncertainty quantification method does not predict non-zero probabilities for unphysical realization due to overshoots and undershoots in the vicinity of discontinuities. It is proven in Chapter 9 that the ASFE method with Newton-Cotes quadrature in simplex elements is an extrema diminishing uncertainty quantification method in probability space. It is also shown that the method is total variation diminishing for one random parameter and for multiple random parameters for first degree Newton-Cotes quadrature.

1.2.4 Unsteady problems

The trends toward unsteady simulations in computational fluid dynamics and high fidelity post-flutter predictions in fluid-structure interaction dictate also an increasing application of uncertainty quantification in time-dependent problems. However, uncertainty quantification methods usually result in a fast increasing number of samples with time to resolve the effect of random parameters in dynamical systems with a constant accuracy. Resolving the asymptotic stochastic effect, which is of practical interest in post-flutter analysis [7], can in these long time integration problems lead to thousands of required samples [107]. The increasing number of samples is caused by the increasing nonlinearity of the response surface for increasing integration times [105]. This effect is especially profound in problems with oscillatory solutions in which the frequency of the response is affected by the random parameters [77, 78, 86]. The frequency differences between the realizations lead to increasing phase differences with time, which in turn result in an increasingly oscillatory response surface and more required samples. A Fourier Chaos basis for approximating oscillatory responses is proposed by Millman et al. [66]. Frequency domain methods have been considered for solving linear stochastic operator equations using Polynomial Chaos expansions by Sarkar and Ghanem [87].

1.2.4.1 Probabilistic Collocation for Limit Cycle Oscillations

In Chapter 5 a special uncertainty quantification methodology for oscillatory problems is developed, which achieves a constant uncertainty quantification interpolation accuracy in time with a constant number of samples, in contrast to the usually fast increasing number of samples required by other methods. The uncertainty quantification interpolation is performed at the level of a time-independent parameterization of oscillatory samples instead of the time-dependent samples themselves. The approach is applicable to the asymptotic range of period-1 limit cycle oscillation responses, for which a suitable parameterization consists of the time-independent functionals frequency, relative phase, amplitude, a reference value, and the normalized period shape. This parameterization was later adopted by Hosder et al. [38]. A period-1 limit cycle oscillation is a stable oscillation which repeats itself after one orbit around a fixed point in phase space [101]. For the actual interpolation of the time-independent functionals the global polynomial approximation and the Gauss quadrature points of Probabilistic Collocation are employed. The methodology is, therefore, referred to as Probabilistic Collocation for Limit Cycle Oscillations (PCLCO). Results for a harmonic oscillator, a two-degree-of-freedom airfoil flutter model, and the fluid-structure interaction of an elastically-mounted cylinder in Chapter 5 illustrate that 3 deterministic samples can already be sufficient for PCLCO to resolve the asymptotic effect of a random input parameter.

1.2.4.2 Unsteady Adaptive Stochastic Finite Elements

The applicability of PCLCO is extended in Chapter 6 by the development of an Unsteady Adaptive Stochastic Finite Elements (UASFE) formulation. In UASFE the time-independent parameterization extended with a damping factor and higher-period shape functions is combined with the Adaptive Stochastic Finite Element interpolation based on Newton-Cotes quadrature in simplex elements developed in Chapter 4. Due to the introduction of the damping parameter, asymptotically non-periodic responses can be parameterized. Higher-period oscillations are captured by using an algorithm for parameterizing more complex shape functions. The robust ASFE interpolation can resolve non-smooth time-independent functionals, which occur at the stochastic bifurcation of dynamical systems. The illustration of these improved properties for a mass-spring-damper system, the Duffing equation, and a rigid-airfoil fluid-structure interaction in Chapter 6 shows that a non-zero probability of negative damping results asymptotically in a diverging output standard deviation.

1.2.4.3 Unsteady Adaptive Stochastic Finite Elements with interpolation at constant phase

In Chapter 7 a second methodology for achieving a constant accuracy in time with a constant number of samples is developed to further improve the accuracy and extend the applicability of UASFE. The approach is based on interpolation of the oscillatory samples at constant phase instead of at constant time. The scaling of the samples with their phase eliminates the effect of the increasing phase differences in the response, which usually leads to the fast increasing number of samples with time. The resulting formulation is not subject to a parameterization error, which improves the convergence behavior of the method. It can also resolve time-dependent functionals that occur, for example, due to transient behavior, which is seen in virtually all nonlinear practical applications. The actual uncertainty quantification interpolation at constant phase is performed using the ASFE method with Newton-Cotes quadrature in simplex elements. The application to a mass-spring-damper system, the damped nonlinear Duffing oscillator, and an elastically mounted airfoil with nonlinearity in the flow and the structure in Chapter 7 shows a fourth-order error convergence. In Chapter 9 it is proven that the UASFE method with interpolation at constant phase results in a bounded error as function of the phase for periodic responses and under certain conditions also in a bounded error in time. The method is also applied to a transonic airfoil flutter problem in Chapter 9.

1.2.4.4 Unsteady Adaptive Stochastic Finite Elements for multi-frequency aeroelastic responses

The interpolation of the samples at constant phase limits the application of UASFE to single-frequency responses of which the phase is well-defined. The dynamic response of fluid-structure interaction problems of practical importance contains, however, often multiple frequencies. The different frequencies can originate from a combination of the natural frequency of the structure and the dominant frequency of the fluid forcing. A continuous structure also naturally exhibits a multi-frequency response in terms of its eigenmodes and eigenfrequencies.

In Chapter 8 the Unsteady Adaptive Stochastic Finite Elements framework is extended to resolve the effect of randomness on fluid-structure interaction systems with multi-frequency responses and continuous structures by employing a wavelet decomposition. The multi-frequency samples are first converted into their single-frequency components in a standard wavelet decomposition pre-processing step. The effect of the input randomness on the different frequency components is then resolved using UASFE interpolation of the single-frequency signals at constant phase. The final effect of the randomness on the multi-frequency response is obtained by summing the contributions of the single-frequency components. The multi-frequency response of a continuous structure is first projected onto either the nodal basis of a finite elements discretization or the modal basis of the natural modes of the structure in vacuum, before the wavelet decomposition is performed. Results for multi-frequency responses and continuous structures in a harmonically forced oscillator, a flutter panel problem, and the three-dimensional transonic AGARD 445.6 wing aeroelastic benchmark in Chapter 8 show a reduction of computational costs of 3 orders of magnitude compared to Monte Carlo simulation.

1.2.5 High-dimensional probability spaces

Another challenge for uncertainty quantification in computationally intensive flow and fluid-structure simulations is the case of many random input parameters. Monte Carlo simulation maintains a constant but relatively slow error convergence of $\mathcal{O}(N_\mathrm{s}^{1/2})$ independent of the number of random parameters. Other methods usually suffer from the curse-of-dimensionality, which refers to a decreasing order of convergence with increasing number of random parameters. Currently there is much attention for sparse grid [28, 117] and other approaches [37, 55] to improve the scalability of non-intrusive approaches with the dimensionality of the random input. Local adaptation in probability space for multi-element methods is seen as another alternative for efficient uncertainty quantification in high-dimensional probability spaces. Kleiber and Hien state in their standard work on perturbation methods [45] that the large number of random inputs in practical engineering problems in the order of hundreds of parameters does not allow for more advanced methods than perturbation and sensitivity techniques. Especially the adjoint based sensitivity method looks promising in this respect, because its computational costs are virtually independent of the number of random input parameters [11].

In this thesis, a relatively low number of random parameters are considered up to a maximum of six, under the assumption that the total number of possible random parameters is reduced to a selection of the most important ones based on, for example, a sensitivity analysis or expert opinion [53]. In Chapter 2 a number of alternative strategies is explored for resolving the effect of multiple random inputs efficiently in the context of Gram-Schmidt Polynomial Chaos applied to heat transfer in pipe flow. First, the effect of the separate parameters is determined using one-dimensional Polynomial Chaos expansions and a multi-dimensional expansion is employed to resolve the combined effect of the most important parameters. Second, the dimensionality of the probability space is reduced by combining multiple random parameters into fewer ones. Third, a first-order estimate of the combined effect of multiple random parameters is established by summing the variance resulting from one-dimensional Polynomial Chaos expansions for the parameters separately. A combination of the three strategies approximates the effect of six random parameters in the channel flow heat transfer problem of Chapter 2 using a two-dimensional probability space.

In the example problems, random fields and random input parameters with various probability distributions for physical parameters, geometrical parameters, and boundary and initial conditions are considered. Their effect on the probability distribution and the statistical moments of an output of practical interest is resolved. Results are compared in error convergence studies to Monte Carlo reference solutions based on uniform sampling in ω. This thesis is concluded in Chapter 10 with a summary of the main conclusions and recommendations for future work. The uncertainty quantification methods presented here for flow and fluid-structure interaction simulation are also applicable to other nonlinear and unsteady problems.

Chapter 2

Gram-Schmidt Polynomial Chaos

Galerkin Polynomial Chaos formulations based on classical polynomials achieve spectral convergence for a limited number of standard input probability distributions only. In this chapter a Gram-Schmidt Polynomial Chaos method is proposed to contribute to the extension of the spectral convergence of Galerkin Polynomial Chaos to arbitrary input probability distributions. Gram-Schmidt orthogonalization is employed to analytically construct a set of suitable orthogonal basis polynomials using the statistical moments of random input instead of using classical polynomials. Since the computational work of an uncertainty analysis can increase rapidly with the number of uncertain parameters, three strategies for reducing the computational costs in case of many random input parameters are also studied: (1) select only the most important parameters; (2) combine multiple parameters into fewer ones; and (3) estimate their first-order combined effect. The second approach usually results in non-standard probability distributions. Due to the development of Gram-Schmidt Polynomial Chaos, this approach can be used effectively. Results for advection-diffusion problems of heat transfer in one-dimensional and two-dimensional pipe flows show spectral convergence for non-standard distributions.

Based on: J.A.S. Witteveen, H. Bijl, Efficient quantification of the effect of uncertainties in advection-diffusion problems using Polynomial Chaos, Numer. Heat Tr. B-Fund. 53 (2008) 437–465.

2.1 Introduction

Uncertainty in heat transfer problems is usually modeled using sensitivity methods [8, 17] or perturbation techniques [24, 103], which result in first and second order approximations of the mean and the variance [45], see Appendix A.2. In this chapter the stochastic Galerkin approach is employed since we are interested in high order approximations of the effect of multiple uncertain input parameters in advection-diffusion heat transfer problems in pipe flows. The resulting detailed knowledge about the effect of uncertainties can lead to more basic understanding of the influence of physical variability on the outputs of interest in the designs of, for example, industrial heat exchangers. The effect of uncertainties in physical parameters, boundary conditions, geometrical parameters, and combinations of those is considered.

The analysis of the combined effect of many uncertain parameters based on standard multi-dimensional Galerkin Polynomial Chaos expansions can result in a fast increase of the computational costs. There is, therefore, a need for alternative strategies to quantify the effect of multiple uncertain parameters in computationally intensive problems more efficiently. Three approximation strategies are studied here:

1. The first approach is to select only the most important uncertain parameters for a multi-dimensional Polynomial Chaos analysis based on the results of their one-dimensional Polynomial Chaos expansions.

2. The second strategy is based on reducing the dimensionality of probability space by combining multiple uncertain parameters into fewer ones. Input uncertainty is usually given in terms of standard distributions for the uncertainty in physical model parameters. Often these uncertain input parameters can be combined into fewer ones, for example, into similarity parameters. These combined parameters have in general non-standard distributions for which a basis of classical polynomials does not result in optimal spectral convergence. Due to the recent development of the Polynomial Chaos formulation for arbitrary input distributions by constructing an appropriate orthogonal basis using Gram-Schmidt orthogonalization [92, 108, 111], this second approach can be used effectively.

3. The third approach is to estimate the combined effect of multiple uncertain parameters by summing the variances resulting from one-dimensional Polynomial Chaos expansions for the separate uncertain parameters.

These strategies for efficient quantification of multiple uncertainties can also be used in combination with non-intrusive Polynomial Chaos formulations. The first and the third approach can be applied in all problems which involve multiple uncertain parameters.

The second strategy is problem dependent, since it is not always possible to combine multiple uncertain parameters into fewer ones.

The Polynomial Chaos formulation and the three strategies for quantifying the effect of multiple uncertain parameters efficiently are discussed in section 2.2. The three Polynomial Chaos strategies are applied to advection-diffusion problems of heat transfer in one-dimensional and two-dimensional pipe flows in sections 2.3 and 2.4. The effect of the uncertain parameters on the solution is analyzed and the effectiveness of the three strategies is studied. Error convergence studies are presented for a one-dimensional advection-diffusion model problem. For heat transfer in a two-dimensional Poisseuille channel flow the effect of six uncertain parameters in the model, the boundary conditions, and the geometry is studied. Firstly, the effect of the uncertain parameters separately and the combined effect of the four most important parameters is predicted. Secondly, the dimensionality of probability space is reduced by combining three of the most important uncertain parameters into one similarity parameter. Thirdly, the additional effect of the other two parameters on the variance of the temperature field is estimated by summing the variance fields resulting from the one-dimensional Polynomial Chaos expansions for these parameters. Results are compared to Monte Carlo reference solutions. The conclusions are summarized in section 2.5.

2.2 Polynomial Chaos formulation for multiple uncertain parameters

Application of the Polynomial Chaos expansion to a differential equation with uncertain input parameters is considered in section 2.2.1. In section 2.2.2 the construction of the polynomial basis using Gram-Schmidt orthogonalization is described. The efficient strategies to handle multiple uncertain parameters in the Polynomial Chaos formulation are detailed in section 2.2.3.

2.2.1 Polynomial Chaos applied to a differential equation with uncertainty

Consider differential equation (1.1) subject to uncertain input parameters in the form of

$$\mathcal{L}(\mathbf{x}, t, \omega; u) = S(\mathbf{x}, t, \omega). \tag{2.1}$$

The Polynomial Chaos expansion of $u(\mathbf{x}, t, \omega)$ is then

$$u(\mathbf{x}, t, \omega) = \sum_{j=0}^{\infty} u_j(\mathbf{x}, t)\boldsymbol{\Psi}_j(\boldsymbol{\xi}(\omega)), \tag{2.2}$$

with $u_j(\mathbf{x}, t)$ the deterministic Polynomial Chaos coefficients and $\boldsymbol{\Psi}_j(\boldsymbol{\xi})$ orthogonal polynomials in terms of the vector of random variables $\boldsymbol{\xi}(\omega) = (\xi_1(\omega), ..., \xi_n(\omega))$. The random variables $\boldsymbol{\xi}(\omega)$ are linear transformations of the uncertain input parameters to standard domains $[-1, 1]$, $[0, \infty)$, or $(-\infty, \infty)$. The resulting probability density of the random variables $\boldsymbol{\xi}(\omega)$ is denoted by $f_{\boldsymbol{\xi}}(\boldsymbol{\xi})$. For the numerical implementation the infinite summation in (2.2) is truncated at the $(N + 1)$th term, with

$$(N + 1) = \frac{(n + p)!}{n!p!}, \tag{2.3}$$

where p is the highest order of the polynomials. Substituting the truncated Polynomial Chaos expansion (2.2) into the governing equation (2.1) results in

$$\mathcal{L}\left(\mathbf{x}, t, \omega; \sum_{j=0}^{N} u_j\boldsymbol{\Psi}_j\right) \approx S(\mathbf{x}, t, \omega). \tag{2.4}$$

A Galerkin projection [122] of (2.4) onto each polynomial basis $\{\boldsymbol{\Psi}_j(\boldsymbol{\xi})\}_{j=0}^{N}$ is employed to obtain a system of $N + 1$ equations

$$\left\langle \mathcal{L}\left(\mathbf{x}, t, \omega; \sum_{j=0}^{N} u_j\boldsymbol{\Psi}_j\right)\boldsymbol{\Psi}_k \right\rangle \approx \langle S, \boldsymbol{\Psi}_k\rangle, \qquad k = 0, 1, \ldots, N. \tag{2.5}$$

This coupled system of deterministic equations can be discretized and solved using standard methods, see for example [31, 35].

2.2.2 Construction of the polynomial basis

The polynomial basis $\{\boldsymbol{\Psi}_j(\boldsymbol{\xi})\}_{j=0}^{N}$ of the Polynomial Chaos expansion in (2.2) satisfies the following orthogonality relation

$$\langle\boldsymbol{\Psi}_j(\boldsymbol{\xi})\boldsymbol{\Psi}_k(\boldsymbol{\xi})\rangle = \langle\boldsymbol{\Psi}_j^2(\boldsymbol{\xi})\rangle\delta_{jk}, \qquad j, k = 0, 1, \ldots, N, \tag{2.6}$$

where δ_{jk} is the Kronecker delta and $\langle . \rangle$ denotes the inner product

$$\langle\boldsymbol{\Psi}_j(\boldsymbol{\xi})\boldsymbol{\Psi}_k(\boldsymbol{\xi})\rangle = \int_{S_{\boldsymbol{\xi}}} \boldsymbol{\Psi}_i(\boldsymbol{\xi})\boldsymbol{\Psi}_j(\boldsymbol{\xi})w(\boldsymbol{\xi})\mathrm{d}\boldsymbol{\xi}. \tag{2.7}$$

where $w(\boldsymbol{\xi})$ is the weighting function corresponding to the polynomials $\{\boldsymbol{\Psi}_j(\boldsymbol{\xi})\}_{j=0}^N$ and $S_{\boldsymbol{\xi}}$ is the support of $\boldsymbol{\xi}$. Exponential convergence can be obtained for sufficiently smooth solutions by a polynomial basis which is orthogonal with respect to a weighting function which equals the probability density of the random variables: $w(\boldsymbol{\xi}) = f_{\boldsymbol{\xi}}(\boldsymbol{\xi})$. This results for several standard distributions in a basis of classical orthogonal polynomials of the Askey scheme [90], for example, Hermite polynomials correspond to the normal distribution [27] and Legendre polynomials correspond to the uniform distribution [114].

For other input distributions the polynomial basis $\{\boldsymbol{\Psi}_j(\boldsymbol{\xi})\}_{j=0}^N$ can be constructed by solving the orthogonal basis problem given by (2.6) and (2.7) using Gram-Schmidt orthogonalization [26, 30]. A set of one-dimensional ($n = 1$) monic orthogonal polynomials, i.e. $\{\Psi_j(\xi)\}_{j=0}^p$ with $\Psi_j(\xi) = \xi^j + \mathcal{O}(\xi^{j-1})$, $j = 0, 1, \ldots, p$, can be constructed using the Gram-Schmidt algorithm by recursively generating

$$\Psi_j(\xi) = e_j(\xi) - \sum_{k=0}^{j-1} c_{jk}\Psi_k(\xi), \qquad c_{jk} = \frac{\langle e_j(\xi)\Psi_k(\xi)\rangle}{\langle \Psi_k(\xi)\Psi_k(\xi)\rangle}, \tag{2.8}$$

for $j = 1, 2, \ldots, p$, where $\Psi_0 = 1$ and the polynomials $\{e_j(\xi)\}_{j=1}^N$ are polynomials of exact degree j, for example, $e_j(\xi) = \xi^j$ with $j = 1, \ldots, p$. The inner products in (2.8) can be evaluated efficiently using the raw moments $\mu'_{\xi,i}$ of the random variable $\xi(\omega)$

$$\mu'_{\xi,i} = \langle \xi(\omega)^i \rangle = \int_0^1 \xi(\omega)^i \mathrm{d}\omega, \qquad i = 0, 1, \ldots, 2p-1, \tag{2.9}$$

with $\mathrm{d}\omega = w(\xi)\mathrm{d}\xi$ and $\omega \in [0, 1]$. Since the polynomials $\{\Psi_j(\xi)\}_{j=0}^p$ can be written as a summation of monomial terms

$$\Psi_j(\xi) = \sum_{j'=0}^{j} c_{j,j'}\xi^{j'}, \qquad j = 0, 1, \ldots, p, \tag{2.10}$$

the inner products of the polynomials, for example $\langle \Psi_j(\xi)\Psi_k(\xi)\rangle$, can be written as double summations over the raw moments $\mu'_{\xi,i}$

$$\langle \Psi_j(\xi)\Psi_k(\xi)\rangle = \sum_{j'=0}^{j}\sum_{k'=0}^{k} c_{j,j'}c_{k,k'}\mu'_{\xi,j'+k'}. \tag{2.11}$$

The raw moments $\mu'_{\xi,i}$ are, in general, known from the linear relation between $\xi(\omega)$ and the uncertain input parameter. They can be expressed in terms of the raw moments of the uncertain input parameter or they can be derived analytically from the known input distribution. For example the raw moments for the lognormal distribution are given by $\mu'_{\xi,i} = \exp(iM_{\ln} + (iS_{\ln})^2/2)$, with $M_{\ln}$ and $S_{\ln}$ parameters of the lognormal distribution. In other cases, the raw moments can be computed numerically for the method to be applicable to arbitrary input distributions by numerically integrating (2.9) using Gauss quadrature integration. The computational work of the one-dimensional numerical integration is negligible compared to solving the uncertainty quantification problem (2.5) itself for problems which are already computationally intensive in the deterministic case. The same approach can be used to determine the inner products involving more than two basis polynomials such as $\langle \Psi_i \Psi_j \Psi_k \rangle$, which can occur in the Polynomial Chaos formulation (2.5).

A basis of multi-dimensional orthogonal polynomials $\{\boldsymbol{\Psi}_j(\boldsymbol{\xi})\}_{j=0}^N$ in case of multiple independent uncertain parameters is constructed using the tensor product of the one-dimensional polynomials $\{\Psi_{j,i}(\xi_i)\}_{j=0}^p$, with $i = 1, \ldots, n$. Inner products of multiple polynomials, such as $\langle \boldsymbol{\Psi}_j(\boldsymbol{\xi}) \boldsymbol{\Psi}_k(\boldsymbol{\xi}) \rangle$, can be written in terms of one-dimensional integrals. The modified Gram-Schmidt algorithm with one reorthogonalization step is used for increased numerical stability, see for example [29, 109]. For multiple dependent uncertain parameters, multidimensional integrals have to be evaluated in (2.9), which can become computationally intensive for many uncertainties.

2.2.3 Efficient strategies for multiple uncertain parameters

The computational work for solving (2.5) can increase rapidly with the number of uncertain parameters n to the equivalence of many deterministic simulations. To keep uncertainty analysis for computationally intensive problems economically feasible in case of many uncertain parameters, alternative strategies to determine their combined effect are needed. Efficient approximations can be made by reducing the number of uncertain parameters or by estimating the combined effect based on results of one-dimensional Polynomial Chaos expansions for the separate parameters. The following three strategies are considered:

1. To analyze the separate effect of the n uncertain parameters using one-dimensional Polynomial Chaos expansions and to select the m uncertain parameters with the largest effect on the variance of the output for the multi-dimensional analysis with $m \leq n$. This results in resolving the combined effect of the most important uncertainties, while reducing the number of parameters from n to m.

2. To reduce the dimensionality of probability space by combining the n uncertain parameters into l parameters with $l \leq n$. Usually the input uncertainty is known in terms of standard distributions for physical model parameters, such

as the diffusion coefficient or the advection velocity. These parameters can be combined into, for example, similarity parameters such as the Péclet number. The probability distributions of the combined parameters are, however, in general non-standard. Since recently, these non-standard distributions can be handled efficiently in the Polynomial Chaos framework by constructing a basis of suitable orthogonal polynomials $\{\boldsymbol{\Psi}_j(\boldsymbol{\xi})\}$ using Gram-Schmidt orthogonalization (2.8). This results in a reduction of the dimensionality of probability space from n to l, while the spectral convergence of the Polynomial Chaos expansion is maintained. The computational work involved in solving the orthogonalization is in practical applications negligible compared to solving the uncertainty quantification problem (2.5) itself.

3. To estimate the combined effect of the n uncertain parameters on the variance of the solution based on the one-dimensional Polynomial Chaos approximations of their separate effects in analogy to the perturbation method. In the perturbation method [45] the variance of the solution $\sigma^2_{\mathrm{u},i}$ due to the uncertain parameter $\xi_i(\omega)$ is given by

$$\sigma^2_{\mathrm{u},i} \approx \left(\left. \frac{\partial u}{\partial \xi_i} \right|_{\mu_{\xi,i}} \right)^2 \sigma^2_{\xi,i}, \tag{2.12}$$

with $\mu_{\xi,i}$ and $\sigma^2_{\xi,i}$ the mean and variance of $\xi_i(\omega)$, respectively. The variance of the solution σ^2_{u} due to the combined effect of n independent uncertain parameters is in the perturbation method then given by a summation of their separate effects $\sigma^2_{\mathrm{u},i}$

$$\sigma^2_{\mathrm{u}} \approx \sum_{i=1}^{n} \sigma^2_{\mathrm{u},i}. \tag{2.13}$$

In the third strategy, (2.13) is used in the Polynomial Chaos framework to estimate the variance σ^2_{u} due to n uncertain parameters based on one-dimensional Polynomial Chaos expansions of the separate parameters. The effect of uncertain parameter $\xi_i(\omega)$ on the variance $\sigma^2_{\mathrm{u},i}$ in (2.13) is then given by the one-dimensional Polynomial Chaos approximation of the variance

$$\sigma^2_{\mathrm{u},i} = \sum_{j=1}^{p} u_j^2(\mathbf{x},t) \langle \Psi_j^2(\xi_i) \rangle. \tag{2.14}$$

instead of by the perturbation approximation (2.12). Approximation (2.13) results in a first order estimate of the combined effect of multiple uncertain pa-

> rameters on the variance of the solution, while avoiding solution of a multi-dimensional Polynomial Chaos formulation. Since the variance $\sigma^2_{\mathrm{u},i}$ is a positive variable, estimate (2.13) shows that in first order approximation the variance due to the combined effects of multiple parameters is always larger than their separate effects.

The three strategies can also be combined by selecting the m most important parameters and reducing the dimensionality of probability space further from m to l by combining the m parameters into l parameters with $l \leq m$. The additional effect of the other $n-m$ parameters on the variance σ^2_{u} can then be estimated by summing their separate effects on the variance $\sigma_{\mathrm{u},i}$ for $i = m+1, \ldots, n$ according to (2.13). In the next sections, the strategies are studied and applied to advection-diffusion heat transfer problems in one-dimensional and two-dimensional pipe flows.

2.3 Results for one-dimensional advection-diffusion

In this section, a standard test problem for advection-diffusion phenomena in one dimension is considered. The one-dimensional advection-diffusion equation is discussed in section 2.3.1. Two physical model parameters, the flow velocity $u(\omega)$ and the diffusion parameter $\kappa(\omega)$, are assumed to be uncertain with a uniform distribution. The standard approach based on a two-dimensional Polynomial Chaos expansion with Legendre polynomials is considered in section 2.3.2. The strategy of reducing the dimensionality of the probability space by combining the two uncertain parameters into one similarity parameter, the Péclet number $\mathrm{Pe}(\omega)$, is studied in section 2.3.3. The approach of estimating the combined effect of the two uncertain parameters based on their one-dimensional Polynomial Chaos expansions is considered in section 2.3.4.

2.3.1 One-dimensional advection-diffusion equation

Steady-state heat transfer in one-dimensional flow in an adiabatic pipe is considered as a standard test problem for advection-diffusion in one dimension, see Figure 2.1a. The problem is governed by the steady linear advection-diffusion equation for nondimensional temperature $T(x,\omega) = (\tilde{T} - \tilde{T}_0)/(\tilde{T}_{\mathrm{L}} - \tilde{T}_0)$ in one-dimension

$$u(\omega)\frac{\partial T}{\partial x} - \kappa(\omega)\frac{\partial^2 T}{\partial x^2} = 0, \qquad x \in [0, L], \tag{2.15}$$

where the length is $L = 1$ and the boundary conditions for the temperature $\tilde{T}(x,\omega)$ are $\tilde{T}(0,\omega) = \tilde{T}_0$ and $\tilde{T}(L,\omega) = \tilde{T}_{\mathrm{L}}$. The two physical model parameters, the advection

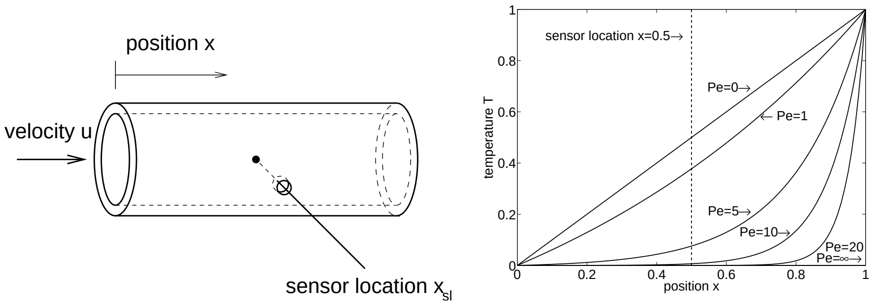

(a) one-dimensional pipe flow

(b) temperature field

Figure 2.1: The steady state heat transfer problem in a one-dimensional pipe flow with the exact solution for $Pe = \{0; 1; 5; 10; 20; \infty\}$.

velocity $u(\omega)$ and the diffusion parameter $\kappa(\omega)$, are considered to be uncertain and independent. The parameters are assumed to have a uniformly distributed uncertainty with mean $\mu_u = 1$ and $\mu_\kappa = 0.1$, and coefficients of variation $\mathrm{CV}_\mu = \mathrm{CV}_\kappa = 10\%$. This corresponds to the assumption of an interval uncertainty with uniform probability, which is often used in practical applications in case not enough information is available to prescribe an uncertainty distribution. The output variable of interest is assumed to be the nondimensional temperature $T(x_{\mathrm{sl}}, \omega)$ at sensor location $x_{\mathrm{sl}} = \frac{1}{2}$, see Figures 2.1a and 2.1b. It has been verified that the choice of the sensor location x_{sl} does not qualitatively affect the results. In nondimensional form the advection-diffusion equation (2.15), which is used in section 2.3.3, reads in terms of the Péclet number

$$Pe(\omega)\frac{\partial T}{\partial \tilde{x}} - \frac{\partial^2 T}{\partial \tilde{x}^2} = 0, \qquad \tilde{x} \in [0, 1], \tag{2.16}$$

with $\mathrm{Pe}(\omega) = \frac{u(\omega)L}{\kappa(\omega)}$ and $\tilde{x} = x/L$. The analytical solution of the deterministic variant of (2.16) is shown in Figure 2.1b for several values of the Péclet number $\mathrm{Pe} = \{0, 1, 5, 10, 20, \infty\}$. The nonstandard probability distribution of $\mathrm{Pe}(\omega)$ can be determined from the combination of the independent uniform distributions of $u(\omega)$ and $\kappa(\omega)$, see Figure 2.2.

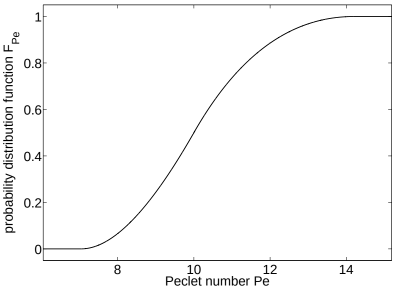

Figure 2.2: Probability distribution function for the Péclet number $\mathrm{Pe}(\omega)$ resulting from the independent uniform distributions of advection velocity $u(\omega)$ and diffusion parameter $\kappa(\omega)$.

2.3.2 Standard two-dimensional Polynomial Chaos approach

The standard approach to solve uncertainty quantification problem (2.15) with two uncertain parameters, $u(\omega)$ and $\kappa(\omega)$, is to use a basis of two-dimensional polynomials $\{\boldsymbol{\Psi}_j(\boldsymbol{\xi})\}_{j=0}^{P}$, which are tensor products of one-dimensional orthogonal polynomials. Two-dimensional Legendre polynomials are employed, because the Legendre polynomials are orthogonal with respect to the uniform input probability density functions of $u(\omega)$ and $\kappa(\omega)$. The vector of random variables $\boldsymbol{\xi}(\omega) = (\xi_1(\omega), \xi_2(\omega))$ consists of uniformly distributed random variables $\xi_i \in U(-1,1)$ with $i = 1, 2$. The Polynomial Chaos expansions of the unknown temperature $T(x,\omega)$ and the two uncertain parameters $u(\omega)$ and $\kappa(\omega)$ are

$$\begin{aligned} T(x,\omega) &= \sum_{i=0}^{N} T_i(x)\boldsymbol{\Psi}_i(\boldsymbol{\xi}(\omega)), \\ u(\omega) &= \sum_{j=0}^{1} u_j \boldsymbol{\Psi}_j(\boldsymbol{\xi}(\omega)), \qquad (2.17) \\ \kappa(\omega) &= \sum_{\substack{l=0 \\ l\neq 1}}^{2} \kappa_l \boldsymbol{\Psi}_l(\boldsymbol{\xi}(\omega)). \end{aligned}$$

The number of terms in the expansion of $T(x,\omega)$, $N+1$, is a function of the polynomial order p and the number of uncertain parameters n as given by (2.3). Substituting

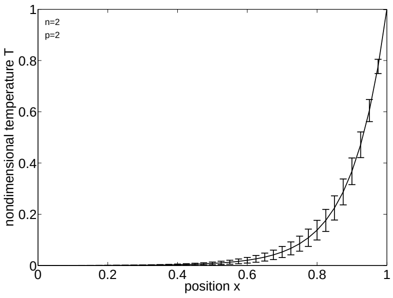

Figure 2.3: Mean value $\mu_{\rm T}(x)$ of the non-dimensional temperature $T(x,\omega)$ and the uncertainty bars based on $\pm\sigma_{\rm T}(x)$ by the two-dimensional Polynomial Chaos expansion with $p = 2$ for uncertain $u(\omega)$ and $\kappa(\omega)$ for the steady state heat transfer problem in a one-dimensional pipe flow.

the Polynomial Chaos expansions of (2.17) into (2.15) and performing a Galerkin projection onto each polynomial basis $\{\boldsymbol{\Psi}_j(\boldsymbol{\xi})\}_{j=0}^N$ results in a system of deterministic equations

$$\sum_{i=0}^{N}\left[\tilde{u}_{ik}\frac{\partial T_i}{\partial x} - \tilde{\kappa}_{ik}\frac{\partial^2 T_i}{\partial x^2}\right] = 0, \qquad k = 0, 1, \ldots, N, \tag{2.18}$$

with

$$\tilde{u}_{ik} = \sum_{j=0}^{1} u_j \langle \boldsymbol{\Psi}_i \boldsymbol{\Psi}_j \boldsymbol{\Psi}_k \rangle, \qquad \tilde{\kappa}_{ik} = \sum_{\substack{l=0\\ l\neq 1}}^{2} \kappa_l \langle \boldsymbol{\Psi}_i \boldsymbol{\Psi}_k \boldsymbol{\Psi}_l \rangle, \tag{2.19}$$

for $i, k = 0, 1, \ldots, N$. Eqs. (2.18) and (2.19) are solved numerically by using a second-order finite volume discretization of the spatial domain. The number of spatial volumes is $1 \cdot 10^4$ to ensure that the spatial error is smaller than the approximation error in probability space. The system of coupled equations (2.18) is solved using block Gauss-Seidel iteration. An error convergence study is performed with respect to a Monte Carlo reference solution based on the analytical solution of (2.16) with 10^6 realizations of $\mathrm{Pe}(\omega)$ evenly spaced in sample space $\omega \in [0, 1]$. The following error measures are used for the approximation error in the mean $\mu_{\rm T}(x)$ and the variance $\sigma_{\rm T}^2(x)$ of the temperature $T(x,\omega)$

$$\varepsilon_{\mu_{\rm T}}(x) = \left|\frac{\mu_{\rm T}(x) - \mu_{\rm T,exact}(x)}{\mu_{\rm T,exact}(x)}\right|, \qquad \varepsilon_{\sigma_{\rm T}^2}(x) = \left|\frac{\sigma_{\rm T}^2(x) - \sigma_{\rm T,exact}^2(x)}{\sigma_{\rm T,exact}^2(x)}\right|. \tag{2.20}$$

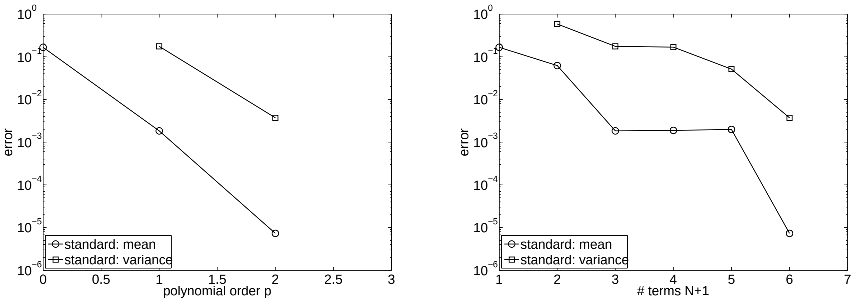

(a) with respect to Polynomial Chaos order p (b) with respect to number of terms $N+1$

Figure 2.4: Error convergence of the two-dimensional Polynomial Chaos expansion for uncertain $u(\omega)$ and $\kappa(\omega)$ with respect to the polynomial order p and the number of terms $N+1$ for the steady state heat transfer problem in a one-dimensional pipe flow.

In Figure 2.3 the Polynomial Chaos approximation of the mean value $\mu_{\mathrm{T}}(x)$ and the uncertainty bars based on $\pm\sigma_{\mathrm{T}}(x)$ are given for $p = 2$. The range of $T(x,\omega)$ agrees with the combination of the deterministic solutions of Figure 2.1b and the variation of the Péclet number given by the distribution in Figure 2.2. The uncertainty vanishes near the deterministic boundary conditions at $x = 0$ and $x = L$. The standard deviation has a maximum of $\sigma_{\mathrm{T}} = 0.052$ at $x = 0.9$.

The error convergence of the two-dimensional Polynomial Chaos expansion is given as function of polynomial order p and number of expansion terms $N+1$ in Figure 2.4. In terms of the Polynomial Chaos order p the error in the mean μ_{T} and the variance σ_{T}^2 in the sensor location converges exponentially fast, see Figure 2.4a. In Figure 2.4b the error convergence is given as function of the number of terms $N+1$ which are required for an approximation up to $p = 2$. The number of terms $N+1$ in the expansion increases rapidly with the order p as given by (2.3), which reduces for $n = 2$ to $N = \frac{1}{2}p(p+3)$. Although the error convergence in terms of $N+1$ is less regular than in terms of p, it is of interest, since the computational work for solving (2.18) is proportional with $N+1$ instead of $p+1$.

2.3.3 Reduction of the dimensionality of probability space

An alternative approach is to combine the uncertain parameters $u(\omega)$ and $\kappa(\omega)$ into one similarity parameter, the Péclet number $\mathrm{Pe}(\omega)$. The advantage of this approach is that it reduces the dimensionality of probability space. On the other hand, the resulting probability distribution of $\mathrm{Pe}(\omega)$ is no longer a standard distribution, such that classical polynomials do not result in exponential convergence. Due to the recent development of a Polynomial Chaos formulation for nonstandard input distributions, this reduction of the dimensionality of probability space can now be applied efficiently.

For the uncertain parameter the Péclet number $\mathrm{Pe}(\omega)$, an appropriate basis of one-dimensional polynomials $\{\Psi_j(\xi)\}_{j=0}^p$ is constructed that is orthogonal with respect to the probability density of $\mathrm{Pe}(\omega)$ using Gram-Schmidt orthogonalization (2.8). The number of terms of the expansion is $p+1$, since $N=p$ in this case of one uncertain parameter $n=1$. The computational work for constructing the polynomials using the raw moments of the uncertain input parameter (2.9) is negligible compared to the computational work for solving the coupled system of equations for determining the Polynomial Chaos coefficients. The one-dimensional Polynomial Chaos expansions for $T(x,\omega)$ and the uncertain parameter $\mathrm{Pe}(\omega)$ are

$$T(x,\omega)=\sum_{i=0}^{p} T_i(x)\Psi_i(\xi(\omega)), \qquad \mathrm{Pe}(\omega)=\sum_{j=0}^{1}\mathrm{Pe}_j\Psi_j(\xi(\omega)), \tag{2.21}$$

which are substituted in the governing equation in the form of (2.16). A Galerkin projection onto each polynomial basis $\{\Psi_j(\xi)\}_{j=0}^p$ results in

$$\sum_{i=\max\{k-1,0\}}^{\min\{k+1,p\}} \tilde{\mathrm{Pe}}_{ik}\frac{\partial T_i}{\partial x}-\frac{\partial^2 T_k}{\partial x^2}=0, \qquad k=0,1,\dots,p, \tag{2.22}$$

where for $\tilde{\mathrm{Pe}}_{ik}$ holds

$$\tilde{\mathrm{Pe}}_{ik}=\frac{1}{\langle\Psi_k^2\rangle}\sum_{j=0}^{1}\mathrm{Pe}_j\langle\Psi_i\Psi_j\Psi_k\rangle, \qquad k=0,1,\dots,p. \tag{2.23}$$

The results of the one-dimensional Polynomial Chaos (PC) expansion for the Péclet number $\mathrm{Pe}(\omega)$ are given in Figure 2.5. In Figure 2.5a, the approximation of the distribution function of the temperature $F_{\mathrm{T}}(T)$ at the sensor location $x_{\mathrm{sl}}=\frac{1}{2}$ is compared to the Monte Carlo (MC) result. The linear deformation of the input distribution for $p=1$ is inadequate to capture the output distribution $F_{\mathrm{T}}(T)$ accurately. This first order approximation allows unphysical negative realizations of the nondimensional temperature $T(\omega)$. The higher order approximation for $p=4$ matches with the Monte Carlo result. This example illustrates that it is important for a robust approximation to choose a sufficiently high Polynomial Chaos order to avoid unphysical predictions. In

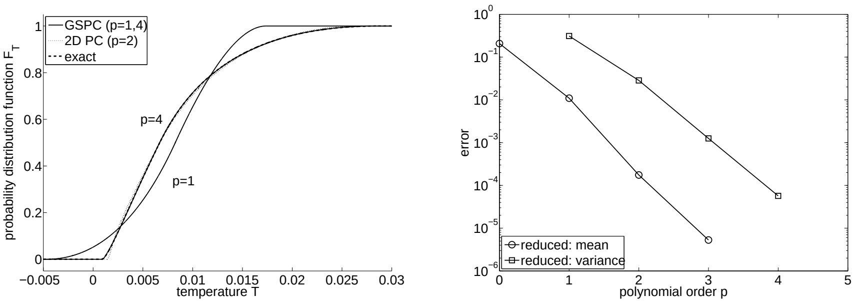

(a) probability distribution $F_{\mathrm{T}}(T)$ (b) error convergence

Figure 2.5: Results of the one-dimensional Polynomial Chaos expansion of the uncertain Péclet number $\mathrm{Pe}(\omega)$ for the steady state heat transfer problem in a one-dimensional pipe flow.

Figure 2.5b the exponential error convergence for the mean and the variance as function of the polynomial order p is shown. For this one-dimensional Polynomial Chaos expansion, the computational work is proportional to $N + 1 = p + 1$.

In Figure 2.5a also the distribution function approximation of the two-dimensional Polynomial Chaos expansion with $p = 2$ of section 2.3.2 is shown. Although the two-dimensional Polynomial Chaos expansion with $p = 2$ contains more terms $N + 1$ than the one-dimensional Polynomial Chaos expansion for $\mathrm{Pe}(\omega)$ with $p = 4$, its approximation of the distribution function is less accurate. This observation is also illustrated by the next figure.

The computational work in terms of the number of terms $N + 1$ is compared to the standard two-dimensional Polynomial Chaos approach of the previous section in Figure 2.6. The Polynomial Chaos expansion reduced to one uncertain parameter $\mathrm{Pe}(\omega)$ converges exponentially as function of the number of terms $N + 1$, see Figure 2.5b. The convergence of the standard two-dimensional Polynomial Chaos expansion is less regular, see Figure 2.4b. This results for the reduced approach for a computational work equivalent to $N + 1 = 4$ terms in a two orders of magnitude smaller error. This demonstrates that reducing the dimensionality of probability space by combining multiple uncertain parameters into fewer ones can in combination with Gram-Schmidt orthogonalization be an efficient strategy to handle multiple uncertain input parameters.

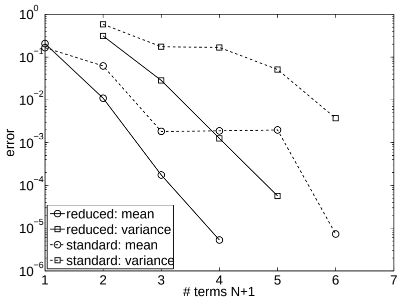

Figure 2.6: Error convergence of the one-dimensional ($n = 1$) and two-dimensional ($n = 2$) Polynomial Chaos expansions as function of the number of terms $N + 1$ as measure of the computational work for the steady state heat transfer problem in a one-dimensional pipe flow.

2.3.4 Estimation of the combined effect of the uncertain parameters

The other strategy to avoid solving a two-dimensional Polynomial Chaos formulation is to estimate the combined effect of $u(\omega)$ and $\kappa(\omega)$ based on their one-dimensional Polynomial Chaos expansions. The Polynomial Chaos approximations of the effect of two uncertain parameters separately on the variance, $\sigma^2_{\mathrm{T},u}$ and $\sigma^2_{\mathrm{T},\kappa}$, is given by (2.14). Their combined effect on the variance σ^2_{T} can then be estimated by their sum according to (2.13). In Figure 2.7 the results of this estimate are given in terms of the standard deviation of the temperature σ_{T} as function of x. The result of the two-dimensional Polynomial Chaos expansion for the combination of $u(\omega)$ and $\kappa(\omega)$ of section 2.3.2 for $p = 2$ is given by the dashed line. It shows the same behavior as the uncertainty bars in Figure 2.3. The standard deviations due to the separate uncertain parameters $u(\omega)$ and $\kappa(\omega)$ are also shown. Combining the results of the two one-dimensional Polynomial Chaos approximations using (2.13) results in the estimate given by the bold line in Figure 2.7. Relation (2.13) gives in this case a good estimate of the combined effect of the two parameters without solving a two-dimensional Polynomial Chaos problem. It can be seen that the estimate of the combined effect of the two parameters on the standard deviation is larger than their separate effects.

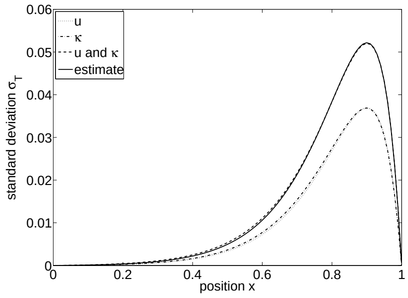

Figure 2.7: Estimate of the combined effect of $u(\omega)$ and $\kappa(\omega)$ compared to their two-dimensional Polynomial Chaos expansion results with $p = 2$ for the steady state heat transfer problem in a one-dimensional pipe flow.

2.4 Uncertainty analysis of heat transfer in a two-dimensional channel flow

In this section Polynomial Chaos is applied to the uncertainty analysis of heat transfer in a two-dimensional channel flow. The deterministic problem is briefly addressed in section 2.4.1. Six input parameters are considered to be uncertain including physical model parameters, boundary conditions, and geometrical parameters. A variety of probability distributions for the uncertain parameters is selected mainly to demonstrate the generality of the approach. The separate effects of the uncertain parameters are studied in section 2.4.2 using one-dimensional Polynomial Chaos expansions. These results are used in sections 2.4.3 and 2.4.4 in the strategies to determine the effect of multiple uncertain parameters efficiently. The combined effect of the four most important parameters resulting from the analysis in section 2.4.2 is determined in section 2.4.3. The dimensionality of the probability space is reduced further by combining three of those parameters into the Péclet number and applying a two-dimensional Polynomial Chaos expansion to the four most important parameters. These three parameters could also have been combined into the Péclet number for the analysis in section 2.4.2, which would have made the importance analysis more efficient in terms of computational costs and integration of the Polynomial Chaos formulation into the deterministic code. However, we are also interested here in studying the separate effects of uncertainty in the physical parameters and their different probability distributions. In section 2.4.4 the one-dimensional Polynomial Chaos results for the other two param-

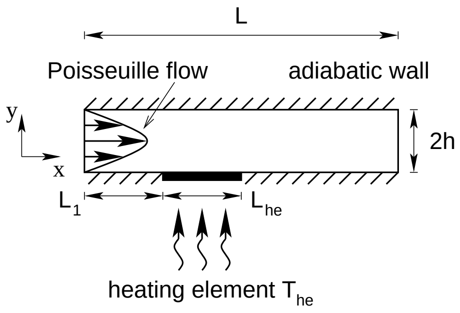

Figure 2.8: Two-dimensional Poisseuille channel flow along a heating element.

eters are used to estimate their additional effect, which results in an approximation of the effect of all six uncertain parameters. The results are compared with Monte Carlo simulations.

2.4.1 Heat transfer in a two dimensional channel flow

Steady-state heat transfer in a two-dimensional Poisseuille channel flow along a heating element is considered, see Figure 2.8. This problem is selected as an example of a heat transfer problem in multiple spatial dimensions in a simple geometry with sufficient multidimensional effects. The velocity component in the x-direction u is assumed to be a function of y only

$$u(y) = -\frac{1}{2\mu}\frac{\mathrm{d}p}{\mathrm{d}x}(h^2 - y^2), \tag{2.24}$$

with dynamic viscosity μ, constant pressure gradient $\mathrm{d}p/\mathrm{d}x$, and height of the channel $2h$. The velocity component in the y-direction is assumed to be zero. The heating element located at the lower wall at $L_1 \leq x \leq L_1 + L_{\mathrm{he}}$ maintains a constant wall temperature T_{he}. The other walls are adiabatic. At the inflow boundary $x = 0$ the temperature is given by $T = T_0 = 273.15$K. Outflow boundary conditions are prescribed at $x = L$, with $L = 0.1$m. It is assumed that the temperature distribution does not influence the flow field. The heat transfer is then given by

$$u(y)\frac{\partial T}{\partial x} - \kappa\left(\frac{\partial^2 T}{\partial x^2} + \frac{\partial^2 T}{\partial y^2}\right) = 0, \tag{2.25}$$

with heat conduction parameter κ, and $u(y)$ given by (2.24). The deterministic values of the parameters for air at standard sea level conditions and their assumed uncertain-

Table 2.1: Uncertain parameters in the heat transfer problem in the two-dimensional channel flow: deterministic value and uncertainty distribution.

parameter	symbol	value	unit	distribution	cov/interval
conduction	κ	$2.595 \cdot 10^{-2}$	J/kgK	lognormal	0.25
viscosity	μ	$1.7894 \cdot 10^{-5}$	kg/ms	uniform	0.25
pres. grad.	$\mathrm{d}p/\mathrm{d}x$	-2.0	kg/m^{2}s^2	polynomial	$[-3.5; -.5]$
h.e. temp.	T_{he}	373.15	K	uniform	0.05
height	h	0.01	m	lognormal	0.025
h.e. length	L_{he}	0.025	m	cosine	$[0.025; 0.026]$

ties are given in Table 2.1. These settings are chosen based on a parameter study for determining a parameter combination for which the temperature field is sensitive to small variations. A variety of input probability distributions is chosen to demonstrate the generality of the approach. Six parameters are assumed to be uncertain described by the following probability distributions, see Table 2.1: heat conduction $\kappa(\omega)$, viscosity $\mu(\omega)$, pressure gradient $\mathrm{d}p/\mathrm{d}x(\omega)$, heating element temperature $T_{\mathrm{he}}(\omega)$, height $h(\omega)$, and heating element length $L_{\mathrm{he}}(\omega)$. Note that both distributions which correspond to classical polynomials and non-standard distributions are selected. The probability distributions of the uncertain parameters and their separate effects are further detailed in section 2.4.2. The outputs of interest are (1) the standard deviation of the temperature field; (2) the uncertainty in the temperature at the upper wall; and (3) the uncertainty distribution of the average outflow temperature.

The governing equation (2.25) is discretized using a second-order finite volume method with an upwind and central discretization of the advection and diffusion terms, respectively. Based on a grid refinement study spatial stepsizes of $\Delta x, \Delta y = 10^{-2}$ have been chosen, which results for the deterministic case in a discretization error of approximately 10^{-5} in the L_2-norm. Grid convergence also for the stochastic problem is an important issue in uncertainty quantification as discussed in [79]. In Figure 2.9 the deterministic solution for the temperature field $T(x, y)$ and the temperature on the lower and the upper wall are given for the mean values of the uncertain parameters. The temperature increases downstream of the inflow boundary from 273.15K to 373.15K at the heating element. Downstream of the heating element the temperature is increasingly uniform in the y-direction due to the conduction of heat. The temperature at the lower wall is at each x larger than or equal to the temperature at the upper wall. The average outflow temperature of the deterministic solution is $T_{\mathrm{out}} = 346.95$K.

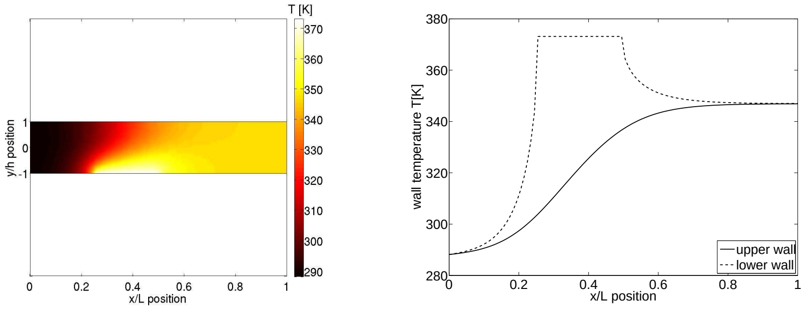

(a) Temperature field

(b) Temperature on the walls

Figure 2.9: Deterministic solution of the heat transfer in the two-dimensional channel flow.

2.4.2 Influence of the uncertain parameters separately

The Polynomial Chaos formulation of the governing system (2.25) is different for every uncertain parameter. Here, the formulation for the uncertain dynamic viscosity $\mu(\omega)$ is considered as an example. The flow velocity $u(y)$ is inversely proportional to the dynamic viscosity $\mu(\omega)$, see (2.24). The inverse $\mu^*(\omega) = 1/\mu(\omega)$ is, therefore, considered as the uncertain input parameter. Although the dynamic viscosity $\mu(\omega)$ is assumed to have a uniform distribution which can be linked to Legendre polynomials, the uncertain parameter $\mu^*(\omega)$ has a distribution which cannot be linked to classical polynomials. The basis polynomials corresponding to the uncertainty distribution of $\mu^*(\omega)$ are constructed using Gram-Schmidt orthogonalization (2.8). After substitution of the Polynomial Chaos expansions into (2.25) and a Galerkin projection onto each polynomial basis $\{\Psi_j(\xi)\}_{j=0}^{p}$, the resulting system of equations is

$$u^*(y) \sum_{i=\max\{k-1,0\}}^{\min\{k+1,p\}} \tilde{\mu}^*_{ik} \frac{\partial T_i}{\partial x} - \kappa \left(\frac{\partial^2 T_k}{\partial x^2} + \frac{\partial^2 T_k}{\partial y^2} \right) = 0, \qquad k = 0, 1, \ldots, p, \quad (2.26)$$

with

$$u^*(y) = -\frac{1}{2} \frac{\mathrm{d}p}{\mathrm{d}x} (h^2 - y^2), \quad (2.27)$$

and

$$\tilde{\mu}^*_{ik} = \frac{1}{\langle \Psi_k^2 \rangle} \sum_{j=0}^{1} \mu^*_j \langle \Psi_i \Psi_j \Psi_k \rangle, \qquad i, k = 0, 1, \ldots, p. \quad (2.28)$$

In a similar way the system of equations for the other uncertain parameters can be derived. Below, the separate effects of the six uncertain parameters on the outputs of interest are analyzed based on Figures 2.10 to 2.12. In Figure 2.10, the solution for the standard deviation of the temperature field resulting from the six uncertain parameters separately is given. The analysis focuses on the standard deviation field, since the mean value of the temperature field for the uncertain parameters is qualitatively similar to the deterministic solution of Figure 2.9a. The mean and the standard deviation of the temperature on the upper wall are compared to a convergence analysis of Monte Carlo simulation for 10, 100, and 1000 evenly spaced samples in $\omega \in [0, 1]$ in Figure 2.11. In Figure 2.12 the probability distribution of the average outflow temperature is compared to Monte Carlo results based on 1000 samples. For each uncertain parameter a convergence study is performed to determine the required Polynomial Chaos order ranging from $p = 1$ to $p = 4$.

Heat conduction The heat conduction parameter $\kappa(\omega)$ is assumed to have a lognormal uncertainty distribution, because the heat conduction parameter is a positive physical parameter. The coefficient of variation is $\mathrm{CV}_\kappa = 0.25$. The Polynomial Chaos approximation with $p = 4$ of the effect on the standard deviation of the temperature field is given in Figure 2.10a. The effect of the uncertainty in $\kappa(\omega)$ on the temperature field vanishes near the inflow boundary and the heating element, since the temperature is prescribed on these boundaries. The uncertainty has the largest effect on the upper wall opposite of the heating element, since the heat conduction $\kappa(\omega)$ affects the rate at which the heat of the heating element is transported through the fluid to the upper wall. Due to the heat conduction, the standard deviation of the temperature field is also increasingly uniform further downstream of the heating element.

The mean and the standard deviation of the temperature on the upper wall are compared with Monte Carlo simulations with 10, 100, and 1000 samples in Figure 2.11a. The mean temperature on the upper wall is a monotonically increasing function of x. The standard deviation has a maximum on the upper wall of $\sigma_{\mathrm{T}} = 7.5$K at $x/L = 0.42$. The results of the Monte Carlo simulations converge to the Polynomial Chaos results for increasing number of samples. For the mean value, the Monte Carlo results converge faster to the Polynomial Chaos result than for the standard deviation. The Monte Carlo simulation with 1000 samples matches the fourth order Polynomial Chaos solution. The Polynomial Chaos formulation is solved by Gauss-Seidel iteration, which results, in this case, in a computational work equivalent to an average of 3 times $N+1 = p+1$ deterministic solves. Therefore, the computational work for the Polynomial Chaos method is more than a factor 50 smaller than for the Monte Carlo method.

The Polynomial Chaos approximation of the probability distribution function of the

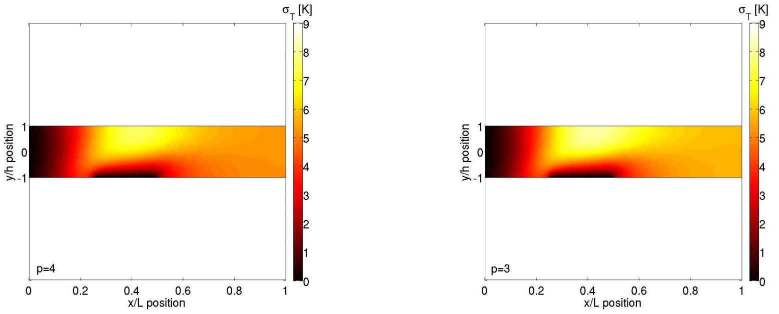

(a) uncertain conduction κ (b) uncertain viscosity μ

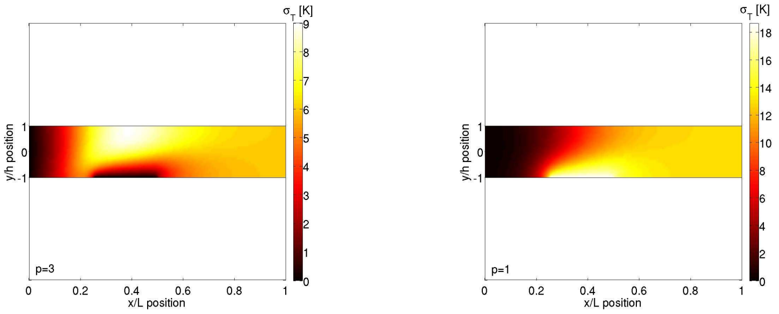

(c) uncertain pressure gradient $\mathrm{d}p/\mathrm{d}x$ (d) uncertain heating element temperature T_{he}

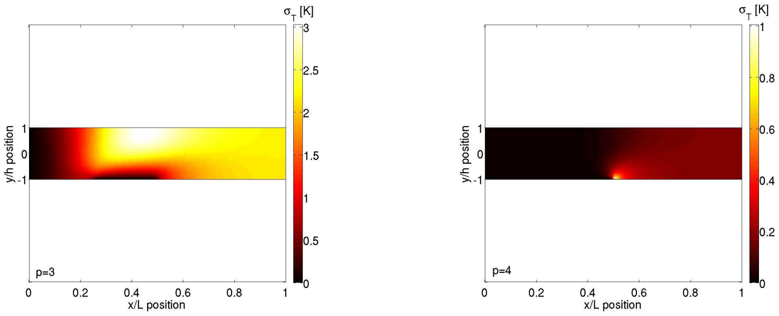

(e) uncertain channel height h (f) uncertain heating element length L_{he}

Figure 2.10: Polynomial Chaos results for the standard deviation of the temperature field σ_{T} for the heat transfer in a two-dimensional channel flow.

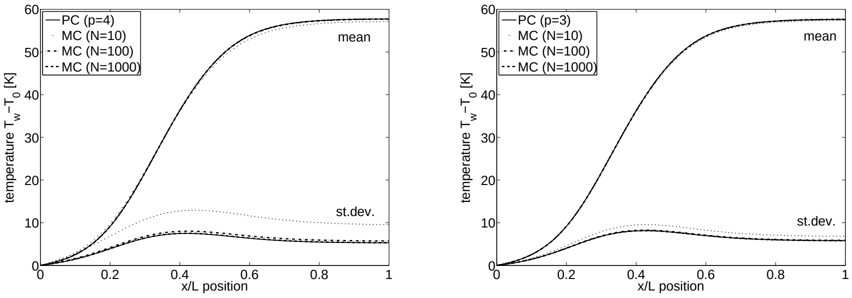

(a) uncertain convection κ　　(b) uncertain viscosity μ

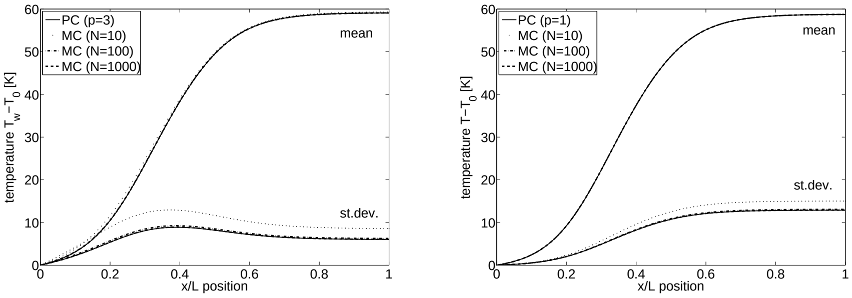

(c) uncertain pressure gradient $\mathrm{d}p/\mathrm{d}x$　　(d) uncertain heating element temperature T_{he}

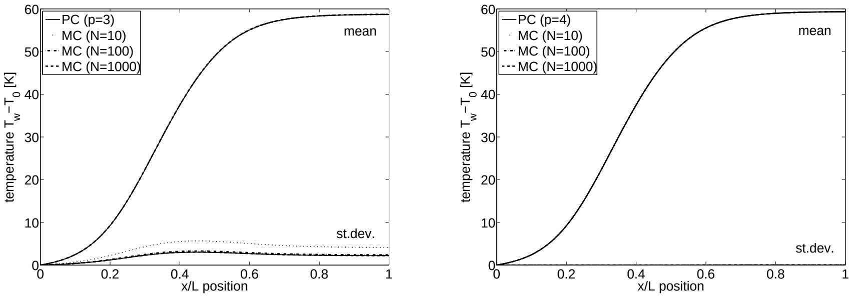

(e) uncertain channel height h　　(f) uncertain heating element length L_{he}

Figure 2.11: Polynomial Chaos (PC) and Monte Carlo (MC) results for the mean and standard deviation of the temperature on the upper wall $T_{\mathrm{w}}(x, \omega)$ for the heat transfer in a two-dimensional channel flow.

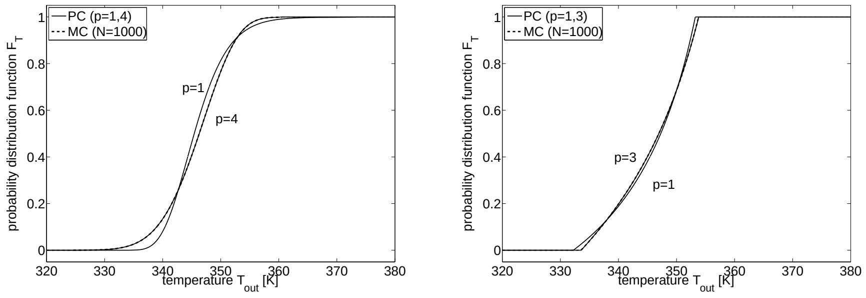

(a) uncertain convection κ

(b) uncertain viscosity μ

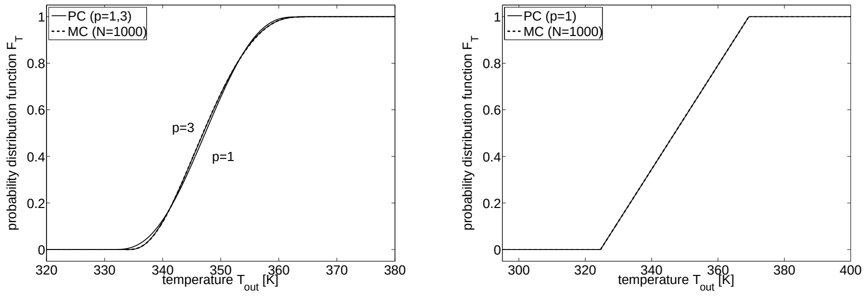

(c) uncertain pressure gradient $\mathrm{d}p/\mathrm{d}x$

(d) uncertain heating element temperature T_{he}

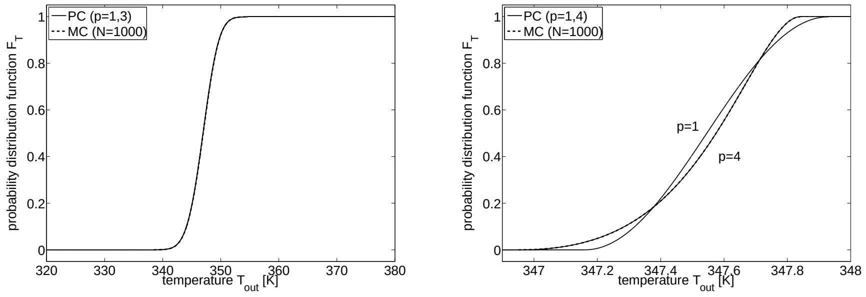

(e) uncertain channel height h

(f) uncertain heating element length L_{he}

Figure 2.12: Polynomial Chaos (PC) and Monte Carlo (MC) results for the probability distribution of the average outflow temperature T_{out} for the heat transfer in a two-dimensional channel flow.

average outflow temperature $T_{\mathrm{out}}(\omega)$ is compared to a Monte Carlo simulation with 1000 samples in Figure 2.12a. Fourth order Polynomial Chaos captures the nonlinear deformation of the input distribution and matches the Monte Carlo result. The linear deformation of the first order Polynomial Chaos approximation with $p = 1$ is not sufficient to capture the output probability distribution accurately.

Viscosity The dynamic viscosity $\mu(\omega)$ is assumed to be uniformly distributed with coefficient of variation $\mathrm{CV}_{\mu} = 0.25$. The viscosity affects the advection-diffusion of the temperature through the velocity profile of the flow (2.24). The Polynomial Chaos formulation for the uncertain viscosity $\mu(\omega)$ is given above in (2.26) to (2.28). The uncertainty in the viscosity $\mu(\omega)$ results in a qualitatively similar, but slightly higher, uncertainty in the temperature field than the conductivity $\kappa(\omega)$ unless their equal coefficient of variation (Figure 2.10b). The maximum of the standard deviation is $\sigma_{\mathrm{T}} = 8.1\mathrm{K}$ at $x/L = 0.43$ on the upper wall (Figure 2.11b). A Polynomial Chaos order of $p = 3$ is sufficient to resolve the effect of $\mu(\omega)$ compared to $p = 4$ for $\kappa(\omega)$. The Monte Carlo method also converges faster to the Polynomial Chaos results for the mean and standard deviation of the temperature on the upper wall for the uncertain viscosity $\mu(\omega)$ than for the uncertain conductivity $\kappa(\omega)$. This is caused by the finite probability interval of the uniform distribution of $\mu(\omega)$ compared to the semi-infinite domain of the lognormal distribution of $\kappa(\omega)$. In Figure 2.12b it can be seen that the polynomial order $p = 3$ is also sufficient for the approximation of the probability distribution of the outflow temperature $T_{\mathrm{out}}(\omega)$.

Pressure gradient In practice, often only a small set of measurements is available for describing the input uncertainty. In that case a functional fit can be made to obtain an approximation of the distribution function of the uncertain parameter. Assume that in this case a fifth order polynomial fit for the distribution function of the pressure gradient $\mathrm{d}p/\mathrm{d}x(\omega)$ on the domain $[-3.5; -0.5]$ is available. The third order Polynomial Chaos expansion shows that uncertainty in the pressure gradient has a slightly larger effect on the standard deviation of the temperature field than the two previous uncertain parameters (Figure 2.10c). The three uncertain parameters, $\kappa(\omega)$, $\mu(\omega)$, and $\mathrm{d}p/\mathrm{d}x(\omega)$ have a qualitatively similar effect on the standard deviation field, since they affect the balance between advection and diffusion of the heat element temperature, see (2.24) and (2.25). The standard deviation reaches a maximum of $\sigma_{\mathrm{T}} = 8.9\mathrm{K}$ on the upper wall at $x/L = 0.39$ (Figure 2.11c). The uncertainty distribution of the outflow temperature $T_{\mathrm{out}}(\omega)$ is only a slight nonlinear deformation of the input distribution of the pressure gradient, since the approximation for $p = 1$ is already close to the Monte Carlo result (Figure 2.12c).

Heating element temperature The uncertain heating element temperature $T_{\mathrm{he}}(\omega)$ is an example of an uncertain boundary condition. The probability distribution of $T_{\mathrm{he}}(\omega)$ is assumed to be uniform with a coefficient of variation $\mathrm{CV}_{\mathrm{T_{he}}} = 0.05$. A first order Polynomial Chaos expansion is employed, since in this case the temperature field depends linearly on the temperature boundary conditions. The standard deviation field of the temperature (Figure 2.10d) is qualitatively similar to the deterministic temperature field of Figure 2.9a. The effect of the uncertain T_{he} is largest at and downstream of the heating element, and smallest near the inflow boundary and the upper wall. The standard deviation of the temperature on the upper wall increases monotonically with x to $\sigma_{\mathrm{T}} = 12.9$K (Figure 2.11d). Due to the linear dependence on the boundary conditions the probability distribution of the outflow temperature is uniform just as the input distribution (Figure 2.12d). The linear deformation is captured exactly by the first order Polynomial Chaos expansion.

Channel height Finally, two geometrical uncertainties are considered. Geometrical uncertainties are often examples of epistemic uncertainty, which can be controlled in the production process. The input variation in the geometric parameters is, therefore, assumed to be smaller than in the other input parameters. The channel height h is assumed to be lognormally distributed with coefficient of variation $\mathrm{CV}_{\mathrm{h}} = 0.025$. The channel height effects the heat transfer geometrically directly and indirectly through the velocity profile. The standard deviation field predicted by a third order Polynomial Chaos expansion for $h(\omega)$ is qualitatively slightly different from those resulting from the uncertainty in $\kappa(\omega)$, $\mu(\omega)$ and $\mathrm{d}p/\mathrm{d}x(\omega)$, especially in front of the heating element (Figure 2.10e), due to the double effect of $h(\omega)$. The uncertainty of the temperature on the upper wall is similar to that of the first three uncertain parameters (Figure 2.11). The maximum of the standard distribution of $\sigma_{\mathrm{T}} = 3.03$K is significantly lower due to the smaller input coefficient of variation CV_{h}. The effect on the uncertainty distribution of the outflow temperature is smaller and accurately resolved by a first order expansion (Figure 2.12e).

Heating element length The heating element length L_{he} is another example of a geometrical uncertainty. It is assumed to have a cosine distribution on the domain $L_{\mathrm{he}}(\omega) \in [0.025; 0.026]$. The resulting standard deviation field is very different compared to that of the other uncertainties (Figure 2.10f). The uncertain heating element length has only a local effect on the uncertainty in the temperature field near the end of the heating element. The uncertainty has, therefore, a small effect on the standard deviation field and the standard deviation of the temperature on the upper wall with a maximum of $\sigma_{\mathrm{T}} = 0.03$K at the outflow boundary (Figure 2.11f). Although the uncertainty in the outflow temperature is small, it requires a fourth order Polynomial Chaos approximation to obtain a comparable relative accuracy compared to the other uncertainties (Figure 2.12f).

2.4.3 Combined effect of the four most important parameters

In case of multiple uncertain parameters it is important to determine their combined effect, since their combined first order effect on the variance is always larger than their separate effects. To reduce the computational costs of a multi-dimensional Polynomial Chaos analysis, the three efficient strategies for multiple uncertain parameters described in section 2.2.3 are combined to solve the current problem. First, the results of the one-dimensional Polynomial Chaos expansions for the separate uncertain parameters of the previous section are used to select the four most important parameters. Based on the maximum standard deviation of the temperature field, the four most important uncertain parameters are: (1) heat conduction $\kappa(\omega)$; (2) viscosity $\mu(\omega)$; (3) pressure gradient $\mathrm{d}p/\mathrm{d}x(\omega)$; and (4) heat element temperature $T_{\mathrm{he}}(\omega)$. Second, the dimensionality of probability space is further reduced by combining the first three uncertain parameters into the Péclet number $\mathrm{Pe}(\omega) = u(y)L/\kappa$. This results in a further reduction of the dimensionality of probability space from $n = 4$ to $n = 2$. The Péclet number has a non-standard uncertainty distribution, which can be determined from the uncertainty distribution of $\kappa(\omega)$, $\mu(\omega)$ and $\mathrm{d}p/\mathrm{d}x(\omega)$. The appropriate polynomial basis for the Péclet number is constructed using Gram-Schmidt orthogonalization (2.8). The third strategy for reducing the computational costs of the multidimensional analysis by estimating the additional effect of the other uncertain parameters is considered in section 2.4.4.

A two-dimensional Polynomial Chaos expansion ($n = 2$) is employed for the uncertain parameters: (1) the Péclet number $\mathrm{Pe}(\omega)$, and (2) the heat element temperature $T_{\mathrm{he}}(\omega)$. Writing (2.25) in terms of the Péclet number results in

$$\mathrm{Pe}(\omega)\frac{\partial T}{\partial \tilde{x}} - \left(\frac{\partial^2 T}{\partial \tilde{x}^2} + \frac{\partial^2 T}{\partial \tilde{y}^2}\right) = 0, \tag{2.29}$$

with $\tilde{x} = x/L$ and $\tilde{y} = y/L$. The Polynomial Chaos formulation for $\mathrm{Pe}(\omega)$ and $T_{\mathrm{he}}(\omega)$ is then

$$\sum_{i=0}^{P} \tilde{\mathrm{Pe}}_{ik}\frac{\partial T_i}{\partial \tilde{x}} - \left(\frac{\partial^2 T_k}{\partial \tilde{x}^2} + \frac{\partial^2 T_k}{\partial \tilde{y}^2}\right) = 0, \qquad k = 0, 1, \ldots, N, \tag{2.30}$$

with

$$\tilde{\mathrm{Pe}}_{ik} = \frac{1}{\langle \mathbf{\Psi}_k^2 \rangle}\sum_{j=0}^{1} \mathrm{Pe}_j \langle \mathbf{\Psi}_i \mathbf{\Psi}_j \mathbf{\Psi}_k \rangle, \qquad i, k = 0, 1, \ldots, N, \tag{2.31}$$

and heat element temperature

$$T_{\mathrm{he}}(\omega) = \sum_{\substack{i=0 \\ i\neq 1}}^{2} T_{\mathrm{he},i} \boldsymbol{\Psi}_i(\boldsymbol{\xi}(\omega)). \tag{2.32}$$

A second order Polynomial Chaos approximation ($p = 2$) is employed, which results in an expansion with $N + 1 = 6$ terms, see (2.3). The standard deviation of the temperature field due to the four uncertain parameters is shown in Figure 2.13a. The four uncertain parameters result in local maxima of the standard deviation field at the heating element and on the upper wall. The uncertainty of the temperature field is maximal at the heating element with $\sigma_{\mathrm{T}} = 18.7$K. The uncertainty at the heating element is caused by the uncertain heating element temperature, since the effect of the other uncertain parameters vanishes at the heating element. The three uncertain model parameters combined in the Péclet number result in a local maximum of the standard deviation field of $\sigma_{\mathrm{T}} = 15.0$K on the upper wall at $x/L = 0.66$. This is approximately two times higher than the standard deviations resulting from $\kappa(\omega)$, $\mu(\omega)$, and $\mathrm{d}p/\mathrm{d}x(\omega)$ separately. Also the average standard deviation at the outflow boundary $\sigma_{\mathrm{T}} = 14.3$K is larger than for the uncertain parameters separately, see Figure 2.10.

In Figure 2.13b the mean value of the temperature on the upper wall T_{w} and the uncertainty bars based on $\pm\sigma_{\mathrm{T}}$ are compared with Monte Carlo simulation results. The Monte Carlo results are based 10^4 samples obtained by the tensor product of 100 evenly spaced samples in $\omega \in [0, 1]$ in both dimensions of probability space, $\mathrm{Pe}(\omega)$ and $T_{\mathrm{he}}(\omega)$. The mean value of the temperature on the upper wall is a monotonically increasing function of x. The length of the uncertainty bars shows a fast increase starting from the inflow boundary up to $x/L = 0.54$ after which their length reduces only slightly. The two-dimensional Polynomial Chaos expansion for $p = 2$ shows good agreement with the Monte Carlo results. The Polynomial Chaos order $p = 4$ required to resolve the effect of an uncertain Péclet number $\mathrm{Pe}(\omega)$ in the one-dimensional advection-diffusion problem of Figure 2.5a, suggests that the effect of $\mathrm{Pe}(\omega)$ in the one-dimensional problem is more nonlinear.

2.4.4 Estimation of the additional effect of the other parameters

The additional effect of the other two parameters, $h(\omega)$ and L_{he}, is approximated using estimate (2.13) and the one-dimensional Polynomial Chaos expansion results for $h(\omega)$ and L_{he} of section 2.4.2. First the accuracy of (2.13) is studied by comparing the results of the estimate with those of the multi-dimensional Polynomial Chaos expansion for the four most important uncertain parameters of section 2.4.3.

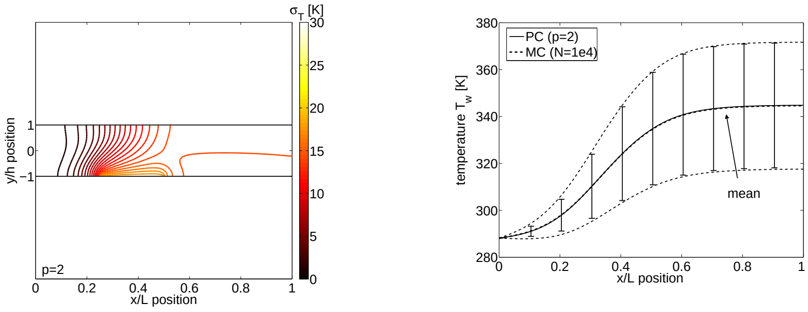

(a) Standard deviation temperature field $\sigma_{\rm T}$

(b) Upper wall temperature $T_{\rm w}$

Figure 2.13: Polynomial Chaos results for the heat transfer in a two-dimensional channel flow for the combined effect of the four most important uncertain parameters κ, μ, $\mathrm{d}p/\mathrm{d}x$ and $T_{\rm he}$.

In Figure 2.14 the estimate of the combined effect of the four most important parameters $\kappa(\omega)$, $\mu(\omega)$, $\mathrm{d}p/\mathrm{d}x(\omega)$, and $T_{\rm he}(\omega)$ on standard deviation field $\sigma_{\rm T}$ based on estimate (2.13) and their one-dimensional Polynomial Chaos expansions of section 2.4.2 is given. The estimate results without solving system (2.30) for the multi-dimensional Polynomial Chaos expansion in a reasonable approximation of the actually computed effect of the four parameters by Polynomial Chaos shown in Figure 2.13a. The two predictions match close to the heating element and the inflow boundary. In the rest of the domain the standard deviation is slightly overpredicted by estimate (2.13).

In Figure 2.15 the three strategies for efficient Polynomial Chaos approximations are combined to determine the joint effect of all six uncertain parameters. The one-dimensional Polynomial Chaos approximations for the separate parameters of section 2.4.2 are used to select the four most important parameters $\kappa(\omega)$, $\mu(\omega)$, $\mathrm{d}p/\mathrm{d}x(\omega)$, and $T_{\rm he}(\omega)$. Three of the uncertain parameters are combined into the Péclet number $\mathrm{Pe}(\omega)$ and a two-dimensional Polynomial Chaos expansion is employed for the resulting two uncertain parameters as in Figure 2.13a. The additional effect of the other two uncertain parameters $h(\omega)$ and $L_{\rm he}(\omega)$ is estimated by using (2.13).

The two less important parameters have indeed a small effect on the standard deviation field, see Figure 2.15, compared to the Polynomial Chaos result for the four most important parameters of Figure 2.13a. After adding the additional effect of the other two uncertain parameters, the maximum uncertainty on the upper wall is slightly increased from $\sigma_{\rm T} = 15.0$K to $\sigma_{\rm T} = 15.2$ mainly due to the additional effect of $h(\omega)$.

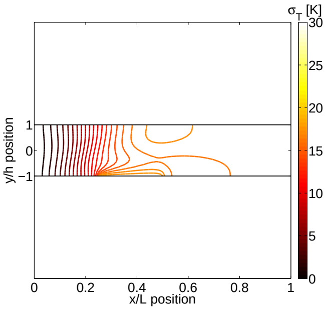

Figure 2.14: Estimate of the combined effect of the uncertain parameters κ, μ, $\mathrm{d}p/\mathrm{d}x$, and T_{he} on the standard deviation of the temperature field σ_{T} based on their one-dimensional Polynomial Chaos expansions for the heat transfer in a two-dimensional channel flow.

Estimate (2.13) is, therefore, appropriate to approximate the additional effect of less important uncertain parameters.

This result is obtained by resolving six one-dimensional Polynomial Chaos expansions and one two-dimensional expansion instead of performing a six-dimensional Polynomial Chaos analysis. This example illustrates that using alternative strategies to reduce the computational burden of uncertainty quantification with many uncertain parameters can be an accurate and efficient approach to increase the understanding of the complex effects of physical variability on the performance of engineering designs.

2.5 Summary

A Gram-Schmidt Polynomial Chaos formulation is developed to contribute to the extension of the spectral convergence of Galerkin Polynomial Chaos to arbitrary input probability distributions. Gram-Schmidt orthogonalization is employed to analytically construct a set of suitable orthogonal basis polynomials using the statistical moments of random input. The method is applied to resolve the effect of uncertainties in advection-diffusion heat transfer in pipe flows.

The analysis of the combined effect of many uncertain parameters based on multidimensional Polynomial Chaos expansions results in a fast increase of the computational costs. Three alternative strategies to quantify the effect of multiple uncertain parameters more efficiently are studied. The first approach is to select only the most important

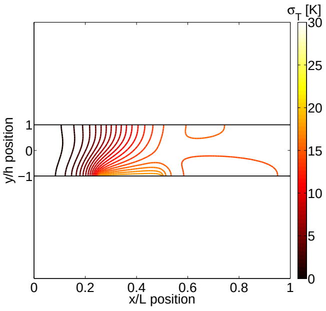

Figure 2.15: Standard deviation of the temperature field σ_{T} by the combination of the three strategies for selecting the four most important uncertain parameters $\kappa(\omega)$, $\mu(\omega)$, $\mathrm{d}p/\mathrm{d}x(\omega)$, and $T_{\mathrm{he}}(\omega)$, combining them into two uncertain parameters $\mathrm{Pe}(\omega)$ and $T_{\mathrm{he}}(\omega)$, and estimating the additional effect of the less important parameters $h(\omega)$ and $L_{\mathrm{he}}(\omega)$ for the heat transfer in a two-dimensional channel flow.

uncertain parameters for a multi-dimensional Polynomial Chaos analysis based on the results of their one-dimensional Polynomial Chaos expansions. The second strategy is based on reducing the dimensionality of probability space by combining multiple uncertain parameters into fewer ones. This second approach can be used effectively due to the extension of the Polynomial Chaos formulation to arbitrary input distributions. The third approach is to estimate the combined effect of multiple uncertain parameters by summing the variances resulting from one-dimensional Polynomial Chaos expansions for the separate uncertain parameters in analogy with the perturbation method.

The three Polynomial Chaos strategies are applied to a one-dimensional advection-diffusion model problem and a heat transfer problem in a two-dimensional Poisseuille channel flow. An error convergence study with respect to a Monte Carlo reference solution illustrate the effectiveness of the second approach for a one-dimensional problem. For the heat transfer in a two-dimensional Poisseuille channel flow the effect of six uncertain parameters in the model, the boundary conditions, and the geometry is studied successfully. The Polynomial Chaos results and Monte Carlo reference solutions demonstrate that different uncertain parameters can have significantly different quantitative and qualitative effects on the temperature field. Their combined effect is determined efficiently by a combination of the three alternative strategies for multiple uncertain parameters, instead of performing a six-dimensional Polynomial Chaos analysis. The combined effect is found to be larger than that of the separate parameters.

Chapter 3

Monomial Chaos

Propagating uncertainty through nonlinear equations can be computationally intensive for Polynomial Chaos methods. It results in a set of nonlinear equations, which is coupled in the Galerkin Polynomial Chaos formulation. A Monomial Chaos approach is presented in this chapter for efficient uncertainty quantification in nonlinear computational problems. The proposed Monomial Chaos approach employs a Polynomial Chaos expansion with monomials as basis functions. The expansion coefficients are solved for using differentiation of the governing equations, instead of a Galerkin projection. This results in a decoupled set of linear equations for problems involving polynomial nonlinearities. This reduces the computational work per additional Polynomial Chaos order to the equivalence of a linear Newton iteration. Error estimates are derived, and Monomial Chaos is applied to uncertainty quantification of the Burgers equation and a two-dimensional boundary layer flow problem. Monomial Chaos results compared to those of the Monte Carlo method, perturbation method, Galerkin Polynomial Chaos method, and a non-intrusive Polynomial Chaos method show a 2–3 times faster error convergence as function of computational work.

3.1 Introduction

Parametric uncertainty is considered in a physical model described by the differential equation (1.1) in the form of

$$\mathcal{L}(\mathbf{x}, t, \alpha(\omega); u(\mathbf{x}, t, \omega)) = S(\mathbf{x}, t, \alpha(\omega)), \tag{3.1}$$

Based on: J.A.S. Witteveen, H. Bijl, A Monomial Chaos approach for efficient uncertainty quantification in nonlinear problems, SIAM J. Sci. Comput. 30 (2008) 1296–1317.

where $\alpha(\omega)$ is an uncertain parameter with known probability distribution. In appendix A, four widely used uncertainty quantification methods are briefly reviewed for comparison with the proposed Monomial Chaos approach: the Monte Carlo method, the perturbation method [45], the Galerkin Polynomial Chaos method [27], and a non-intrusive Polynomial Chaos method [36].

These uncertainty quantification methods result in a significant increase of the computational costs compared to a deterministic simulation. The non-intrusive Polynomial Chaos method results, for example, in a multiplication of computational work by a factor $(p + 1)$, where p is the Polynomial Chaos order. For computationally very intensive problems this increase of computational work can be a major drawback for the application of uncertainty quantification. Consider, for example, practical applications of nonlinear computational fluid dynamics in time dependent problems involving complex geometries. These deterministic problems can already take weeks or even longer to solve. An increase of this amount of computational work by a factor $(p+1)$ is significant. Especially in iterative design processes of industrial applications this can make uncertainty quantification impractical. On the other hand, uncertainty quantification is in these cases essential for robust design optimization. Therefore, there is a need for a further reduction of the computational costs of uncertainty quantification methods.

In this chapter, a Monomial Chaos approach is proposed to reduce the costs of uncertainty quantification in computationally intensive nonlinear problems. The computational work per Monomial Chaos order is equivalent to a linear Newton iteration due to the differentiation of the governing equations for obtaining the coefficients of the Polynomial Chaos expansion with Monomials as basis functions. Therefore, Monomial Chaos can be a computationally efficient alternative for existing uncertainty quantification methods in nonlinear problems. The Monomial Chaos approach is introduced in this chapter for one uncertain input parameter to demonstrate the properties of the method and to make a basic comparison with other uncertainty quantification methods. The extension of Monomial Chaos to multiple uncertain parameters and random fields is briefly addressed.

The Monomial Chaos is introduced and error estimates are derived in section 3.2. In section 3.3 the Monomial Chaos is applied to the Burgers equation to demonstrate the properties of the proposed approach for a standard nonlinear advection-diffusion test problem in one dimension. The results are compared with results of the perturbation method, the Galerkin Polynomial Chaos method, and the non-intrusive Polynomial Chaos method in section 3.4. In section 3.5 the Monomial Chaos is applied to a two-dimensional boundary layer flow problem as an example of a standard nonlinear test problem from two-dimensional incompressible fluid dynamics. In section 3.6 the conclusions are summarized.

3.2 The Monomial Chaos approach

In this section the Monomial Chaos approach is proposed. In section 3.2.1 the Monomial Chaos approach is introduced in general as applied to (3.1). Error estimates are given in section 3.2.2.

3.2.1 The Monomial Chaos formulation

The Monomial Chaos approach employs a Polynomial Chaos expansion with monomials as basis functions to determine the uncertainty distribution of the output. The equations for the Monomial Chaos expansion coefficients are obtained by differentiating the deterministic equation with respect to the uncertain input parameter. This results in a decoupled set of $(p+1)$ equations for the $(p+1)$ coefficients of a $p\mathrm{th}$-order Monomial Chaos expansion, in which each equation solves for a Monomial Chaos coefficient sequentially. Due to the product rule the differentiation of the governing equations also results in a set of linear equations even for problems involving polynomial nonlinearities. This reduces the additional computational work per Polynomial Chaos order to the equivalence of a single Newton iteration. Therefore, Monomial Chaos can be an efficient alternative for uncertainty quantification in computationally intensive nonlinear problems.

Consider the application of Monomial Chaos to a physical model involving polynomial nonlinearities and parametric uncertainty given by (3.1),

$$\mathcal{L}(\mathbf{x}, t, \alpha(\omega); u(\mathbf{x}, t, \omega)) = S(\mathbf{x}, t, \alpha(\omega)).$$

The uncertain parameter $\alpha(\omega)$ and the solution $u(\mathbf{x}, t, \omega)$ are expanded into a Polynomial Chaos expansion

$$\alpha(\omega) = \sum_{j=0}^{1} \alpha_j \Psi_j(\xi(\omega)), \qquad u(\mathbf{x}, t, \omega) = \sum_{i=0}^{\infty} u_i(\mathbf{x}, t) \Psi_i(\xi(\omega)), \tag{3.2}$$

where the random variable $\xi(\omega)$ is given by a linear transformation of the uncertain input parameter $\alpha(\omega)$ to an appropriate standard domain, i.e., $[-1, 1]$, $[0, \infty)$, or $(-\infty, \infty)$ [114]. Due to this linear transformation the Polynomial Chaos expansion of $\alpha(\omega)$ in (3.2) is exact within the first two terms. In the Monomial Chaos the basis polynomials $\{\Psi_i(\xi)\}_{i=0}^{\infty}$ are monomials around $\xi(\omega) = \mu_\xi$ with $\mu_\xi \equiv \mathbb{E}[\xi(\omega)]$:

$$\Psi_i(\xi(\omega)) = (\xi(\omega) - \mu_\xi)^i, \qquad i = 0, 1, \ldots . \tag{3.3}$$

These monomials are chosen as basis functions because they satisfy the property

$$\left.\frac{\mathrm{d}^j \Psi_i}{\mathrm{d}\xi^j}\right|_{\xi=\mu_\xi} = \begin{cases} i!, & i = j, \\ 0, & i \neq j, \end{cases} \tag{3.4}$$

which says that taking the $j\mathrm{th}$ derivative of the monomials $\{\Psi_i(\xi)\}_{i=0}^{\infty}$ with respect to ξ at $\xi(\omega) = \mu_\xi$ results in a nonzero term for $i = j$ only. This property of monomials results in the decoupled set of equations for the Monomial Chaos coefficients $\{u_i(\mathbf{x}, t)\}$. Substitution of the Monomial Chaos expansions (3.2) with (3.3) into the governing equation (3.1) results in

$$\mathcal{L}\left(\mathbf{x}, t, \sum_{j=0}^{1} \alpha_j \Psi_j(\xi); \sum_{i=0}^{\infty} u_i(\mathbf{x}, t)\Psi_i(\xi)\right) = S\left(\mathbf{x}, t, \sum_{j=0}^{1} \alpha_j \Psi_j(\xi)\right). \tag{3.5}$$

To obtain a set of equations for the expansion coefficients of the solution $\{u_i(\mathbf{x}, t)\}$, (3.5) is differentiated with respect to ξ for $\xi(\omega) = \mu_\xi$. Taking the $k\mathrm{th}$ derivative of (3.5) results in an equation for the $k\mathrm{th}$ expansion coefficient $u_k(\mathbf{x}, t)$,

$$\begin{aligned} &\left.\frac{\partial^k}{\partial \xi^k}\mathcal{L}\left(\mathbf{x}, t, \sum_{j=0}^{1} \alpha_j \Psi_j(\xi); \sum_{i=0}^{\infty} u_i(\mathbf{x}, t)\Psi_i(\xi)\right)\right|_{\xi=\mu_\xi} \\ &\qquad = \left.\frac{\partial^k}{\partial \xi^k} S\left(\mathbf{x}, t, \sum_{j=0}^{1} \alpha_j \Psi_j(\xi)\right)\right|_{\xi=\mu_\xi} \end{aligned} \tag{3.6}$$

for $k = 0, 1, \ldots$. This set of equations can be discretized using standard discretization techniques [35]. Due to the combination of differentiation of (3.5) and property (3.4), all higher-order coefficients $\{u_i(\mathbf{x}, t)\}_{i=k+1}^{\infty}$ drop out of the equation, which results in a decoupled set of equations for $u_k(\mathbf{x}, t)$ in terms of $\{u_i(\mathbf{x}, t)\}_{i=0}^{k-1}$. This is illustrated in section 3.3 where the Monomial Chaos is applied to the Burgers equation. Furthermore, the decoupled set of equations (3.6) is linear in $u_k(\mathbf{x}, t)$ due to the product rule in differentiation, even if the governing equation (3.1) contains polynomial nonlinearities (except for $k = 0$). The equation for $k = 0$ coincides with the deterministic problem for the expected value of the uncertain parameter μ_α. For nonlinear problems solved using Newton linearization, the additional computational work per Polynomial Chaos order is proportional to one Newton iteration.

A $p\mathrm{th}$-order Monomial Chaos approximation of the solution $u(\mathbf{x}, t, \omega)$ is given by truncating the Monomial Chaos expansion for $u(\mathbf{x}, t, \omega)$ in (3.2) at p. The Monomial

Chaos coefficients $\{\alpha_j\}_{j=0}^{1}$ of the uncertain parameter $\alpha(\omega)$ with a known uncertainty distribution can be determined by differentiating the Monomial Chaos expansion for $\alpha(\omega)$ in (3.2) with respect to ξ for $\xi(\omega) = \mu_\xi$, which results, using property (3.4), in

$$\alpha_j = \frac{1}{j!} \frac{\mathrm{d}^j \alpha}{\mathrm{d}\xi^j}\bigg|_{\xi=\mu_\xi}, \qquad j = 0, 1, \tag{3.7}$$

where $\frac{\mathrm{d}^j \alpha}{\mathrm{d}\xi^j}|_{\mu_\xi}$ is known and $\alpha_0 = \mu_\alpha$.

Equations (3.6) are similar to the continuous sensitivity equations (A.4) of the perturbation method, which are obtained by implicit differentiation. The Monomial Chaos method can be viewed as an extension of the perturbation method, which is usually limited to second-order approximations of the first two moments. The Monomial Chaos approach can be employed for obtaining higher-order approximations of the uncertainty distribution and the statistical moments of the output at computational costs equivalent to those of the perturbation method.

On the other hand, in the Monomial Chaos approach the uncertain parameter and variables are expanded in a polynomial expansion as in the Polynomial Chaos method, using monomials instead of orthogonal polynomials in the Polynomial Chaos method. The Monomial Chaos approach can therefore be applied to the same set of arbitrary input probability distributions as the Polynomial Chaos method. The outputs of the Monomial Chaos approach are higher-order approximations of the distribution and the statistical moments by solving a decoupled set of linear equations, instead of a possibly coupled set of nonlinear equations in the Polynomial Chaos method.

Next to the relatively low computational work per Polynomial Chaos order the Monomial Chaos has additional advantages which are important for practical applications. First, the Polynomial Chaos order of the Monomial Chaos approximation can be determined during the computation while solving for the higher-order coefficients sequentially. Second, the equations (3.6) depend only on the mean value of the uncertain input parameter μ_α. Therefore, the influence of different input uncertainty distributions and variances can be studied after solving (3.6) once. This is an important property since in practical problems the input distribution itself can also be subject to uncertainty.

The Monomial Chaos is moderately intrusive, since for solving (3.6) the summation of the matrix and vector entries in the deterministic solver have to be modified. For decreasing the intrusiveness of the Monomial Chaos, the differentiation of the governing equations can be replaced by finite difference differentiation in random space.

Here, the Monomial Chaos approach is considered for a single uncertain input parameter. The Monomial Chaos approach can be extended to multiple uncertain input parameters by introducing a vector of random variables $\boldsymbol{\xi}(\omega) = (\xi_1(\omega), \ldots, \xi_n(\omega))$, where n is the number of uncertain input parameters. The basis consists in that case of multidimensional monomials $\mathbf{\Psi}_i(\boldsymbol{\xi}(\omega))$, which are tensor products of one-dimensional monomials $\Psi_i(\xi_j(\omega))$. The set of equations for the Monomial Chaos coefficients (3.6) is then derived using mixed partial derivatives of (3.5) with respect to the random variables $\{\xi_j(\omega)\}_{j=0}^{n}$.

The uncertainty quantification methods reviewed in section 3.1 can also be extended to multiple uncertain input parameters. For comparison, in the extension of the perturbation method to multiple uncertain input parameters, the statistical moments of the output are expanded around the expected value of the uncertain parameters using multidimensional Taylor series expansions. The Polynomial Chaos method can be extended to n uncertain parameters by using a multidimensional Polynomial Chaos expansion in (A.5). The multidimensional Polynomial Chaos expansion is based on a vector of random variables $\boldsymbol{\xi}(\omega) = (\xi_1(\omega), \ldots, \xi_n(\omega))$ and multidimensional orthogonal polynomials $\mathbf{\Phi}_i(\boldsymbol{\xi}(\omega))$.

A random field can be handled by the Monomial Chaos method by first representing the random field in terms of a finite number of independent random input parameters using a Karhunen-Loève expansion [52] as in the Polynomial Chaos method. For a random field with a relatively high spatial correlation, the number of random input parameters needed to reach a reasonable accuracy with the Karhunen-Loève expansion can be small. In that case the Monomial Chaos method can be applied to the random input parameters to resolve the effect of the random field. For random fields and random processes with low correlation the required number of random input parameters can be much higher, and approaches other than the Monomial Chaos method or the Polynomial Chaos method can be more competitive.

3.2.2 Error estimates

In this section error estimates for the Monomial Chaos approach are derived. For simplicity the arguments $\mathbf{x}$ and t are dropped. After computing the Monomial Chaos coefficients in (3.6), approximations of the mean μ_{u}, variance σ_{u}^2, higher-order moments, and the distribution function can be derived. If the uncertain variable $u(\omega)$ is expanded in an infinite Monomial Chaos series, the mean μ_{u} is given in terms of the Monomial Chaos coefficients $\{u_i\}_{i=0}^{\infty}$ by

$$\mu_{\mathrm{u}} = \sum_{i=0}^{\infty} u_i \mu_{\xi,i}, \tag{3.8}$$

with $\mu_{\xi,i}$ the $i\mathrm{th}$ central statistical moment of $\xi(\omega)$,

$$\mu_{\xi,i} = \int_{\mathrm{supp}(\xi)} \Psi_i(\xi) p_\xi(\xi) \mathrm{d}\xi, \tag{3.9}$$

with $\mu_{\xi,0} = 1$, $\mu_{\xi,1} = 0$ and where $\mathrm{supp}(\xi)$ and $p_\xi(\xi)$ are the support and the probability density of $\xi(\omega)$, respectively. The variance σ_{u}^2 is given by

$$\sigma_{\mathrm{u}}^2 = \sum_{i=0}^{\infty}\sum_{j=0}^{\infty} \tilde{u}_i \tilde{u}_j \mu_{\xi,i+j}, \tag{3.10}$$

with

$$\tilde{u}_i = \begin{cases} u_i - \mu_{\mathrm{u}}, & i = 0, \\ u_i, & i = 1, 2, \dots . \end{cases} \tag{3.11}$$

In the numerical implementation the infinite series in (3.8) and (3.10) are truncated at a Polynomial Chaos order p. The errors in the approximation in the mean $\varepsilon_{\mu_{\mathrm{u}}}$ and the variance $\varepsilon_{\sigma_{\mathrm{u}}^2}$ due to the truncation of the Monomial Chaos expansion are then given by

$$\varepsilon_{\mu_{\mathrm{u}}} = -\sum_{i=p+1}^{\infty} u_i \mu_{\xi,i}, \tag{3.12}$$

and

$$\varepsilon_{\sigma_{\mathrm{u}}^2} = -2 \sum_{i=p+1}^{\infty}\sum_{j=p+1}^{\infty} u_i u_j \mu_{\xi,i+j}. \tag{3.13}$$

If the Monomial Chaos coefficients u_i decrease fast enough with i for $i = p+1, p+2, \dots$, such that the leading truncation error term is due to neglecting the $(p+1)\mathrm{th}$ coefficient, then the truncation errors can be estimated as

$$\varepsilon_{\mu_{\mathrm{u}}} \approx -u_{p+1}\mu_{\xi,p+1} \tag{3.14}$$

and

$$\varepsilon_{\sigma_{\mathrm{u}}^2} \approx -2u_{p+1}^2 \mu_{\xi,p+1}^2, \tag{3.15}$$

which says that the leading error term in the approximation of the variance σ_{u}^2 results in an underestimation. These a posteriori error estimates can be used in a stopping criterion for determining the Polynomial Chaos order p of the Monomial Chaos approximation.

Another contribution to the error in the mean μ_{u} and the variance σ_{u}^2 can be due to the divergence of the Monomial Chaos expansion in a part of the domain of $\xi(\omega)$. In case of an input distribution with an infinite support, i.e., $\xi(\omega) \in (-\infty, \infty)$, there is always a domain $\xi(\omega) \in (-\infty, \xi^-] \cup [\xi^+, \infty)$ in which the Monomial Chaos expansion of $u(\omega)$, (3.2), diverges. However, it is demonstrated in the following propositions that the divergence of the Monomial Chaos expansion in $\xi(\omega) \in (-\infty, \xi^-] \cup [\xi^+, \infty)$ results in errors $\tilde{\varepsilon}_{\mu_\mathrm{u}}$, $\tilde{\varepsilon}_{\sigma^2_\mathrm{u}}$ which are in general small with respect to the truncation errors $\varepsilon_{\mu_\mathrm{u}}$ and $\varepsilon_{\sigma^2_\mathrm{u}}$, and the mean μ_u and variance σ^2_u.

Proposition 1. *Let $\xi(\omega) \in (-\infty, \infty)$ and let $\xi(\omega) \in (\xi^-, \xi^+)$ be the domain of convergence of the Monomial Chaos expansion of $u(\omega)$, (3.2). If the probability density $p_\xi(\xi)$ of $\xi(\omega)$ decreases fast enough as $\xi \to \pm\infty$ such that*

$$\sum_{i=0}^{\infty} |u_i| \left| \int_{(-\infty,\xi^-]\cup[\xi^+,\infty)} \Psi_i(\xi) p_\xi(\xi) \mathrm{d}\xi \right| \ll \left| \sum_{i=p+1}^{\infty} u_i \int_{\xi^-}^{\xi^+} \Psi_i(\xi) p_\xi(\xi) \mathrm{d}\xi \right|, \quad (3.16)$$

then the error in the Monomial Chaos approximation of the mean μ_u due to the divergence of the Monomial Chaos expansion in $\xi(\omega) \in (-\infty, \xi^-] \cup [\xi^+, \infty)$ is small compared to the truncation error; i.e., $|\tilde{\varepsilon}_{\mu_\mathrm{u}}| \ll |\varepsilon_{\mu_\mathrm{u}}|$.

Proof. The error $\tilde{\varepsilon}_{\mu_\mathrm{u}}$ in the Monomial Chaos approximation of the mean μ_u due to the divergence in $\xi(\omega) \in (-\infty, \xi^-] \cup [\xi^+, \infty)$ is defined as

$$\tilde{\varepsilon}_{\mu_\mathrm{u}} = \sum_{i=0}^{\infty} u_i \int_{(-\infty,\xi^-]\cup[\xi^+,\infty)} \Psi_i(\xi) p_\xi(\xi) \mathrm{d}\xi, \quad (3.17)$$

with

$$\left| \sum_{i=0}^{\infty} u_i \int_{(-\infty,\xi^-]\cup[\xi^+,\infty)} \Psi_i(\xi) p_\xi(\xi) \mathrm{d}\xi \right| \leq$$

$$\sum_{i=0}^{\infty} |u_i| \left| \int_{(-\infty,\xi^-]\cup[\xi^+,\infty)} \Psi_i(\xi) p_\xi(\xi) \mathrm{d}\xi \right| .$$

The truncation error $\varepsilon_{\mu_\mathrm{u}}$ in the Monomial Chaos approximation of the mean μ_u due to the truncation of the Monomial Chaos expansion at p is given by (3.12),

$$\begin{aligned}
\varepsilon_{\mu_{\mathrm{u}}} &= -\sum_{i=p+1}^{\infty} u_i \int_{-\infty}^{\infty} \Psi_i(\xi) p_\xi(\xi) \mathrm{d}\xi \\
&= -\sum_{i=p+1}^{\infty} u_i \int_{(-\infty,\xi^-]\cup[\xi^+,\infty)} \Psi_i(\xi) p_\xi(\xi) \mathrm{d}\xi \\
&\quad -\sum_{i=p+1}^{\infty} u_i \int_{\xi^-}^{\xi^+} \Psi_i(\xi) p_\xi(\xi) \mathrm{d}\xi, \qquad (3.18)
\end{aligned}$$

with

$$\left|\sum_{i=p+1}^{\infty} u_i \int_{(-\infty,\xi^-]\cup[\xi^+,\infty)} \Psi_i(\xi) p_\xi(\xi) \mathrm{d}\xi\right| \leq$$

$$\sum_{i=0}^{\infty} |u_i| \left|\int_{(-\infty,\xi^-]\cup[\xi^+,\infty)} \Psi_i(\xi) p_\xi(\xi) \mathrm{d}\xi\right|.$$

According to the assumption, $|\tilde{\varepsilon}_{\mu_{\mathrm{u}}}| \ll |\varepsilon_{\mu_{\mathrm{u}}}|$. ☐

Proposition 2. *Let $\xi(\omega) \in (-\infty, \infty)$, and let $\xi(\omega) \in (\xi^-, \xi^+)$ be the domain of convergence of the Monomial Chaos expansion of $u(\omega)$, (3.2). If* (i) *the probability density $p_\xi(\xi)$ of $\xi(\omega)$ decreases fast enough as $\xi \rightarrow \pm\infty$ such that*

$$\left|\sum_{i=0}^{\infty} u_i \int_{(-\infty,\xi^-]\cup[\xi^+,\infty)} \Psi_i(\xi) p_\xi(\xi) \mathrm{d}\xi\right| \ll \left|\sum_{i=0}^{\infty} u_i \int_{\xi^-}^{\xi^+} \Psi_i(\xi) p_\xi(\xi) \mathrm{d}\xi\right|, \qquad (3.19)$$

or (ii) *the probability density $p_\xi(\xi)$ of $\xi(\omega)$ decreases fast enough as $\xi \rightarrow \pm\infty$ such that (3.16) holds and the probability density $p_\xi(\xi)$of $\xi(\omega)$ decreases fast enough as $\xi \rightarrow \pm\infty$ such that*

$$\left|\sum_{i=p+1}^{\infty} u_i \int_{-\infty}^{\infty} \Psi_i(\xi) p_\xi(\xi) \mathrm{d}\xi\right| \ll \left|\sum_{i=0}^{p} u_i \int_{-\infty}^{\infty} \Psi_i(\xi) p_\xi(\xi) \mathrm{d}\xi\right|, \qquad (3.20)$$

then $|\tilde{\varepsilon}_{\mu_{\mathrm{u}}}| \ll |\mu_{\mathrm{u}}|$.

Proof. The error $\tilde{\varepsilon}_{\mu_\mathrm{u}}$ in the Monomial Chaos approximation of the mean μ_u due to the divergence in $\xi(\omega) \in (-\infty, \xi^-] \cup [\xi^+, \infty)$ is given by (3.17),

$$\tilde{\varepsilon}_{\mu_\mathrm{u}} = \sum_{i=0}^{\infty} u_i \int_{(-\infty,\xi^-]\cup[\xi^+,\infty)} \Psi_i(\xi) p_\xi(\xi) \mathrm{d}\xi.$$

The mean μ_u is given by (3.8) and (3.9), which can be written as

$$\mu_\mathrm{u} = \sum_{i=0}^{\infty} u_i \int_{(-\infty,\xi^-]\cup[\xi^+,\infty)} \Psi_i(\xi) p_\xi(\xi) \mathrm{d}\xi + \sum_{i=0}^{\infty} u_i \int_{\xi^-}^{\xi^+} \Psi_i(\xi) p_\xi(\xi) \mathrm{d}\xi. \quad (3.21)$$

According to assumption (i), $|\tilde{\varepsilon}_{\mu_\mathrm{u}}| \ll |\mu_\mathrm{u}|$. The mean μ_u based on an infinite Monomial Chaos series expansion of $u(\omega)$ is given by (3.8) and (3.9), which can also be written as

$$\mu_\mathrm{u} = \sum_{i=0}^{p} u_i \int_{-\infty}^{\infty} \Psi_i(\xi) p_\xi(\xi) \mathrm{d}\xi + \sum_{i=p+1}^{\infty} u_i \int_{-\infty}^{\infty} \Psi_i(\xi) p_\xi(\xi) \mathrm{d}\xi. \quad (3.22)$$

The error $\varepsilon_{\mu_\mathrm{u}}$ in the Monomial Chaos approximation of the mean μ_u due to the truncation of the Monomial Chaos expansion at p is given by (3.12),

$$\varepsilon_{\mu_\mathrm{u}} = - \sum_{i=p+1}^{\infty} u_i \int_{-\infty}^{\infty} \Psi_i(\xi) p_\xi(\xi) \mathrm{d}\xi. \quad (3.23)$$

According to assumption (ii), we have $|\varepsilon_{\mu_\mathrm{u}}| \ll |\mu_\mathrm{u}|$. The result of Proposition 3.1 gives $|\tilde{\varepsilon}_{\mu_\mathrm{u}}| \ll |\mu_\mathrm{u}|$. ☐

An example of a probability distribution that can satisfy the assumptions of Propositions 1 and 2 is the Gaussian distribution with density function $p_\xi(\xi) = (1/\sqrt{2\pi\sigma_\xi^2}) \exp(-(\xi - \mu_\xi)^2/(2\sigma_\xi^2))$, and μ_ξ and σ_ξ^2 the mean and variance of $\xi(\omega)$, respectively. This probability density function is exponentially decreasing as $\xi \to \pm\infty$. Whether a given Gaussian probability distribution satisfies the assumptions depends on the combination of a not too large variance of the uncertain input parameter through σ_ξ^2 and sufficient regularity of the uncertain variable $u(\omega)$ through $\{u_i\}_{i=0}^{\infty}$, ξ^-, and ξ^+. One can use (3.16), (3.19), and (3.20) to verify whether the Monomial Chaos expansion of a certain order p is appropriate to use in a particular application. Similar propositions hold for the variance σ_u^2 and the errors $\tilde{\varepsilon}_{\sigma_\mathrm{u}^2}$ and $\varepsilon_{\sigma_\mathrm{u}^2}$.

3.3 Application of Monomial Chaos

In this section the Monomial Chaos is applied to the Burgers equation. The test problem is intended for demonstrating the properties of Monomial Chaos applied to a nonlinear problem and for comparing the results to those of other methods. The Burgers equation is often used to study the nonlinear advection-diffusion phenomena of fluid dynamics in one dimension [1], and also in combination with the effect of uncertainty [63, 103, 116]. The efficiency of uncertainty quantification in computational fluid dynamics applications is important, since deterministically fluid dynamics simulations can already result in high computational costs. The Monomial Chaos formulation for the Burgers equation is given in section 3.3.1. In section 3.3.2 numerical results for Monomial Chaos are presented.

3.3.1 Burgers' equation

In this section the one-dimensional steady nonlinear advection-diffusion problem known as the viscous Burgers equation is considered [1]. The Burgers equation for the velocity $u(x,\omega)$ in one dimension is given by

$$u\frac{\partial u}{\partial x} - \nu\frac{\partial^2 u}{\partial x^2} = 0, \qquad x \in [0,1], \tag{3.24}$$

with an uncertain viscosity $\nu(\omega)$. The deterministic boundary conditions are $u(0,\omega) = 1$ and $u(1,\omega) = 0$. The solution of the deterministic variant of (3.24) is shown in Figure 3.1 for several values of the viscosity $\nu = \{0; 0.25; 0.5; 1; 2; \infty\}$. In Figure 3.1 also the sensor location $x_{\mathrm{sl}} = 0.5$ is shown. The Monomial Chaos expansions for the uncertain viscosity $\nu(\omega)$ and the velocity $u(x,\omega)$ are

$$\nu(\omega) = \sum_{j=0}^{1} \nu_j \Psi_j(\xi(\omega)), \qquad u(x,\omega) = \sum_{i=0}^{\infty} u_i(x)\Psi_i(\xi(\omega)), \tag{3.25}$$

where $\xi(\omega)$ is a linear transformation of $\nu(\omega)$ to a standard domain and $\{\Psi_i(\xi)\}_{i=0}^{\infty}$ are monomials around $\xi(\omega) = \mu_\xi$ given by (3.3). The expansion coefficients $\{\nu_j\}_{j=0}^{1}$ of the viscosity with a known uncertainty distribution are given by

$$\nu_j = \frac{1}{j!}\frac{\mathrm{d}^j \nu}{\mathrm{d}\xi^j}\bigg|_{\xi=\mu_\xi}, \qquad j = 0, 1, \tag{3.26}$$

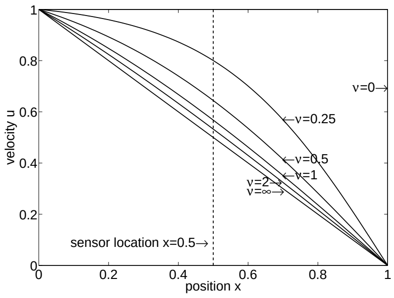

Figure 3.1: Deterministic solution of the nonlinear advection-diffusion problem for several values of the viscosity parameter $\nu = \{0; 0.25; 0.5; 1; 2; \infty\}$.

where $\frac{\mathrm{d}^j \nu}{\mathrm{d}\xi^j}|_{\mu_\xi}$ is known. Substituting the Monomial Chaos expansions (3.25) into the Burgers equation (3.24) results in

$$\sum_{i=0}^{\infty}\sum_{j=0}^{\infty} \Psi_i(\xi)\Psi_j(\xi) u_j \frac{\mathrm{d}u_i}{\mathrm{d}x} - \sum_{i=0}^{\infty}\sum_{j=0}^{1} \Psi_i(\xi)\Psi_j(\xi)\nu_j \frac{\mathrm{d}^2 u_i}{\mathrm{d}x^2} = 0. \tag{3.27}$$

Taking the $k\mathrm{th}$ derivative of (3.27) with respect to ξ for $\xi(\omega) = \mu_\xi$ and using the Leibniz identity and property (3.4) results in a differential equation for $u_k(x)$,

$$\sum_{l=0}^{k} \binom{k}{l} u_{k-l}(x) \frac{\mathrm{d}u_l}{\mathrm{d}x} - \sum_{l=\max\{0,k-1\}}^{k} \binom{k}{l} \nu_{k-l} \frac{\mathrm{d}^2 u_l}{\mathrm{d}x^2} = 0, \tag{3.28}$$

for $k = 0, 1, \ldots$. Terms without $u_k(x)$ can be brought to the right-hand side of (3.28), which results in

$$u_0 \frac{\mathrm{d}u_0}{\mathrm{d}x} - \nu_0 \frac{\mathrm{d}^2 u_0}{\mathrm{d}x^2} = 0, \tag{3.29}$$

for $k = 0$ and

$$u_k \frac{\mathrm{d}u_0}{\mathrm{d}x} + u_0 \frac{\mathrm{d}u_k}{\mathrm{d}x} - \nu_0 \frac{\mathrm{d}^2 u_k}{\mathrm{d}x^2} = -\sum_{l=1}^{k-1} \binom{k}{l} u_{k-l}(x) \frac{\mathrm{d}u_l}{\mathrm{d}x} + k\nu_1 \frac{\mathrm{d}^2 u_{k-1}}{\mathrm{d}x^2}, \tag{3.30}$$

for $k = 1, 2, \ldots$. As mentioned before, the equation for $k = 0$, (3.29), coincides with the deterministic problem for the mean value of the uncertain viscosity ν_0. Equations (3.30) form a decoupled set of equations for the higher-order Monomial Chaos coefficients $u_k(x)$, with $k = 1, 2, \ldots$, as function of $\{u_j(x)\}_{j=0}^{k-1}$ which can be solved sequentially for increasing k. These equations are linear in $u_k(x)$. The computational work for solving each equation of (3.30) is equivalent to one Newton iteration for solving (3.29). Therefore, Monomial Chaos results in relatively low computational costs per additional Polynomial Chaos order compared to the deterministic solve.

A $p\mathrm{th}$-order approximation of the solution for $u(x, \omega)$ can be obtained by truncating the monomial expansion for $u(x, \omega)$ in (3.25) at p. The error estimates (3.14) and (3.15) can be used to determine a suitable Polynomial Chaos order p of the approximation. Equations (3.8) and (3.10) can be used to determine the approximation of the mean and the variance of the velocity $u(x, \omega)$.

3.3.2 Results for Burgers' equation

In this section results of the Monomial Chaos for the Burgers equation are presented. In section 3.4, the results of the Monomial Chaos approach are compared to results of the perturbation method, the Galerkin Polynomial Chaos method, and a non-intrusive Polynomial Chaos method as reviewed in appendix A. For this comparison two error measures are used for the error in the mean $\varepsilon_{\mu_\mathrm{u}}(x)$ and the variance $\varepsilon_{\sigma^2_\mathrm{u}}(x)$ at the sensor location $x_\mathrm{sl} = 0.5$:

$$\varepsilon_{\mu_\mathrm{u}} = \left| \frac{\mu_\mathrm{u}(x_\mathrm{sl}) - \mu_\mathrm{u,ref}(x_\mathrm{sl})}{\mu_\mathrm{u,ref}(x_\mathrm{sl})} \right|, \qquad \varepsilon_{\sigma^2_\mathrm{u}} = \left| \frac{\sigma^2_\mathrm{u}(x_\mathrm{sl}) - \sigma^2_\mathrm{u,ref}(x_\mathrm{sl})}{\sigma^2_\mathrm{u,ref}(x_\mathrm{sl})} \right|. \tag{3.31}$$

The reference solution is a Monte Carlo simulation based on 10^6 realizations of the uncertain parameter $\nu(\omega)$ evenly spaced in sample space $\omega \in [0, 1]$. Approximations of the probability distribution function and the probability density function are also presented. A second-order finite volume method is used to discretize the spatial domain. The nonlinear problem is solved using Newton linearization with an appropriate convergence criterion $\varepsilon_\mathrm{nl} = 10^{-9}$ for the L_∞-norm of the residual, which results for this problem in four Newton iterations.

The mean value of the uncertain input is assumed to be $\mu_\nu = 1$. Probability distributions with either a finite or a (semi-)infinite support of the uncertain viscosity $\nu(\omega)$ are considered. The uniform distribution is chosen for the distribution on the finite domain. This corresponds to the assumption of an interval uncertainty, which is often used in practical applications in case not enough information is available to prescribe an uncertainty distribution. The input coefficient of variation for the uniform distribution is $\mathrm{cov}_\nu = 0.3$. Physical uncertainties are often described using a normal distribution. Since the viscosity is a positive physical parameter, the lognormal distribution is selected instead of the normal distribution for the distribution on the (semi-)infinite

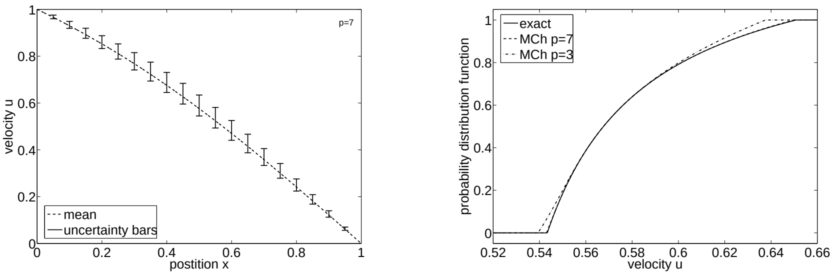

(a) mean and uncertainty bars

(b) distribution function at x_{sl}

Figure 3.2: Monomial Chaos (MCh) results for the uniform input distribution.

domain. For the lognormal distribution an input coefficient of variation of $\mathrm{cov}_\nu = 0.2$ is considered to limit the main parameter variations to the same range as for the uniform distribution. It has been verified that variation of the input coefficient of variation cov_ν and the choice of the sensor location x_{sl} do not affect the results significantly in comparison with the other methods.

3.3.2.1 Results for the uniform input distribution

In Figure 3.2 the Monomial Chaos results for the uniform input distribution are presented. In Figure 3.2a the mean μ_{u} and the 90% uncertainty intervals are given as function of x. The uncertainty is largest in the interior of the domain due to the deterministic boundary conditions. The uncertainty bars are asymmetrical with respect to the mean, which was expected from the deterministic parameter study of Figure 3.1. In Figure 3.2b the approximation of the probability distribution function at the sensor location x_{sl} is shown. The Monomial Chaos approximations for $p = 3$ and $p = 7$ are compared to the reference solution. The $7\mathrm{th}$-order approximation is very accurate, and the $3\mathrm{rd}$-order approximation results in a less accurate resolution of the tails of the distribution.

In Figure 3.3 the error convergence of the Monomial Chaos is given as a function of both the Polynomial Chaos order and the computational work for the uniform input distribution. In the same figure results for the perturbation method are given, which are discussed in section 3.4. The mean and the variance converge on average exponentially as functions of Polynomial Chaos order; see Figure 3.3a. The odd coefficients do

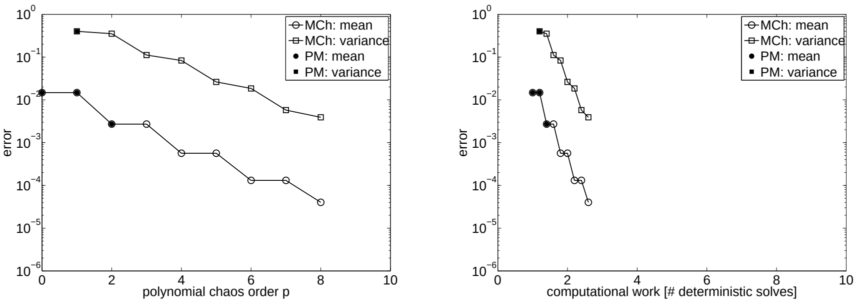

(a) Polynomial Chaos order (b) computational work

Figure 3.3: Error convergence of the Monomial Chaos (MCh) and the perturbation method (PM) for the uniform input distribution.

not contribute to the approximation of the mean (3.8), since the central moments $\mu_{\nu,i}$ of $\nu(\omega)$ are zero for odd i. This is the reason for the staircase convergence of the approximation of the mean.

In Figure 3.3b, the error convergence as a function of the computational work is given in terms of the equivalent number of deterministic solves. The error convergence with respect to computational work is four times faster than the convergence with respect to Polynomial Chaos order. For $p = 0$ the Monomial Chaos results in a deterministic solve for the mean value of the uncertain input μ_ν. In this case four Newton iterations are required to solve the nonlinear problem. Per additional Polynomial Chaos order a linear problem has to be solved. The computational work for these linear solves is equivalent to one Newton iteration for the nonlinear problem. For an 8th-order Monomial Chaos approximation of the mean with an error of $1 \cdot 10^{-5}$ this results in computational costs equivalent to three deterministic solves. These results depend on the number of Newton iterations required for the deterministic problem.

3.3.2.2 Results for the lognormal input distribution

The results of the Monomial Chaos for the lognormal input distribution are given in Figure 3.4. In Figure 3.4a the Monomial Chaos approximation of the probability density function for $p = 3$ and $p = 7$ is compared to the reference solution at the sensor location x_{sl}. Especially near the tails of the distribution the 7th-order approximation is more accurate than the 3rd-order approximation. In Figure 3.4b the weighted error

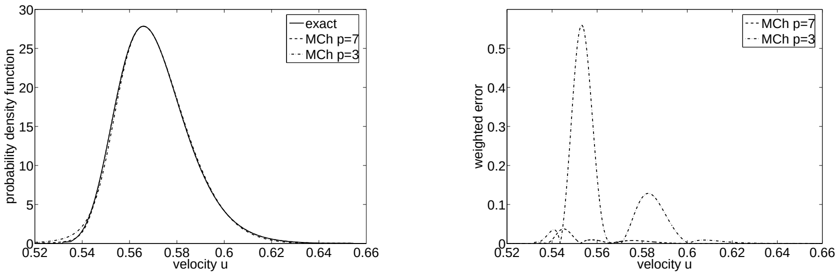

(a) probability density

(b) weighted error

Figure 3.4: Monomial Chaos (MCh) results for the lognormal input distribution.

in the approximation of the probability density function is shown. The error weighted with its probability is small near the point of highest probability, which corresponds approximately to μ_ν, and it vanishes in the tails.

In Figure 3.5 the error convergence of the Monomial Chaos is given for the lognormal input distribution. The mean and the variance converge, but the error convergence is less regular than for the uniform input distribution. Initially the convergence is less smooth due to the alternating over- and underestimation in combination with the asymmetrical input distribution. The first-order coefficient $u_1(x_{\mathrm{sl}})$ has no contribution to the approximation of the mean, since the first-order central moment $\mu_{\nu,1}$ of $\nu(\omega)$ is by definition zero. The error convergence with respect to computational work is again four times faster than with respect to polynomial order; see Figure 3.5b.

3.4 Comparison with other methods

In this section the results of the Monomial Chaos for the Burgers equation are compared to the results of the perturbation method [45], the Polynomial Chaos method [27], and a non-intrusive Polynomial Chaos method [36]. An error convergence study with respect to the Monte Carlo reference solution is performed as a function of Polynomial Chaos order and computational work. For the Galerkin Polynomial Chaos method an optimal polynomial basis is constructed based on the input uncertainty distribution. For a non-intrusive Polynomial Chaos method the solution is not unique since the samples ξ_k in random space in (A.8) can be chosen arbitrarily [36]. Here the sampling points are

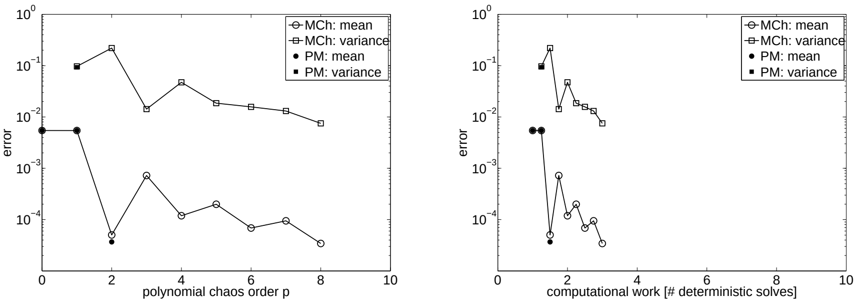

(a) polynomial order (b) computational work

Figure 3.5: Error convergence of the Monomial Chaos (MCh) and the perturbation method (PM) for the lognormal input distribution.

chosen uniformly distributed in ω.

3.4.1 Comparison with the perturbation method

In contrast with the Monomial Chaos approach, the perturbation method results only in low-order approximations of the mean and the variance. These results are compared to the results of the Monomial Chaos in Figures 3.3 and 3.5 for the uniform and lognormal input distribution, respectively. The results of the perturbation method are similar to those of the Monomial Chaos for $p = 0, 1, 2$. Higher-order Monomial Chaos approximations for the uniform input distribution are orders of magnitude more accurate than those of the perturbation method. This demonstrates that the Monomial Chaos method can be viewed as an extension of the perturbation method to higher-order approximations of the mean, the variance, and the distribution function. Also the computational costs of the Monomial Chaos approach and the perturbation method of the same order are similar; see Figures 3.3b and 3.5b. For higher-order approximations the Monomial Chaos approach maintains these low computational costs per additional Polynomial Chaos order.

3.4.2 Comparison with the Galerkin Polynomial Chaos method

The mean and variance approximations of the Monomial Chaos approach and the Galerkin Polynomial Chaos method are compared in Figures 3.6 and 3.7 for the uni-

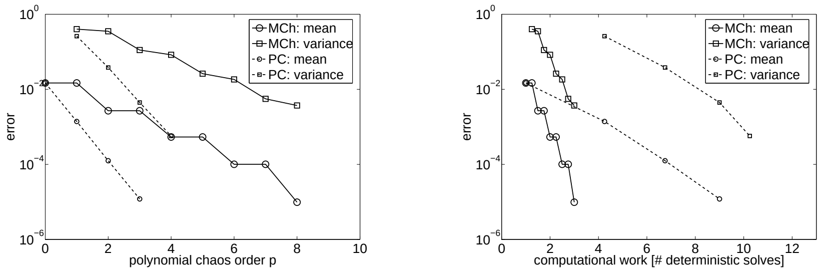

(a) polynomial order

(b) computational work

Figure 3.6: Error convergence of the Monomial Chaos (MCh) and the Galerkin Polynomial Chaos (PC) for the uniform input distribution.

form and lognormal input distribution, respectively. In terms of Polynomial Chaos order, the Galerkin Polynomial Chaos method results in exponential and faster convergence than the Monomial Chaos approach; see Figures 3.6a and 3.7a. However, solving the coupled set of nonlinear equations in the Galerkin Polynomial Chaos method results in a relatively fast increase of computational work per Polynomial Chaos order in comparison with the Monomial Chaos approach. Let p be the Polynomial Chaos order, n_{N} be the number of Newton iterations for solving the nonlinear problem, and n_{GS} be the number of Gauss-Seidel iterations for solving the coupled system of the Galerkin Polynomial Chaos. Then the Monomial Chaos approach results in an amount of computational work equivalent to $(\frac{p}{n_{\mathrm{N}}} + 1)$ deterministic solves. The computational work for the Galerkin Polynomial Chaos is equivalent to $n_{\mathrm{GS}}(p + 1)$ deterministic solves. Therefore, in this case the Monomial Chaos approach converges as a function of computational work by approximately a factor of three faster than the Galerkin Polynomial Chaos method; see Figures 3.6b and 3.7b.

3.4.3 Comparison with a non-intrusive Polynomial Chaos method

In Figures 3.8 and 3.9 the error convergence of the Monomial Chaos and a non-intrusive Polynomial Chaos method is compared for the uniform and lognormal distribution, respectively. The non-intrusive Polynomial Chaos method achieves a slightly higher error convergence rate as a function of the Polynomial Chaos order; see Figures 3.8a and 3.9a. The absolute errors are approximately of the same order of magnitude as

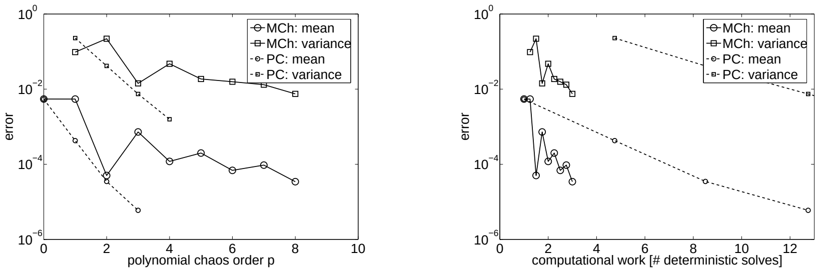

(a) polynomial order

(b) computational work

Figure 3.7: Error convergence of the Monomial Chaos (MCh) and the Galerkin Polynomial Chaos (PC) for the lognormal input distribution.

those of the Monomial Chaos. The computational work of the non-intrusive Polynomial Chaos method per additional Polynomial Chaos order is equivalent to a nonlinear deterministic solve. So, the non-intrusive Polynomial Chaos results in an amount of computational work equivalent to $(p+1)$ deterministic solves compared to $(\frac{p}{n_{\mathrm{N}}}+1)$ for the Monomial Chaos approach. This results in this case in an approximately two times higher error convergence rate as a function of computational work for the Monomial Chaos approach compared to the non-intrusive Polynomial Chaos method; see Figures 3.8b and 3.9b.

3.5 Application to two-dimensional boundary layer flow

In this section the Monomial Chaos approach is applied to a two-dimensional incompressible boundary layer flow as a standard test problem of computational fluid dynamics [89]. Uncertainty quantification in computational fluid dynamics can be highly expensive in practical applications due to the large computational work already involved in solving the deterministic problem. Monomial Chaos can be a computationally efficient alternative for uncertainty quantification in this type of problem.

For two-dimensional flow along a flat plate the Navier-Stokes equations of viscous fluid dynamics reduce to the nonlinear two-dimensional incompressible boundary layer equations

$$\frac{\partial u}{\partial x}+\frac{\partial v}{\partial y}=0, \tag{3.32}$$

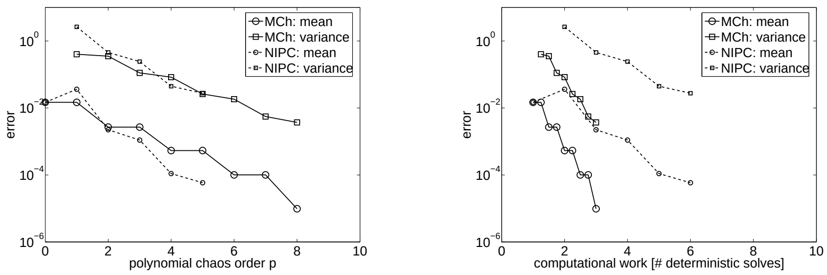

(a) polynomial order

(b) computational work

Figure 3.8: Error convergence of the Monomial Chaos (MCh) and a non-intrusive Polynomial Chaos method (NIPC) for the uniform input distribution.

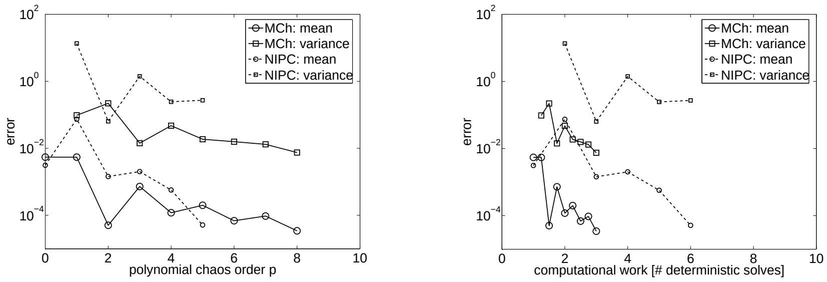

(a) polynomial order

(b) computational work

Figure 3.9: Error convergence of the Monomial Chaos (MCh) and a non-intrusive Polynomial Chaos method (NIPC) for the lognormal input distribution.

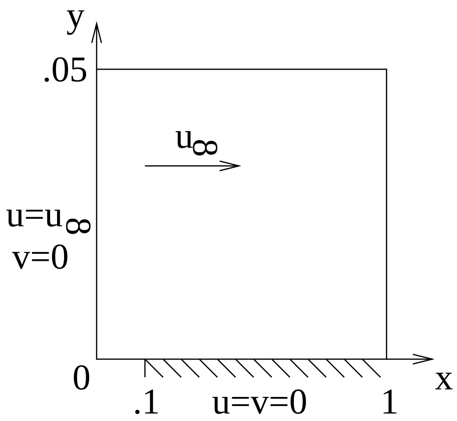

Figure 3.10: The two-dimensional boundary layer flow problem.

$$\rho u \frac{\partial u}{\partial x} + \rho v \frac{\partial u}{\partial y} - \mu \frac{\partial^2 u}{\partial y^2} = 0, \tag{3.33}$$

where u and v are the velocity components parallel and perpendicular to the plate, respectively. The flow is assumed to be laminar, the pressure gradient normal to the plate is neglected, and the density ρ and viscosity μ are assumed to be uniform and independent of temperature. The boundary layer equations describe the conservation of mass (3.32) and the conservation of momentum in the free stream direction (3.33). The flat plate is aligned with the free stream direction x; see Figure 3.10. The free stream velocity u_∞ equals unity, and the density at standard sea level conditions, $\rho_{\mathrm{ISA}} = 1.225$kg/m^3, is used. The computational domain has length 1m and height 0.05m and is discretized with cells of length $\Delta x = 1 \cdot 10^{-3}$m with an aspect ratio of 2. A mixed upwind-central discretization is used. The flat plate of length 0.9m starts at $x = 0.1$m. To solve the deterministic problem, eight Newton iterations were required to reach the convergence criterion of $\varepsilon_{\mathrm{u}} = 1 \cdot 10^{-4}$ in the L$_1$-norm.

The uncertainty is introduced in terms of an uncertain dynamic viscosity coefficient $\mu(\omega)$. The uncertainty is described by a lognormal distribution, since viscosity is a positive physical parameter. The mean value is the viscosity at standard sea level conditions, $\mu_{\mathrm{ISA}} = 1.789 \cdot 10^{-5}$kg/ms, and the coefficient of variation is $\mathrm{cov}_\mu = 5\%$. The effect of the uncertainty in the viscosity on the velocity field and the drag of the flat plate are considered.

A third-order Monomial Chaos expansion is employed to solve for the uncertainty

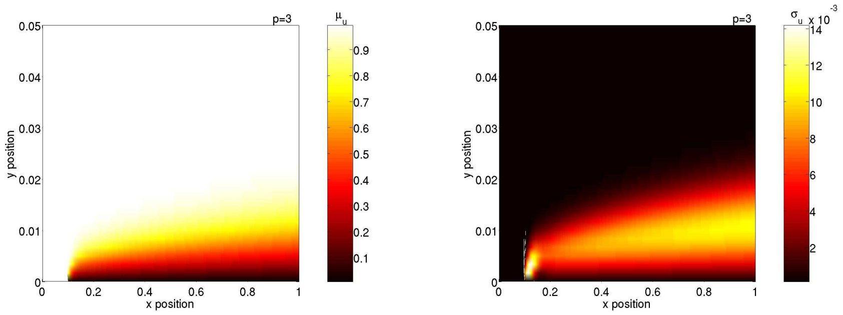

(a) mean $\mu_u(x,y)$ (b) standard deviation $\sigma_\mu(x,y)$

Figure 3.11: Uncertain u-velocity field in the two-dimensional boundary layer flow problem subject to uncertain viscosity.

propagation in the boundary layer flow. The uncertain velocity components $u(x,y,\omega)$ and $v(x,y,\omega)$ and the viscosity $\mu(\omega)$ are expanded in a Monomial Chaos expansion. After substitution and differentiation of the governing equations (3.32) and (3.33), the uncertainty quantification problem is given by

$$\frac{\partial u_k}{\partial x}+\frac{\partial v_k}{\partial y}=0, \tag{3.34}$$

$$\sum_{l=0}^{k}\binom{k}{l}u_{k-l}\frac{\partial u_l}{\partial x}+\sum_{l=0}^{k}\binom{k}{l}v_{k-l}\frac{\partial u_l}{\partial y}-\sum_{l=\max\{0,k-1\}}^{k}\binom{k}{l}\mu_{k-l}\frac{\partial^2 u_l}{\partial y^2}=0, \tag{3.35}$$

for $k=\{0,1,2,3\}$. In Figure 3.11 the results for the mean $\mu_{\mathrm{u}}(x,y)$ and the standard deviation $\sigma_{\mathrm{u}}(x,y)$ of the u-velocity field are shown. The presence of the flat plate results in a typical boundary layer behavior of the mean u-velocity field; see Figure 3.11a. The standard deviation of the u-velocity field has local maxima inside the boundary layer and near the leading edge of the flat plate. It vanishes both near the flat plate further downstream and in the outer flow; see Figure 3.11b. The error estimates (3.14) and (3.15) estimate a maximum error of $4\cdot 10^{-6}$ and $8\cdot 10^{-5}$ in the mean and variance field, respectively.

The drag $F_{\mathrm{drag}}(\omega)$ of the two-sided flat plate is a function of the uncertain viscosity

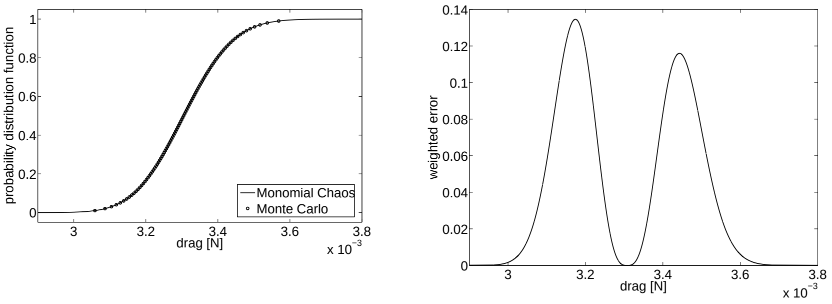

(a) probability distribution function

(b) weighted error

Figure 3.12: Uncertainty distribution of the drag in the two-dimensional boundary layer flow problem subject to uncertain viscosity.

$\mu(\omega)$ and the uncertain velocity gradient at the wall $\frac{\partial u}{\partial y}|_{y=0}(\omega)$,

$$F_{\mathrm{drag}}(\omega) = 2\int_L \tau_{\mathrm{w}}(\omega)\mathrm{d}x = 2\int_{0.1}^{1} \mu(\omega)\frac{\partial u}{\partial y}\bigg|_{y=0}(\omega)\mathrm{d}x, \tag{3.36}$$

where $\tau_{\mathrm{w}}(\omega)$ is the skin friction. In Figure 3.12 the third-order Monomial Chaos approximation of the uncertainty distribution of the drag is shown. In Figure 3.12a the probability distribution function is compared to a Monte Carlo simulation based on 100 realizations uniformly sampled in ω. The results show good agreement. In Figure 3.12b the error in the distribution function weighted by its probability is given. The error is minimal for the drag corresponding to the mean value of the viscosity and vanishes in the tails.

The additional computational costs of the presented uncertainty quantification are equivalent to less than a deterministic solve. As mentioned before, solving the nonlinear deterministic problem requires eight Newton iterations. The third-order Monomial Chaos results in three linear solves in addition to the deterministic solve for the mean value of the uncertain input parameter. So, the additional computational costs for the uncertainty quantification using Monomial Chaos are in this case equivalent to $\frac{3}{8}$ of the computational cost for solving the deterministic problem. Performing uncertainty quantification in computationally intensive practical applications is economically feasible with this order of computational costs.

3.6 Summary

A Monomial Chaos approach is proposed for efficient uncertainty quantification in computationally intensive nonlinear problems. The proposed approach employs a Polynomial Chaos expansion with monomials as basis functions. The equations for the deterministic coefficients are obtained by differentiating the governing equations. Propagating uncertainty through nonlinear equations can be computationally intensive for other Polynomial Chaos methods. It usually results in a set of nonlinear equations which can be coupled. The proposed Monomial Chaos approach results in a decoupled set of linear equations for problems involving polynomial nonlinearities. This reduces the computational work per additional Polynomial Chaos order to the equivalence of a linear Newton iteration. Error estimates for the Monomial Chaos approach have been presented. It has been demonstrated numerically that the Monomial Chaos approach can achieve a 2–3 times faster convergence as a function of computational work than other Polynomial Chaos methods. Application to a two-dimensional flow problem demonstrated that the additional computational work for performing an uncertainty quantification using Monomial Chaos can be smaller than a single deterministic solve.

Chapter 4

Adaptive Stochastic Finite Elements with Newton-Cotes quadrature in simplex elements

Discontinuous solutions of shock waves in supersonic flow and bifurcations phenomena of aeroelastic systems can lead to a high output sensitivity to small input variations. Global polynomial approximations of Polynomial Chaos methods can for these cases result in unreliable predictions of unphysical realizations due to oscillatory overshoots and undershoots at the singularity. More robust multi-element Polynomial Chaos methods based on Gauss-quadrature in hyperrectangular elements can still result locally in unphysical oscillations in the elements and they require completely recomputing the solution in adaptively refined domains. In this chapter an alternative non-intrusive Adaptive Stochastic Finite Elements (ASFE) method based on Newton-Cotes quadrature in simplex elements is developed. The method does not result in unphysical predictions since it preserves the extrema of the samples. The required number of deterministic solves is relatively low, since the samples are both used in approximating the response in multiple elements and reused after refinements. Fourth-order convergence results for a piston problem, a stall flutter model, and transonic flow over a NACA0012 airfoil illustrate that the method resolves the amplification of the input randomness in these problems with discontinuous solutions reliably.

Based on: J.A.S. Witteveen, G.J.A. Loeven, H. Bijl, An Adaptive Stochastic Finite Elements approach based on Newton-Cotes quadrature in simplex elements, Comput. Fluids (2009) in press, DOI:10.1016/j.compfluid.2008.12.002.

4.1 Introduction

In the proposed Adaptive Stochastic Finite Elements approach based on Newton-Cotes quadrature in simplex elements the response is represented by a piecewise polynomial approximation by subdividing probability space into multiple elements. In the elements the response is approximated by collocating the problem in Newton-Cotes quadrature points. Simplex elements are employed, since they are the natural elements for Newton-Cotes quadrature in multiple dimensions. The quadrature approximation in the elements leads to a non-intrusive approach, in which uncoupled deterministic problems are solved for varying parameter values. The required accuracy is obtained by adaptively refining the elements using a refinement measure based on the curvature of the approximation of the response surface weighted by the probability represented by the elements. As measure for the curvature the largest absolute eigenvalue of the Hessian in the elements is used.

The required number of deterministic solves is relatively low compared to a Gauss quadrature adaptive multi-element method based on hypercube elements with respect to the following three points:

1. The tensor grid of Gauss quadrature points for constructing a polynomial approximation of order p results for n uncertain parameters in $(p+1)^n$ samples per element. For Newton-Cotes quadrature in simplex elements the number of samples per element of $(n+p)!/n!p!$ increases less rapidly with p and n.

2. In the Gauss quadrature discretization the decoupled elements all contain $(p+1)^n$ samples. In contrast, most Newton-Cotes quadrature points are located on the boundaries of the elements. The samples are, therefore, used in approximating the response in multiple elements. In the examples it is illustrated that this reduces the average number of samples per element to approximately 2 instead of $(n+p)!/n!p!$.

3. Refining an element using Gauss quadrature points, requires the computation of $(p+1)^n$ new samples in every new element. The deterministic solves on intermediate refinement levels are, therefore, not directly used in the final approximation. The Newton-Cotes quadrature points in the new elements include those of the refined element, such that all samples are reused after successive refinements.

These advantages of Newton-Cotes quadrature typically come forward in a multi-element discretization. For a single-element approximation Gauss quadrature can be more favorable. The number of 3^n samples for the initial grid of $n!$ simplex elements can become large for higher dimensional probability spaces.

Since lower-order expansions are efficient for complex problems [61], the degree of the Newton-Cotes quadrature is limited in this chapter to two, which is known in one-dimension as Simpson's rule. This results in a piecewise quadratic approximation of the response. To preserve extrema of the samples in the piecewise polynomial approximation, the elements are subdivided in subelements with a linear trapezoidal rule approximation of the response where necessary.

The Stochastic Finite Elements formulation considered in this chapter is developed in section 4.2. The adaptive Stochastic Finite Elements approach with Newton-Cotes quadrature in simplex elements is in section 4.3 applied to typical flow problems involving shock waves and bifurcations, which result in singularities in probability space. The properties of the adaptive Stochastic Finite Elements approach are first studied using a one-dimensional piston problem. Separate cases with a discontinuity, a discontinuous derivative, and a smooth response are considered. The input uncertainty is given by up to three independent uncertain parameters. The extension to more than three random dimensions is a geometrical exercise. The effect of the adaptive grid refinement and the degree of the Newton-Cotes quadrature is investigated. The results are compared to those of a global polynomial Stochastic Collocation method and Monte Carlo simulation. The comparison with the global polynomial approximation of the Stochastic Collocation method should be interpreted as mainly a qualitative comparison. Next the method is applied to the bifurcation behavior of an airfoil stall flutter problem with a lognormally distributed external forcing to study the effect of uncertainty on the bifurcation plot. Finally, the adaptive Stochastic Finite Elements approach is applied to transonic flow over a NACA0012 airfoil. The transonic flow field proves to be sensitive to the free stream conditions. The conclusions are summarized in section 4.4.

4.2 Adaptive Stochastic Finite Elements

In this section the adaptive Stochastic Finite Elements approach with Newton-Cotes quadrature in simplex elements is developed. The stochastic adaptive grid refinement strategy is considered in section 4.2.2.

4.2.1 Newton-Cotes quadrature in simplex elements

In a probabilistic description of uncertainty, one is typically interested in the statistical moments of the response. The m^{th} moment $\mathbb{E}(u(\mathbf{x},t,\omega)^m)$ of the probability distribution of the response $u(\mathbf{x},t,\omega)$ given by

$$\mathbb{E}(u(\mathbf{x},t,\omega)^m) = \int_\Omega u(\mathbf{x},t,\omega)^m \mathrm{d}\omega, \tag{4.1}$$

is an integral quantity over probability space. The space of functions mapping probability space Ω onto parameter space A is denoted by Θ. The mapping Θ gives the parameter values which correspond to a realization in probability space Ω. This mapping is defined by the probability distribution of the uncertain parameters.

Stochastic Finite Elements methods divide the integral (4.1) over probability space Ω in a summation of integrals over N_Ω non-overlapping elements Ω_i for $i = 1, \dots, N_\Omega$

$$\mathbb{E}(u(\mathbf{x}, t, \omega)^m) = \sum_{i=1}^{N_\Omega} \int_{\Omega_i} u(\mathbf{x}, t, \omega)^m \mathrm{d}\omega. \tag{4.2}$$

To obtain an uncoupled non-intrusive sampling based approach the integrals over the elements Ω_i are approximated by a quadrature integration rule based on N_s deterministic samples in each element

$$\mathbb{E}(u(\mathbf{x}, t, \omega)^m) \approx \sum_{i=1}^{N_\Omega} \sum_{j=1}^{N_\mathrm{s}} c_{i,j} u_{i,j}(\mathbf{x}, t)^m, \tag{4.3}$$

where $c_{i,j}$ are the quadrature weights and $u_{i,j}(\mathbf{x}, t)$ are the realizations of the response $u(\mathbf{x}, t, \omega)$ for the parameter values $\{a_1(\omega), \dots, a_n(\omega)\}_{i,j}$ in the N_s quadrature points in element i.

Here Newton-Cotes quadrature points are employed, since most of these points are located on the boundaries of the elements. In this way the samples at the quadrature points are used to construct the approximation in multiple elements. The choice of Newton-Cotes quadrature points also implies that some of the samples are located on the outer boundary of parameter domain. If the probability approaches zero at the parameter domain boundary as for a unimodal beta distribution, the sampling points on the domain boundary contribute nonetheless to the construction of the response approximation in the interior of the parameter domain.

The quadrature weights $c_{i,j}$ are defined by the mapping Θ^{-1} of the n-dimensional Newton-Cotes formula of degree d from parameter space A to probability space Ω. The Newton-Cotes quadrature weights are normally given by the integrals of the Lagrange basis polynomials through the quadrature points. Here the weights $c_{i,j}$ are given by the integrals weighted by the probability density of the uncertain input parameters

$$c_{i,j} = \int_{A_i} L_{i,j}(a_1, \dots, a_n) f_\mathrm{a}(a_1, \dots, a_n) \mathrm{d}\mathbf{a}, \tag{4.4}$$

for $i = 1, \dots, N_\Omega$, where $\mathbf{a} = \{a_1, \dots, a_n\}$ is the vector of uncertain input parameters and A_i is the mapping Θ of the element Ω_i to parameter space. This results in a

"Polynomial Chaos" formulation of the Newton-Cotes formulas. The values for the weights $c_{i,j}$ are computed numerically for each element using "normal" Newton-Cotes integration in the element A_i on a fine subgrid with $N_{\mathrm{A_{sub}}}$ n-simplex subelements with $N_{\mathrm{s_{sub}}}$ quadrature points

$$c_{i,j} \approx \sum_{k=1}^{N_{\mathrm{A_{sub}}}} \sum_{l=1}^{N_{\mathrm{s_{sub}}}} e_l L_{i,j,k,l} f_{\mathrm{a}}(a_1, \dots, a_n)_{i,k,l}, \tag{4.5}$$

for $i = 1, \dots, N_\Omega$ and $j = 1, \dots, N_{\mathrm{s}}$, where e_l are the "normal" Newton-Cotes quadrature weights, and $L_{i,j,k,l}$ and $f_{\mathrm{a}}(a_1, \dots, a_n)_{i,k,l}$ are the values of the Lagrange polynomial $L_{i,j}(a_1, \dots, a_n)$ and the probability density of the uncertain parameters $f_{\mathrm{a}}(a_1, \dots, a_n)$ in the quadrature points on the fine subgrid in element A_i. The weights $c_{i,j}$ can be different for every element, since the mapping Θ^{-1} between A and Ω is in general different for different elements.

The elements Ω_i in probability space are defined by discretizing parameter space A by N_Ω n-simplex elements A_i, with $i = 1, \dots, N_\Omega$. An n-simplex is the n-dimensional analogue of a triangle, which results for one-dimensional parameter space in a line segment, for two-dimensions in a triangle, for three-dimensions in a tetrahedron, etc, see Figure 4.1. For more random parameters ($n > 3$) n-dimensional simplex elements can be used. The n-simplex elements are the natural elements for Newton-Cotes quadrature in n dimensions. The volume V_i of the n-simplex elements in parameter space A is given by

$$V_i = \frac{1}{n!} |\det(a_{i,0} - a_{i,1} \quad a_{i,1} - a_{i,2} \quad \dots \quad a_{i,n-1} - a_{i,n})|. \tag{4.6}$$

where $a_{i,j}$ are the $n+1$ vertices of the n-simplex A_i in parameter space A.

The choice of the degree of the Newton-Cotes quadrature is a balance between high-order accuracy in smooth regions and the effectiveness of lower-order approximations near singularities. For complex problems lower-order representations are therefore more effective than higher-order ones. In most of the paper second-degree ($d = 2$) Newton-Cotes quadrature is used, which is known as Simpson's rule. This corresponds to a piecewise quadratic approximation of the response. Extensions to higher orders are possible by using Newton-Cotes quadrature rules of higher degree such as Boole's rule. Second-degree Newton-Cotes quadrature results in $N_{\mathrm{s}} = \binom{n+2}{2}$ samples per element A_i, see Figure 4.1. Most the quadrature points are located on the boundary of the elements ∂A_i such that they can be used for approximating the response in multiple elements.

Near singularities the piecewise quadratic approximation of the second-degree Newton-Cotes quadrature can result in unphysical oscillations. To preserve the extrema of the samples in the piecewise polynomial approximation, where necessary the

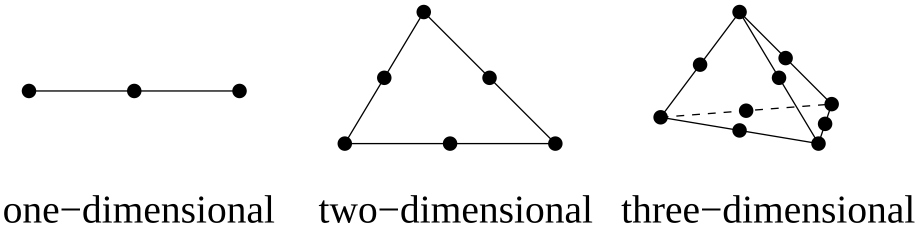

Figure 4.1: The n-simplex elements in parameter space A with the $\binom{n+2}{2}$ samples of the second-degree Newton-Cotes quadrature approximation.

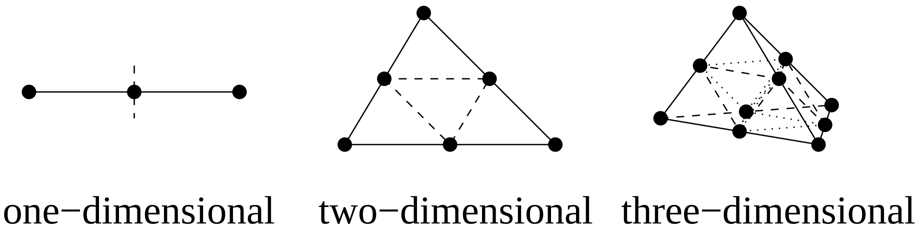

Figure 4.2: The 2^n subelements given by the dashed lines with $n+1$ samples for the linear trapezoidal rule approximation of the response for preserving the extrema of the samples.

elements are subdivided in n-simplex subelements with a linear trapezoidal rule approximation of the response. The 2^n subelements each contain $n+1$ of the $\binom{n+2}{2}$ samples of the original element, see Figure 4.2. An element is split into subelements when the polynomial approximation of the response has an extremum in the element other than in a quadrature point.

4.2.2 Stochastic adaptive grid refinement

For complex, high-dimensional problems multi-element approaches may result in large computational costs. An adaptive refinement strategy can lead to more efficient approximations of complex situations. Here the refinement measure is based on the curvature of the approximation of the response surface in the elements weighted by the probability represented by the elements. As measure for the curvature of the approximation of the response surface the largest absolute eigenvalue of the Hessian in the elements is used, which is common in adaptive refinement of deterministic finite element methods. The Hessian of the polynomial approximation in the element A_i in parameter space is given by

$$H_i(u(\mathbf{x}, t, \omega)) = \begin{bmatrix} \frac{\partial^2 u}{\partial a_1^2} & \frac{\partial^2 u}{\partial a_1 \partial a_2} & \cdots & \frac{\partial^2 u}{\partial a_1 \partial a_n} \\ \frac{\partial^2 u}{\partial a_2 \partial a_1} & \frac{\partial^2 u}{\partial a_2^2} & \cdots & \frac{\partial^2 u}{\partial a_2 \partial a_n} \\ \vdots & \vdots & \ddots & \vdots \\ \frac{\partial^2 u}{\partial a_n \partial a_1} & \frac{\partial^2 u}{\partial a_n \partial a_2} & \cdots & \frac{\partial^2 u}{\partial a_n^2} \end{bmatrix}_i, \tag{4.7}$$

which is constant in the element for the piecewise quadratic approximation of the second-degree Newton-Cotes quadrature. The second-order derivatives are derived from the quadratic approximation of the response through the sampled quadrature points in the elements. In one-dimension the Hessian reduces to the absolute value of the second-order derivative of the response. This refinement measure can be extended to higher-order approximations ($d > 2$) by using the maximum of the Hessian in the elements or by employing higher-order derivatives. In the step of determining the Hessian, no elements are subdivided into subelements with a linear trapezium rule approximation.

The refinement measure is weighted by the probability P_i represented by the elements. For the refinement measure this probability is approximated by a similar relation as (4.6), since the probability of an element is equivalent to its volume in probability space

$$P_i = \frac{1}{n!} |\det(\omega_{i,0} - \omega_{i,1} \quad \omega_{i,1} - \omega_{i,2} \quad \ldots \quad \omega_{i,n-1} - \omega_{i,n})|, \tag{4.8}$$

where $\omega_{i,j}$ is given by the mapping Θ^{-1} of the the vertices $a_{i,j}$ of element A_i to probability space Ω. The refinement measure r_i in the i^{th} element is then defined as

$$r_i = P_i V_i^{N_\text{V}} \max(|\text{eig}_1(H_i(u))|, \ldots, |\text{eig}_n(H_i(u))|), \tag{4.9}$$

where, the factor $V_i^{N_\text{V}}$ compensates for the, in general, increase of the second-order derivatives in smaller elements if they contain a singularity.

The value of N_V is chosen here based on the following theoretical argument. Consider an element Δa in a one-dimensional parameter space $a \in A$, which contains the discontinuity of a step function response surface $u(a)$, see Figure 4.3a. The Hessian (4.7) then reduces to the second derivative in finite difference approximation

$$\frac{\partial^2 u}{\partial a^2} = \frac{u_{-1} - 2u_0 + u_{+1}}{\Delta a^2}. \tag{4.10}$$

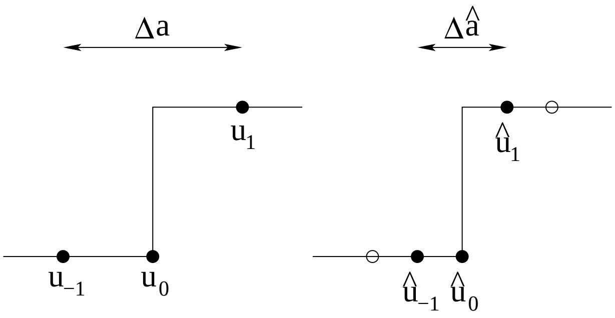

(a) Element Δa (b) Element $\Delta \hat{a}$

Figure 4.3: Sketch of two elements of size Δa and $\Delta \hat{a}$ containing the discontinuity of a step function for deriving the general value $N_{\mathrm{V}} = 2$.

Assume that the element is refined to a smaller element $\Delta \hat{a}$ for which holds $\hat{u}_{-1} = u_{-1}$, $\hat{u}_0 = u_0$, and $\hat{u}_{+1} = u_{+1}$, see Figure 4.3b. The Hessian in the new element is

$$\frac{\partial^2 \hat{u}}{\partial a^2} = \frac{\hat{u}_{-1} - 2\hat{u}_0 + \hat{u}_{+1}}{\Delta \hat{a}^2}. \tag{4.11}$$

Factor N_{V} is then chosen such that the contribution of the Hessian to refinement measure (4.9) in the element with the discontinuity is independent of the size of the element

$$\Delta a^{N_{\mathrm{V}}} \frac{u_{-1} - 2u_0 + u_{+1}}{\Delta a^2} = \Delta \hat{a}^{N_{\mathrm{V}}} \frac{\hat{u}_{-1} - 2\hat{u}_0 + \hat{u}_{+1}}{\Delta \hat{a}^2}, \tag{4.12}$$

$$\left(\frac{\Delta a}{\Delta \hat{a}}\right)^{N_{\mathrm{V}}} = \frac{\hat{u}_{-1} - 2\hat{u}_0 + \hat{u}_{+1}}{u_{-1} - 2u_0 + u_{+1}} \frac{\Delta a^2}{\Delta \hat{a}^2} = \left(\frac{\Delta a}{\Delta \hat{a}}\right)^2, \tag{4.13}$$

which results in $N_{\mathrm{V}} = 2$. The rigorous derivation for this abstract example results in a general value for N_{V}, since every discontinuous response surface can locally be approximated by a step function.

The element with the highest value of the refinement measure is then refined into two n-simplex elements, see Figure 4.4. The longest edge of the element is split into two halves of equal length. An alternative is to use the eigenvector corresponding to the highest absolute eigenvalue to determine which edge to split.

Due to the Newton-Cotes quadrature points there is no need to completely recompute the solution in the refined elements. In fact, only a maximum of $n+1$ new samples

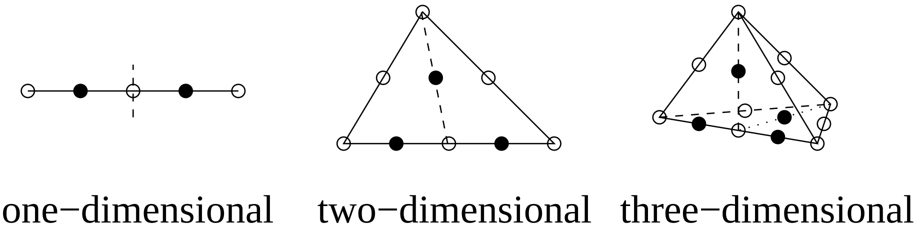

Figure 4.4: Refinement of the n-simplex elements into two elements with the $n + 1$ new samples and the $\binom{n+2}{2}$ samples of the original element given by the dots and the open circles, respectively, for second-degree Newton-Cotes quadrature.

has to be computed for the refinement of second-degree Newton-Cotes quadrature, even though both new elements contain $\binom{n+2}{2}$ quadrature points each. First, all samples in the original element are reused in the refined elements. Second, part of the new samples is used by both refined elements, since most Newton-Cotes quadrature points are located on the boundaries of the elements. Furthermore, the new samples are located on the boundary of the original element can already have been computed while refining neighboring elements.

For comparison, a standard multi-element, piecewise quadratic Stochastic Collocation approach based on the tensor product of Gauss quadrature points in hexahedral elements would require $2 \cdot 3^n$ new deterministic solves for refining an element into two new elements instead of a maximum of $n + 1$ for Newton-Cotes quadrature. This would result for three uncertain input parameters in 54 deterministic solves instead of a maximum of 4 for Newton-Cotes quadrature. A sparse grid approach can reduce the number of deterministic solves required in Stochastic Collocation [117]. Due to the adaptive stochastic grid refinement the number of required Newton-Cotes quadrature samples for discretizing an n dimensional parameter space of n random parameters scales with less than the n-dimensional tensor product.

After the refinement the new refinement measure is computed in the refined elements and the element with the largest refinement measure is again refined, etc. The refinement is stopped when a threshold value for the maximum refinement measure or the maximum number of samples is reached.

The initial grid is given by the coarsest discretization of the n-dimensional rectangle describing the ranges of parameter space using $n!$ n-simplex elements, see Figure 4.5. For more than $n = 3$ random parameters the n-dimensional hyperrectangle describing parameter space is divided in $n!$ n-dimensional simplex elements. Finding

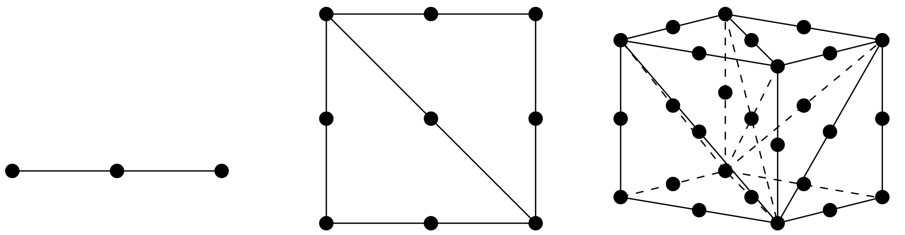

one−dimensional two−dimensional three−dimensional

Figure 4.5: Initial discretization of the n-dimensional cuboid describing the ranges of parameter space A with $n!$ n-simplex elements and 3^n second-degree Newton-Cotes quadrature points.

the initial grid discretization for more than $n = 3$ random parameters is a geometrical exercise in the n-dimensional parameter space. Finite ranges of parameter space can reasonably be obtained by truncating an infinite domain at a threshold value for the distribution without affecting the accuracy significantly in practical applications. The number of samples in the initial grid is given by 3^n.

The algorithm for adaptive Stochastic Finite Elements with Newton-Cotes quadrature in simplex elements can be summarized as follows:

1. Solve the 3^n deterministic problems for the parameter values corresponding to the collocation points in the initial grid of Figure 4.5;

2. Determine the refinement measure (4.9) in the elements of the initial grid;

3. Refine the element with the highest value of the refinement measure according to Figure 4.4;

4. Solve the maximal $n + 1$ deterministic problems for the parameter values corresponding to the new collocation points in the refined element, if they have not been computed before;

5. Determine the refinement measure in the two new elements;

6. Return to step 3 if the threshold value of the maximum refinement measure or the maximum number of samples has not been reached;

7. Split the elements into subelements as in Figure 4.2 with a linear approximation of the response if the quadratic approximation has a maximum in the element other than in a quadrature point;

8. Determine the N_{s} quadrature weights $c_{i,j}$ in the N_Ω elements using (4.5), with $i = 1, \ldots, N_\Omega$ and $j = 1, \ldots, N_{\mathrm{s}}$;

9. Determine the statistical moments of the output $\mathbb{E}(u(\mathbf{x}, t, \omega)^m)$ using (4.3).

The probability distribution function can be found by sorting the response $u(\mathbf{x}, t, \omega)$ to a monotonically increasing function in ω, with $\omega \in [0, 1]$. The algorithm can be parallelized by solving the maximal $n + 1$ deterministic problems in step 4 in parallel and by refining multiple elements with the highest value of the refinement measure simultaneously instead of a single element in step 3.

4.3 Numerical results

In this section numerical results of the adaptive Stochastic Finite Elements approach with Newton-Cotes quadrature in simplex elements are presented for a piston problem, a stall flutter model and transonic flow over a NACA0012 airfoil with uniformly and lognormally distributed random parameters. These test problems are typical examples of practical flow applications involving shock waves and bifurcations, which result in singularities in probability space. The effect of the adaptive grid refinement and the degree of the Newton-Cotes quadrature rule is investigated. The results are compared to those of a Stochastic Collocation approach based on a global polynomial approximation of the response through Gauss quadrature points. The comparison with the Stochastic Collocation approach has mainly to be considered as a qualitative assessment. Reference solutions are obtained by Monte Carlo simulation.

4.3.1 Piston problem

The properties of the adaptive Stochastic Finite Elements approach with Newton-Cotes quadrature in simplex elements are studied for a one-dimensional piston problem with discontinuities and discontinuous derivatives in the response. The effect of a single up to three uncertain input parameters on the instantaneous and total mass flow is considered.

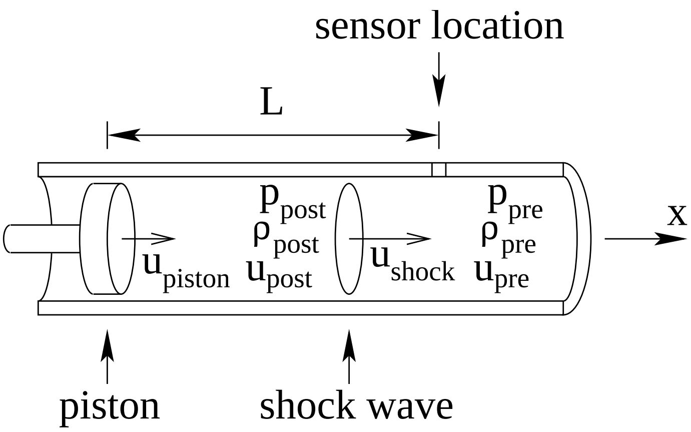

Figure 4.6: The piston problem.

4.3.1.1 Problem description

The piston problem, see Figure 4.6, consists of a one-dimensional flow domain filled with air enclosed by a piston at its left. The piston starts to move to the right at $t = 0$ with a velocity $u_{\mathrm{piston}} > 0$. A shock wave runs with velocity u_{shock} into the ideal gas with constant initial conditions for the pressure p_{pre}, density ρ_{pre} and velocity $u_{\mathrm{pre}} = 0$. Neglecting the effects of viscosity the uniform pressure p_{post}, density ρ_{post} and velocity $u_{\mathrm{post}} = u_{\mathrm{piston}}$ behind the shock wave are governed by the Euler equations. The pressure p_{post} is given by the Rankine-Hugoniot relation

$$p_{\mathrm{post}} - p_{\mathrm{pre}} = \rho_{\mathrm{pre}} c_{\mathrm{pre}} (u_{\mathrm{post}} - u_{\mathrm{pre}}) \sqrt{1 + \frac{\gamma+1}{2\gamma} \frac{p_{\mathrm{post}} - p_{\mathrm{pre}}}{p_{\mathrm{pre}}}}, \tag{4.14}$$

with initial speed of sound $c_{\mathrm{pre}} = \sqrt{\frac{\gamma p_{\mathrm{pre}}}{\rho_{\mathrm{pre}}}}$ and the ratio of specific heats $\gamma = 1.4$. The other flow conditions can be determined from the one-dimensional shock wave relations [15] using the Mach number of the shock wave $\mathrm{Ma}_{\mathrm{shock}}$ given by

$$\mathrm{Ma}_{\mathrm{shock}} = \sqrt{1 + \frac{\gamma+1}{2\gamma} \left(\frac{p_{\mathrm{post}}}{p_{\mathrm{pre}}} - 1 \right)}. \tag{4.15}$$

The instantaneous and total mass flow, $m(t)$ and $M(t)$, are the outputs of interest. Their behavior is considered at a sensor location at a distance L to the right of the initial position of the piston. The response surfaces for $m(t)$ and $M(t)$ contain a discontinuity and a discontinuous derivative, respectively. In terms of the pre- and post-shock conditions the instantaneous mass flow $m(t)$ can be written as

$$m(t) = \begin{cases} \rho_{\mathrm{pre}} u_{\mathrm{pre}}, & t < \frac{L}{u_{\mathrm{shock}}}, \\ \rho_{\mathrm{post}} u_{\mathrm{post}}, & t > \frac{L}{u_{\mathrm{shock}}}. \end{cases} \tag{4.16}$$

The total mass flow $M(t)$ is then given by

$$M(t) = \int_0^t m(\tau)\mathrm{d}\tau. \tag{4.17}$$

In the following the variables are nondimensionalized using a_{pre}, ρ_{pre} and the mean sensor position L. The mean piston velocity and the mean initial pressure are chosen to be $u_{\mathrm{piston}} = 1$ and $p_{\mathrm{pre}} = 1$ for simplicity. The instantaneous and total mass flow are considered at $t = 0.5$.

4.3.1.2 Uncertain piston velocity

First the piston velocity u_{piston} is assumed to be uncertain with a lognormal distribution and coefficient of variation $CV_{\mathrm{u_{piston}}} = 10\%$. The infinite domain of the probability distribution is truncated at a threshold value ε for the distribution. A convergence study demonstrated that the effect of the threshold value of $\varepsilon = 10^{-4}$ on the results is negligible.

Instantaneous mass flow m In Figure 4.7 the response surface u_{piston}–m and the resulting probability distribution function of m are given. The adaptive Stochastic Finite Elements approximation with second-degree Newton-Cotes quadrature is compared with the exact solution for 2, 4 and 8 elements. The samples are given by the dots and the boundaries of the elements are denoted by the bars. The exact solution shows a discontinuity in probability space for the u_{piston} value at which $u_{\mathrm{shock}} = \frac{L}{t}$, see (4.16). In the approximation with 2 elements, the second element is split into two subelements with a linear approximation of the response, see Figures 4.7a and 4.7b. Even for this coarse approximation the solution preserves the monotonicity of the samples, and no artificial oscillations or unphysical values are predicted. The error due to the coarse approximation of the discontinuity is restricted to the subelement containing the discontinuity.

The results of using stochastic adaptive grid refinement are given in Figures 4.7c to 4.7f for an approximation with 4 and 8 elements. The region around the discontinuity is refined with smaller elements while the elements in the rest of the domain remain

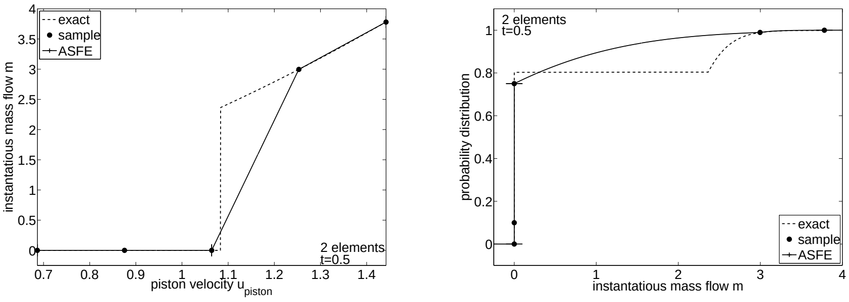

(a) response, 2 elements (b) distribution, 2 elements

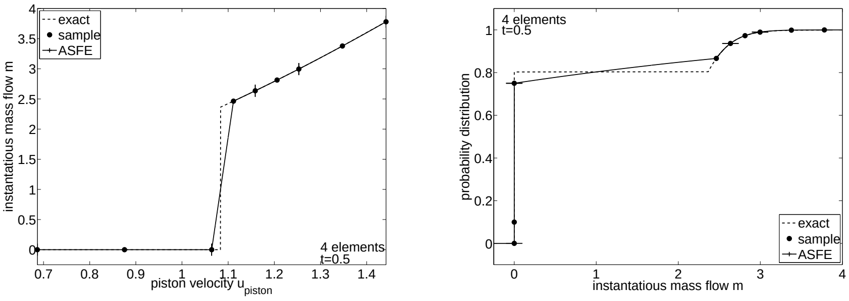

(c) response, 4 elements (d) distribution, 4 elements

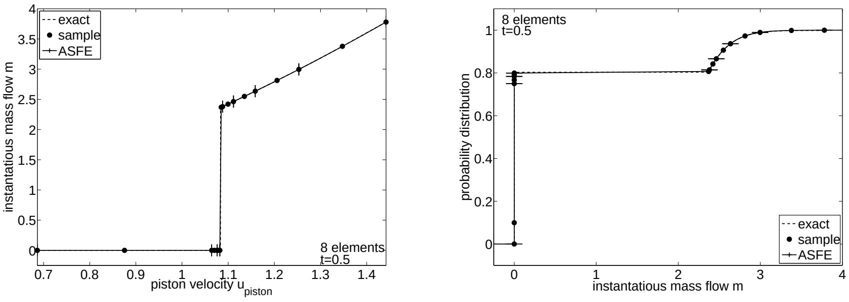

(e) response, 8 elements (f) distribution, 8 elements

Figure 4.7: Response surface and probability distribution of the instantaneous mass flow m at $t = 0.5$ with an uncertain piston velocity u_{piston} by adaptive Stochastic Finite Elements (ASFE) for the piston problem.

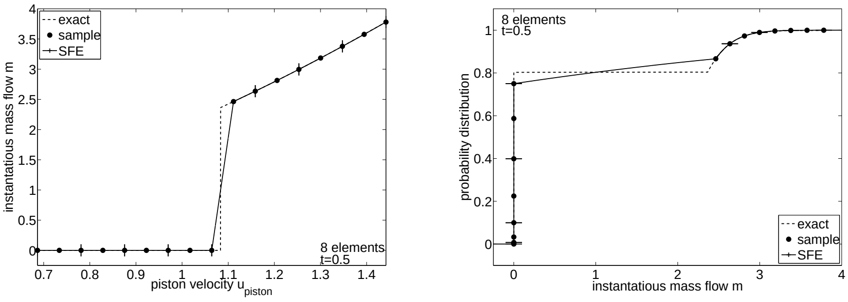

(a) response, 8 elements

(b) distribution, 8 elements

Figure 4.8: Response surface and probability distribution of the instantaneous mass flow m at $t = 0.5$ with an uncertain piston velocity u_{piston} by Stochastic Finite Elements (SFE) based on a uniform grid for the piston problem.

relatively large. This results in an efficient discretization of probability space, which gives for 8 elements a sharp resolution of the discontinuity in both the response surface and the probability distribution function, see Figures 4.7e and 4.7f. The approximation with 8 elements requires 17 deterministic samples.

The effectiveness of the stochastic adaptive grid refinement is demonstrated in comparison with results for a uniform grid. In Figure 4.8 the approximation of the response surface and the probability distribution for a uniform grid of 8 elements is given. The solution is less accurate than the result of stochastic adaptive grid refinement with the same number of elements, see Figures 4.7e and 4.7f. The elements are less refined near the discontinuity, which results in a larger error.

The results of the commonly used Stochastic Collocation approach for the instantaneous mass flow are shown in Figure 4.9. The approximation of the response surface and the probability distribution for 8 samples is shown. The global polynomial approximation of the response surface results in an oscillatory solution due to the discontinuity in probability space. This behavior, which is known as the stochastic Gibbs phenomenon [114], results in an inaccurate approximation of the response surface and the probability distribution. It results in the prediction of unphysical negative values of the instantaneous mass flow m for positive values of the piston velocity u_{piston}. In this case an over 30% probability of unphysical negative m values is predicted, see Figure 4.9b. Increasing the number of samples increases the oscillatory behavior.

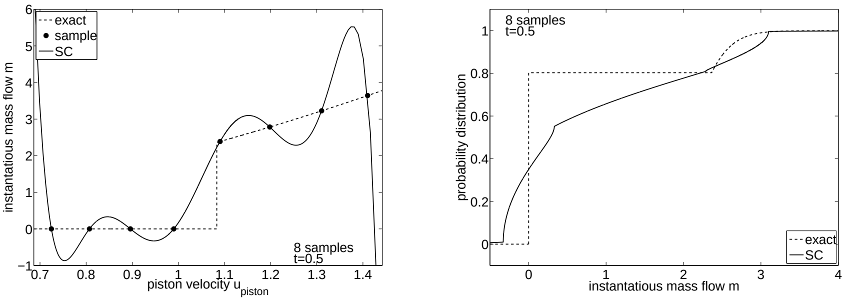

(a) response, 8 samples

(b) distribution, 8 samples

Figure 4.9: Response surface and probability distribution of the instantaneous mass flow m at $t = 0.5$ with an uncertain piston velocity u_{piston} by Stochastic Collocation (SC) for the piston problem.

Effect of the degree of the Newton-Cotes quadrature The effect of the degree of the Newton-Cotes quadrature is studied by considering, next to Simpson's rule, also the midpoint rule and the trapezoid rule approximations in the elements. In Figure 4.10 the approximation of the response surface and probability distribution of m for the midpoint rule and the trapezoid rule are shown for 8 uniformly distributed elements. Employing the midpoint rule in the elements results in a piecewise constant approximation of the response and distribution similar to results of Wiener-Haar expansions [60]. The trapezoid rule results in a piecewise linear approximation of the mass flow. This results for the part of probability space behind the shock wave $u_{\mathrm{piston}} > 1.1$ in a more accurate approximation for one additional deterministic solve compared to using the midpoint rule in this case of a single uncertain parameter.

The effect of the degree of the Newton-Cotes quadrature on the error convergence is studied and compared to that of the Stochastic Collocation approach in Figure 4.11 for the instantaneous mass flow m at $t = 1$ instead of $t = 0.5$ and with a mean piston velocity of $u_{\mathrm{piston}} = 0.5$. At $t = 1$ the shock wave has passed the sensor location for all $u_{\mathrm{piston}} > 0$, since $u_{\mathrm{shock}} > a_{\mathrm{pre}}$. This results in a smooth response surface m–u_{piston}. The approximations with the midpoint rule ($d = 0$), trapezoid rule ($d = 1$), and Simpson's rule ($d = 2$) are considered. The error convergence for the mean and variance of the instantaneous mass flow m at $t = 1$ without stochastic adaptive grid refinement is shown.

Both the midpoint rule and the trapezoid rule converge with second-order accu-

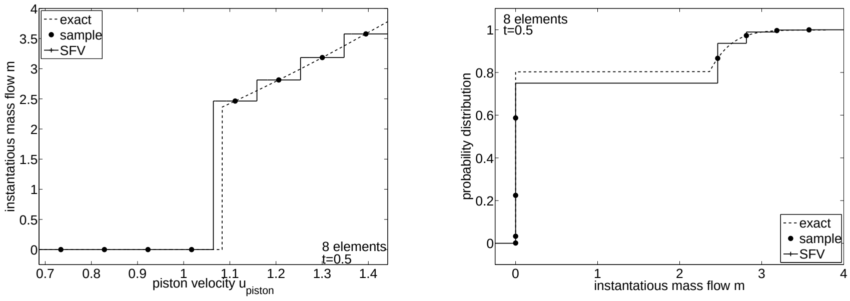

(a) midpoint, response (b) midpoint, distribution

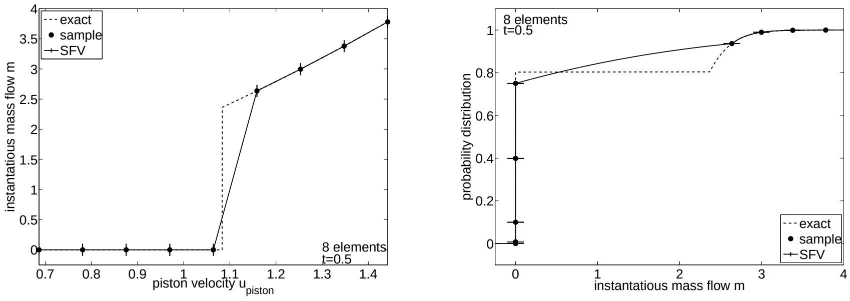

(c) trapezoid, response (d) trapezoid, distribution

Figure 4.10: Response surface and probability distribution of Stochastic Finite Elements (SFE) based on the midpoint rule and trapezoid rule on a uniform grid of 8 elements for the instantaneous mass flow m at $t = 0.5$ with an uncertain piston velocity u_{piston} for the piston problem.

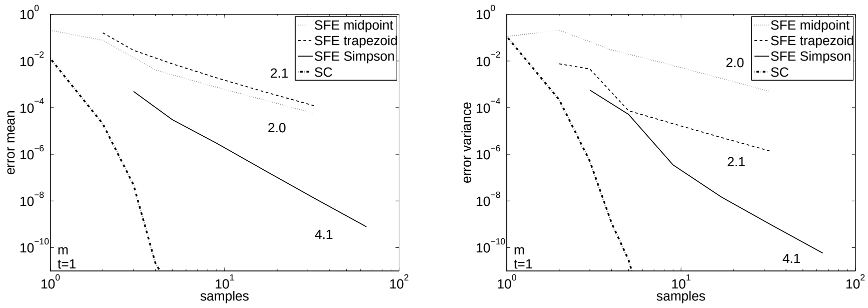

(a) mean

(b) variance

Figure 4.11: Error convergence of Stochastic Finite Elements (SFE) with the midpoint rule, trapezoid rule, and Simpson's rule, and Stochastic Collocation (SC) for the instantaneous mass flow m at $t = 1$ with an uncertain piston velocity u_{piston} with $\mu_{\mathrm{u_{piston}}} = 0.5$ for the piston problem.

racy with respect to the number of samples, see Figure 4.11. For the mean the error of the midpoint rule and the trapezoid rule are similar, but for the variance the trapezoid rule is two orders of magnitude more accurate. Simpson's rule results for both the mean and the variance in fourth-order error convergence due to the asymmetrical weighting of the probability distribution in the elements. In the rest of this work the Simpson's rule is employed for fourth-order error convergence in elements with a smooth response. The subelements with a trapezoid rule approximation of the response for a robust extrema preserving approximation result in a local second-order error convergence. The Stochastic Collocation approach results in superior convergence for the mean and the variance, since it can achieve exponential convergence for a sufficiently smooth response, see Figure 4.11.

The convergence results for the discontinuous response surface for $\mu_{\mathrm{u_{piston}}} = 1$ at $t = 0.5$ of Figure 4.12 lead to different observations. The convergence rate of the Stochastic Finite Elements methods with uniform refinement based on the midpoint, trapezium, and Simpson's rule reduce to first-order due to the first-order error in the approximation of the unknown discontinuity location between the samples. The discontinuity leads also to a first-order error in the Stochastic Collocation results. The effectiveness of adaptive grid refinement for discontinuous solutions is demonstrated by Adaptive Stochastic Finite Elements with Simpson's rule, which maintains fourth-order error convergence.

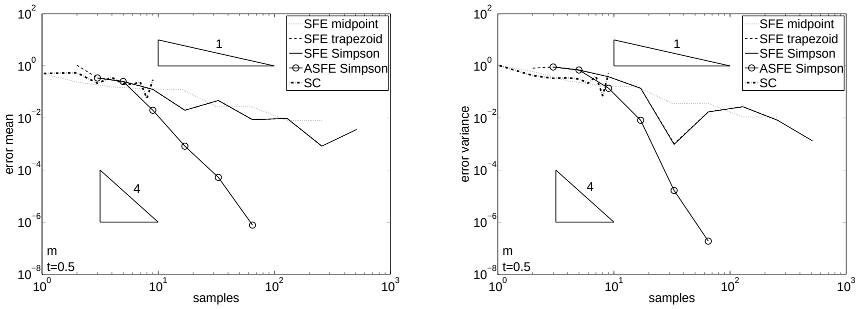

(a) mean

(b) variance

Figure 4.12: Error convergence of Stochastic Finite Elements (SFE) with the midpoint rule, trapezoid rule, and Simpson's rule, Adaptive Stochastic Finite Elements (ASFE) with Simpson's rule, and Stochastic Collocation (SC) for the instantaneous mass flow m at $t = 0.5$ with an uncertain piston velocity u_{piston} with $\mu_{u_{\mathrm{piston}}} = 1$ for the piston problem.

Total mass flow M The discontinuity in the response surface of the instantaneous mass flow m given by (4.16) results in a discontinuous derivative in the response surface of the total mass flow M at $t = 0.5$, see (4.17). In Figure 4.13 the approximation of the response surface and the probability distribution of the total mass flow M by Stochastic Finite Elements with and without stochastic adaptive grid refinement for 8 elements and Stochastic Collocation for 8 samples is given.

The adaptive Stochastic Finite Elements algorithm refines probability space near the discontinuous derivative and in the post-shock region $u_{\mathrm{piston}} > 1.1$ with the continuous variation of M, see Figures 4.13a and 4.13b. It results in an accurate representation of the response and the distribution. Stochastic Finite Elements with a uniform grid result in a larger local error near the discontinuous derivate than with adaptive stochastic grid refinement, see Figures 4.13c and 4.13d. The discontinuous derivative in probability space results in oscillations in the global polynomial approximation of the Stochastic Collocation approach, see Figures 4.13e and 4.13f. The amplitude of the oscillations is smaller than in the case of a stochastic discontinuity, nonetheless, a 40% probability of unphysical negative values of the total mass flow is predicted.

The refinement measure for the adaptive refinement of Stochastic Finite Elements is shown in Figure 4.14 for the approximation of the total mass flow M. The measure r_i given by (4.9) is shown for 4 and 8 elements. For the coarse grid of 4 elements

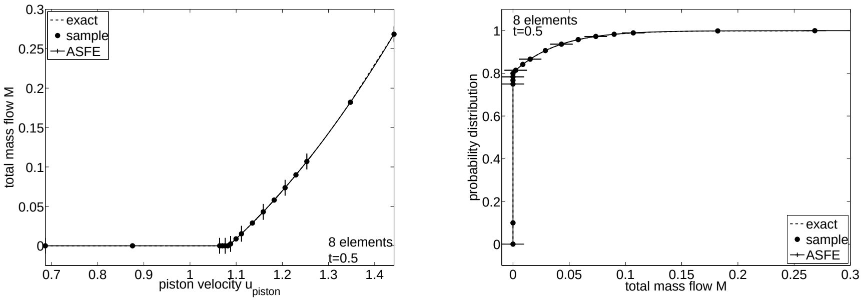

(a) ASFE, response (b) ASFE, distribution

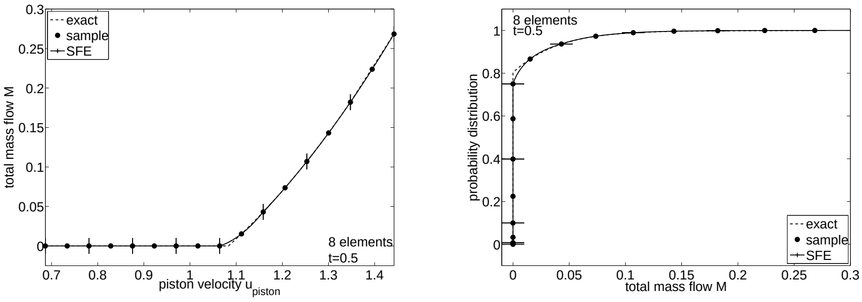

(c) SFE, response (d) SFE, distribution

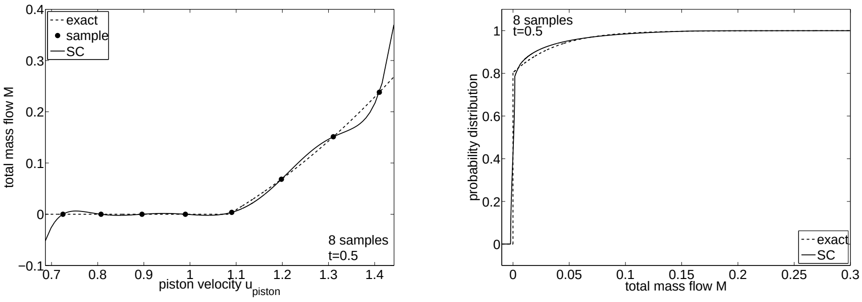

(e) SC, response (f) SC, distribution

Figure 4.13: Response surface and probability distribution of Stochastic Finite Elements with (ASFE) and without (SFE) stochastic adaptive grid refinement, and Stochastic Collocation (SC) for the total mass flow M at $t = 0.5$ with an uncertain piston velocity u_{piston} for the piston problem.

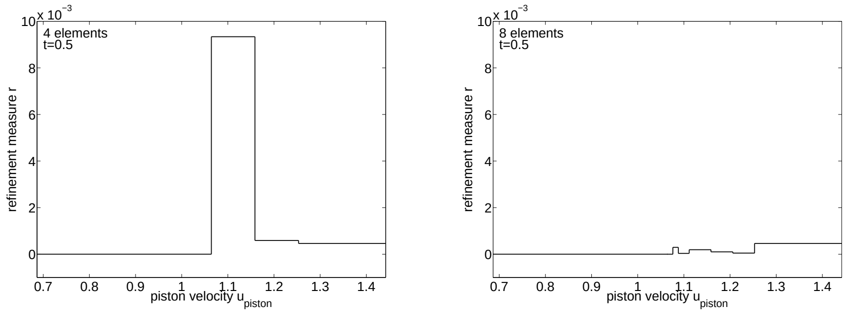

(a) ASFE, 4 elements

(b) ASFE, 8 elements

Figure 4.14: Refinement measure for the adaptive refinement of Stochastic Finite Elements (ASFE) with 4 and 8 elements for the total mass flow M at $t = 0.5$ with an uncertain piston velocity u_{piston} for the piston problem.

the refinement measure is highest in the element which contains the discontinuous derivative in the response surface for M, see Figure 4.14a. After 4 more refinement steps for a grid of 8 elements, see Figure 4.14b, the refinement measure in the element that contains the discontinuous derivative is no longer dominant. This results in the refinement of also elements in the region with the continuous variation of M, $u_{\mathrm{piston}} > 1.1$. The value $N_{\mathrm{V}} = 2$ in (4.9) determines the balance between the refinement near the discontinuous derivative and in the smooth region.

Two uncertain parameters In this section two independent input parameters are assumed to be uncertain. Next to the uncertain piston velocity u_{piston}, also the initial pressure p_{pre} is assumed to be uncertain described by a lognormal distribution with mean $\mu_{p_{\mathrm{pre}}} = 1$ and coefficient of variation $CV_{p_{\mathrm{pre}}} = 10\%$. This results in a two-dimensional probability space Ω, to which two-dimensional Stochastic Finite Elements are applied for resolving the effect on the instantaneous mass flow m.

In Figure 4.15 the adaptive Stochastic Finite Elements approximation of the instantaneous mass flow m at $t = 0.5$ as function of the uncertain parameters u_{piston} and p_{pre} is given for a discretization with 100 elements. For relatively low values of u_{piston} and p_{pre} the mass flow is identically zero. For higher values of u_{piston} and p_{pre} the shock wave passes the sensor location, which results in a discontinuous change of the instantaneous mass flow. For even higher parameter values, m varies continuously with u_{piston} and p_{pre}. These results agree with the results of the Monte Carlo simula-

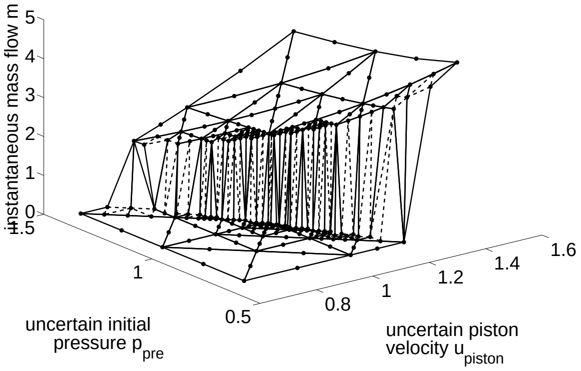

Figure 4.15: Response surface of the instantaneous mass flow m at $t = 0.5$ as function of the uncertain piston velocity u_{piston} and initial pressure p_{pre} by adaptive Stochastic Finite Elements (ASFE) with 100 elements for the piston problem.

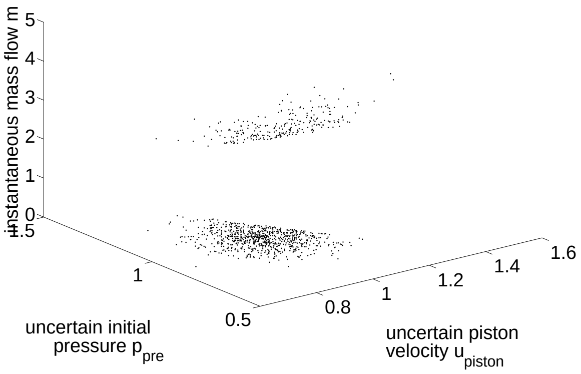

Figure 4.16: Response surface of the instantaneous mass flow m at $t = 0.5$ as function of the uncertain piston velocity u_{piston} and initial pressure p_{pre} by Monte Carlo (MC) simulation with 1000 samples for the piston problem.

tion with 1000 samples of Figure 4.16. The stochastic adaptive grid refinement results in relatively small elements near the discontinuity. The smallest elements in this discretization with 100 elements are 1024 times smaller than the elements in the initial grid. The elements are especially refined where also the probability density of u_{piston} and p_{pre} is high, i.e. $u_{\mathrm{piston}}, p_{\mathrm{pre}} \approx 1$, where the density of the Monte Carlo realizations in Figure 4.16 is also high. The subelements which contain the discontinuity are subdivided into subelements with a linear approximation of the response. These subelements are given by the dotted lines.

The adaptation of the solution and the grid is shown for a discretization with 2, 10, and 50 elements in Figure 4.17. The results for the initial grid with 2 elements are given in Figures 4.17a and 4.17b. One of the two elements with a quadratic approximation of the solution is split into four subelements with a linear approximation of the response. In Figure 4.17c and 4.17d the refinement of the grid to 10 elements is shown. The elements are mainly refined to better capture the discontinuity. For the discretization with 50 elements also the domain where the instantaneous mass flow m changes continuously is refined, see Figure 4.17e and 4.17f.

In Figure 4.18 the grid in probability space is given for a discretization with 50 elements. The grid in Figure 4.18 is the result of the mapping Θ^{-1} of the grid in parameter space A of Figure 4.17f to probability space Ω. The grid in probability space is considerably different from the grid in parameter space. For example, the elements that capture the discontinuity are approximately of the same size, since in parameter space the elements are more refined in the region where the uncertain parameters u_{piston} and p_{pre} have a higher probability density, near $u_{\mathrm{piston}}, p_{\mathrm{pre}} \approx 1$. The topology of both grids is the same.

The approximation of the mean and the variance of the instantaneous mass flow m of adaptive Stochastic Finite Elements is compared in Tables 4.1 and 4.2 to the result of Monte Carlo simulations. In Table 4.1 the results are given for a smooth response surface with $t = 1$ and $\mu_{\mathrm{u_{piston}}} = 0.5$. Adaptive Stochastic Finite Elements are converged already for a discretization with 10 elements to a mean of $\mu_{\mathrm{m}} = 0.750$ and a variance of $\sigma_{\mathrm{m}}^2 = 0.011$. The Monte Carlo results converge to the same values for the mean and variance at a much higher number of samples. Minor differences with the Monte Carlo results can be explained by the inherent variability in Monte Carlo simulations.

The results for the case with $t = 0.5$ are given in Table 4.2. Both methods converge less fast than for the case with $t = 1$ due the high output variance and the presence of the discontinuity in the response surface. Adaptive Stochastic Finite Elements predict $\mu_{\mathrm{m}} = 0.566$ and $\sigma_{\mathrm{m}}^2 = 1.087$ using 10^3 second-degree elements. This result is obtained using 2217 deterministic solves. It can be seen in Table 4.2 that standard Monte Carlo simulation for approximately the same number of deterministic solves results in

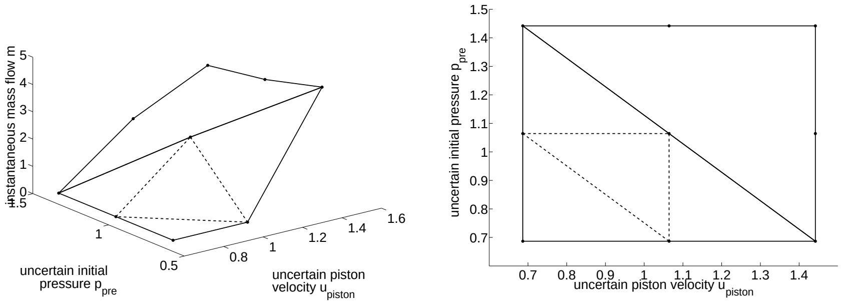

(a) 2 elements, m (b) 2 elements, grid

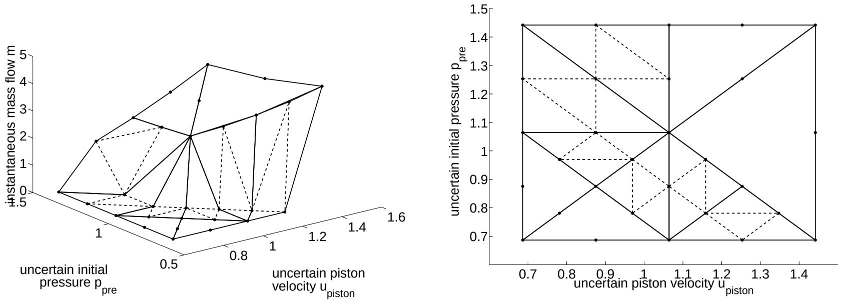

(c) 10 elements, m (d) 10 elements, grid

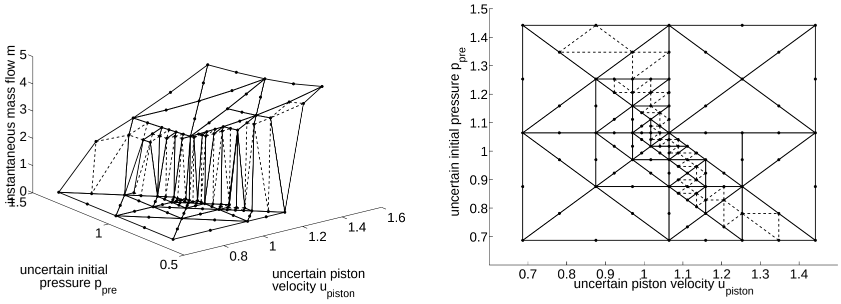

(e) 50 elements, m (f) 50 elements, grid

Figure 4.17: Response surface and the grid for the instantaneous mass flow m at $t = 0.5$ as function of the uncertain piston velocity u_{piston} and initial pressure p_{pre} by adaptive Stochastic Finite Elements (ASFE) with 2, 10, and 50 elements for the piston problem.

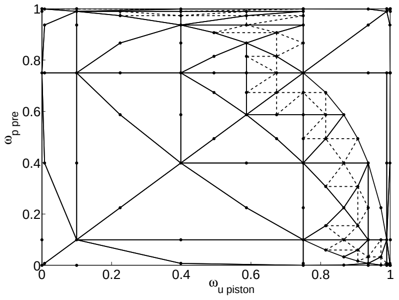

Figure 4.18: Grid in probability space for the instantaneous mass flow m at $t = 0.5$ as function of the uncertain piston velocity u_{piston} and initial pressure p_{pre} by adaptive Stochastic Finite Elements (ASFE) with 50 elements for the piston problem.

Table 4.1: Mean and the variance of the instantaneous mass flow m at $t = 1$ with an uncertain piston velocity u_{piston} with $\mu_{\text{u}_{\text{piston}}} = 0.5$ and initial pressure p_{pre} by adaptive Stochastic Finite Elements (ASFE) and Monte Carlo (MC) simulations.

adaptive Stochastic Finite Elements (ASFE)				Monte Carlo (MC)		
elements	samples	mean	variance	samples	mean	variance
10	31	0.750	0.011	10	0.808	0.009
10^2	230	0.750	0.011	10^2	0.741	0.009
10^3	2084	0.750	0.011	10^3	0.754	0.012
				10^4	0.749	0.011
				10^5	0.749	0.011
				10^6	0.749	0.011

Table 4.2: Mean and the variance of the instantaneous mass flow m at $t = 0.5$ with $\mu_{\mathrm{u_{piston}}} = 0.5$ and initial pressure p_{pre} by adaptive Stochastic Finite Elements (ASFE) and Monte Carlo (MC) simulations.

adaptive Stochastic Finite Elements (ASFE)				Monte Carlo (MC)		
elements	samples	mean	variance	samples	mean	variance
10	30	0.863	0.879	10	0.793	1.654
10^2	232	0.562	1.044	10^2	0.693	1.261
10^3	2217	0.566	1.087	10^3	0.549	1.081
				10^4	0.573	1.100
				10^5	0.561	1.085
				10^6	0.563	1.088

a significantly less accurate approximation. Monte Carlo simulation requires $10^5 - 10^6$ samples to obtain a comparable accuracy.

Even though every second-order element contains 6 quadrature points, for this case the average number of deterministic solves per element seems to approach 2. This number of samples is relatively low, since the samples which are located on the boundaries of the elements are used for the polynomial approximation in multiple elements. Furthermore, all samples are reused in the successive refinement steps. For complex computational problems in the order of 10^3 deterministic solves may result in high computational costs, however, already an approximation with a realistic 5% error for practical applications is obtained with between 10 to 100 elements.

The relatively high coefficient of variation of the instantaneous mass flow $CV_{\mathrm{m}} = 1.842$ compared to the input coefficients of variation $CV_{\mathrm{u_{piston}}}, CV_{\mathrm{p_{pre}}} = 0.1$ demonstrates that singularities in probability space can result in a high output sensitivity on the input uncertainty.

Three uncertain parameters In this section the sensor location L is assumed to be uncertain with a lognormal distribution with mean $\mu_{\mathrm{L}} = 1$ and coefficient of variation $CV_{\mathrm{L}} = 10\%$. In combination with the uncertain piston velocity u_{piston} and initial pressure p_{pre}, it results in three independent uncertain input parameters. Three-dimensional adaptive Stochastic Finite Elements are employed to approximate the mean and the variance of the instantaneous mass flow m at $t = 0.5$. For this case the problem is made dimensionless using the mean sensor location μ_{L}.

The three-dimensional Stochastic Finite Elements grid is given in Figure 4.19. In Figure 4.19a the initial grid with 6 tetrahedral elements is shown. The result of

Table 4.3: Mean and the variance of the instantaneous mass flow m at $t = 1$ with an uncertain piston velocity u_{piston} with $\mu_{\mathrm{u_{piston}}} = 0.5$, initial pressure p_{pre}, and sensor location L with $\mu_{\mathrm{L}} = 0.75$ by adaptive Stochastic Finite Elements (ASFE) and Monte Carlo (MC) simulations.

adaptive Stochastic Finite Elements (ASFE)				Monte Carlo (MC)		
elements	samples	mean	variance	samples	mean	variance
10	27	0.749	0.011	10	0.699	0.019
10^2	241	0.751	0.011	10^2	0.754	0.010
10^3	1943	0.751	0.011	10^3	0.751	0.012
				10^4	0.747	0.011
				10^5	0.749	0.011
				10^6	0.749	0.011

the stochastic adaptive grid refinement for 10, 50, and 100 elements is given in Figures 4.19b to 4.19d.

In Tables 4.3 and 4.4 the convergence of the solution for the mean and the variance of the instantaneous mass flow m is compared to results of Monte Carlo simulations. For the smooth response surface with $t = 1$, $\mu_{\mathrm{u_{piston}}} = 0.5$, and $\mu_{\mathrm{L}} = 0.75$ the results are given in Table 4.3. Adaptive Stochastic Finite Elements results in an accurate approximation already for a discretization of 10 elements and 27 deterministic solves for the smooth response surface.

The results for the case with $t = 0.5$ are given in Table 4.4. Adaptive Stochastic Finite Elements needs for this complex problem with a discontinuity in a three-dimensional probability space 10^4 elements for an accurate approximation. It results in a mean $\mu_{\mathrm{m}} = 0.851$ and variance $\sigma_{\mathrm{m}}^2 = 1.198$, which corresponds with a relatively high coefficient of variation $CV_{\mathrm{m}} = 1.286$. Also for three uncertain parameters the average number of deterministic solves per element is close to 2 even though each element contains 10 quadrature points on its boundary. This demonstrates that also in multiple dimensions adaptive Stochastic Finite Elements with Newton-Cotes quadrature in simplex elements require a relatively low number of deterministic solves to approximate complex problems with singularities.

In Figure 4.20 the Adaptive Stochastic Finite Elements error convergence for an increasing number of uncertain parameters is compared with one to three uncertain parameters for the discontinuous response surface of the instantaneous mass flow m at $t = 0.5$. In a one-dimensional probability space with one uncertain parameter the method gives a fourth-order error convergence as shown in Figure 4.12. For two and

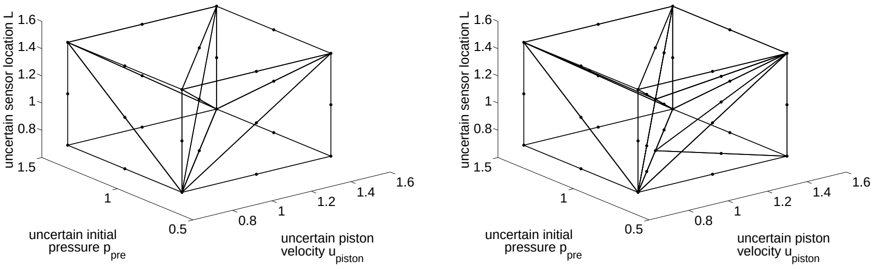
uncertain sensor location L
1.6
1.4
1.2
1
0.8
1.5
1
0.5
uncertain initial pressure p_pre
0.8
1
1.2
1.4
1.6
uncertain piston velocity u_piston
uncertain sensor location L
1.6
1.4
1.2
1
0.8
1.5
1
0.5
uncertain initial pressure p_pre
0.8
1
1.2
1.4
1.6
uncertain piston velocity u_piston

(a) 6 elements (b) 10 elements

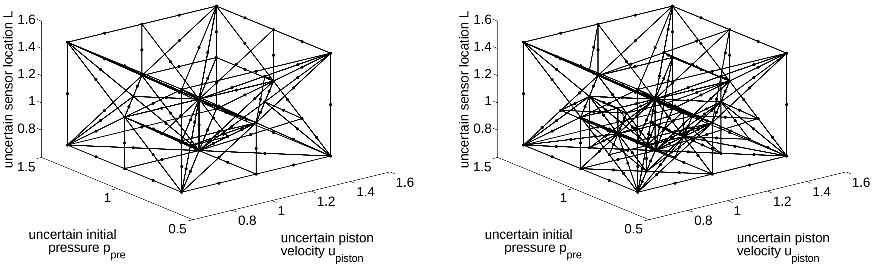
uncertain sensor location L
1.6
1.4
1.2
1
0.8
1.5
1
0.5
uncertain initial pressure p_pre
0.8
1
1.2
1.4
1.6
uncertain piston velocity u_piston
uncertain sensor location L
1.6
1.4
1.2
1
0.8
1.5
1
0.5
uncertain initial pressure p_pre
0.8
1
1.2
1.4
1.6
uncertain piston velocity u_piston

(c) 50 elements (d) 100 elements

Figure 4.19: Grid for the instantaneous mass flow m at $t = 0.5$ as function of the uncertain piston velocity u_{piston}, initial pressure p_{pre} and sensor location L by adaptive Stochastic Finite Elements (ASFE) with 6, 10, 50, and 100 elements for the piston problem.

Table 4.4: Mean and the variance of the instantaneous mass flow m at $t = 0.5$ with an uncertain piston velocity u_{piston}, initial pressure p_{pre}, and sensor location L by adaptive Stochastic Finite Elements (ASFE) and Monte Carlo (MC) simulations.

adaptive Stochastic Finite Elements (ASFE)				Monte Carlo (MC)		
elements	samples	mean	variance	samples	mean	variance
10	38	0.578	0.371	10	1.506	1.729
10^2	235	0.811	0.895	10^2	0.761	1.191
10^3	1946	0.854	1.111	10^3	0.831	1.181
10^4	17786	0.851	1.198	10^4	0.820	1.191
				10^5	0.845	1.204
				10^6	0.847	1.208

three uncertain parameters the convergence rate decreases, which results in an increasing number of required samples to discretize the higher dimensional probability space with sufficient accuracy. It is expected that this trend continues for further increasing the number of uncertain parameters up to the point that for many parameters Monte Carlo simulation can be a more viable option. On the other hand, the adaptive scheme is more efficient than a tensorial extension of an uncertainty quantification method to multiple dimensions. It is also observed that due to the robust adaptive scheme the method remains convergent for this complex problem with a sharp discontinuity in a three-dimensional probability space.

4.3.2 Stall flutter model

In this section adaptive Stochastic Finite Elements are used to study the effect of uncertainty on the bifurcation behavior of a two-dimensional airfoil stall flutter model, see Figure 4.21. Bifurcation behavior of a fluid-structure interaction system is a practical engineering example of an application with a singularity in probability space.

A structure surrounded by fluid flow can exhibit an unsteady motion due to the interaction of the pressure forces of the flow and the motion of the structure. In a stable situation the unsteady motion results in a damped oscillation. Beyond a critical fluid velocity, nonlinear fluid-structure interaction systems can exhibit a time periodic instability that can grow in an unbounded fashion, which is known as flutter [22, 25]. Nonlinearities in the flow and the structural stiffness can limit the unbounded motion to a periodic response, which is called a limit cycle oscillation. Stall is a nonlinear phenomenon in the flow which corresponds to a sudden loss of lift force and an increase

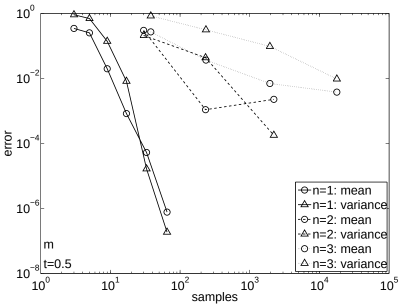

Figure 4.20: Error convergence of Adaptive Stochastic Finite Elements (ASFE) with one to three uncertain parameters, $n = \{1, 2, 3\}$, for the instantaneous mass flow m at $t = 0.5$ in the piston problem.

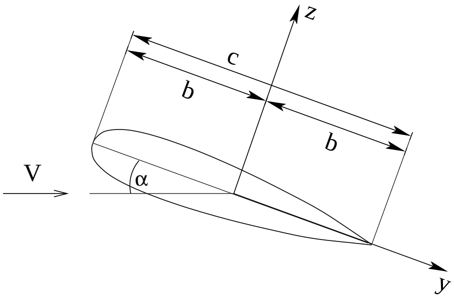

Figure 4.21: The pitching airfoil stall flutter model with free stream velocity V, angle of attack α, half chord $b = c/2$, and the spatial coordinates y and z parallel and perpendicular to the airfoil chord, respectively.

of the drag force due to separation of the flow from the surface of the airfoil. The critical velocity at which the stable damped response changes into a periodic response is the bifurcation point.

For engineering applications a standard approach is to model fluid-structure interaction systems by a two-dimensional rigid airfoil with a concentrated structural mass and stiffness [22, 25]. The aerodynamic forces are commonly modeled by an aerodynamic model. This approach results in a system of differential equations, which governs the motion of the airfoil.

Since the predominant vibration mode in stall flutter is in the torsional direction, a single-degree-of-freedom pitch motion is considered in contrast with the common two-degree-of-freedom pitch-plunge flutter problem [22, 25]. The nondimensional equation of motion for the pitch angle $\alpha(\tau)$ of the rigid airfoil is given by [25]

$$\frac{\mathrm{d}^2\alpha}{\mathrm{d}\tau^2} + \frac{\alpha(\tau)}{U^2} + K_{\mathrm{nl}}\alpha^3 = F_{\mathrm{ext}} + 2\frac{C_{\mathrm{m}}(\tau)}{\pi\mu r_\alpha^2}, \tag{4.18}$$

where $\tau = tV/b$ is the nondimensional time, $U = V/b\omega_\alpha$ is the nondimensional velocity, K_{nl} is the nondimensional structural stiffness, F_{ext} is a nondimensional external forcing, $C_{\mathrm{m}}(\tau)$ is the aerodynamic moment coefficient, and $\mu = m/(\pi\rho b^2)$ and $r_\alpha = I_\alpha/(mb^2)$ are the mass ratio and the radius of gyration, with velocity V, semi-chord b, ω_α the natural pitch frequency, m the structural mass, ρ the air density, and I_α the pitch moment of inertia. The initial condition is α_{init}.

The aerodynamic moment coefficient $C_{\mathrm{m}}(\tau)$ is described by the Onera dynamic stall model [23, 25, 98]. This is a semi-empirical, dynamical aerodynamic model which takes the complex unsteady stall phenomena into account in the form of a set of differential equations for the inviscid and the viscous contribution to the aerodynamic moment C_{m_1} and C_{m_2}, respectively:

$$C_{\mathrm{m}}(\tau) = s_{\mathrm{m}}\frac{\mathrm{d}\alpha}{\mathrm{d}\tau} + k_{\mathrm{vm}}\frac{\mathrm{d}^2\alpha}{\mathrm{d}\tau^2} + C_{\mathrm{m}_1} + C_{\mathrm{m}_2}, \tag{4.19}$$

$$\frac{\mathrm{d}C_{\mathrm{m}_1}}{\mathrm{d}\tau} + \lambda_{\mathrm{m}}C_{\mathrm{m}_1} = \lambda_{\mathrm{m}}\left(a_{\mathrm{om}}\alpha + \sigma_{\mathrm{m}}\frac{\mathrm{d}\alpha}{\mathrm{d}\tau}\right) + \alpha_{\mathrm{m}}\left(a_{\mathrm{om}}\frac{\mathrm{d}\alpha}{\mathrm{d}\tau} + \sigma_{\mathrm{m}}\frac{\mathrm{d}^2\alpha}{\mathrm{d}\tau^2}\right), \tag{4.20}$$

$$\frac{\mathrm{d}^2C_{\mathrm{m}_2}}{\mathrm{d}\tau^2} + 2dw\frac{\mathrm{d}C_{\mathrm{m}_2}}{\mathrm{d}\tau} + w^2(1+d^2)C_{\mathrm{m}_2} = -w^2(1+d^2)\left(\Delta C_{\mathrm{m}} + e\frac{\mathrm{d}\Delta C_{\mathrm{m}}}{\mathrm{d}\tau}\right), \tag{4.21}$$

where s_{m}, k_{vm}, λ_{m}, a_{om}, α_{m}, σ_{m}, d, w, and e are constants associated with the aerodynamic forces and ΔC_{m} accounts for the effects of stall on the aerodynamic moment

Table 4.5: Parameter values for the pitching airfoil stall flutter model.

K_{nl}	0	
μ	100	
r_α	0.5	
α_{init}	10	[deg]
s_{m}	$-\frac{\pi}{4}$	
k_{vm}	$-\frac{3\pi}{16}$	
λ_{m}	0	
a_{om}	0	
σ_{m}	$-\frac{\pi}{4}$	
α_{m}	1	
a_{ol}	5.73	
$\alpha_{\mathrm{stall,l}}$	16	[deg]
$\alpha_{\mathrm{stall,m}}$	12	[deg]
ΔC_{l}	0	$\lvert\alpha\rvert < \alpha_{\mathrm{stall,l}}$
	$(a_{\mathrm{ol}} + 10.02)(\alpha - \alpha_{\mathrm{stall,l}})$	$\alpha > \alpha_{\mathrm{stall,l}}$
	$(a_{\mathrm{ol}} + 10.02)(\alpha + \alpha_{\mathrm{stall,l}})$	$\alpha < -\alpha_{\mathrm{stall,l}}$
ΔC_{m}	0	$\lvert\alpha\rvert < \alpha_{\mathrm{stall,m}}$
	$(0.3/(0.3142 - \alpha_{\mathrm{stall,m}}))(\alpha - \alpha_{\mathrm{stall,m}})$	$\alpha > \alpha_{\mathrm{stall,m}}$
	$(0.3/(0.3142 - \alpha_{\mathrm{stall,m}}))(\alpha + \alpha_{\mathrm{stall,m}})$	$\alpha < -\alpha_{\mathrm{stall,m}}$
a	$0.25 + 0.1(\Delta C_{\mathrm{l}}^2)$	
r	$(0.2 + 0.1(\Delta C_{\mathrm{l}}^2))^2$	
d	$a/(\sqrt{4r - a^2})$	
w	$1/(2d)$	
e	$-0.6(\Delta C_{\mathrm{l}}^2)$	

above the static stall angle. Here the empirically determined values of these constants from Dunn and Dugundji [23] for the NACA0012 airfoil are used.

The external forcing F_{ext} is assumed to be uncertain with a lognormal distribution. The mean of the nondimensional external forcing is $\mu_{\mathrm{F_{ext}}} = 0.002$ and the coefficient of variation is $CV_{\mathrm{F_{ext}}} = 10\%$. The time integration is performed with the explicit fourth-order Runge-Kutta algorithm with a stepsize of $\Delta\tau = 0.01$ up to $\tau = 800$. The other parameter values can be found in Table 4.5.

In Figure 4.22 the deterministic bifurcation plot for the pitch angle α as function of bifurcation parameter U is given for the mean value of the external forcing $\mu_{\mathrm{F_{ext}}}$. The minimum and maximum pitch angles $\alpha_{\min}$ and $\alpha_{\max}$ of one period of the periodic

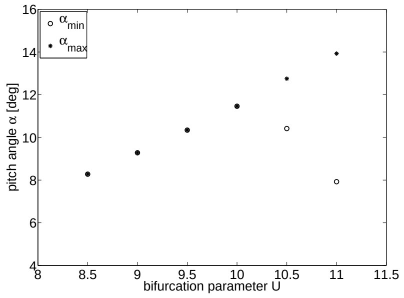

Figure 4.22: Deterministic bifurcation plot for $\mu_{\mathrm{F}_{\mathrm{ext}}}$ for the pitching airfoil stall flutter model.

response are shown. For a damped response, i.e. for $U < 10$, $\alpha_{\min}$ and $\alpha_{\max}$ are equal. For $U > 10$ the dynamic stall model gives a periodic limit cycle oscillation response, of which the amplitude increases for increasing U. Between $U = 10$ and $U = 10.5$ a supercritical Hopf bifurcation occurs.

The effect of uncertainty in the external forcing F_{ext} on the bifurcation plot of Figure 4.22 is shown in Figure 4.23. The mean values of the minimum and maximum pitch angles $\alpha_{\min}$ and $\alpha_{\max}$, and their uncertainty bars based on ± one standard deviation are shown. Results of both adaptive Stochastic Finite Elements and Stochastic Collocation are given.

After including the uncertainty the bifurcation occurs already between $U = 9$ and $U = 9.5$ instead of between $U = 10$ and $U = 10.5$ for the deterministic case. Below the bifurcation point, i.e. $U < 9.5$, the mean values and the uncertainty bars of $\alpha_{\min}$ and $\alpha_{\max}$ are equal. Beyond the bifurcation point, i.e. $U > 9.5$, the uncertainty bars increase in length, while the uncertainty in $\alpha_{\min}$ is larger than the uncertainty in $\alpha_{\max}$.

The results of adaptive Stochastic Finite Elements and Stochastic Collocation are approximately equal before the bifurcation and for $\alpha_{\max}$ after the bifurcation. The two methods predict a slightly different effect of the uncertainty on the mean and the standard deviation of $\alpha_{\min}$ especially near the bifurcation point at $U = 10$. To understand this difference the results of adaptive Stochastic Finite Elements and Stochastic Collocation for the response $\alpha_{\min}$ and $\alpha_{\max}$ as function of F_{ext}, and their probability distributions are shown for $U = 10$ in Figure 4.24. In Figure 4.24a the Stochastic Finite Elements approximation of the response $\alpha_{\min}$,$\alpha_{\max}$–F_{ext} with 7 elements is compared to a Monte Carlo simulation with 1000 uniformly sampled realizations. The pitch

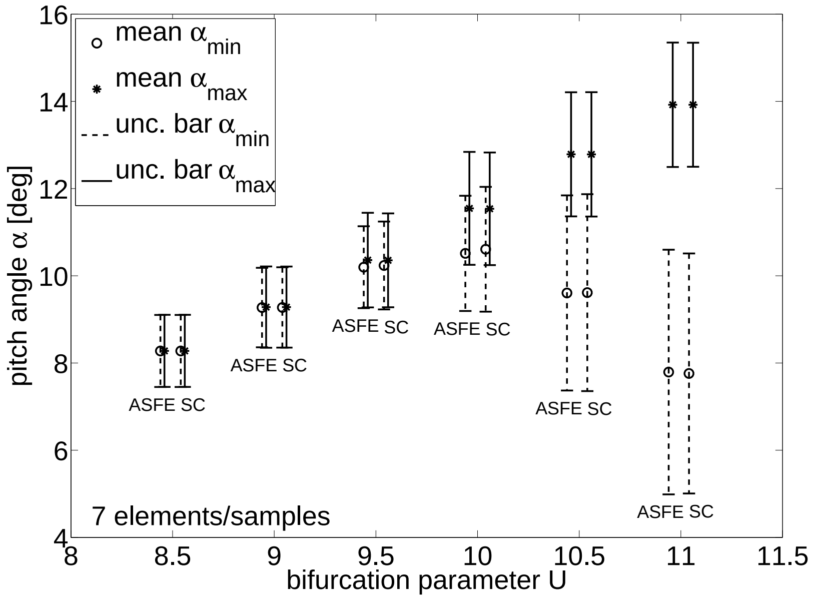

Figure 4.23: Effect of uncertainty in the external forcing F_{ext} on the bifurcation plot in terms of the mean and the uncertainty bars based on ± a standard deviation by adaptive Stochastic Finite Elements (ASFE) and Stochastic Collocation (SC) for the pitching airfoil stall flutter model.

angle shows a supercritical Hopf bifurcation also as function of the external forcing F_{ext}. The stochastic adaptive grid refinement, based on the response of $\alpha_{\min}$, results in smaller elements near the bifurcation point, which results in an accurate approximation of the response of $\alpha_{\min}$ and $\alpha_{\max}$. In Figure 4.24b the results of Stochastic Collocation with 7 samples are shown. The global polynomial approximation of Stochastic Collocation results in an oscillatory approximation of the response of $\alpha_{\min}$ caused by the bifurcation as function of F_{ext}. Especially near the outer collocation points the oscillatory prediction results in large errors. The approximation of the response of $\alpha_{\max}$ shows smaller oscillations, because the bifurcation affects the behavior of $\alpha_{\max}$ less than $\alpha_{\min}$.

The accuracy of the approximation of the probability distribution of $\alpha_{\min}$ and $\alpha_{\max}$ is mainly determined by that of the response, see Figures 4.24c to 4.24f. Adaptive Stochastic Finite Elements result in accurate approximations of the distribution functions. The less accurate approximation of the response of $\alpha_{\min}$ for Stochastic Collocation leads to relatively large errors in the approximation of the distribution function, see Figure 4.24d.

The oscillatory approximation of the response by Stochastic Collocation has an effect on the convergence behavior for the mean and the standard deviation. In Figure 4.25 the convergence of the mean and standard deviation of $\alpha_{\min}$ and $\alpha_{\max}$ of adaptive Stochastic Finite Elements and Probabilistic Collocation is given as function of the number of elements and samples, respectively. Stochastic Finite Elements show a smooth convergence behavior, see Figures 4.25a and 4.25c. Stochastic Collocation results especially for $\alpha_{\min}$ in an undesirable oscillatory convergence behavior due to the oscillations in the approximation of the response, see Figures 4.25b and 4.25d. This results in a less accurate prediction of the mean and uncertainty bar of $\alpha_{\min}$ at $U = 10$ in Figure 4.23 for Stochastic Collocation than for adaptive Stochastic Finite Elements.

4.3.3 Transonic flow over a NACA0012 airfoil

In this section transonic Euler flow over a NACA0012 airfoil subject to an uncertain free stream Mach number Ma_∞ is considered. This is an example of uncertainty in a practical flow problem with a shock wave, which results in a discontinuity in probability space. A transonic flow problem is also of interest since it is known that a transonic flow field can be sensitive to small input variations. The distribution of Ma_∞ is assumed to be lognormal with a mean Mach number of $\mu_{\mathrm{Ma}_\infty} = 0.8$ and a coefficient of variation of $CV_{\mathrm{Ma}_\infty} = 1\%$. Due to the small input coefficient of variation, the free stream Mach numbers Ma_∞ with a significant probability are restricted to the transonic range. The angle of attack is equal to 1.25° and the airfoil has a chord with length c.

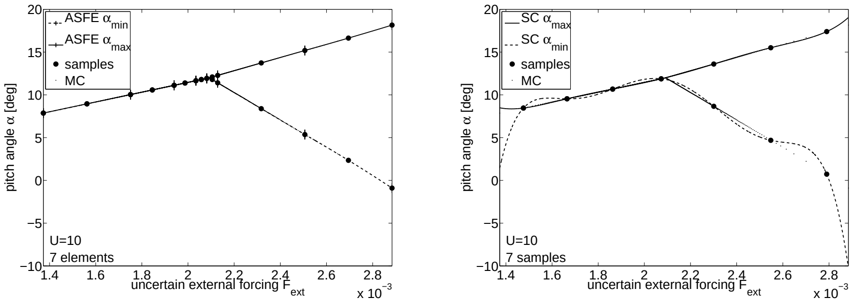

(a) ASFE, response

(b) SC, response

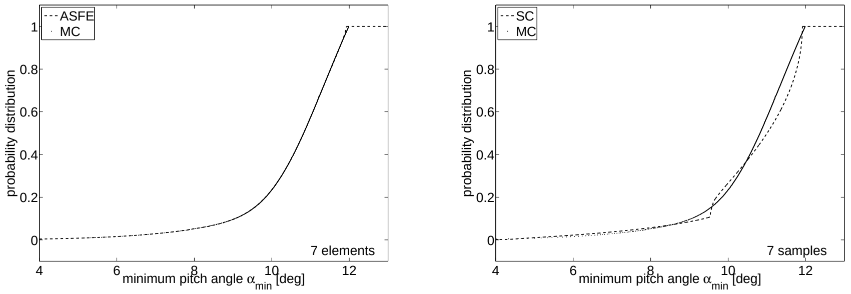

(c) ASFE, distribution $\alpha_{\min}$

(d) SC, distribution $\alpha_{\min}$

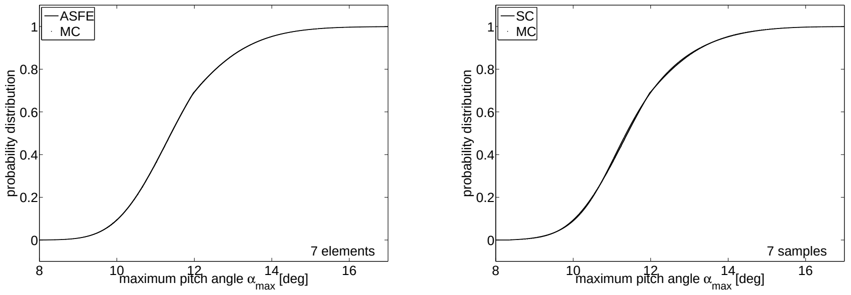

(e) ASFE, distribution $\alpha_{\max}$

(f) SC, distribution $\alpha_{\max}$

Figure 4.24: Response and probability distribution of the minimum and maximum angle of attack, $\alpha_{\min}$ and $\alpha_{\max}$, for $U = 10$ by adaptive Stochastic Finite Elements (ASFE) and Stochastic Collocation (SC) for the pitching airfoil stall flutter model.

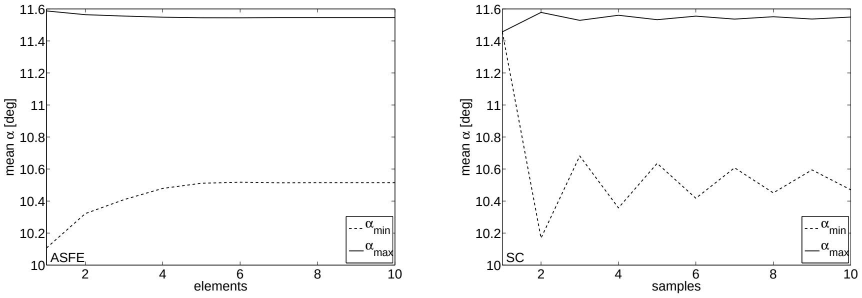

(a) ASFE, mean

(b) SC, mean

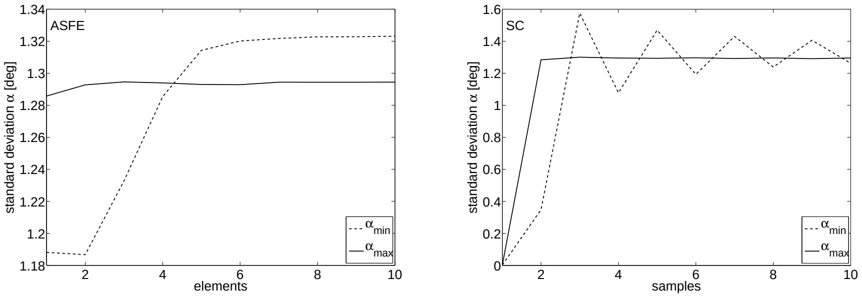

(c) ASFE, standard deviation

(d) SC, standard deviation

Figure 4.25: Convergence of the mean and standard deviation of the minimum and maximum angle of attack, $\alpha_{\min}$ and $\alpha_{\max}$, for $U = 10$ by adaptive Stochastic Finite Elements (ASFE) and Stochastic Collocation (SC) for the pitching airfoil stall flutter model.

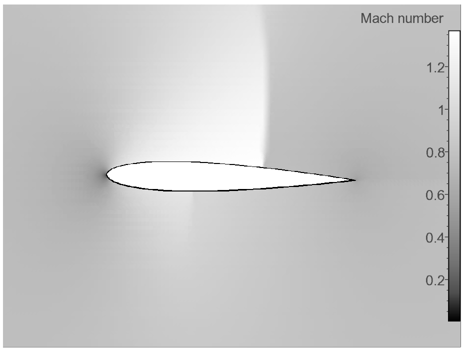

Figure 4.26: Transonic flow over a NACA0012 airfoil for the mean free stream Mach number μ_{Ma_∞} with the deterministic shock wave positions of $x = 0.6c$ and $x = 0.35c$ on the upper and lower surface, respectively.

The two-dimensional flow problem is discretized using a second-order upwind spatial finite volume scheme on a unstructured hexahedral mesh with $3 \cdot 10^4$ spatial volumes. The steady state solution is found by time integration with a CFL number of 0.5. In Figure 4.26 the flow field in terms of the local Mach number is shown for the mean value of the free stream Mach number μ_{Ma_∞}. Above the wing a large supersonic domain is present for which $\mathrm{Ma} > 1$, which ends at a shock wave at $x = 0.6c$. Under the wing a small supersonic region and a weak shock wave at $x = 0.35c$ are present.

The effect of the uncertainty in Ma_∞ is given in Figure 4.27 in terms of the Mach number along the airfoil surface. The mean Mach number and the 99% uncertainty range are shown. Stochastic Finite Elements are applied with 4 elements, which results in 9 deterministic solves. The output variables are the Mach numbers at all $6 \cdot 10^2$ volumes on the airfoil surface. Uniform grid refinement is applied, since refining adaptively based on a combination of $6 \cdot 10^2$ output variables effectively results in uniform refinement as well. The results are compared with Stochastic Collocation based on 5 deterministic solves.

Stochastic Finite Elements predict that the uncertainty smears the shock wave in the mean Mach number along the upper surface around its deterministic location, see Figure 4.27a. The 99% uncertainty range shows that the position of the shock wave is sensitive to the 1% uncertainty in the free stream Mach number. The shock wave strength is nearly unaffected. Stochastic Collocation predicts less sensitivity of the shock position and a much larger effect on the possible Mach numbers near the shock

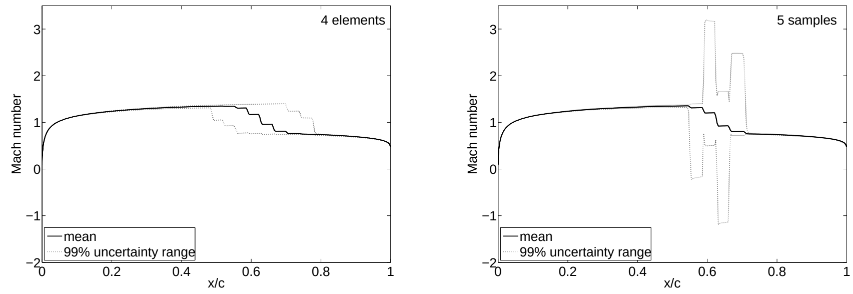

(a) SFE, upper surface

(b) SC, upper surface

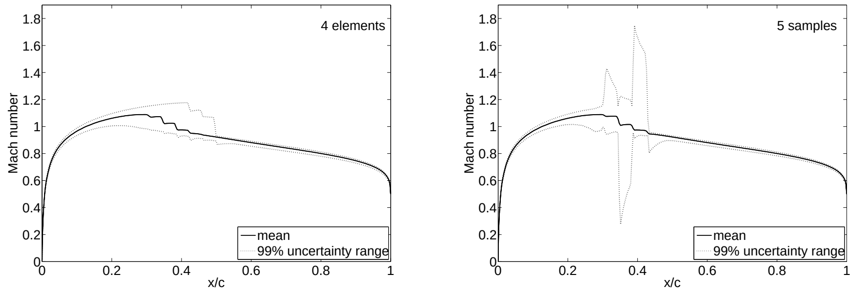

(c) SFE, lower surface

(d) SC, lower surface

Figure 4.27: Mean Mach number and 99% uncertainty range along the surface by Stochastic Finite Elements (SFE) and Stochastic Collocation (SC) for the uncertain free stream Mach number Ma_∞ in the transonic flow over a NACA0012 airfoil.

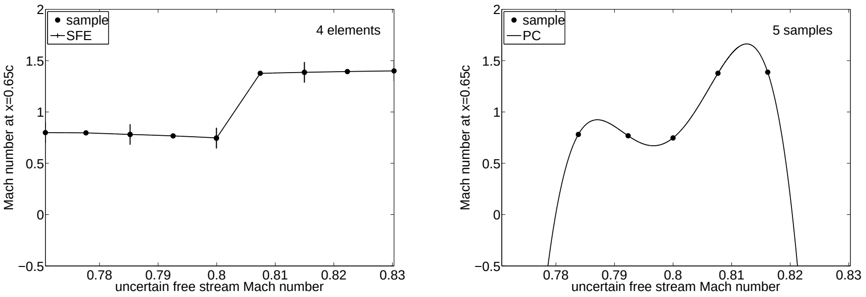

(a) SFE

(b) SC

Figure 4.28: Response of the local Mach number in $x = 0.65c$ on the upper surface by Stochastic Finite Elements (SFE) and Stochastic Collocation (SC) for the uncertain free stream Mach number Ma_∞ in the transonic flow over a NACA0012 airfoil.

wave, see Figure 4.27b. The large uncertainty range given by Stochastic Collocation includes unrealistically high Mach numbers of up to 3 and unphysical negative Mach numbers. Increasing the number of collocation points in Stochastic Collocation increases the oscillatory behavior. In Figures 4.27c and 4.27d qualitatively the same characteristics can be seen for the Mach number along the lower surface.

The difference in the results of Stochastic Finite Elements and Stochastic Collocation is studied by considering the response surface approximations in $x = 0.65c$ on the upper surface in Figure 4.28. Due to the uncertainty in the free stream Mach number, location $x = 0.65c$ can be either in the subsonic or supersonic domain. This results in a discontinuity in probability space between $\mathrm{Ma}_\infty = 0.80$ and $\mathrm{Ma}_\infty = 0.81$. Stochastic Finite Elements result in a monotonicity preserving approximation of the response surface through the samples without artificial oscillations, see Figure 4.28a. The resolution of the shock wave can be improved by increasing the number of elements. The global polynomial approximation of Stochastic Collocation results in an oscillatory response approximation due to presence of the discontinuity. This results in a prediction including too high Mach numbers and unphysical negative Mach numbers, which are not reflected in the samples themselves. Increasing the number of samples would increase the oscillatory behavior of the response surface approximation. These results show that the 99% uncertainty range prediction of Stochastic Finite Elements in Figure 4.27 is more reliable than that of Stochastic Collocation.

4.4 Summary

An adaptive Stochastic Finite Elements approach based on Newton-Cotes quadrature in simplex elements is developed. A piecewise polynomial approximation of the response is obtained by solving uncoupled deterministic problems in quadrature points in elements in probability space. The elements are refined adaptively to be able to resolve singularities in probability space effectively. Resolving singularities is important since they can result in high output sensitivity on input uncertainty, and oscillatory or unphysical predictions. The refinement measure consists of the highest absolute eigenvalue of the Hessian of the approximation of the response in the elements scaled by their volume and weighted by the probability represented by the elements.

Due to the Newton-Cotes quadrature the required number of deterministic solves is relatively low, since (*i*) the deterministic samples are reused in successive refinement steps due to the location of the quadrature points, and (*ii*) the samples are used in approximating the response in multiple elements, because most quadrature points are located on the boundaries of the elements. The extrema of the samples are preserved in the piecewise polynomial approximation of the response by subdividing the elements where necessary in subelements with a linear approximation of the response.

The method is applied to a piston problem, a stall flutter model and transonic flow over a NACA0012 airfoil with random input parameters with a lognormal distribution, which involve shock waves and bifurcations in probability space. The results for the piston problem are compared to those of Monte Carlo simulations for one up to three independent uncertain input parameters, piston velocity $u_{\mathrm{piston}}(\omega)$, initial pressure $p_{\mathrm{pre}}(\omega)$, and sensor location L. For random piston velocity, results for zeroth, first, and second degree Newton-Cotes quadrature are compared to global polynomial Stochastic Collocation. The importance of singularities in probability space has been demonstrated by an output variation of 184% caused by input coefficients of variation of 10% for random piston velocity and initial pressure. It is observed in the piston problem that the average number of deterministic solves per element is close to 2 only, which seems to be independent of the dimension of probability space.

Results of second-degree Newton-Cotes quadrature for random external forcing $F_{\mathrm{ext}}(\omega)$ in the stall flutter model and random free stream Mach number $\mathrm{Ma}(\omega)$ in the transonic flow problem demonstrate that Adaptive Stochastic Finite Elements based on Newton-Cotes quadrature in simplex elements are capable of resolving complex situations involving singularities in probability space in practical applications effectively. These results are compared to Stochastic Collocation approximations and for the stall flutter model also Monte Carlo reference simulations are performed. Artificial oscillations or unphysical predictions have not been encountered.

Chapter 5

Probabilistic Collocation for Limit Cycle Oscillations

Polynomial Chaos methods usually require a fast increasing polynomial chaos order with time to resolve the effect of random parameters in dynamical systems with a constant accuracy. Resolving the asymptotic stochastic effect can for non-intrusive and multi-element Polynomial Chaos methods result in thousands of required samples or elements. This effect is especially profound in problems with oscillatory solutions in which the frequency of the response is affected by the random parameters. The frequency differences between the realizations lead to increasing phase differences with time, which in turn result in an increasingly oscillatory response surface and more required samples. In this chapter Probabilistic Collocation for Limit Cycle Oscillations (PCLCO) is developed, which achieves a constant uncertainty quantification interpolation accuracy in time with a constant number of samples. The method is based on performing uncertainty quantification interpolation for a time-independent parameterization of periodic samples instead of the time-dependent samples themselves. Numerical results for the harmonic oscillator, a two-degree-of-freedom airfoil flutter model, and the fluid-structure interaction of an elastically-mounted cylinder show that a low number of 3 samples can be sufficient to resolve the asymptotic effect of a random input parameter.

Based on: J.A.S. Witteveen, G.J.A. Loeven, S. Sarkar, H. Bijl, Probabilistic Collocation for period-1 Limit Cycle Oscillations, J. Sound Vib. 311 (2008) 421–439.

5.1 Introduction

In this chapter a Probabilistic Collocation formulation for modeling the long-term stochastic behavior of limit cycle oscillations (PCLCO) in linear and nonlinear problems is proposed. The idea is to apply Probabilistic Collocation to a time-independent parameterization of the response instead of to the time-dependent response itself. Due to the time-independent parameterization the accuracy of the PCLCO interpolation is independent of time, which enables it to resolve the long-term stochastic behavior of dynamical systems. For limit cycle oscillations a suitable parameterization of the periodic response consists of the frequency, the relative phase, the amplitude, a reference value and the normalized period. A Probabilistic Collocation approach is employed since it can approximate these functionals of the response more effectively than a Stochastic Galerkin method.

In flutter analysis, one is usually interested in the effect of uncertainty on the bifurcation point from a damped response to a limit cycle oscillation. At the flutter point the damped response often changes to a period-1 oscillation with one main frequency. An initial quantification of the effect of uncertainty usually focuses on the effect of individual parameters. The application of the formulation of PCLCO is therefore limited to period-1 limit cycle oscillations with one main frequency subject to one uncertain parameter. It is assumed that these oscillations exist in the relevant parameter domain.

In practical applications it might not be trivial to ensure a priori that periodic solutions exist for the relevant input parameter range. It is therefore determined a posteriori whether the deterministic samples are periodic. The response is considered to be periodic, if after sufficiently long integration time, $t_{\max}$, the response results within a threshold value in identical orbits in phase-space. The effect of the threshold on the approximation with PCLCO at $t_{\max}$ is small, since the parameterization is extracted from the last full period before $t_{\max}$. If all samples have a periodic response, then PCLCO post-processing is applied to the samples. Otherwise normal Probabilistic Collocation post-processing applied, since both PCLCO and Probabilistic Collocation are based on the same deterministic samples.

The Probabilistic Collocation approach for limit cycle oscillations is introduced in section 5.2. Numerical results are presented for the harmonic oscillator, the airfoil flutter model and the elastically-mounted cylinder in section 5.3. A harmonic oscillator problem with an uncertain spring stiffness is considered to demonstrate that PCLCO is able of capturing the long-term stochastic behavior of limit cycle oscillations successfully. This model problem, which is similar to the sinusoidal model problem studied by Pettit and Beran [78], does not involve a transient part in the deterministic response. An error convergence study up to a Polynomial Chaos order of 8 is performed. Subsequently, PCLCO is applied to other engineering applications involving periodic response. A two-degree-of-freedom airfoil flutter model is considered subject to uncertainty in the structure. This problem is used to study the effect of a deterministic transient behavior on the PCLCO approach. Finally, a combination of PCLCO and Probabilistic Collocation is employed to propagate the uncertainty through a fluid-structure interaction simulation of an elastically-mounted cylinder with an uncertain free stream velocity. In that case, Probabilistic Collocation is applied for short-term integration in the transient part of the deterministic time series. The stochastic transient behavior and the long-term stochastic response are resolved using PCLCO. This chapter is concluded in section 5.4.

5.2 Probabilistic Collocation for limit cycle oscillations

In this section the Probabilistic Collocation method for limit cycle oscillations is introduced. It is based on the time-independent parameterization of limit cycle oscillations given in section 5.2.2. First the general Probabilistic Collocation framework is briefly reviewed in section 5.2.1.

5.2.1 Probabilistic Collocation method

Probabilistic Collocation is based on collocating the stochastic problem in Gauss quadrature points in the probability space [5, 54]. Suitable Gauss points are the zeros of polynomials orthogonal with respect to the probability density of the uncertain input. The stochastic moments of the output are computed by Gauss quadrature based on a polynomial approximation of the response and a Polynomial Chaos description of the probability distribution.

Differential equation (1.1) is considered subject to parametric input uncertainty with a probabilistic description in the form of

$$\mathcal{L}(a)u = 0. \tag{5.1}$$

The uncertain variable $u(x,t,\omega)$ is then approximated in the Probabilistic Collocation method as

$$u(x,t,\omega) = \sum_{k=1}^{N} u_k(x,t) l_k(a(\omega)), \tag{5.2}$$

where N is the number of collocation points $\{a_k\}_{k=1}^N$ in probability space and $N-1$ is the Polynomial Chaos order of the approximation (5.2). The collocation points $\{a_k\}_{k=1}^N$ are the zeros of the polynomial $\pi_{N+1}(a)$, where $\{\pi_i(a)\}_{i=0}^{N+1}$ is the set of polynomials up to order $N+1$ orthogonal with respect to the probability density function $p_\mathrm{a}(a)$ of the uncertain input parameter $a(\omega)$. The polynomials $\{\pi_i(a)\}_{i=0}^{N+1}$ are given by the orthogonality relation

$$\langle \pi_i(a)\pi_j(a)\rangle = \int \pi_i(a)\pi_j(a)p_\mathrm{a}(a)\mathrm{d}a = \langle \pi_i(a)^2\rangle\delta_{ij}, \tag{5.3}$$

for $i, j = 1, \ldots, N+1$, where $\langle . \rangle$ denotes an inner product. For several standard input distributions the polynomials $\{\pi_i(a)\}_{i=0}^{N+1}$ in (5.3) are (scaled) classical polynomials [90] of which the roots are tabulated to full accuracy. For other input distributions the collocation points can be computed numerically [54].

The deterministic coefficients $\{u_k(x,t)\}_{k=1}^{N}$ in (5.2) are then the deterministic solutions of (5.1) for the parameter values $\{a_k\}_{k=1}^{N}$. The basis polynomials $\{l_k(a)\}_{k=1}^{N}$ of the expansion (5.2) are Lagrange polynomials with respect to the collocation points $\{a_k\}_{k=1}^{N}$ for which holds

$$l_k(a_j) = \delta_{jk}, \qquad j, k = 1, \ldots, N, \tag{5.4}$$

where δ_{jk} is the Kronecker delta. The mean $\mu_\mathrm{u}(x,t)$ and variance $\sigma_\mathrm{u}^2(x,t)$ of the solution $u(x,t,\omega)$ are computed using Gauss quadrature integration based on the quadrature points $\{a_k\}_{k=1}^{N}$, for example,

$$\mu_\mathrm{u}(x,t) = \sum_{k=1}^{N} w_k u_k(x,t), \tag{5.5}$$

where w_k are Gauss quadrature weights. Multidimensional collocation points can be obtained from tensor products of the one-dimensional collocation points or a sparse grid approach [117].

5.2.2 Time-independent parameterization of limit cycle oscillations

In long-term time integration of unsteady problems subject to uncertainty the uncertainty response surface $u(x,t,\omega)$ can be a highly nonlinear function of the uncertain input parameter $a(\omega)$ [78]. In that case, the global polynomial representation in the Polynomial Chaos description is not adequate for approximating the response surface. Increasing the Polynomial Chaos order in Probabilistic Collocation or the number of elements in the multi-element generalized Polynomial Chaos extends the valid integration time [105]. However, the Polynomial Chaos approximation fails asymptotically due to the growing nonlinearity of the response surface in time.

The long-term periodic response $u(x,t,\omega)$ can be parameterized by a vector of time-independent parameters $z(x,\omega)$ than time t. For a periodic response $z(x,\omega)$ can consist of the frequency, the relative phase, the amplitude, a reference value and the normalized period. This results in a time-independent parameterization of the periodic response $u_{\text{periodic}}(x,z(x,\omega),\omega)$. Probabilistic Collocation can then be applied to the parameterization $z(x,\omega)$ instead of the time-dependent response $u(x,t,\omega)$ itself. The realizations of the parameterization $z_k(x,\omega)$ are extracted from the same time series $u_k(x,t,\omega)$ as in Probabilistic Collocation obtained from solving (5.1) at the collocation points $\{a_k\}_{k=1}^N$. This enables the use of existing deterministic time integration solvers. The accuracy of the Polynomial Chaos approximation of the parameterization $z(x,\omega)$:

$$z(x,\omega) = \sum_{k=1}^{N} z_k(x) l_k(a(\omega)). \tag{5.6}$$

is then independent of time t. If the parameterization $z(x,\omega)$ depends not too nonlinearly on the uncertain input parameter $a(\omega)$, the Polynomial Chaos order of the approximation of the long-term behavior can be relatively low. The PCLCO approximation of the response $u(x,t,\omega)$ is given by substitution of (5.6) into a parameterized description of the response. This formulation of Probabilistic Collocation for limit cycle oscillations is capable of resolving the effect of the uncertain input parameter $a(\omega)$ on the long-term stochastic response.

As mentioned before, a suitable time-independent parameterization of the asymptotic periodic response of limit cycle oscillations is a parameterization in terms of the frequency $f(x,\omega)$, the relative phase $\phi(x,\omega)$, the amplitude $A(x,\omega)$, a reference value $u_0(x,\omega)$ and the normalized period $u_{\text{period}}(x,\tau,\omega)$, with $\tau \in [0,2\pi]$. The time series $u_k(x,t,\omega)$ for the N collocation points $\{a_k\}_{k=1}^N$ in probability space result in N realizations of the frequency $f_k(x)$, the phase $\phi_k(x)$, the amplitude $A_k(x)$, the reference value $u_{0_k}(x)$ and the normalized period $u_{\text{period}_k}(x,\tau)$ of the periodic response:

- the frequency $f_k(x)$ is defined as the inverse of the period length, which is the smallest time $t_{\text{period}_k}(x) > 0$ for which holds in the asymptotic region $u_k(x,t+t_{\text{period}_k}(x)) = u_k(x,t)$;
- The relative phase $\phi_k(x)$ of the time series is defined as the phase of the oscillation at $t = t_{\max}$ with respect to the time of the latest maximum $t_{\text{u}_{\max k}}(x)$ by $\phi_k(x) = n_{\text{periods}_k}(x) + (t_{\max} - t_{\text{u}_{\max k}}(x))f_k(x)$ with $n_{\text{periods}_k}(x)$ the integer number of completed cycles;
- The amplitude $A_k(x)$ is equal to half the difference between the minimum and the maximum of the period $A_k(x) = \frac{1}{2}(u_{\max_k}(x) - u_{\min_k}(x))$;

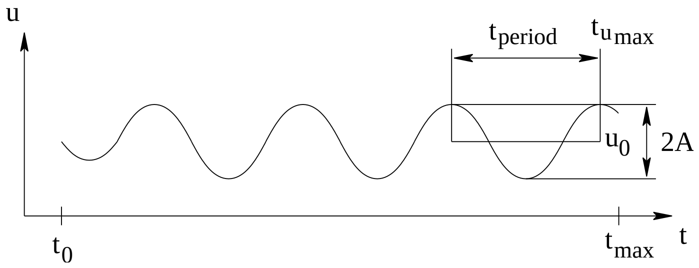

Figure 5.1: Definition of parameters to describe limit cycle oscillation in PCLCO.

- the reference value $u_{0_k}(x)$ is chosen to be the average of the minimum and maximum of the period $u_{0_k} = \frac{1}{2}(u_{\min_k}(x) + u_{\max_k}(x))$.

This parameterization is obtained from the last full period of the simulation after establishing a sufficiently long integration time for the development of the periodic oscillation, see Figure 5.1. The Polynomial Chaos approximation of the parameterization $f(x,\omega)$, $\phi(x,\omega)$, $A(x,\omega)$ and $u_0(x,\omega)$ is then determined using (5.6). The PCLCO approximation of the response is given by substituting (5.6) into the parameterized description of the response given by

$$u(x,t,\omega) = u_0(x,\omega) + A(x,\omega)u_{\text{period}}(x,\tau(x,\omega),\omega), \tag{5.7}$$

with $\tau(x,\omega) = 2\pi(\phi(x,\omega) + (t - t_{\max})f(x,\omega)) \pmod{2\pi}$. This results in a non-polynomial response surface approximation. For this expression also an expansion of the normalized period $u_{\text{period}}(x,\tau,\omega)$ similar to (5.6) is required. The shape of the period of the deterministic time series $u'_{\text{period}_k}(x,t'_k(x))$ with $t'_k(x) = [0, t_{\text{period}_k}(x)]$ is extracted from the last full period of the functions $u_k(x,t)$. The normalized period $u_{\text{period}_k}(x,\tau)$, with $\tau \in [0,2\pi]$, is obtained by scaling the periods $u'_{\text{period}_k}(x,t'_k(x))$ by their frequency $f_k(x)$, amplitude $A_k(x)$ and equilibrium $u_{0_k}(x)$

$$u_{\text{period}_k}(x,\tau) = \frac{1}{A_k(x)}\left(u'_{\text{period}_k}\left(x, \frac{\tau}{2\pi f_k(x)}\right) - u_{0_k}(x)\right), \tag{5.8}$$

with $k = 1,\dots,N$ and $\tau \in [0,2\pi]$. The Polynomial Chaos approximation of $u_{\text{period}}(x,\tau,\omega)$ based on the representations $u_{\text{period}_k}(x,\tau)$ is given by

$$u_{\text{period}}(x,\tau,\omega) = \sum_{k=1}^{N} u_{\text{period}_k}(x,\tau)l_k(a(\omega)). \tag{5.9}$$

In practice $u_{\mathrm{period}}(x, \tau, \omega)$ is determined at n_τ discrete angles $\{\tau_j\}_{j=1}^{n_\tau} \in [0, 2\pi]$ and interpolation can be employed to obtain $u_{\mathrm{period}}(x, \tau, \omega)$ from $\{u_{\mathrm{period}}(x, \tau_j, \omega)\}_{j=1}^{n_\tau}$. One could also use a Fourier transform to discretize the normalized period. In pseudo algorithmic form PCLCO can be represented as follows:

1. Solve N deterministic problems for the parameter values corresponding to the N collocation points in probability space;
2. Extract $f_k(x)$, $\phi_k(x)$, $A_k(x)$, $u_{0_k}(x)$, and $u_{\mathrm{period}_k}(x, \tau)$ for $k = 1, \dots, N$ from the N deterministic solutions;
3. Construct the global polynomial approximations $f(x, \omega)$, $\phi(x, \omega)$, $A(x, \omega)$, $u_0(x, \omega)$, and $u_{\mathrm{period}}(x, \tau, \omega)$ using (5.6) and (5.9);
4. Substitute $f(x, \omega)$, $\phi(x, \omega)$, $A(x, \omega)$, $u_0(x, \omega)$, and $u_{\mathrm{period}}(x, \tau, \omega)$ into (5.7) to find the approximation of the response $u(x, t, \omega)$.

The mean and variance of the response $u(x, t, \omega)$ are determined by numerically integrating of the response surface (5.7). The distribution function is given by sorting the function u–ω, with $\omega \in [0, 1]$, to a monotonically increasing reconstruction.

5.3 Numerical results

In this section numerical results of PCLCO are presented for the analytical harmonic oscillator problem, a two-degrees-of-freedom airfoil flutter model and a fluid-structure interaction simulation of an elastically mounted cylinder. The results are compared to those of Probabilistic Collocation (PC), see section 5.2.1, and Monte Carlo (MC) simulations.

5.3.1 Harmonic oscillator

The analytical harmonic oscillator problem with an uncertain spring stiffness is considered to demonstrate the properties of PCLCO for a problem with no transient part in the deterministic response. PCLCO is compared to Probabilistic Collocation in an error convergence study with respect to an MC reference solution. The motion of the harmonic oscillator is described by

$$m \frac{\partial^2 x(t, \omega)}{\partial t^2} + k(\omega) x(t, \omega) = 0, \qquad t \in [0, \infty), \tag{5.10}$$

with deterministic initial conditions $x(0) = \tilde{x}_0 = 1$ and $\frac{\partial x}{\partial t}(0) = \tilde{x}_1 = 1$, mass $m = 1$ and uncertain spring stiffness $k(\omega)$ with a lognormal distribution with mean $\mu_\mathrm{k} = 1$ and coefficient of variation $CV_\mathrm{k} = 10\%$. The analytical solution of (5.10) can be written as

$$x(t, \omega) = x_0(\omega) + A(\omega)\cos(2\pi f(\omega)t + \phi(\omega)), \tag{5.11}$$

with frequency $f(\omega) = \frac{1}{2\pi}\sqrt{\frac{k(\omega)}{m}}$, phase $\tan\phi = \frac{\tilde{x}_1}{\tilde{x}_0\sqrt{k/m}}$, amplitude $A = \frac{\tilde{x}_0}{\cos\phi}$ and reference value $x_0(\omega) = 0$. The response $x(t, \omega)$ given by (5.11) is a periodic function of time with no transient part. The solution is considered until $t_\mathrm{max} = 100$ which corresponds to approximately 16 periods for μ_k.

PCLCO is employed with three collocation points $\{k_i\}_{i=1}^N$, with $N = 3$, for the uncertain parameter $k(\omega)$. The time series $x_i(t)$ are parameterized by f_i, ϕ_i, A_i and x_{0_i}. For this simple model problem the scaled periodic motion $x_\mathrm{period}(\tau, \omega)$ is independent of ω since $x_\mathrm{period}(\tau, \omega) = \cos(\tau)$ with $\tau \in [0, 2\pi]$. The parameterization describes the time series $x_i(t)$ for $t > 0$ exactly.

In Figure 5.2 the three samples $\{x_i(t)\}_{i=1}^N$ are shown. The periodic responses start at the deterministic initial condition without transient behavior. The uncertainty affects the amplitude and the frequency of the response α. The effect on the frequency results in an increasing phase difference between the time series. The functions diverge from each other in time, since the frequency and amplitude of the time series depend on the sample value k_i.

The mean $\mu_\mathrm{x}(t)$ and the variance $\sigma_\mathrm{x}^2(t)$ of the response $x(t, \omega)$ are shown in Figure 5.3 as function of time t. The approximations of PCLCO and Probabilistic Collocation for $N = 3$ are compared to a MC simulation with 1000 uniformly distributed samples. In contrast to the periodic deterministic solutions, the MC solution for the mean $\mu_\mathrm{x}(t)$ is a damped oscillation, see Figure 5.3a. The decaying oscillation is caused by the effect of the uncertainty on the frequency of the time series. Due to the increasing phase difference in time, time series with opposite signs increasingly cancel each other.

The result of PCLCO is indistinguishable from the MC result for all times $t \in [0, t_\mathrm{max}]$. The PC approximation of the mean is accurate up to approximately $t = 25$. For later times the error of the Probabilistic Collocation approximation rises to unacceptable levels. Using a higher Polynomial Chaos order or a multi-element approach elongates the domain in which the approximation is accurate. However, without continuously increasing the order the approximation would fail asymptotically for long-term integration at some t [78, 107].

The variance $\sigma_\mathrm{x}^2(t)$ shows a transient oscillatory behavior until it damps to the steady value of $\sigma_\mathrm{x}^2(t) = 1.0$ for $t > 50$, see Figure 5.3b. Although the samples shown

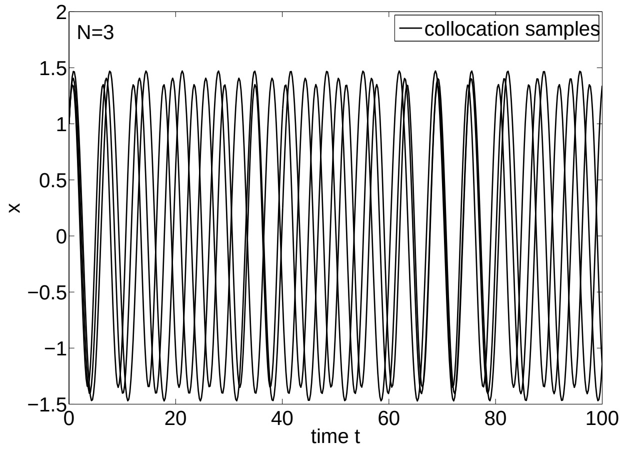

Figure 5.2: The three deterministic realizations at the collocation points for the harmonic oscillator.

in Figure 5.2 do not exhibit transient behavior and are unsteady for all t, the stochastic solution has a transient behavior due to the deterministic initial condition and reaches a steady solution for long-term integration. PCLCO resolves both the transient and the asymptotic stochastic solution as the results of MC and PCLCO are indistinguishable also for the variance. The accuracy of Probabilistic Collocation deteriorates for the variance at approximately $t = 15$ which is earlier than for the mean. Probabilistic Collocation is unable to predict the asymptotic steady solution of the variance which results in large errors.

The reason that PCLCO accurately approximates the long-term stochastic behavior already with $N = 3$ is that in PCLCO the polynomial approximation of Probabilistic Collocation is not applied to the response in terms of the time series $x_i(t)$ directly, but to the parameterization f_i, ϕ_i and A_i. This parameterization of the periodic response is independent of time which enables for an approximation of the asymptotic behavior. In addition, the parameterization $f(\omega)$, $\phi(\omega)$ and $A(\omega)$ depends almost linearly on the uncertain input parameter $k(\omega)$ which results in an accurate approximation with $N = 3$.

In Figure 5.4 the approximation of the frequency $f(\omega)$ is given in terms of its response surface with respect to $k(\omega)$ and its probability distribution function. The com-

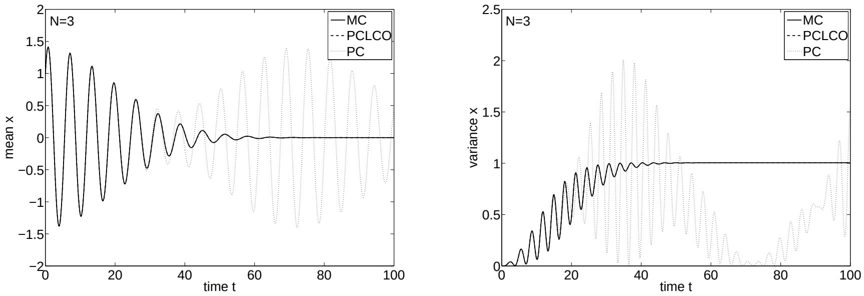

(a) Mean

(b) Variance

Figure 5.3: Response of the harmonic oscillator by Monte Carlo (MC), PCLCO and Probabilistic Collocation (PC).

parison of the PCLCO approximation and the MC results in Figure 5.4a shows that the frequency $f(\omega)$ depends almost linearly on $k(\omega)$. The polynomial PCLCO approximation based on the collocation points results for $N = 3$ in an adequate approximation of the frequency response surface. Therefore, also the probability distribution function of the frequency is accurately resolved, see Figure 5.4b. Similar results are obtained for the phase $\phi(\omega)$ and amplitude $A(\omega)$.

Based on the time-independent approximations of $f(\omega)$, $\phi(\omega)$, and $A(\omega)$, the analytical solution (5.11) gives the time-dependent approximation of $x(t, \omega)$. In Figure 5.5 the approximations of the response surface $x(t, \omega)$–$k(\omega)$ and the probability distribution of $x(t, \omega)$ are given for $t = \{1, 20, 100\}$ for MC, PCLCO and Probabilistic Collocation. The response surface is almost linear after short-term integration, see Figure 5.5a. For this case both PCLCO and Probabilistic Collocation result in accurate approximations of the response surface at $t = 1$. This time interval corresponds to approximately 0.16 periods for μ_{k}. The approximation of the probability distribution of $x(t, \omega)$ at $t = 1$ is also accurate in Figure 5.5b.

After long-term integration the response surface is increasingly nonlinear, see Figures 5.5c and 5.5e for the results at $t = 20$ and $t = 100$, which corresponds to approximately 3.2 and 16 periods for μ_{k}, respectively. The PCLCO approximation based on the three collocation points and the parameterization (5.11) maintains a similar accuracy in the approximation of the response surface independent of the time t. The polynomial approximation of Probabilistic Collocation through the three collocation points is clearly not adequate to represent the increasingly nonlinear response surface.

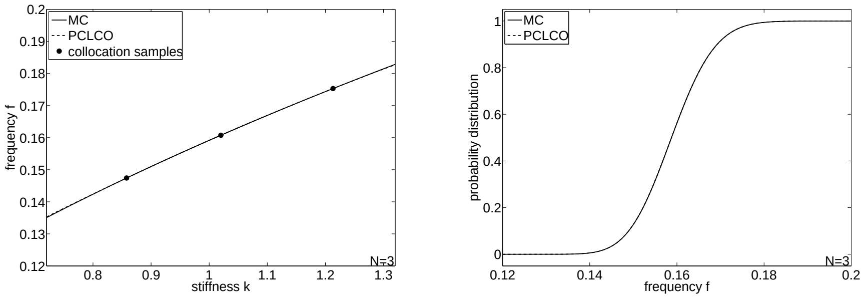

(a) Response surface (b) Probability distribution

Figure 5.4: Frequency of the harmonic oscillator by Monte Carlo (MC) and PCLCO.

In Figures 5.5d and 5.5f the probability distribution of $x(t,\omega)$ after long-term integration is shown for $t = 20$ and $t = 100$. The probability distribution function reaches a steady solution asymptotically. PCLCO resolves the detailed features of the probability distribution function also near $x = \pm 1.5$ for all times $t \in [0, t_{\max}]$.

An error convergence study is performed to compare the accuracy of PCLCO and Probabilistic Collocation for a range of Polynomial Chaos orders up to $N = 9$ at different times t, see Figure 5.6. The convergence study focuses on the contribution of the Polynomial Chaos expansion to the error in the long-term behavior of the stochastic system, since in this analytical test problem numerical time integration errors are absent. The time-averaged L_1-errors in the approximation of the mean and the variance in different time intervals are considered. In Figure 5.6a the error convergence of PCLCO and Probabilistic Collocation up to $t = 1$ is shown for the error in the mean $\mu_{\mathrm{x}}(t)$. Probabilistic Collocation results for this short-term integration problem in fast exponential convergence which reaches machine precision for $N = 7$. PCLCO convergences three orders of magnitude to an error lower than 10^{-6} at $N = 9$.

In Figure 5.6c the error convergence for the mean at $t = 20$ is shown. PCLCO convergences again to an error lower than 10^{-6} for $N = 9$. Probabilistic Collocation convergences significantly slower than for the $t = 1$ case to an error of 10^{-3}, which is higher than for PCLCO. This is also demonstrated by the error convergence of the mean for $t = 100$ in Figure 5.6e, for which Probabilistic Collocation hardly convergences, but PCLCO still convergences beyond an error of 10^{-6} for $N = 9$. In Figures 5.6b, 5.6d and 5.6f similar results are shown for the error in the approximation of the variance at $t = 1$, $t = 20$, and $t = 100$.

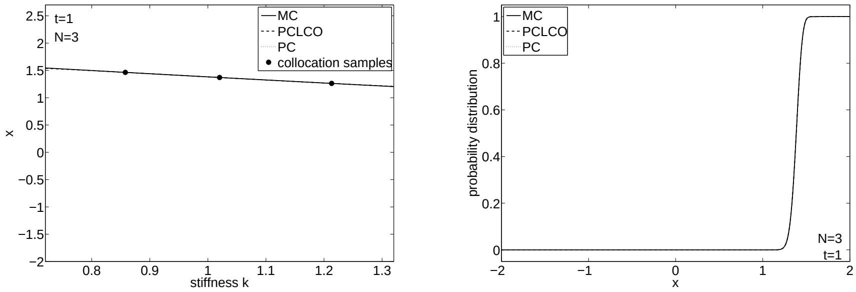

(a) Response at $t = 1$ (b) Distribution at $t = 1$

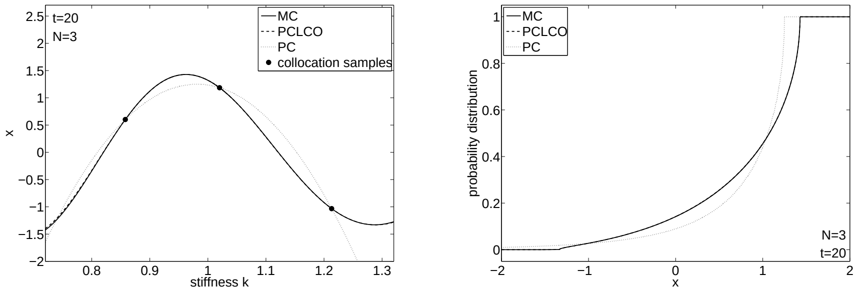

(c) Response at $t = 20$ (d) Distribution at $t = 20$

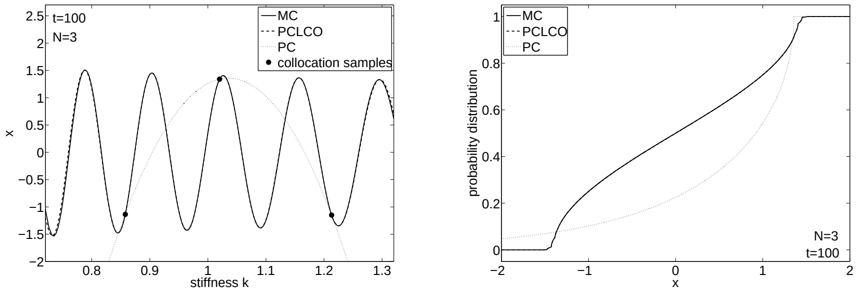

(e) Response at $t = 100$ (f) Distribution at $t = 100$

Figure 5.5: Response surface $x(t, \omega)$–$k(\omega)$ and its probability distribution by Monte Carlo (MC), PCLCO and Probabilistic Collocation (PC) for the harmonic oscillator.

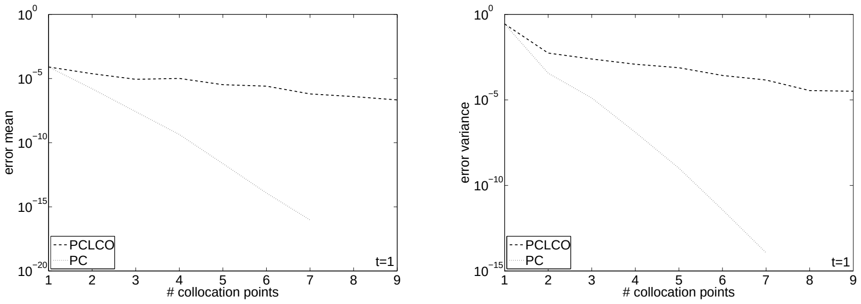

(a) Error mean at $t = 1$ (b) Error variance at $t = 1$

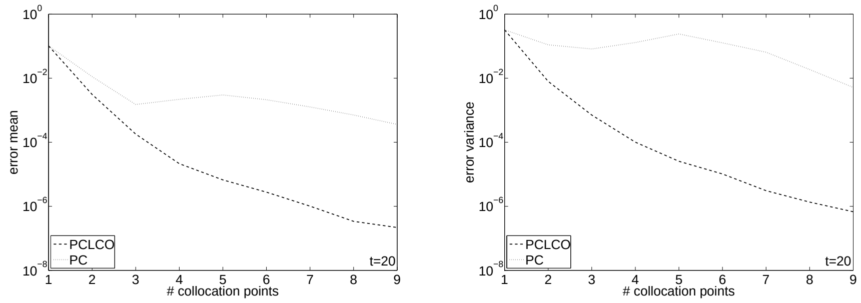

(c) Error mean at $t = 20$ (d) Error variance at $t = 20$

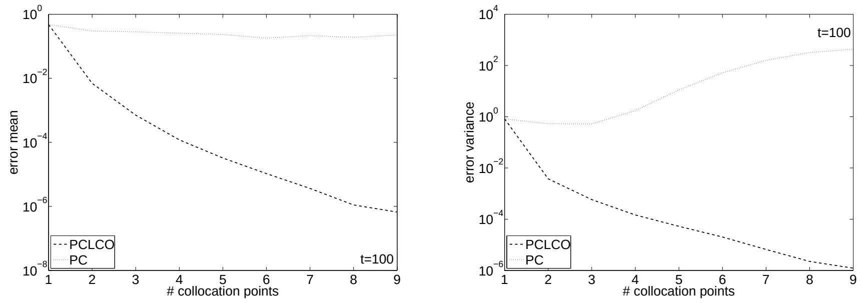

(e) Error mean at $t = 100$ (f) Error variance at $t = 100$

Figure 5.6: Error convergence of PCLCO and Probabilistic Collocation (PC) for the mean and variance for the harmonic oscillator.

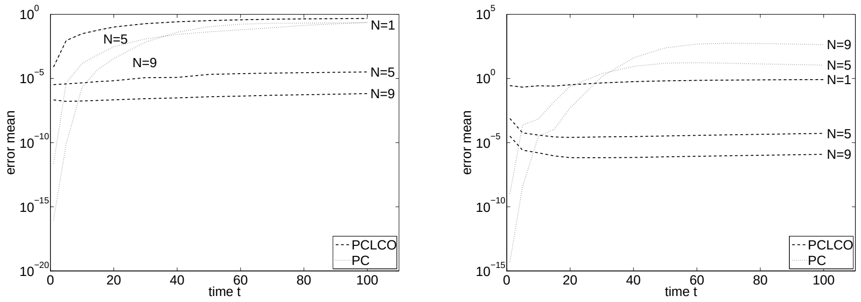

(a) Error mean

(b) Error variance

Figure 5.7: Error of PCLCO and Probabilistic Collocation (PC) as function of time for the harmonic oscillator.

To demonstrate that the accuracy of PCLCO is nearly independent of time, the errors in the approximation of the mean and the variance of PCLCO and Probabilistic Collocation are given as function of time in Figure 5.7 for $N = 1$, $N = 5$, and $N = 9$. For $N = 1$ both PCLCO and Probabilistic Collocation reduce to a deterministic solve for the mean value of the uncertain input parameter μ_{k}. For higher Polynomial Chaos orders $N = 5$ and $N = 9$ PCLCO results in a error which is nearly constant in time and decreases for increasing N. The error in the approximation of the variance even decreases with time for short-term integration $t < 20$, see Figure 5.7b. The accuracy of Probabilistic Collocation depends strongly on time. For long-term integration the error in the Probabilistic Collocation approximation even increases with an increasing Polynomial Chaos order. The post-processing of the samples is in PCLCO computationally more intensive than in Probabilistic Collocation. However, the computational costs in engineering applications are dominated by computing the deterministic samples. The number of samples in the PCLCO computation is over a factor 10^2 smaller than in the MC simulation.

5.3.2 2 DOF flutter model

In this section PCLCO is applied to a relevant model for flutter analysis. Flutter models are often used instead of full unsteady fluid-structure interaction simulations. Here a two-degree-of-freedom model for the pitch and plunge motion of an airfoil, see Figure 5.8, is used which was studied deterministically for example by Lee et al. [49] and

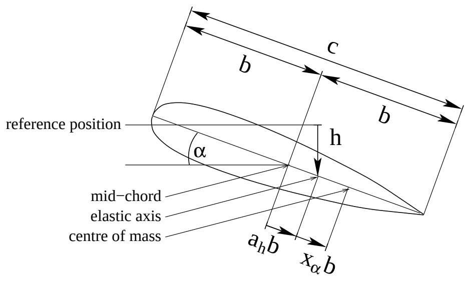

Figure 5.8: The two-degree-of-freedom airfoil flutter model.

stochastically using Fourier Chaos by Millman et al. [66]. The aeroelastic equations of motion with cubic restoring springs in both pitch and plunge are given in [49] as

$$\xi'' + x_\alpha \alpha'' + 2\zeta_\xi \frac{\bar{\omega}}{U^*}\xi' + \left(\frac{\bar{\omega}}{U^*}\right)^2 (\xi + \beta_\xi \xi^3) = -\frac{1}{\pi\mu} C_{\mathrm{L}}(\tau), \tag{5.12}$$

$$\frac{x_\alpha}{r_\alpha^2}\xi'' + \alpha'' + 2\frac{\zeta_\alpha}{U^*}\alpha' + \frac{1}{U^{*2}}(\alpha + \beta_\alpha \alpha^3) = \frac{2}{\pi\mu r_\alpha^2} C_{\mathrm{M}}(\tau), \tag{5.13}$$

where α is the pitch angle, $\xi = h/b$ is the non-dimensional plunge displacement of the elastic axis, with $b = c/2$ the half-chord, β_ξ and β_α are the nonlinear spring constants, r_α is the radius of gyration about the elastic axis, and ζ_ξ and ζ_α are the viscous damping coefficients in plunge and pitch, respectively. The ratio of natural frequencies is $\bar{\omega} = \omega_\xi/\omega_\alpha$, where ω_ξ and ω_α are the natural frequencies of the uncoupled plunging and pitching modes, respectively. The bifurcation parameter is defined as $U^* = U/(b\omega_\alpha)$. The non-dimensionalized time is $\tau = Ut/b$. The expressions for the aerodynamic force and moment coefficients, $C_{\mathrm{L}}(\tau)$ and $C_{\mathrm{M}}(\tau)$ are given by Fung [25] as

$$\begin{aligned} C_{\mathrm{L}}(\tau) &= \pi(\xi'' - a_{\mathrm{h}}\alpha'' + \alpha') + 2\pi\left\{\alpha(0) + \xi'(0) + \left[\frac{1}{2} - a_{\mathrm{h}}\right]\alpha'(0)\right\}\phi(\tau) + \\ &\quad 2\pi\int_0^\tau \phi(\tau - \sigma)\left[\alpha'(\sigma) + \xi''(\sigma) + \left(\frac{1}{2} - a_{\mathrm{h}}\right)\alpha''(\sigma)\right]\mathrm{d}\sigma, \end{aligned} \tag{5.14}$$

$$\begin{aligned} C_{\mathrm{M}}(\tau) \quad = \quad & \pi\left(\frac{1}{2}+a_{\mathrm{h}}\right)\left\{\alpha(0)+\xi'(0)+\left(\frac{1}{2}-a_{\mathrm{h}}\right)\alpha'(0)\right\}\phi(\tau)+ \\ & \pi\left(\frac{1}{2}+a_{\mathrm{h}}\right)\int_0^\tau \phi(\tau-\sigma)\Big\{\alpha'(\sigma)+. \\ & \xi''(\sigma)+\left(\frac{1}{2}-a_{\mathrm{h}}\right)\alpha''(\sigma)\Big\}\mathrm{d}\sigma+ \\ & \frac{\pi}{2}a_{\mathrm{h}}(\xi''-a_{\mathrm{h}}\alpha'')-\left(\frac{1}{2}-a_{\mathrm{h}}\right)\frac{\pi}{2}\alpha'-\frac{\pi}{16}\alpha'', \end{aligned} \tag{5.15}$$

where the elastic axis is located at a distance $a_{\mathrm{h}}b$ from mid-chord, the mass center is located at a distance $x_\alpha b$ from the elastic axis and $\phi(\tau)$ is the Wagner function

$$\phi(\tau)=1-\psi_1\mathrm{e}^{-\varepsilon_1\tau}-\psi_2\mathrm{e}^{-\varepsilon_2\tau}, \tag{5.16}$$

with the constants $\psi_1 = 0.165$, $\psi_2 = 0.335$, $\varepsilon_1 = 0.0455$ and $\varepsilon_2 = 0.3$ given by Jones [43]. Based on (5.12) to (5.16), a set of first-order ordinary differential equations for the motion of the airfoil is derived in [49]. Following [66, 49], these equations are integrated numerically until $\tau = 2000$ using the explicit fourth-order Runge-Kutta method with a time step of $\Delta\tau = 0.1$, which is approximately $1/256$ of the smallest period.

The following parameter values are used: $\mu = 100$, $a_{\mathrm{h}} = -0.5$, $x_\alpha = 0.25$, $r_\alpha = 0.5$ and $\zeta_\alpha = \zeta_\xi = 0$, as in [66, 49]. For a hard spring model in the pitch degree of freedom ($\beta_\alpha > 0$) the system exhibits a limit cycle oscillation [48]. The nonlinear torsional spring stiffness parameter is set to $\beta_\alpha = 3$. The ratio of uncoupled plunging and pitching modes natural frequencies $\bar{\omega}$ is assumed to be uncertain described by a lognormal distribution. The mean value $\mu_{\bar{\omega}} = 0.2$ is chosen to be equal to the deterministic value used in [66, 49] with a coefficient of variation of $CV_{\bar{\omega}} = 10\%$. The effect of the input uncertainty on the mean and variance of the pitch angle $\alpha(\omega)$ and its bifurcation plot is considered. Results for the plunge deflection $\zeta(\omega)$ are qualitatively similar.

The bifurcation parameter U^* is set to 6.6 as in [66]. PCLCO is applied with $N = 3$ and the results are compared to those of Probabilistic Collocation, and MC based on 1000 uniformly sampled realizations. To cancel the effect of the finite number of MC samples, the mean and variance of PCLCO and Probabilistic Collocation are determined based on the same sampling in their response surface approximation as MC. The collocation samples of PCLCO are shown in Figure 5.9. The samples show a periodic response with a transient behavior for $\tau < 100$. The uncertainty in $\bar{\omega}$ affects the frequency and the amplitude of the samples. The periodic reconstruction of the time series samples by PCLCO, see (5.7), is given by the dashed lines. The periodic

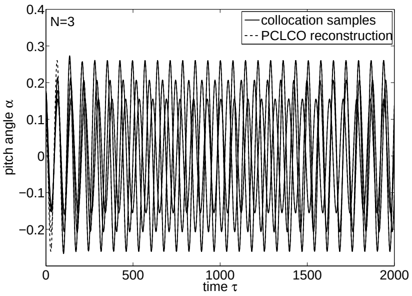

Figure 5.9: The three deterministic realizations and their PCLCO reconstruction at the collocation points for the airfoil flutter model.

oscillations for $\tau > 100$ are exactly represented. The transient behavior of the samples for $\tau < 100$ is not modeled in the periodic reconstruction.

In Figure 5.10 the mean pitch angle $\mu_\alpha(\tau)$ is given. It shows a transient behavior for $\tau < 100$ after which the mean develops a decaying oscillation. PCLCO results in an excellent match of the long-term MC results. The mean for $\tau < 100$ is not accurately resolved by PCLCO, since it does not model the transient part of the deterministic samples. Probabilistic Collocation gives an accurate approximation of the mean for $\tau < 800$. For higher values of the non-dimensional time τ, Probabilistic Collocation does not predict the asymptotic damped oscillation.

The variance of the pitch angle $\sigma^2_\alpha(\tau)$ is given in Figure 5.11. The variance is an oscillating increasing function of τ until $\tau \approx 1000$ at which it reaches a steady asymptotic value of approximately $\sigma^2_\alpha = 1.96 \cdot 10^{-2}$. PCLCO gives an accurate approximation of the steady behavior for $\tau > 1000$. The transient behavior of the variance for $\tau \in [100, 1000]$ is also accurately resolved, since the stochastic transient behavior is due to the deterministic initial condition and not due to the transient behavior of the deterministic samples. The variance for $\tau < 100$ for which the deterministic samples are in their transient is not accurately resolved by PCLCO. However, the transient of the deterministic samples takes less than one-tenth of the stochastic transient part. Probabilistic Collocation does give an accurate approximation for $\tau < 100$, but it fails for long-term integration for $\tau > 500$.

So, PCLCO and Probabilistic Collocation seem complementary, where a Probabilistic Collocation post-processing should be used for the initial time interval in which the deterministic samples exhibit transient behavior. To the long-term periodic behav-

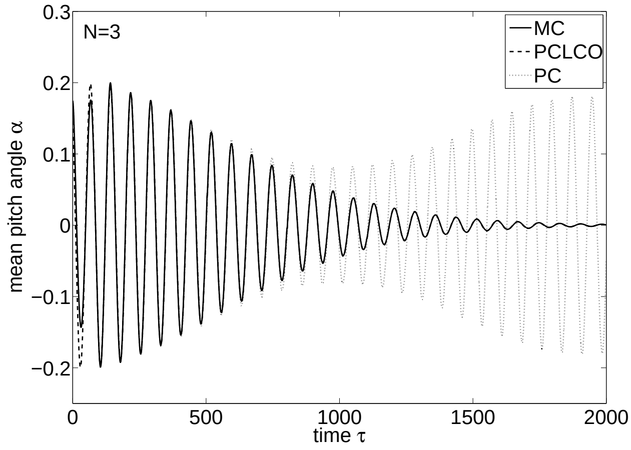

Figure 5.10: Mean pitch angle by Monte Carlo (MC), PCLCO and Probabilistic Collocation (PC) for the two-degree-of-freedom airfoil flutter model.

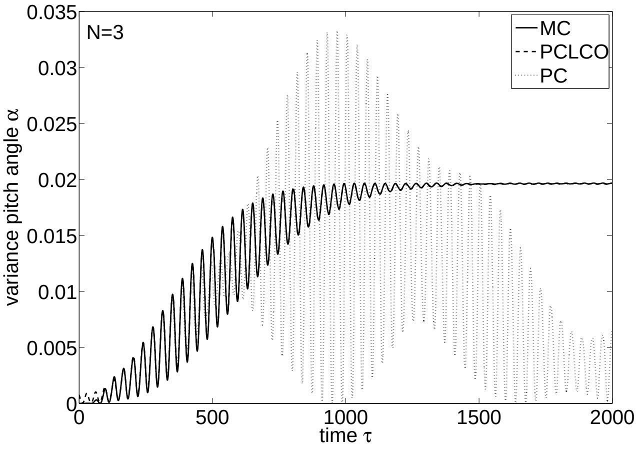

Figure 5.11: Variance of the pitch angle by Monte Carlo (MC), PCLCO and Probabilistic Collocation (PC) for the two-degree-of-freedom airfoil flutter model.

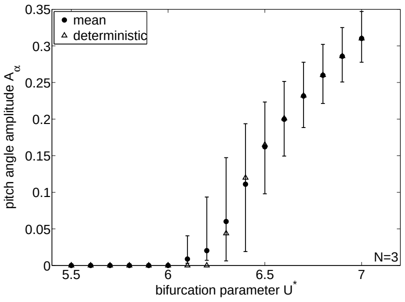

Figure 5.12: Stochastic bifurcation plot of the pitch angle amplitude A_α with the mean and 90% uncertainty bars compared to the deterministic case as function of the bifurcation parameter U^*.

ior of the deterministic samples after their transient, PCLCO post-processing should be applied. This combined approach is demonstrated in the next test problem.

In Figure 5.12 the stochastic bifurcation plot of the pitch angle $\alpha(t,\omega)$ is given in terms of the amplitude $A_\alpha(\omega)$ at $\tau = 2000$ with U^* as bifurcation parameter and $\bar{\omega}$ uncertain. The PCLCO approximation of the mean amplitude μ_{A_α} and uncertainty bars based on the 90% confidence interval are shown. The results are compared to the deterministic bifurcation plot for $\bar{\omega} = \mu_{\bar{\omega}}$. The stochastic bifurcation plot is shown in this way, since it is of practical interest to visualize the distortion of the deterministic bifurcation as a result of the input uncertainty. A supercritical Hopf bifurcation [97] is observed in the deterministic bifurcation plot between $U^* = 6.2$ and $U^* = 6.3$, which is the transition of a damped solution to a limit cycle oscillation. The damped oscillation of the response $\alpha(t,\omega)$ below the bifurcation point results in very small amplitudes at $\tau = 2000$.

The interpretation of the bifurcation of the stochastic system is more complex in terms of D-bifurcation and P-bifurcation [3, 80]. D- or dynamical-bifurcation is concerned with the loss of stability of an equilibrium point at a qualitative change of its eigenvalues or largest Lyapunov exponent. Phenomenological- or P-bifurcation is associated with a qualitative change in the output probability distribution. For a deterministic system the D- and P-bifurcation point coincide.

The stochastic problem is here solved using PCLCO based on $N = 3$ samples, $\bar{\omega}_i = \{0.172; 0.204; 0.243\}$, and a global polynomial interpolation of the response. Near the bifurcation point the true response surface contains a discontinuity in the first derivative. This kink is not resolved as a discontinuity by the global polynomial approximation. Near the bifurcation point the method gives approximate results, which capture the qualitative bifurcation behavior correctly.

The mean of the amplitude $A_\alpha(\omega)$ and the 90% scatter given in Figure 5.12 are functionals of probability space. The bifurcation behavior of these functionals appears to be consistent with a deterministic bifurcation. Below $U^* = 6.0$ PCLCO resolves that both the mean and the 90% interval vanish. The uncertainty in the ratio of natural frequencies $\bar{\omega}$ has no effect on the pre-bifurcation amplitudes $A_\alpha(\omega)$.

Between $U^* = 6.0$ and $U^* = 6.1$, one of the three time-series $\alpha(t, \bar{\omega}_3)$, for the sample $\bar{\omega}_3 = 0.243$, bifurcates from a damped oscillation to a limit cycle oscillation. This results in a bifurcation in the mean and the 90% interval between $U^* = 6.0$ and $U^* = 6.1$. The uncertainty in $\bar{\omega}$ has reduced the flutter point from $U^* \in [6.2; 6.3]$ in the deterministic case to $U^* \in [6.0; 6.1]$. For $U^* > 6.1$ the amount of uncertainty in $A_\alpha(\omega)$ increases rapidly until it starts to decrease at $U^* = 6.4$ to an uncertainty bar with a length of approximately 0.07 for $U^* > 6.8$. The mean value μ_{A_α} differs significantly from the deterministic case in the domain $U^* \in [6.0, 6.5]$ around the deterministic bifurcation point.

In addition to the bifurcation of the mean and the 90% interval, the probability density function (PDF) of the amplitude $A_\alpha(\omega)$ exhibits a P-bifurcation. Because near the bifurcation point the approach gives qualitatively correct answers, the qualitative P-bifurcation behavior of the PDF of $A_\alpha(\omega)$ is described below. Below $U^* = 6.0$ the PDF is a delta function in the origin. After the bifurcation point of $\alpha(t, \bar{\omega}_3)$ in $U^* \in [6.0; 6.1]$ the PDF has a maximum in the origin and decays monotonically for larger $A_\alpha(\omega)$. This P-bifurcation point coincides with the bifurcation of the mean of $A_\alpha(\omega)$ and the 90% interval. The PDF shows a bell-shape with a maximum at a positive $A_\alpha(\omega)$ value after the bifurcation of the second sample $\alpha(t, \bar{\omega}_2)$, with $\bar{\omega}_2 = 0.204$, in $U^* \in [6.2; 6.3]$.

5.3.3 Flow past an elastically-mounted cylinder

The two-dimensional fluid-structure interaction problem of an elastically-mounted circular cylinder in a laminar Navier-Stokes flow is considered in this section, see Figure 5.13. Another study of stochastic cylinder flow can be found in [56]. The gas flow around the cylinder with diameter d is governed by the two-dimensional compressible Navier-Stokes equations [2]:

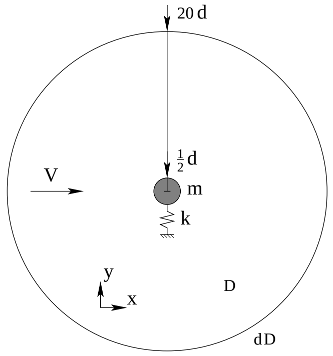

Figure 5.13: The elastically-mounted cylinder in a uniform free stream flow.

$$\begin{aligned}
\frac{\partial \rho}{\partial t} + \frac{\partial \rho u}{\partial x} + \frac{\partial \rho v}{\partial y} &= 0, && (5.17)\\
\rho \frac{Du}{Dt} &= -\frac{\partial p}{\partial x} + \frac{\partial \tau_{\mathrm{xy}}}{\partial y}, && (5.18)\\
\rho \frac{Dv}{Dt} &= -\frac{\partial p}{\partial y} + \frac{\partial \tau_{\mathrm{xy}}}{\partial x}, && (5.19)\\
\rho \frac{DE}{Dt} &= \frac{\partial}{\partial x}\left(k\frac{\partial T}{\partial x}\right) + \frac{\partial}{\partial y}\left(k\frac{\partial T}{\partial y}\right) + \\
& -\frac{\partial p u}{\partial x} - \frac{\partial p v}{\partial y} + \frac{\partial \tau_{\mathrm{xy}} v}{\partial x} + \frac{\partial \tau_{\mathrm{xy}} u}{\partial y} && (5.20)
\end{aligned}$$

with density ρ, velocity components u and v in the x-direction and y-direction, respectively, static pressure p, total energy E, Newtonian viscous stress $\tau_{\mathrm{xy}} = \mu(\partial v/\partial x + \partial u/\partial y)$, dynamic viscosity μ, and thermal conductivity k. The ideal gas equation of state is given by $p = \rho R T$, with specific gas constant R. The cylinder is only free to move in the cross flow y-direction. The structural stiffness is modeled by a linear spring:

$$\frac{\partial^2 y_{\mathrm{cyl}}}{\partial t^2} + \omega_{\mathrm{n}}^2 y_{\mathrm{cyl}} = F_{\mathrm{y}}(t), \qquad (5.21)$$

where $y_{\mathrm{cyl}}(t,\omega)$ is the y-position of the center of the cylinder, $\omega_{\mathrm{n}} = \sqrt{0.1} \approx 0.316$ is the angular natural frequency of the structure, and $F_{\mathrm{y}}(t)$ is the y-component of the resulting pressure force of the flow onto the structure given by

$$F_{\mathrm{y}}(t) = -\int_{\partial D_{\mathrm{cyl}}} p(x,y,t)\mathbf{n}_{\mathrm{cyl}} \cdot \mathbf{e}_{\mathrm{y}} ds, \tag{5.22}$$

with $\mathbf{n}_{\mathrm{cyl}}$ the outward pointing normal of the cylinder surface $\partial D_{\mathrm{cyl}}$ and $\mathbf{e}_{\mathrm{y}}$ the unit vector in the y-direction.

The field equations (5.17) to (5.20) are discretized on a circular spatial domain D with diameter $40d$ using a second-order finite volume method on a grid of $1.2 \cdot 10^4$ volumes. An Arbitrary Lagrangian-Eulerian formulation is employed to couple the fluid mesh with the movement of the structure. Time integration is performed using a BDF-2 method with a stepsize of $\Delta t = 0.25$ until $t = 250$. The boundary conditions on the surface of the cylinder $\partial D_{\mathrm{cyl}}$ are $u = 0$ and $v = \partial y_{\mathrm{cyl}}/\partial t$. The uniform undisturbed flow conditions $u = V$ and $v = 0$ are imposed on the outer boundary of the fluid domain ∂D. Initially the flow field is uniform and the cylinder is at rest with an initial deflection of $y_{\mathrm{cyl}} = 0.5d$ with respect to its equilibrium position.

The undisturbed velocity in the x-direction, V, is assumed to be uncertain described by a truncated lognormal distribution with a coefficient of variation of $CV_{\mathrm{V}} = 10\%$. The mean value of the velocity $\mu_{\mathrm{V}} = 0.3$ corresponds to a Reynolds number of $Re = 1000$. The truncated lognormal distribution limits the variation of the Reynolds number to the range for which the frequency of the periodic fluid motion is typically given by a Strouhal number of $St = fd/V = 0.2$. This corresponds for μ_{V} to an angular frequency of $\omega_{\mathrm{flow}} = 0.38$. For this range the cylinder exhibits a period-1 oscillation. The variation in V affects the frequency of the vortex pattern behind the cylinder and, therefore, influences the frequency of the motion of the cylinder.

A combination of PCLCO and Probabilistic Collocation is used to solve for the stochastic response of the cylinder in the whole time domain. For the short-term integration in the transient part of the deterministic time series Probabilistic Collocation is applied. PCLCO is employed for resolving the stochastic transient behavior and the long-term stochastic response. In Figures 5.14 and 5.15 the evolution of the mean and the variance of the cylinder displacement $y(t,\omega)$ is shown. To demonstrate the convergence of the combined approach for short-term and long-term integration, the approximations for $N = 2$ to $N = 4$ are shown. Probabilistic Collocation is applied to the deterministic samples in an initial time interval starting at $t = 0$. From the time where the PCLCO and Probabilistic Collocation approximations match, the PCLCO approach is applied. These points are in Figures 5.14 and 5.15 denoted by the symbols.

A similar behavior of the mean and the variance can be seen as for the previous test problem. The mean is a decaying oscillation after the transient part of the deterministic

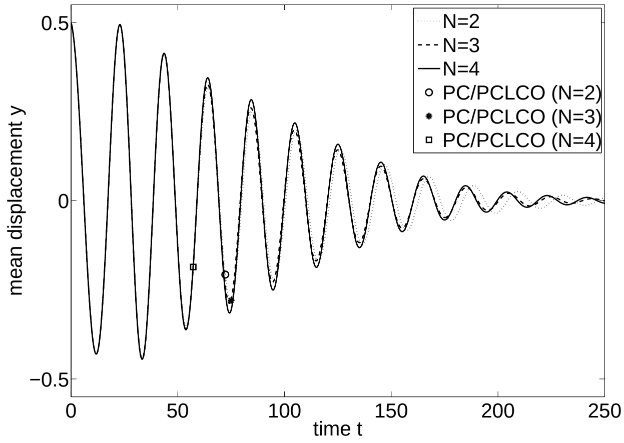

Figure 5.14: Mean deflection of the elastically-mounted cylinder for the combination of PCLCO and Probabilistic Collocation (PC).

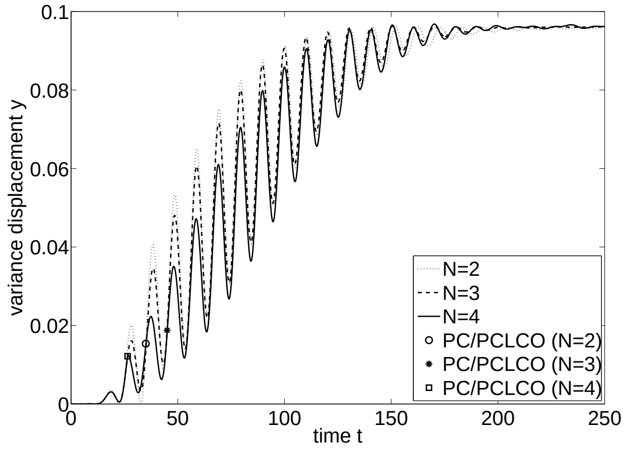

Figure 5.15: Variance of the deflection of the elastically-mounted cylinder for the combination of PCLCO and Probabilistic Collocation (PC).

solves, see Figure 5.14. The variance approaches an asymptotic value of approximately $9.6 \cdot 10^{-2}$ after an oscillatory stochastic transient, which extends beyond the deterministic transient, see Figure 5.15.

In the initial time interval Probabilistic Collocation gives a converged solution already for the low order approximations, which is demonstrated by the coinciding approximations for $N = \{2, 3, 4\}$. PCLCO also shows a converging solution, especially for the long term integration results $t > 150$. In the stochastic transient $t \in [50, 150]$ the results of PCLCO seem to converge less rapidly.

5.4 Summary

A Probabilistic Collocation formulation for modeling the long-term stochastic behavior of limit cycle oscillations (PCLCO) is proposed. In PCLCO, Probabilistic Collocation (PC) is applied to a time-independent parameterization of the periodic time series at the collocation point in probability space. Due to its independence of time the PCLCO approximation is capable of modeling the long-term stochastic behavior of dynamic systems. For limit cycle oscillations (LCO) a suitable parameterization of the periodic deterministic solutions consists of the frequency, relative phase, amplitude, reference value and normalized period. PCLCO is applied to period-1 oscillations with one main frequency subject to an uncertain parameter. Numerical results are presented for the harmonic oscillator, an airfoil flutter model and the flow around an elastically-mounted cylinder.

It has been demonstrated that standard Polynomial Chaos computed using Probabilistic Collocation is initially accurate, but that it is unable to predict the long-term stochastic behavior as its accuracy depends strongly on time. PCLCO accurately predicts the long-term stochastic response and the stochastic transient solution caused by deterministic initial conditions. The accuracy of the PCLCO approximation of the mean and the variance is shown to be independent of time. In practice the error can slightly increase with time due to numerical integration errors. PCLCO does however not resolve the stochastic solution in the transient part of the deterministic response, since it does reconstruct the periodic behavior of the collocation samples. PCLCO and Probabilistic Collocation therefore seem complementary, where Probabilistic Collocation should be used to model the stochastic response for the initial time interval in which the deterministic functions are in their transient part. For resolving the long-term stochastic solution after the transient behavior of the deterministic samples, PCLCO should be employed.

Chapter 6

Unsteady Adaptive Stochastic Finite Elements

The Probabilistic Collocation for Limit Cycle Oscillations (PCLCO) approach developed in the previous chapter results in a constant uncertainty quantification interpolation accuracy for smooth period-1 responses. Dynamical systems with bifurcations to higher-period oscillations and non-periodic responses are know to be especially sensitive to input variations. In this chapter the applicability of PCLCO is extended by introducing a damping factor and higher-period shape functions into the time-independent parameterization, and by combining it with robust Adaptive Stochastic Finite Elements (ASFE) based on Newton-Cotes quadrature in simplex elements developed in Chapter 4. The resulting Unsteady Adaptive Stochastic Finite Elements (UASFE) formulation based on time-independent parameterization is able to resolve non-periodic responses, higher-period oscillations, and bifurcation phenomena, while it maintains a constant uncertainty quantification interpolation accuracy. The extended applicability of UASFE is illustrated by applications to a mass-spring-damper system, the Duffing equation, and a rigid-airfoil fluid-structure interaction problem with multiple random input parameters.

Based on: J.A.S. Witteveen, H. Bijl, An Unsteady Adaptive Stochastic Finite Elements formulation for rigid-body fluid-structure interaction, Comput. Struct. 86 (2008) 2123–2140.

6.1 Introduction

An Adaptive Stochastic Finite Elements approach for unsteady problems is developed based on a combination of the robust ASFE formulation with Newton-Cotes quadrature in simplex elements and an extension of the time-independent parameterization of PCLCO to damped and higher-period oscillations. The applicability of Unsteady Adaptive Stochastic Finite Elements (UASFE) extends beyond that of PCLCO with respect to the four points mentioned below:

1. The robustness of ASFE enables the application of the proposed approach to problems with bifurcations, in which the time-independent functionals are non-smooth;

2. The effect of positive and negative damping is resolved by the inclusion of a damping parameter in the time-independent parameterization, such that there is no need to ensure the existence of periodic solutions;

3. The proposed UASFE formulation includes an algorithm for parameterizing higher-period oscillations;

4. Applications to dynamical systems with inputs consisting of multiple random parameters are presented.

UASFE is applicable to problems with oscillatory solutions in which the functionals frequency, phase, amplitude, reference value, damping, and period shape are well defined in the asymptotic range.

The proposed approach is applied to a linear mass-spring-damper system, the nonlinear Duffing equation, and a rigid-airfoil fluid-structure interaction simulation with random input parameters. The results are compared to those of Monte Carlo simulations. The mass-spring-damper system is considered to study the effect of positive and negative damping on the stochastic results. Input randomness is assumed in the spring stiffness parameter, damping parameter, and a combination of both. The effect of random initial conditions is studied for the Duffing equation. The bifurcation behavior of the Duffing system results in a long-term solution which is highly sensitive to variations in the initial conditions. The rigid-airfoil fluid-structure interaction application shows in the asymptotic range a diverging mean and standard deviation of the system energy in case of a non-zero probability of flutter. The current applications are limited to the asymptotic behavior of single-frequency rigid-body motions.

Unsteady Adaptive Stochastic Finite Elements are introduced in section 6.2. Numerical results for the mass-spring-damper system, the Duffing equation, and the rigid-

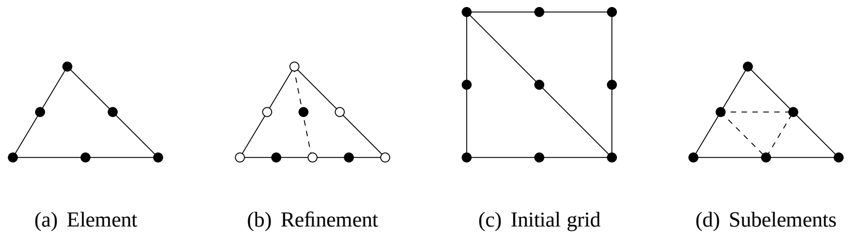
(a) Element (b) Refinement (c) Initial grid (d) Subelements

Figure 6.1: The 2-simplex element A_i in parameter space A and the second-degree Newton-Cotes quadrature points given by the dots.

airfoil fluid-structure interaction subject to random parameters are presented in section 6.3. The chapter is concluded in section 6.4.

6.2 Unsteady Adaptive Stochastic Finite Elements

In this section Unsteady Adaptive Stochastic Finite Elements (UASFE) with Newton-Cotes quadrature in simplex elements are developed. The employed Adaptive Stochastic Finite Elements (ASFE) framework is discussed in section 6.2.1. In section 6.2.2 the formulation for unsteady problems is introduced.

6.2.1 Adaptive Stochastic Finite Elements

Consider that the effect of the random parameters $\mathbf{a}(\omega)$ on dynamical system (1.1)

$$\mathcal{L}(\mathbf{x}, t; u(\mathbf{x}, t, \omega)) = S(\mathbf{x}, t), \tag{6.1}$$

is resolved using the Adaptive Stochastic Finite Elements method based on Newton-Cotes quadrature in simplex elements developed in chapter 4, see Figure 6.1.

The formulation for unsteady problems developed below is independent of the type of non-intrusive Stochastic Finite Elements method used. Other non-intrusive Stochastic Finite Elements methods than the one used here can also be employed in the time-independent formulation. A non-intrusive approach is chosen, since it can approximate the functionals in the time-independent parameterization more effectively than a coupled method.

The central moments are integral quantities over probability space. The consequence of the partition of probability space at the level of the central moments is that these integrals are evaluated in every element of the partition separately. The approximation of the moments is then obtained by summing the contributions of all elements. This results in a piecewise division of the whole probability space and element refinement in important regions of high probability. In contrast, in reliability assessment one is interested in approximation of the limit state function of failure, which usually occurs at low probability values.

The proposed Adaptive Stochastic Finite Elements method has in some sense a relationship to Latin Hypercube Sampling [39, 64], in which probability space is also divided into elements. Latin Hypercube Sampling approximates the statistical moments of the output using random sampling in square elements such that each row and column contains a single sample. On the other hand, Adaptive Stochastic Finite Elements result in a higher-order approximation of the response surface using a piecewise polynomial interpolation of deterministic samples in Newton-Cotes quadrature points in triangular elements.

6.2.2 Adaptive Stochastic Finite Elements for unsteady problems

Adaptive Stochastic Finite Elements methods can in unsteady problems result in a fast increasing number of elements with time. The Unsteady Adaptive Stochastic Finite Elements (UASFE) formulation proposed here is based on a time-independent parameterization of the sampled time series to enable a constant interpolation accuracy in time with a constant number of samples. The time-independent parameterization developed below is an extension of the parameterization employed in Probabilistic Collocation for Limit Cycle Oscillations (PCLCO) to damped and higher-period oscillations. For the parameterization, $u(t,\omega)$ is approximated by the following representation $\tilde{u}(t,\omega)$:

$$\tilde{u}(t,\omega) = u_0(\omega) + \mathrm{e}^{\gamma(\omega)(t_{\mathrm{stop}}-t)} A(\omega) u_{\mathrm{period}}(\tau(t,\omega),\omega), \tag{6.2}$$

with $\tau(t,\omega) = 2\pi(\phi(\omega) + (t - t_{\mathrm{stop}})f(\omega)) \pmod{2\pi}$, with t_{stop} the end time of the numerical time integration. The argument $\mathbf{x}$ has been dropped here for convenience of the notation. The response $u(t,\omega)$ is parameterized by (6.2) in terms of the time-independent functionals: frequency $f(\omega)$; relative phase $\phi(\omega)$; amplitude $A(\omega)$; reference value $u_0(\omega)$; damping $\gamma(\omega)$; and normalized period shape $u_{\mathrm{period}}(\tau(\omega),\omega)$, with $\tau(\omega) \in [0, 2\pi]$. These functions of ω are constructed using ASFE interpolation of the time-independent parameterization of the sampled time series $u_k(t)$ for the parameter values $\mathbf{a}_k$ in the quadrature points

$$\tilde{u}_k(t) = u_{0_k} + \mathrm{e}^{\gamma_k(t_{\mathrm{stop}}-t)} A_k u_{\mathrm{period}_k}(\tau_k(t),\omega), \tag{6.3}$$

with $\tau_k(t) = 2\pi(\phi_k + (t - t_{\text{stop}})f_k) \pmod{2\pi}$ and $k = 1, \ldots, N_{\text{s}}$. The approximation of the m^{th} statistical moment of, for example, frequency $f(\omega)$ is then

$$\mathbb{E}(f(\omega)^m) = \int_{\Omega} f(\omega)^m \mathrm{d}\omega \approx \sum_{i=1}^{N_{\text{e}}} \sum_{j=1}^{\tilde{N}_{\text{s}}} c_{i,j} f_{\tilde{k}_{i,j}}^m . \tag{6.4}$$

In the UASFE approach (6.2) to (6.4), the ASFE interpolation (6.4) is performed at the level of the time-independent functional $f(\omega)$, instead of at the level of the time-dependent function $u(t, \omega)$. UASFE, therefore, result in a time-independent interpolation error.

The approximations of the statistical moments of $u(t, \omega)$ are then computed using Newton-Cotes integration of $\tilde{u}(t, \omega)$ on a uniform subgrid of $\tilde{N}_{\text{e}_{\text{sub}}}$ simplex subelements per element without performing additional deterministic solves. The distribution function is given by sorting the function $\tilde{u}$–ω, with $\omega \in [0, 1]$, to a monotonically increasing function.

The 11 steps of the UASFE algorithm are listed below and, subsequently, the definitions using in the description of the UASFE algorithm, and the algorithm for detecting higher-period oscillations are detailed.

1. Compute the $N_{\text{s}_{\text{ini}}}$ deterministic time series $u_k(t)$ by solving (6.1) for the parameter values $\mathbf{a}_k$ corresponding to the quadrature points in the initial stochastic grid with $k = 1, \ldots, N_{\text{s}_{\text{ini}}}$;

2. Extract the local optima from the function $u_k(t)$ for $k = 1, \ldots, N_{\text{s}_{\text{ini}}}$;

3. Determine the last completed period of $u_k(t)$ based on its local optima for $k = 1, \ldots, N_{\text{s}_{\text{ini}}}$;

4. Extract the time-independent functionals f_k, ϕ_k, A_k, u_{0_k}, γ_k, and $u_{\text{period}_k}(\tau)$ from the last completed period of $u_k(t)$ for $k = 1, \ldots, N_{\text{s}_{\text{ini}}}$, see Figure 6.2;

5. Compute parameterization error $\varepsilon_{\text{u}_k}(t)$ of the reconstruction $\tilde{u}_k(t)$ given by (6.3) of the sample $u_k(t)$ for $k = 1, \ldots, N_{\text{s}_{\text{ini}}}$;

6. Determine time interval $\tilde{T}_k$ in which reconstruction $\tilde{u}_k(t)$ is valid, i.e. $\varepsilon_{\text{u}_k}(t)$ smaller than a threshold value $\bar{\varepsilon}$, for $k = 1, \ldots, N_{\text{s}_{\text{ini}}}$;

7. Determine valid time interval $\tilde{T}$ for the combination of the $N_{\text{s}_{\text{ini}}}$ samples;

8. Construct the response approximation $\tilde{u}(t, \omega)$ on the initial stochastic grid using (6.2) and its mean $\mu_{\tilde{u}}(t)$ and standard deviation $\sigma_{\tilde{u}}(t)$ using (6.4);

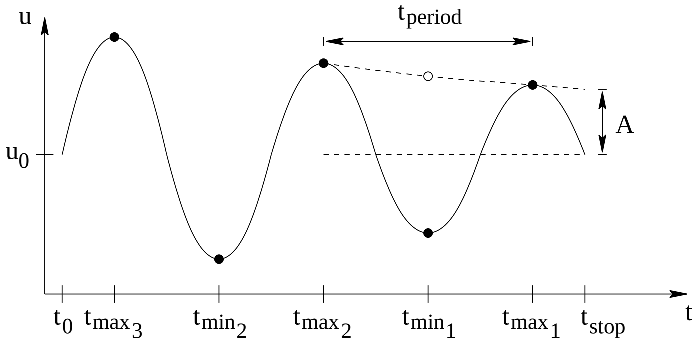

Figure 6.2: Time-independent parameterization of oscillatory time series employed in Unsteady Adaptive Stochastic Finite Elements.

9. Determine the refinement measure ρ_i in the elements for $i = 1, \ldots, N_\mathrm{e}$ and refine the element with the highest value for refinement measure ρ_i;
10. Compute the deterministic time series $u_k(t)$ by solving (6.1) for the parameter values $\mathbf{a}_k$ corresponding to the new quadrature points in the refined element and repeat steps 2 to 9 for the new samples $u_k(t)$ with $k = N_{\mathrm{s}_\mathrm{old}} + 1, \ldots, N_{\mathrm{s}_\mathrm{new}}$;
11. Stop the adaptive stochastic grid refinement based on convergence in the L_∞-norm or threshold $\bar{N}_\mathrm{s}$ for the maximum number of samples.

The definitions used in the 11 steps of the UASFE algorithm are given below in relation with the steps in which they are first presented.

4. Damping γ_k is iteratively computed in combination with amplitude A_k and reference value u_{0_k} by solving

$$u_k(t) = u_{0_k} \pm A_k \mathrm{e}^{\gamma_k (t_\mathrm{stop} - t)}, \tag{6.5}$$

for the local optima of the last completed period for $k = 1, \ldots, N_\mathrm{s}$, where the minus sign holds for a local minimum, see Figure 6.2. Damping is also accounted for in normalizing the period shape function $u'_{\mathrm{period}_k}(t_l)$ according to

$$\begin{aligned} u_{\mathrm{period}_k}(\tau_l) \quad = \quad & \frac{1}{A_k} \mathrm{e}^{-\gamma_k \left(t_\mathrm{stop} - \left(t_{k_{\mathrm{max},2}} + \frac{\tau_l}{2\pi f_k} \right) \right)} \\ & \cdot \left[u'_{\mathrm{period}_k} \left(t_{k_{\mathrm{max},2}} + \frac{\tau_l}{2\pi f_k} \right) - u_{0_k} \right], \end{aligned} \tag{6.6}$$

which is interpolated on a discrete grid of $\tau_l = l\Delta\tau$ for $l = 0, \ldots, N_\tau$, with $\Delta\tau = 2\pi/N_\tau$. Frequency f_k and phase ϕ_k are obtained as in Chapter 5;

5. Parameterization error $\varepsilon_{\mathrm{u}_k}(t)$ of the reconstruction $\tilde{u}_k(t)$ of the sample $u_k(t)$ is defined as
$$\varepsilon_{\mathrm{u}_k}(t) = \frac{|\tilde{u}_k(t) - u_k(t)|}{|u_k(t)|_\infty}, \tag{6.7}$$
for $k = 1, \ldots, N_\mathrm{s}$;

6. The reconstruction $\tilde{u}_k(t)$ is considered to be a valid representation of $u_k(t)$ in the time interval $\tilde{T}_k$, for which $\varepsilon_{\mathrm{u}_k}(t)$ is smaller than a threshold value $\bar{\varepsilon}$ for all $t \in \tilde{T}_k$:
$$\tilde{T}_k = \{t \in T \mid \varepsilon_{\mathrm{u}_k}(\tilde{t}) < \bar{\varepsilon} \quad \forall \tilde{t} \geq t\},$$
for $k = 1, \ldots, N_\mathrm{s}$;

7. UASFE are applied to time interval $\tilde{T}$, in which the N_s reconstructions $\tilde{u}_k(t)$ are valid:
$$\tilde{T} = \tilde{T}_1 \bigcap \ldots \bigcap \tilde{T}_{\mathrm{N_s}}.$$
Outside time interval $\tilde{T}$ ASFE post-processing is applied to the samples $u_k(t)$ for $k = 1, \ldots, N_\mathrm{s}$;

9. Refinement measure ρ_i in the elements is a combination of the refinement measures for the time-independent parameters according to
$$\rho_i = \rho_{\mathrm{f}_i} + \rho_{\phi_i} + \rho_{\mathrm{A}_i} + \rho_{\mathrm{r}_i} + \rho_{\gamma_i} + \frac{1}{N_\tau}\sum_{l=1}^{N_\tau} \rho_{\mathrm{u}_{\mathrm{period},i}}(\tau_l), \tag{6.8}$$
where refinement measures ρ_{f_i}, ρ_{ϕ_i}, ρ_{A_i}, ρ_{r_i}, ρ_{γ_i}, and $\rho_{\mathrm{u}_{\mathrm{period},i}}(\tau_l)$ for $l = 1, \ldots, N_\tau$ and $i = 1, \ldots, N_\mathrm{e}$ are defined as (4.9) in chapter 4.

11. Stochastic grid refinement is terminated when $\delta_{N_\mathrm{e}} < \bar{\delta}$, where δ_{N_e} is defined as
$$\begin{aligned}\delta_{N_\mathrm{e}} \quad = \quad & \max\Big(\frac{|\mu_{\mathrm{u}_{\lfloor N_\mathrm{e}/2\rfloor}}(t) - \mu_{\mathrm{u}_{N_\mathrm{e}}}(t)|_\infty}{|\mu_{\mathrm{u}_{N_\mathrm{e}}}(t)|_\infty}, \\ & \frac{|\sigma_{\mathrm{u}_{\lfloor N_\mathrm{e}/2\rfloor}}(t) - \sigma_{\mathrm{u}_{N_\mathrm{e}}}(t)|_\infty}{|\sigma_{\mathrm{u}_{N_\mathrm{e}}}(t)|_\infty}\Big),\end{aligned} \tag{6.9}$$
or when a threshold for the maximum number of samples $\bar{N}_\mathrm{s}$ is reached.

The following parameter values are used for the numerical results presented in this paper: $N_{\mathrm{V}} = 2$, $N_\tau = 90$, $\bar{\varepsilon} = 10\%$, $\bar{c} = 2$, $N_{\max} = 7$, $\bar{\delta} = 5 \cdot 10^{-2}$, and $\bar{N}_{\mathrm{s}} = 200$.

The algorithm for detecting higher-period oscillations uses the last $N_{\max}$ local maxima of the function $u_k(t)$ for $k = 1, \ldots, N_{\mathrm{s}}$. Period-1 oscillations can be identified using $N_{\max} = 2$, multi-period motions require $N_{\max} > 2$. The analysis of steps 4 to 6 is performed for all combinations of two of the $N_{\max}$ selected local maxima and a local minimum at an intermediate time level. If the valid time interval $\tilde{T}_k$ determined in step 6 is larger than a threshold value $\bar{c}t_{\mathrm{period}_k}$, then it is assumed that the correct period has been found. In order to ensure that the algorithm results in a unique period shape $u_{\mathrm{period}_k}(\tau)$, two additional criteria are required. The unique period is defined as the period which possesses: (1) the smallest time interval between its local minimum and its latest local maximum; and (2) the latest local minimum. If none of the periods results in a $\tilde{T}_k$ larger than $\bar{c}t_{\mathrm{period}_k}$, then steady ASFE post-processing is applied to the samples $u_k(t)$ for $k = 1, \ldots, N_{\mathrm{s}}$ and $t \in T$.

The proposed UASFE method is not subject to stability issues in either the time domain nor in probability space. In the time domain the time step of the UASFE post-processing is not limited by stability requirements. The post-processing time step can, therefore, be chosen based on time resolution requirements and can be much larger than in the actual deterministic simulations. In probability space the robust ASFE interpolation ensures a stable monotonicity and extrema preserving solution.

In reliability analysis, the results are subject to an approximation error and a pure random error, which are both taken into account in the extended response surface method [12, 13]. The approximation of the response surface using a simpler function introduces an interpolation error due to a systematic lack of fit. This error can be assessed using the error variance of a least-square fit of enough experiments. Random variability in experimental results leads to the pure random error contribution. The random error variance is found through repeated central point experiments. The replication of central points is not useful for computer experiments, since its repetition leads to exactly the same result. In a numerical context, the pure error is introduced by the random effect of discretization and simplification assumptions. Initially neglected less important random input parameters are, therefore, varied in numerical experiment replications in order to determine the pure random error.

In the proposed approach the approximation error and the random error are dealt with in the following way. The approximation error of the adaptive scheme is monitored by measure $\delta_{\mathrm{N_e}}$ for the convergence of successive refinements. The refinement stop criterion $\delta_{\mathrm{N_e}} < \bar{\delta}$ ensures that the approximation error of the final discretization is sufficiently small. The random error is caused by modeling only the most important random input parameters and neglecting the less important sources of randomness. This approach is allowed here, since the effect of this simplification error on the accuracy of the global probability distribution approximation is relatively small. In reliability analysis the random error has a significantly larger relative effect on the small probability of failure, which results in the need of experiment replications.

6.3 Results

The Unsteady Adaptive Stochastic Finite Elements (UASFE) formulation is applied to a mass-spring-damper system, the Duffing equation, and a rigid-airfoil fluid-structure interaction problem with random parameters in sections 6.3.1, 6.3.2, and 6.3.3, respectively. The properties of the proposed method and the effect of the random parameters are studied. The discussion of the applications concentrates on the approximation of the response surface of the output, and the resulting probability distribution function and stochastic moments, i.e. the mean and variance. The results are compared to those of Monte Carlo (MC) simulations. The required number of samples in the Monte Carlo simulations is established in convergence studies.

6.3.1 Mass-spring-damper system

A mass-spring-damper system of a mass attached to a spring and a damper is considered with randomness in the spring stiffness parameter $K(\omega)$ and the damping constant $C(\omega)$. The governing equation for the motion of the mass is given in section 6.3.1.1. The effects of randomness in $K(\omega)$ and $C(\omega)$ separately are considered in sections 6.3.1.2 and 6.3.1.3. In section 6.3.1.4 their combined effect is studied.

6.3.1.1 Governing mass-spring-damper equation

Consider a mass attached to a spring and a damper as shown in Figure 6.3. This can be a model for a more complex structure with internal damping and stiffness. The test problem is used here to illustrate the properties of the proposed approach and to study the effect of damping in a dynamical system with randomness. The mass-spring-damper system is governed by

$$M\frac{\partial^2 x}{\partial t^2} + C(\omega)\frac{\partial x}{\partial t} + K(\omega)x = 0, \qquad t \in [0, \infty), \tag{6.10}$$

with mass $M = 1$, position of the mass $x(t, \omega)$, and initial conditions $x(0) = 1$ and $\partial x/\partial t(0) = 1$. The randomness in the positive spring stiffness $K(\omega)$ is given by a lognormal distribution with mean $\mu_{\mathrm{K}} = 1$ and coefficient of variation $\mathrm{COV_K} = 10\%$. A normal distribution is assumed for $C(\omega)$ with mean $\mu_{\mathrm{C}} = 0$ and standard deviation

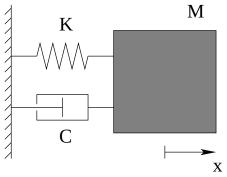

Figure 6.3: The mass-spring-damper system.

$\sigma_{\mathrm{C}} = 0.01$. As is common in multi-element methods, the tails of the probability distributions for $K(\omega)$ and $C(\omega)$ are truncated such that the resolved parameter domains account for 99.8% of the realizations. The resulting truncation error is small compared to the usual discretization and time integration errors in solving computational engineering problems. The results below are based on the analytical solution of (6.10)

$$x(t, \omega) = c_1 e^{c_2 t} \sin(c_3 t) + c_4 e^{c_5 t} \cos(c_6 t), \tag{6.11}$$

where c_i with $i = 1, \dots, 6$ are functions of M, $K(\omega)$, $C(\omega)$, $x(0)$, and $\partial x/\partial t(0)$. Eq. (6.11) is evaluated at discrete time levels $t_l = l\Delta t$, with $l = 0, \dots, N_{\mathrm{t}}$, $N_{\mathrm{t}} = t_{\mathrm{stop}}/\Delta t$, $t_{\mathrm{stop}} = 100$, and $\Delta t = 0.01$, for the results to be comparable with the results of the other test problems obtained by numerical time integration. The time interval corresponds to approximately 16 periods for the deterministic case with $K = \mu_{\mathrm{K}}$ and $C = \mu_{\mathrm{C}}$.

6.3.1.2 Random spring stiffness parameter $K(\omega)$

The effect of randomness in the spring stiffness parameter $K(\omega)$ in combination with a deterministic value of the damping parameter C is studied in this section. Cases with zero damping $C = 0$, and positive and negative damping $C = \pm 0.03$ are considered.

Zero damping First the mass-spring-damper system is considered with zero damping $C = 0$ and random $K(\omega)$. The one-dimensional Unsteady Adaptive Stochastic Finite Elements formulation for random parameter $K(\omega)$ is applied with an initial stochastic grid of $N_{\mathrm{e_{ini}}} = 1$ element with $N_{\mathrm{s_{ini}}} = 3$ samples $x_k(t)$ for 3 parameter values K_k. The samples $x_k(t)$ are periodic oscillations due to $C = 0$ as shown in Figure 6.4a by the bold lines. The algorithm extracts the frequency f_{x_k}, phase ϕ_{x_k}, amplitude A_{x_k}, reference value r_{x_k}, damping γ_{x_k}, and period shape $u_{\mathrm{period}_{\mathrm{x}_k}}$ from the last full period of the samples $x_k(t)$ and uses parameterization (6.3) to develop reconstructions $\tilde{x}_k(t)$ of the time histories. The reconstructed time histories are given in

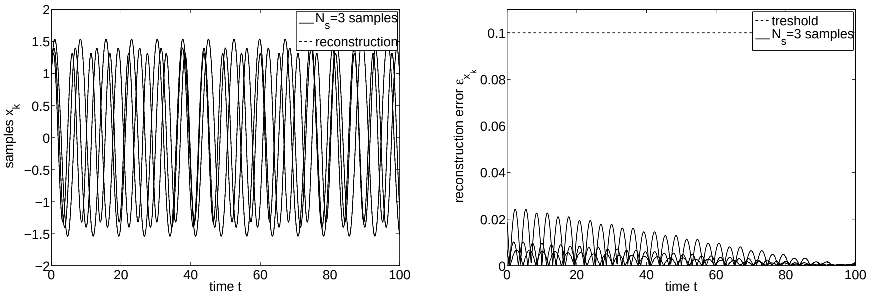

(a) samples $x_k(t)$

(b) reconstruction error $\varepsilon_{\mathrm{x}_k}(t)$

Figure 6.4: Samples $x_k(t)$, reconstructions $\tilde{x}_k(t)$, and reconstruction error $\varepsilon_{\mathrm{x}_k}(t)$ for $N_{\mathrm{e}_{\mathrm{ini}}} = 1$ ($N_{\mathrm{s}_{\mathrm{ini}}} = 3$) for the mass-spring-damper system with random spring stiffness $K(\omega)$ and $C = 0$.

Figure 6.4a by the dashed lines. The time series $\tilde{x}_k(t)$ are accurate approximations of the samples $x_k(t)$, since the samples can in this case be described exactly by the form of (6.3). The parameterization error $\varepsilon_{\mathrm{x}_k}(t)$ given by (6.7) is shown in Figure 6.4b. The error $\varepsilon_{\mathrm{x}_k}(t)$ slightly increases with decreasing time t due to the amplification of the numerical error in extracting the optima of the last completed period from the discrete time series $x_k(t)$. The parameterization error $\varepsilon_{\mathrm{x}_k}(t)$ stays well below the threshold value of $\bar{\varepsilon} = 10\%$ for $t \in [0, t_{\mathrm{stop}}]$.

The approximation of the mean $\mu_{\mathrm{x}}(t)$ and standard deviation $\sigma_{\mathrm{x}}(t)$ for $N_{\mathrm{e}} = 2$ elements and $N_{\mathrm{s}} = 5$ samples is given in Figure 6.5. The solution for $N_{\mathrm{e}} = 2$ is converged below $\bar{\delta} = 5 \cdot 10^{-2}$ according to (6.9). The results are compared to a Monte Carlo (MC) simulation with $N_{\mathrm{s}} = 1000$ samples. The UASFE approximation shows a good agreement with the Monte Carlo results for the mean $\mu_{\mathrm{x}}(t)$ and standard deviation $\sigma_{\mathrm{x}}(t)$ on the whole time domain $t \in [0, t_{\mathrm{stop}}]$. The relative error in the L_∞ norm in the approximation of $\mu_{\mathrm{x}}(t)$ and $\sigma_{\mathrm{x}}(t)$ compared to the Monte Carlo results is $1.34 \cdot 10^{-2}$ and $0.898 \cdot 10^{-2}$, respectively. The error seems, therefore, of the same order as the convergence criterion $\bar{\delta}$. The approximation errors are caused by the reconstruction error $\varepsilon_{\mathrm{x}_k}(t)$ shown in Figure 6.4b and the error due to using a finite number of N_{e} elements.

The mean $\mu_{\mathrm{x}}(t)$ is a damped oscillation to zero in contrast to the periodic oscillations of the deterministic samples $x_k(t)$ of Figure 6.4a. The standard deviation $\sigma_{\mathrm{x}}(t)$ shows initially an oscillation with an increasing amplitude until it damps out to a steady

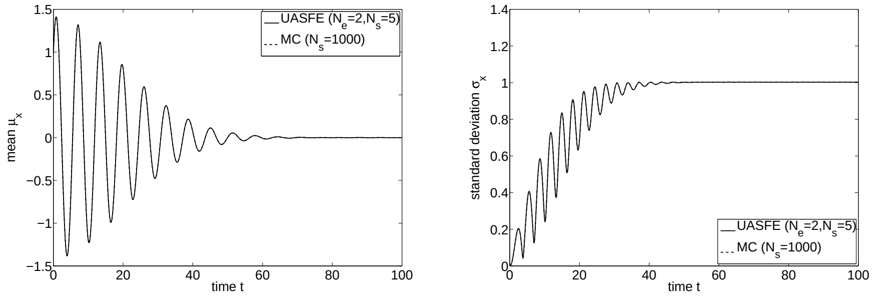

(a) mean $\mu_{\mathrm{x}}(t)$ (b) standard deviation $\sigma_{\mathrm{x}}(t)$

Figure 6.5: Mean $\mu_{\mathrm{x}}(t)$ and standard deviation $\sigma_{\mathrm{x}}(t)$ by Unsteady Adaptive Stochastic Finite Elements (UASFE) with $N_{\mathrm{e}} = 2$ ($N_{\mathrm{s}} = 5$) and Monte Carlo (MC) simulation with $N_{\mathrm{s}} = 1000$ for the mass-spring-damper system with random spring stiffness $K(\omega)$ and $C = 0$.

value of $\sigma_{\mathrm{x}} = 1.0$ at approximately $t = 50$. These results can be explained by the effect of the random spring stiffness parameter $K(\omega)$ on the frequency of the periodic oscillations, see Figure 6.4a. Realizations with opposite signs increasingly cancel each other due increasing phase differences with increasing time. The finite asymptotic value of the standard deviation is caused by the finite amplitude of the sampled time series.

The solution for $N_{\mathrm{e}} = 2$ elements and $N_{\mathrm{s}} = 5$ samples is examined further in Figure 6.6 by considering the approximations of the frequency $f_{\mathrm{x}}(\omega)$, phase $\phi_{\mathrm{x}}(\omega)$, amplitude $A_{\mathrm{x}}(\omega)$, and the resulting response surface of $x(t_{\mathrm{stop}}, \omega)$ as function of random parameter $K(\omega)$. The response surface of the position of the mass at $t = t_{\mathrm{stop}}$, $x(t_{\mathrm{stop}}, \omega)$, is highly oscillatory as shown in Figure 6.6a. The UASFE solution results in a close approximation of the oscillatory response predicted by Monte Carlo simulation. The UASFE result is based on the piecewise quadratic approximation of the relatively smooth response surfaces of the frequency $f_{\mathrm{x}}(\omega)$, phase $\phi_{\mathrm{x}}(\omega)$, and amplitude $A_{\mathrm{x}}(\omega)$ shown in Figures 6.6b to 6.6d. The damping $\gamma_{\mathrm{x}}(\omega)$ and reference value $r_{\mathrm{x}}(\omega)$ are not shown, since they are identically zero. The probability distribution $F_{\mathrm{x}}(x, t)$ of the response $x(t_{\mathrm{stop}}, \omega)$ can be determined by sorting the function $x(t, \omega)$–ω with $\omega \in [0, 1]$ to a monotonically increasing function, see Figure 6.7.

Positive and negative damping Next the effect of randomness in the spring stiffness parameter $K(\omega)$ is considered for a positive and negative damping parameter $C =$

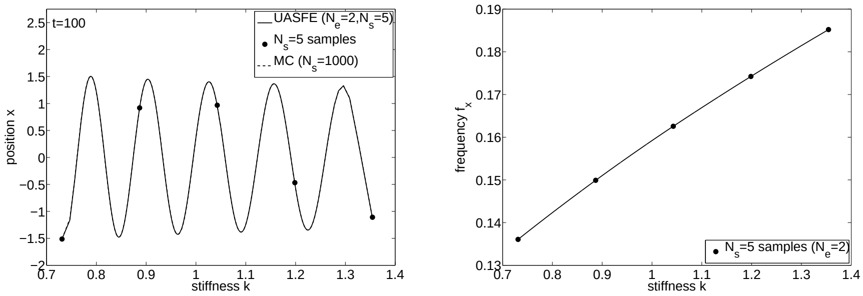

(a) position x (b) frequency f_{x}

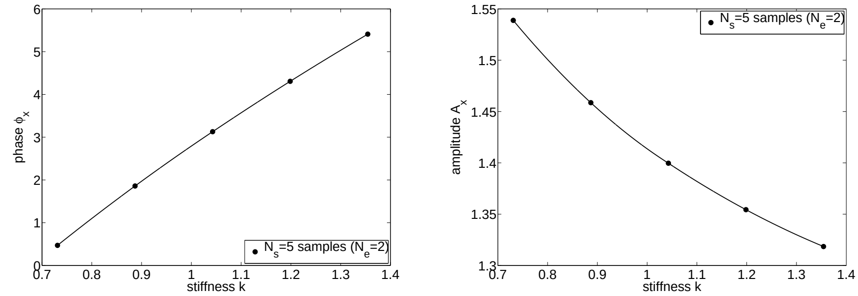

(c) phase ϕ_{x} (d) amplitude A_{x}

Figure 6.6: Response surface approximations of $x(t_{\mathrm{stop}}, \omega)$, $f_{\mathrm{x}}(\omega)$, $\phi_{\mathrm{x}}(\omega)$, and $A_{\mathrm{x}}(\omega)$ by Unsteady Adaptive Stochastic Finite Elements (UASFE) with $N_{\mathrm{e}} = 2$ ($N_{\mathrm{s}} = 5$) and Monte Carlo (MC) simulation with $N_{\mathrm{s}} = 1000$ for the mass-spring-damper system with random spring stiffness $K(\omega)$ and $C = 0$.

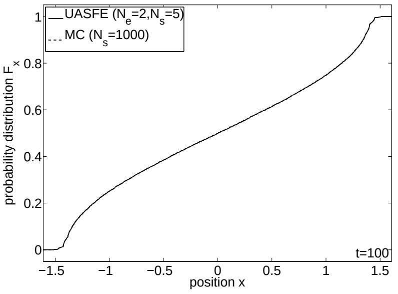

Figure 6.7: Probability distribution function $F_{\mathrm{x}}(x,t)$ of $x(t,\omega)$ at $t = t_{\mathrm{stop}}$ by Unsteady Adaptive Stochastic Finite Elements (UASFE) with $N_{\mathrm{e}} = 2$ ($N_{\mathrm{s}} = 5$) and Monte Carlo (MC) simulation with $N_{\mathrm{s}} = 1000$ for the mass-spring-damper system with random spring stiffness $K(\omega)$ and $C = 0$.

± 0.03. The $N_{\mathrm{s_{ini}}} = 3$ sampled time series $x_k(t)$ of the initial grid with $N_{\mathrm{e_{ini}}} = 1$ are shown in Figure 6.8 for both positive and negative damping. The time series are damped oscillations for $C = 0.03$ and diverging oscillations for $C = -0.03$. The randomness of spring stiffness $K(\omega)$ affects the frequency of the samples. The parameterization error $\varepsilon_{\mathrm{x}_k}(t)$ is smaller than $\bar{\varepsilon}$ for all $t \in [0, t_{\mathrm{stop}}]$.

The resulting UASFE approximations of the mean $\mu_{\mathrm{x}}(t)$ and standard deviation $\sigma_{\mathrm{x}}(t)$ are compared to Monte Carlo results in Figures 6.9 and 6.10, respectively. The results for $N_{\mathrm{e}} = 2$ elements and $N_{\mathrm{s}} = 5$ samples are converged below $\bar{\delta} = 5 \cdot 10^{-2}$. In both cases the mean $\mu_{\mathrm{x}}(t)$ is a damped oscillation to zero due to the effect of the randomness in $K(\omega)$ on the frequency and the phase of the oscillation. Damping C influences the rate at which $\mu_{\mathrm{x}}(t)$ decays. For $C = 0.03$ the mean decays faster than for the case with zero damping of Figure 6.5a and vise versa for $C = -0.03$. The close agreement with the Monte Carlo results show that UASFE can successfully resolve the effects of positive and negative damping.

For the zero damping problem the standard deviation $\sigma_{\mathrm{x}}(t)$ showed an oscillating transient up to $t = 50$ where it reached a steady value, see Figure 6.5b. After including damping, see Figure 6.10, $\sigma_{\mathrm{x}}(t)$ has initially still an oscillating behavior, however, it results at approximately $t = 50$ in a monotonically decreasing function for $C = 0.03$ and in a monotonically increasing behavior for $C = -0.03$. This difference is caused by the decreasing and increasing amplitudes of the samples $x_k(t)$ with increasing time for positive and negative damping, respectively. In Figure 6.10a it can be seen that the

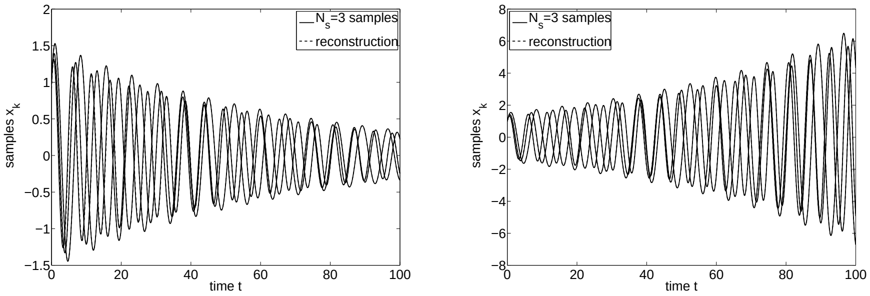

(a) positive damping $C = 0.03$

(b) negative damping $C = -0.03$

Figure 6.8: Samples $x_k(t)$ and reconstructions $\tilde{x}_k(t)$ for $N_{\mathrm{e}_{\mathrm{ini}}} = 1$ ($N_{\mathrm{s}_{\mathrm{ini}}} = 3$) with positive and negative damping $C = \pm 0.03$ for the mass-spring-damper system with random spring stiffness $K(\omega)$.

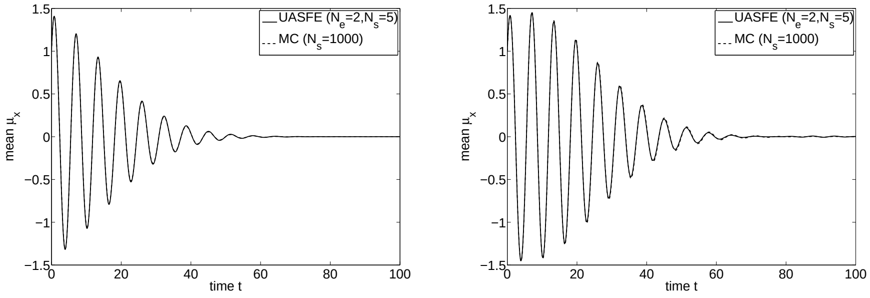

(a) positive damping $C = 0.03$

(b) negative damping $C = -0.03$

Figure 6.9: Mean $\mu_{\mathrm{x}}(t)$ by Unsteady Adaptive Stochastic Finite Elements (UASFE) with $N_{\mathrm{e}} = 2$ ($N_{\mathrm{s}} = 5$) and Monte Carlo (MC) simulation with $N_{\mathrm{s}} = 1000$ with positive and negative damping $C = \pm 0.03$ for the mass-spring-damper system with random spring stiffness $K(\omega)$.

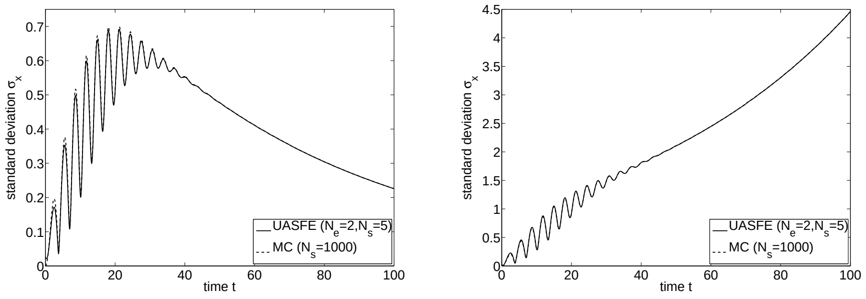

(a) positive damping $C = 0.03$

(b) negative damping $C = -0.03$

Figure 6.10: Standard deviation $\sigma_{\mathrm{x}}(t)$ by Unsteady Adaptive Stochastic Finite Elements (UASFE) with $N_{\mathrm{e}} = 2$ ($N_{\mathrm{s}} = 5$) and Monte Carlo (MC) simulation with $N_{\mathrm{s}} = 1000$ with positive and negative damping $C = \pm 0.03$ for the mass-spring-damper system with random spring stiffness $K(\omega)$.

error in the UASFE approximation of $\sigma_{\mathrm{x}}(t)$ for $C = 0.03$ is slightly larger for smaller t, due to parameterization error $\varepsilon_{\mathrm{x}_k}(t)$. UASFE predicts a maximum standard deviation of $\sigma_{\mathrm{x}} = 0.691$ at $t = 21.2$.

6.3.1.3 Random damping parameter $C(\omega)$

In order to study the effect of random damping, the damping parameter $C(\omega)$ is assumed to be a normally distributed random parameter with a mean $\mu_{\mathrm{C}} = 0$ and standard deviation $\sigma_{\mathrm{C}} = 0.01$ such that the interval $C(\omega) \in [-0.03; 0.03]$ accounts for 99.7% of the realizations. The spring stiffness parameter K is assumed to be deterministic with $K = \mu_{\mathrm{K}}$. The $N_{\mathrm{s_{ini}}} = 3$ samples $x_k(t)$ of the initial grid with $N_{\mathrm{e_{ini}}} = 1$ element are shown in Figure 6.11. Their reconstructions $\tilde{x}_k(t)$ have an error $\varepsilon_{\mathrm{x}_k}(t)$ smaller than the threshold $\bar{\varepsilon}$ for all $t \in [0, t_{\mathrm{stop}}]$. In contrast to random stiffness $K(\omega)$, randomness in the damping $C(\omega)$ has mainly an effect on the amplitude of the motion and only a small effect on the frequency given by the factor $(1 - C^2/4KM)^{1/2}$.

Due to the small effect of the damping $C(\omega)$ on the frequency of the motion, the mean $\mu_{\mathrm{x}}(t)$ does in the considered time interval not develop a decaying oscillation, see Figure 6.12a. In fact, the mean $\mu_{\mathrm{x}}(t)$ is a slightly diverging oscillation due to the asymmetric effect of positive and negative damping on the amplitude. The frequency of $\mu_{\mathrm{x}}(t)$ is comparable to that of the samples of Figure 6.11. For this problem a dis-

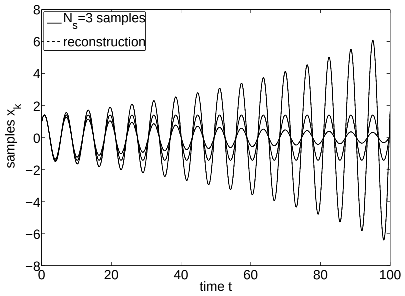

Figure 6.11: Samples $x_k(t)$ and reconstructions $\tilde{x}_k(t)$ for $N_\mathrm{e} = 1$ ($N_\mathrm{s} = 3$) for the mass-spring-damper system with random damping $C(\omega)$ and $K = \mu_\mathrm{K}$.

cretization with $N_\mathrm{e} = 4$ elements and $N_\mathrm{s} = 9$ samples is required to obtain a UASFE approximation which is converged below $\bar{\delta} = 5 \cdot 10^{-2}$. The standard deviation $\sigma_\mathrm{x}(t)$ is a diverging oscillation with half the period of $\mu_\mathrm{x}(t)$, see Figure 6.12b. Due to the effect of $C(\omega)$ on the amplitude of the motion, $\sigma_\mathrm{x}(t)$ increases rapidly with time. A non-zero probability of negative damping, therefore, results asymptotically in a diverging standard deviation of the position of the mass $x(t, \omega)$. The effect of the parameterization error $\varepsilon_\mathrm{x}(t)$ can be observed in the UASFE result for $\sigma_\mathrm{x}(t)$ at $t < 10$.

6.3.1.4 Random $K(\omega)$ and $C(\omega)$

Next the combined effect of randomness in both the spring stiffness parameter $K(\omega)$ and the damping $C(\omega)$ is considered. To this end, a two-dimensional UASFE formulation is employed to discretize the two-dimensional probability space. The approximations of the response surface of $x(t, \omega)$ at t_stop as function of the random parameters $K(\omega)$ and $C(\omega)$ by UASFE and Monte Carlo simulation are given in Figure 6.13. The UASFE approximation on the initial grid of $N_{\mathrm{e}_\mathrm{ini}} = 2$ elements and $N_{\mathrm{s}_\mathrm{ini}} = 9$ samples is shown and the Monte Carlo simulation result for $N_\mathrm{s} = 1.2 \cdot 10^5$ samples is considered. The chosen number of Monte Carlo samples required for a converged solution has been established after a convergence study. The response surface shows an oscillatory behavior in the $K(\omega)$-dimension. In the $C(\omega)$-dimension the initial deflection of $x_0(0) = 1$ is damped for $C(\omega) > 0$ and amplified for $C(\omega) < 0$. UASFE capture this complex nonlinear behavior already for the $N_{\mathrm{s}_\mathrm{ini}} = 9$ samples of the initial grid. In the post-processing of UASFE, $N_{\mathrm{e}_\mathrm{sub}} = 4^6$ subelements are employed per element for the

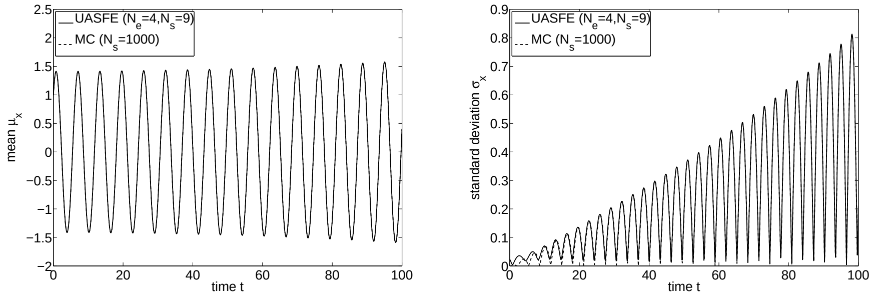

(a) mean $\mu_{\mathrm{x}}(t)$

(b) standard deviation $\sigma_{\mathrm{x}}(t)$

Figure 6.12: Mean $\mu_{\mathrm{x}}(t)$ and standard deviation $\sigma_{\mathrm{x}}(t)$ by Unsteady Adaptive Stochastic Finite Elements (UASFE) with $N_{\mathrm{e}} = 4$ ($N_{\mathrm{s}} = 9$) and Monte Carlo (MC) simulation with $N_{\mathrm{s}} = 1000$ for the mass-spring-damper system with random damping $C(\omega)$.

result of Figure 6.13a without performing additional deterministic solves.

The results of UASFE and Monte Carlo simulation for mean $\mu_{\mathrm{x}}(t)$ and standard deviation $\sigma_{\mathrm{x}}(t)$ are shown in Figure 6.14. UASFE converge for $N_{\mathrm{e}} = 16$ elements and $N_{\mathrm{s}} = 47$ samples below $\bar{\delta} = 5 \cdot 10^{-2}$. The post-processing converges for $N_{\mathrm{e_{sub}}} = 4^4$ subelements per element. The parameterization of the $N_{\mathrm{s}} = 47$ samples results in an error $\varepsilon_{\mathrm{x}}(t)$ smaller than $\bar{\varepsilon}$ for all $t \in [0, t_{\mathrm{stop}}]$. The mean $\mu_{\mathrm{x}}(t)$ is a decaying oscillation and the standard deviation $\sigma_{\mathrm{x}}(t)$ has initially an oscillatory behavior until approximately $t = 50$ due to the random spring stiffness $K(\omega)$. For $t > 50$, $\sigma_{\mathrm{x}}(t)$ shows a monotonically increasing behavior due to the non-zero probability of negative values for the damping $C(\omega)$. The standard deviation $\sigma_{\mathrm{x}}(t)$ is for all $t \in [0, t_{\mathrm{stop}}]$ larger than or equal to the standard deviations due to the random parameters separately. The results match with those of the Monte Carlo simulation at a reduction of the number of samples N_{s} by a factor of $2.6 \cdot 10^3$.

6.3.2 Duffing equation

In this section the effect of random initial conditions for the Duffing differential equation is studied. The Duffing equation is a model for an oscillator with a cubic nonlinear spring. Parameter variations are selected for which the response shows a discontinuous change to a qualitatively different behavior. The Duffing differential equation is described in section 6.3.2.1. The effect of one and two random initial conditions is

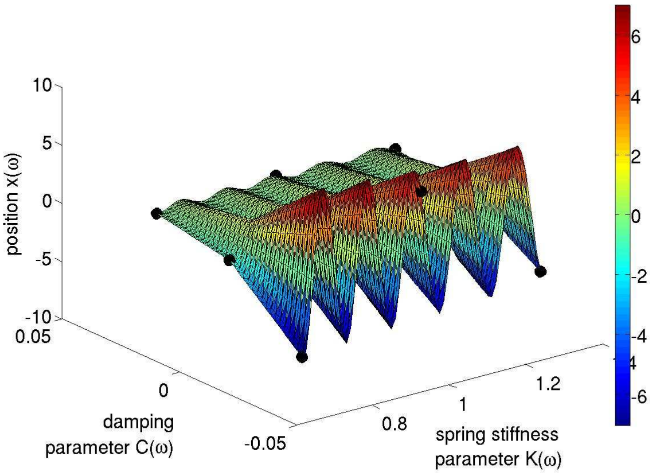

(a) UASFE, $N_\mathrm{s} = 9$ samples

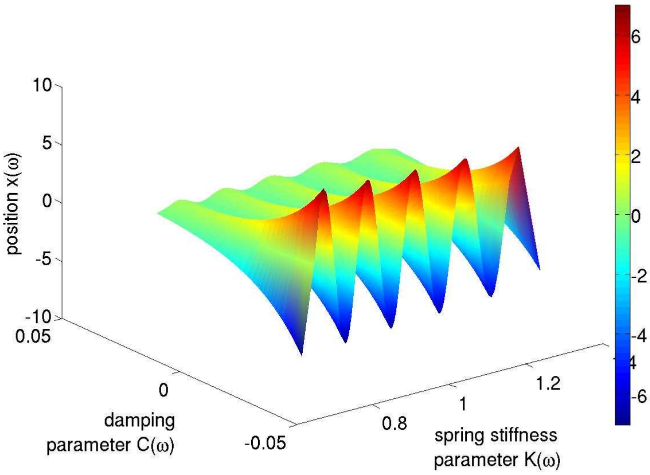

(b) Monte Carlo, $N_\mathrm{s} = 1.2 \cdot 10^5$ samples

Figure 6.13: Two-dimensional response surface of $x(t,\omega)$ at $t_\mathrm{stop} = 100$ as function of the random stiffness $K(\omega)$ and damping $C(\omega)$ by two-dimensional Unsteady Adaptive Stochastic Finite Elements (UASFE) with $N_\mathrm{e} = 2$ ($N_{\mathrm{e}_\mathrm{sub}} = 4^6$, $N_\mathrm{s} = 9$) and Monte Carlo (MC) simulation with $N_\mathrm{s} = 1.2 \cdot 10^5$ for the mass-spring-damper system.

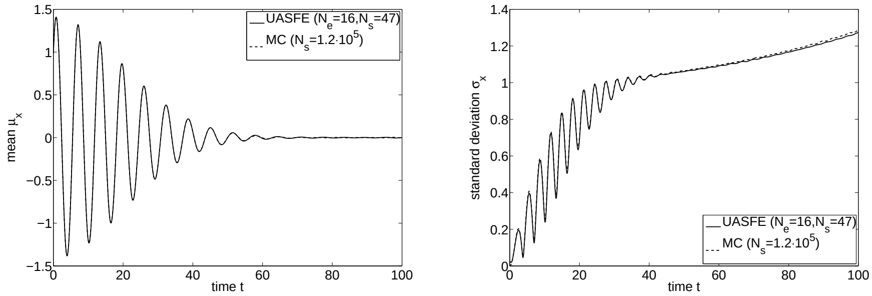

(a) mean $\mu_{\mathrm{x}}(t)$

(b) standard deviation $\sigma_{\mathrm{x}}(t)$

Figure 6.14: Mean $\mu_{\mathrm{x}}(t)$ and standard deviation $\sigma_{\mathrm{x}}(t)$ by two-dimensional Unsteady Adaptive Stochastic Finite Elements (UASFE) with $N_{\mathrm{e}} = 16$ ($N_{\mathrm{s}} = 47$) and Monte Carlo (MC) simulation with $N_{\mathrm{s}} = 1.2 \cdot 10^5$ for the mass-spring-damper system with random spring stiffness $K(\omega)$ and damping $C(\omega)$.

considered in sections 6.3.2.2 and 6.3.2.3, respectively.

6.3.2.1 Duffing system of differential equations

The Duffing system of equations is given by the following differential equations:

$$\frac{\partial x}{\partial t} = y, \tag{6.12}$$

$$\frac{\partial y}{\partial t} = \omega_0^2 x - \beta x^3 - \delta y + \gamma \cos(\omega_\gamma t + \phi), \tag{6.13}$$

for $t \in [0, \infty)$ with initial conditions $x(0) = x_0$ and $y(0) = y_0$. The Duffing equation is a model for a nonlinear oscillator with a cubic nonlinear spring stiffness term with parameter β, damping δ, and a harmonic forcing with amplitude γ. According to (6.12), $x(t)$ can be interpreted as a deflection of a mass with velocity $y(t)$. The acceleration $\partial y/\partial t$ is then governed by (6.13). A hard spring with increasing spring stiffness as function of deflection $x(t)$ is modeled by $\beta > 0$ and $\beta < 0$ holds for a soft spring. Structural stiffness behaves as a cubic hard spring in, for example, the torsional direction of wing structures [113]. Here, the cubic spring stiffness parameter is assumed to be $\beta = 1$. The undamped and unforced Duffing equation is considered, i.e. $\delta = 0$ and $\gamma = 0$, and ω_0 is chosen to be unity.

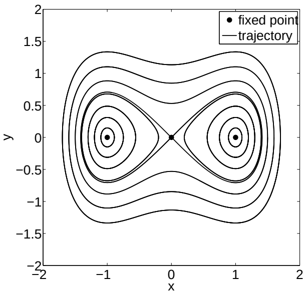

Figure 6.15: Phase diagram for the Duffing equation in terms of fixed points $(\pm 1, 0)$ and $(0, 0)$, and trajectories for $\beta = 1$, $\delta = 0$, $\gamma = 0$, and $\omega_0 = 1$.

The resulting dynamical system has fixed points (x, y) in $(-1, 0)$, $(0, 0)$, and $(1, 0)$. The fixed point $(0, 0)$ is unstable, and $(-1, 0)$ and $(1, 0)$ are linearly stable, see the x–y phase diagram in Figure 6.15. The solution exhibits a periodic trajectory around either the linearly stable points $(-1, 0)$ or $(1, 0)$, or around all three fixed points. Which type of system response is found, depends on the initial conditions x_0 and y_0. Since the qualitative behavior of the solution is sensitive to the initial conditions, randomness is considered in $x_0(\omega)$ and $y_0(\omega)$. The system (6.12) and (6.13) is solved numerically up to $t_{\mathrm{stop}} = 100$ using fourth-order explicit Runge-Kutta time integration with a time step of $t = 0.01$.

6.3.2.2 Random $x_0(\omega)$

First, the randomness in initial condition $x_0(\omega)$ is studied in combination with a deterministic value for y_0. The initial conditions consist of a uniform distribution $x_0(\omega) = U(1.4; 1.45)$ and $y_0 = 0$. This corresponds for $x_0(\omega)$ in a mean of $\mu_{\mathrm{x}_0} = 1.425$ and a standard deviation of $\sigma_{\mathrm{x}_0} = 1.4 \cdot 10^{-2}$. The variation of the initial condition $x_0(\omega)$ is chosen such that the trajectories can be either period-1 oscillations around $(1, 0)$ or more complex periodic solutions around all three fixed points.

The effect of the initial condition $x_0(\omega)$ on the response $x(t, \omega)$ is illustrated in Figure 6.16. The response surface of $x(t, \omega)$ at $t_{\mathrm{stop}} = 100$ as function of $x_0(\omega)$ is shown in Figure 6.16a. For $x_0 < 1.414$, $x(t, \omega)$ is positive, which corresponds to periodic solutions around fixed point $(1, 0)$. The time series $x(t, \omega)$ are periodic solutions around all three fixed point for $x_0 > 1.414$, which results in both positive and negative values of the response $x(t,\omega)$. Since the solutions for all samples are periodic, the parameterization error $\varepsilon_{\mathrm{x}_k}(t)$ is smaller than threshold value $\bar{\varepsilon}$ for all $t \in [0, t_{\mathrm{stop}}]$. The UASFE approximation has converged below $\bar{\delta} = 5 \cdot 10^{-2}$ for $N_{\mathrm{e}} = 16$ elements and $N_{\mathrm{s}} = 33$ samples. Resolving the bifurcation at $x_0 = 1.414$ results in a larger number of required samples N_{s} than for the mass-spring-damper system In Figure 6.16a the UASFE response approximation matches with that of a Monte Carlo simulation of $N_{\mathrm{s}} = 1000$ samples.

In Figures 6.16b to 6.16f the UASFE approximations of the period shape functions $x_{\mathrm{period}_k}(\tau,\omega)$, frequency $f_{\mathrm{x}}(\omega)$, relative phase $\phi_{\mathrm{x}}(\omega)$, amplitude $A_{\mathrm{x}}(\omega)$, and reference value $r_{\mathrm{x}}(\omega)$ are given. The period shapes $x_{\mathrm{period}_k}(\tau,\omega)$ are shown for the $N_{\mathrm{s_{ini}}} = 3$ samples of the initial grid with $x_{0_k} = \{1.4; 1.425; 1.45\}$ in Figure 6.16b. A qualitative change in the shape function can be observed for samples below and above $x_0 = 1.414$, which can also be recognized in the response of Figure 6.16a. The discontinuous change of the solution at $x_0 = 1.414$ is clearly illustrated by $f_{\mathrm{x}}(\omega)$, $\phi_{\mathrm{x}}(\omega)$, $A_{\mathrm{x}}(\omega)$, and $r_{\mathrm{x}}(\omega)$ in Figures 6.16c to 6.16f. The frequency $f_{\mathrm{x}}(\omega)$ and relative phase $\phi_{\mathrm{x}}(\omega)$ change from monotonically decreasing to monotonically increasing at $x_0 = 1.414$. The frequency for $x_0 > 1.414$ results in twice the period length of that for $x_0 < 1.414$, which is typical for a period-doubling bifurcation. The reference value $r_{\mathrm{x}}(\omega)$ vanishes and the amplitude $A_{\mathrm{x}}(\omega)$ increases discontinuously at $x_0 = 1.414$. The UASFE discretization captures this discontinuous behavior without over- or undershoots by refining the elements near $x_0 = 1.414$. The solution in the continuous subdomains is also refined for a balance between the approximation error at the discontinuity and in the smooth regions due to exponent N_{V} in refinement measure 4.9. The damping γ_{x} is not shown, since the periodic solutions have zero damping.

The resulting UASFE approximations of the mean $\mu_{\mathrm{x}}(t)$ and the standard deviation $\sigma_{\mathrm{x}}(t)$ are compared to Monte Carlo results in Figure 6.17. The results of UASFE with $N_{\mathrm{s}} = 33$ samples show a good agreement with those of Monte Carlo simulation with $N_{\mathrm{s}} = 1000$ samples. The mean is a decaying oscillation to a positive value of approximately $\mu_{\mathrm{x}} = 0.2$. This result is a combination of the asymptotically zero mean oscillations around the origin for $x_0 > 1.414$ and the positive $x(t,\omega)$ values for $x_0 < 1.414$. The standard deviation $\sigma_{\mathrm{x}}(t)$ shows a complex oscillatory behavior in Figure 6.17b. UASFE capture this highly oscillatory solution accurately. The standard deviation approaches a finite asymptotic value of approximately $\sigma_{\mathrm{x}} = 0.75$ due to the finite amplitude of the periodic trajectories. The asymptotic output standard deviation σ_{x} is a factor 52.0 larger than the input standard deviation of its initial condition σ_{x_0}. These results illustrate that UASFE can successfully be applied to dynamical systems with bifurcations which are extremely sensitive to random initial conditions.

The results for the effect of the random initial condition $x_0(\omega)$ on $y(t,\omega)$ are given in Figure 6.18. In Figure 6.18a, a qualitative change in the response of $y(t_{\mathrm{stop}},\omega)$ as

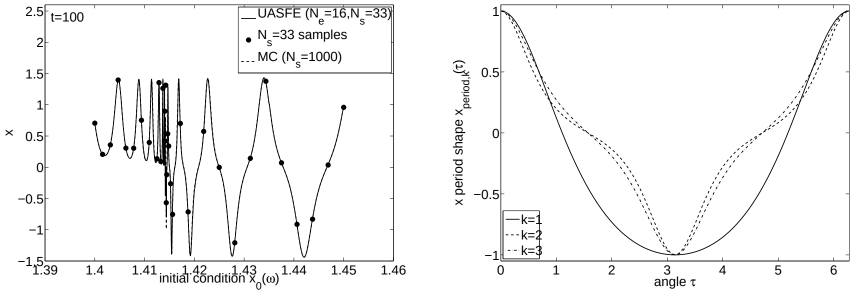

(a) response surface x (b) period shape $x_{\mathrm{period}_k}(\tau)$

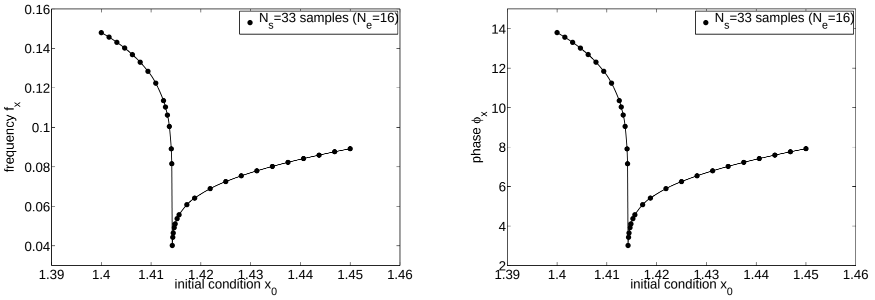

(c) frequency f_{x} (d) phase ϕ_{x}

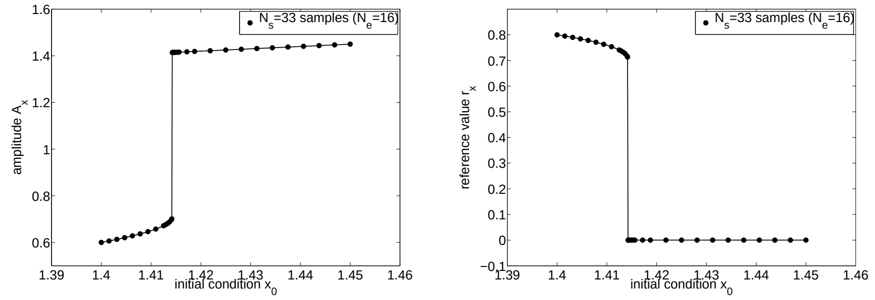

(e) amplitude A_{x} (f) reference value r_{x}

Figure 6.16: Response surface approximations of $x(t_{\mathrm{stop}},\omega)$, $x_{\mathrm{period}_k}(\tau)$, $f_{\mathrm{x}}(\omega)$, $\phi_{\mathrm{x}}(\omega)$, $A_{\mathrm{x}}(\omega)$, and $r_{\mathrm{x}}(\omega)$ by Unsteady Adaptive Stochastic Finite Elements (UASFE) with $N_{\mathrm{e}} = 16$ ($N_{\mathrm{s}} = 33$) and Monte Carlo (MC) simulation with $N_{\mathrm{s}} = 1000$ for the Duffing equation with random initial condition $x_0(\omega)$.

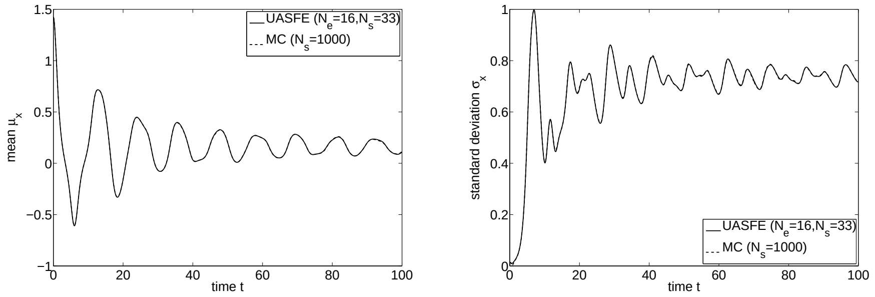

(a) mean $\mu_{\mathrm{y}}(t)$

(b) standard deviation $\sigma_{\mathrm{y}}(t)$

Figure 6.17: Mean $\mu_{\mathrm{x}}(t)$ and standard deviation $\sigma_{\mathrm{x}}(t)$ of $x(t,\omega)$ by Unsteady Adaptive Stochastic Finite Elements (UASFE) with $N_{\mathrm{e}} = 16$ ($N_{\mathrm{s}} = 33$) and Monte Carlo (MC) simulation with $N_{\mathrm{s}} = 1000$ for the Duffing equation with random initial condition $x_0(\omega)$.

function of $x_0(\omega)$ can be seen at $x_0 = 1.414$. Period-doubling can be recognized in the period shape functions $y_{\mathrm{period}_k}(\tau)$ of the $N_{\mathrm{s_{ini}}} = 3$ samples on the initial grid given in Figure 6.18b. UASFE capture both the period-1 and the higher-period oscillations effectively. The UASFE approximation of the complex oscillatory behavior of the mean $\mu_{\mathrm{y}}(t)$ and the standard deviation $\sigma_{\mathrm{y}}(t)$ is in agreement with the Monte Carlo results. The mean is a decaying oscillation to zero and the standard deviation approaches a positive asymptotic value of approximately $\sigma_{\mathrm{y}} = 0.46$. The results for the frequency, phase, amplitude, reference value, and damping are not shown, since they are similar to those of $x(t,\omega)$.

6.3.2.3 Random $x_0(\omega)$ and $y_0(\omega)$

Assuming randomness in both initial conditions $x_0(\omega)$ and $y_0(\omega)$ results in a two-dimensional probability space, to which two-dimensional Unsteady Adaptive Stochastic Finite Elements are applied. The initial conditions $x_0(\omega)$ and $y_0(\omega)$ are assumed to be uniformly distributed in the interval $[0.45; 0.55]$. This interval corresponds to a mean of $\mu_{\mathrm{x}_0} = \mu_{\mathrm{y}_0} = 0.5$ and standard deviation of $\sigma_{\mathrm{x}_0} = \sigma_{\mathrm{y}_0} = 2.9 \cdot 10^{-2}$. This parameter domain is chosen since it contains a bifurcation of the Duffing equation. Since the time series are periodic solutions, the UASFE reconstruction is valid for all $t \in [0, t_{\mathrm{stop}}]$. The presented results are converged below $\bar{\delta} = 5 \cdot 10^{-2}$.

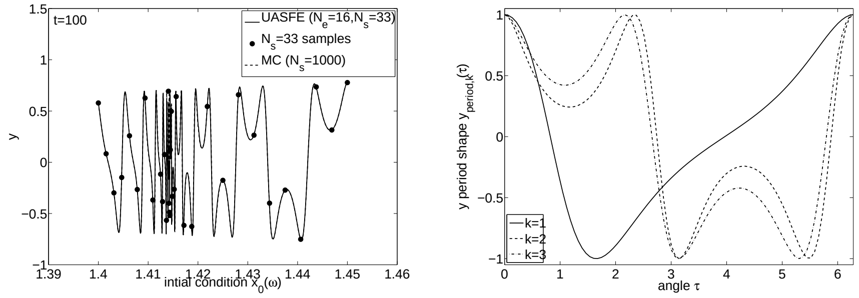

(a) response surface y

(b) period shape functions $y_{\mathrm{period}_k}(\tau)$

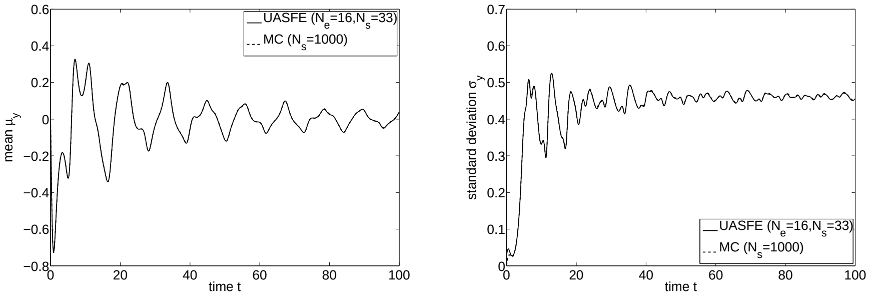

(c) mean $\mu_{\mathrm{y}}(t)$

(d) standard deviation $\sigma_{\mathrm{y}}(t)$

Figure 6.18: Response surface approximations of $y(t_{\mathrm{stop}}, \omega)$, $y_{\mathrm{period},k}(\tau)$, and mean $\mu_{\mathrm{y}}(t)$ and standard deviation $\sigma_{\mathrm{y}}(t)$ by Unsteady Adaptive Stochastic Finite Elements (UASFE) with $N_{\mathrm{e}} = 16$ ($N_{\mathrm{s}} = 33$) and Monte Carlo (MC) simulation with $N_{\mathrm{s}} = 1000$ for the Duffing equation with random initial condition $x_0(\omega)$.

The bifurcation of the solution is illustrated by the two-dimensional response surfaces of $x(t,\omega)$ and $y(t,\omega)$ at $t = t_{\mathrm{stop}}$ as function of the random initial conditions $x_0(\omega)$ and $y_0(\omega)$ shown in Figure 6.19. In Figures 6.19a and 6.19b the approximation of the response surface of $x(t,\omega)$ by UASFE with $N_{\mathrm{e}} = 64$ elements ($N_{\mathrm{e_{sub}}} = 4^4$) and $N_{\mathrm{s}} = 151$ samples, and Monte Carlo with $N_{\mathrm{s}} = 10^4$ samples are given, respectively. For $y(t,\omega)$ the corresponding results are shown in Figures 6.19c and 6.19d. The UASFE approximation agrees well with the Monte Carlo results at a reduction of the number of samples N_{s} by a factor 66.2. The response surfaces for $x(t,\omega)$ and $y(t,\omega)$ are highly oscillatory due to the alternating positive and negative values of both $x(t,\omega)$ and $y(t,\omega)$. In the response of $x(t,\omega)$ a bifurcation can be recognized approximately at the line between (x_0, y_0) equal to $(0.475; 0.45)$ and $(0.55; 0.5)$, see Figures 6.19a and 6.19b. Below this line, only positive values of $x(t,\omega)$ are found, which corresponds to periodic trajectories around fixed point $(1,0)$. Positive and negative values of $x(t,\omega)$ occur above the bifurcation line, which corresponds to periodic solutions around all three fixed points. In the response surface of $y(t,\omega)$ the bifurcation can be identified at the same location.

UASFE capture the discontinuous bifurcation behavior by refining the elements near the bifurcation line. In Figure 6.20 the grid of UASFE with $N_{\mathrm{e}} = 64$ elements in probability space is given. The $N_{\mathrm{s}} = 151$ samples are denoted by the dots. The elements are clearly more refined near the bifurcation than in the continuous domains. The smallest elements in the grid are 16 times smaller than the largest ones.

In Figure 6.21 it is demonstrated that UASFE agrees with the Monte Carlo results also for the mean and the standard deviation of $x(t,\omega)$ and $y(t,\omega)$ for $t \in [0, t_{\mathrm{stop}}]$. The results are comparable to those for the random initial condition $x_0(\omega)$ of Figures 6.17 and 6.18. The mean $\mu_{\mathrm{x}}(t)$ of $x(t,\omega)$ is a damped oscillation with a positive asymptotic value of $\mu_{\mathrm{x}} = 0.15$, see Figure 6.21a. The mean $\mu_{\mathrm{y}}(t)$ of $y(t,\omega)$ is an oscillation which decays to zero. Both standard deviations $\sigma_{\mathrm{x}}(t)$ and $\sigma_{\mathrm{y}}(t)$ are irregular oscillations which approach finite asymptotic values of $\sigma_{\mathrm{x}}(t) = 0.75$ and $\sigma_{\mathrm{y}}(t) = 0.46$. The results show an amplification of the standard deviation of the random initial conditions by factors 26.0 and 15.9 for $x_0(\omega)$ and $y_0(\omega)$, respectively. The differences between the UASFE results and those of Monte Carlo simulation are slightly higher than for one random initial condition. These differences decrease further by decreasing $\bar{\delta}$. The slower convergence for smaller values of t is due to the parameterization errors $\varepsilon_{\mathrm{x}_k}(t)$ and $\varepsilon_{\mathrm{y}_k}(t)$.

6.3.3 Rigid-airfoil fluid-structure interaction

The rigid-body fluid-structure interaction of an elastically mounted airfoil in an Euler flow subject to a random parameter is studied in this section. This is a practical example

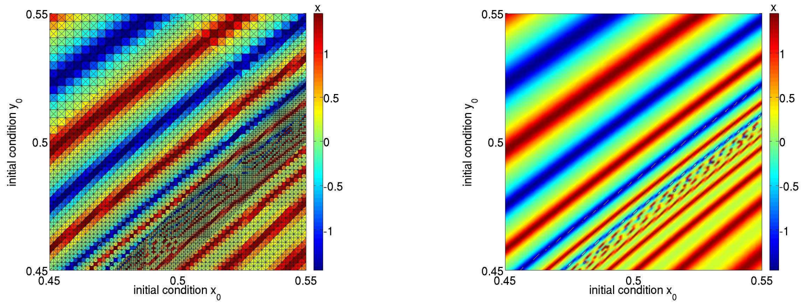

(a) UASFE $x(t, \omega)$

(b) MC $x(t, \omega)$

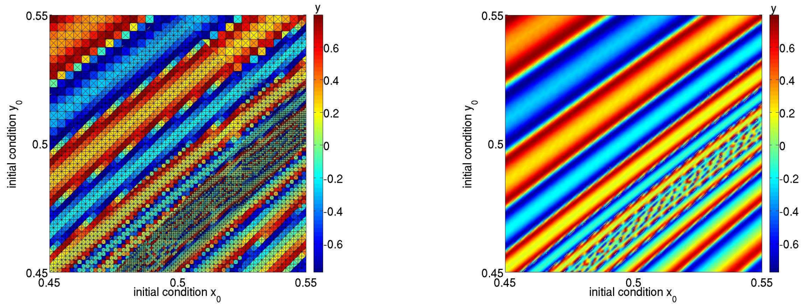

(c) UASFE $y(t, \omega)$

(d) MC $y(t, \omega)$

Figure 6.19: Two-dimensional response surface approximations for $x(t_{\mathrm{stop}}, \omega)$ and $y(t_{\mathrm{stop}}, \omega)$ as function of random initial conditions $x_0(\omega)$ and $y_0(\omega)$ by Unsteady Adaptive Stochastic Finite Elements (UASFE) with $N_{\mathrm{e}} = 64$ ($N_{\mathrm{e_{sub}}} = 4^4$, $N_{\mathrm{s}} = 151$) and Monte Carlo (MC) with $N_{\mathrm{s}} = 10^4$ for the Duffing equation with random initial conditions $x_0(\omega)$ and $y_0(\omega)$.

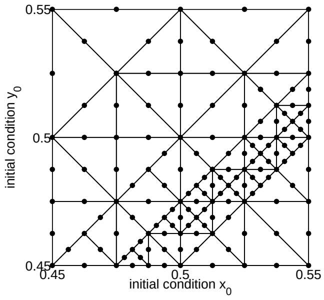

Figure 6.20: Unsteady Adaptive Stochastic Finite Elements (UASFE) grid in two-dimensional parameter space $x_0(\omega)$–$y_0(\omega)$ with $N_\mathrm{e} = 64$ and $N_\mathrm{s} = 151$ samples given by the dots for the Duffing equation with random initial conditions $x_0(\omega)$ and $y_0(\omega)$.

of an aeroelastic system which is subject to negative aerodynamic damping beyond the flutter speed. The governing equations for the motion of the structure and the aerodynamic forces are given in section 6.3.3.1. In section 6.3.3.2 numerical results are presented for a random center of mass location.

6.3.3.1 Two-degree-of-freedom airfoil model with Euler flow

The structure dynamics is governed by a two-degree-of-freedom linear model for coupled pitch and plunge motion. The aerodynamic forces are computed by solving the two-dimensional unsteady Euler equations for compressible flow. The structure model is given by [25]:

$$\xi'' + x_\alpha \alpha'' + \left(\frac{\bar{\omega}}{U^*}\right)^2 \xi = -\frac{1}{\pi\mu} C_\mathrm{l}(\tau), \tag{6.14}$$

$$\frac{x_\alpha}{r_\alpha^2}\xi'' + \alpha'' + \frac{1}{U^{*2}}\alpha = \frac{2}{\pi\mu r_\alpha^2} C_\mathrm{m}(\tau), \tag{6.15}$$

where $\xi(\tau) = h/b$ is the non-dimensional plunge displacement of the elastic axis, $\alpha(\tau)$ is the pitch angle, and ($'$) denotes differentiation with respect to nondimensional time $\tau = Ut/b$, with half-chord length $b = c/2$ and free stream velocity U. The frequency ratio $\bar{\omega}$ is defined as $\bar{\omega} = \omega_\xi/\omega_\alpha$, U^* is defined as $U^* = U/(b\omega_\alpha)$, the radius of gyration around the elastic axis is $r_\alpha b$, and the airfoil/air mass ratio is $\mu = m/\pi\rho b^2$, with ω_ξ and ω_α the natural frequencies in pitch and plunge, respectively, m the airfoil

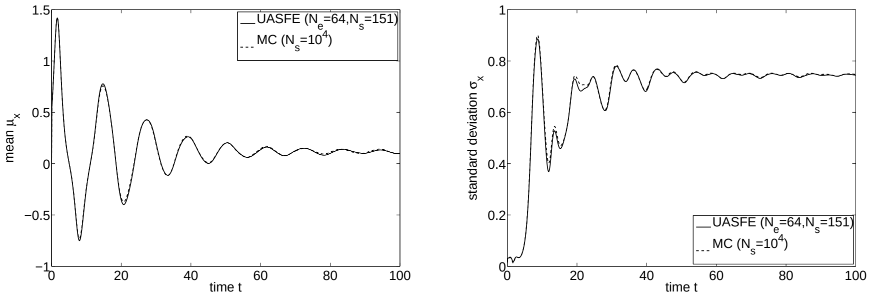

(a) mean $\mu_\mathrm{x}(t)$ (b) standard deviation $\sigma_\mathrm{x}(t)$

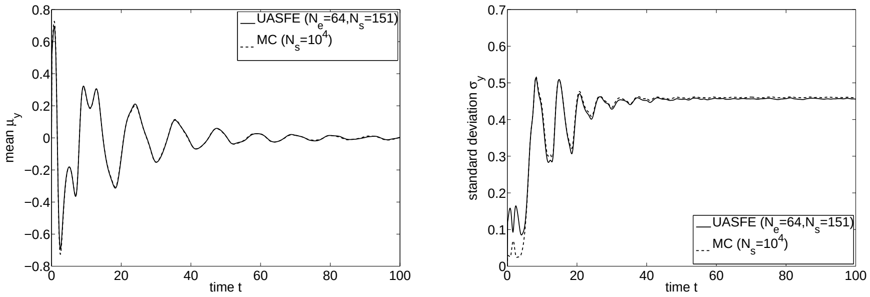

(c) mean $\mu_\mathrm{y}(t)$ (d) standard deviation $\sigma_\mathrm{y}(t)$

Figure 6.21: Mean $\mu_\mathrm{x}(t)$ and $\mu_\mathrm{y}(t)$, and standard deviation $\sigma_\mathrm{x}(t)$ and $\sigma_\mathrm{y}(t)$ by Unsteady Adaptive Stochastic Finite Elements (UASFE) with $N_\mathrm{e} = 64$ ($N_\mathrm{s} = 151$) and Monte Carlo (MC) with $N_\mathrm{s} = 10^4$ for the Duffing equation with random initial conditions $x_0(\omega)$ and $y_0(\omega)$.

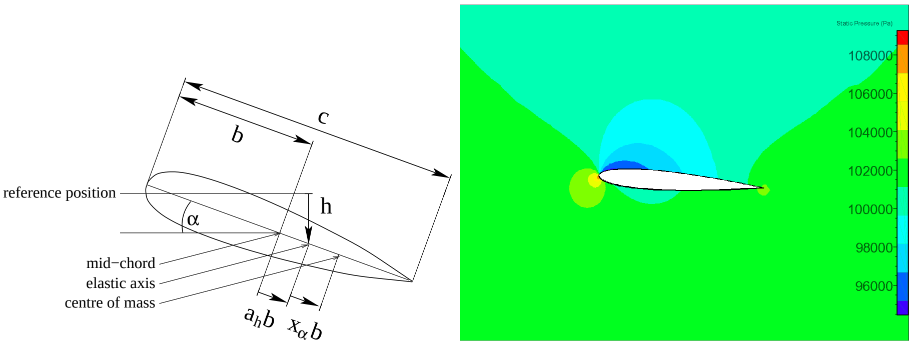

(a) two-degree-of-freedom structure model (b) static fluid pressure field at $\tau = 110$

Figure 6.22: The rigid-airfoil fluid-structure interaction system.

mass, and ρ the free stream air density. The elastic axis is located at a distance $a_{\mathrm{h}}b$ from the mid-chord position and the mass center is located at a distance $x_\alpha b$ from the elastic axis, see Figure 6.22a. Pitch rotation $\alpha(\tau)$ is defined positive in the nose up direction and plunge deflection $\xi(\tau)$ is defined positive in the downward direction. The nondimensional aerodynamic lift and moment coefficients, $C_{\mathrm{l}}(\tau)$ and $C_{\mathrm{m}}(\tau)$, are computed by solving the Euler equations for inviscid flow [15]:

$$\frac{\partial U}{\partial t} + \frac{\partial F(U)}{\partial x} + \frac{\partial G(U)}{\partial y} = 0, \tag{6.16}$$

$$U = \begin{pmatrix} \rho \\ \rho u \\ \rho v \\ E \end{pmatrix}, \qquad F = \begin{pmatrix} \rho u \\ p + \rho u^2 \\ \rho u v \\ u(E+p) \end{pmatrix}, \qquad G = \begin{pmatrix} \rho v \\ \rho u v \\ p + \rho v^2 \\ v(E+p) \end{pmatrix},$$

with $u(\mathbf{x}, t)$ and $v(\mathbf{x}, t)$ the velocities in x and y direction, respectively, $p(\mathbf{x}, t)$ the static pressure of the gas, $E(\mathbf{x}, t)$ the internal energy, which for a perfect gas reads $E(\mathbf{x}, t) = p(\mathbf{x}, t)/((\gamma - 1)\rho(\mathbf{x}, t)) + (u(\mathbf{x}, t)^2 + v(\mathbf{x}, t)^2)/2$, with γ the ratio of specific heats. Field equation (6.16) is discretized using a second-order finite volume scheme on an unstructured hexahedral mesh with $7.5 \cdot 10^3$ volumes in spatial domain D with dimensions $30c \times 20c$. An Arbitrary Lagrangian-Eulerian formulation is employed to couple the fluid mesh with the movement of the structure. The fluid mesh is deformed using radial basis function interpolation of the boundary displacements [9]. Time integration is performed using the BDF-2 method with stepsize $\Delta\tau = 0.22$ until

$\tau_{\mathrm{stop}} = 110$, which corresponds to approximately 10 period lengths for the deterministic case.

6.3.3.2 Effect of a random center of mass location

Randomness is considered in the airfoil center of mass location $x_\alpha(\omega)b$, which affects both the aerodynamic damping and the frequency of the airfoil motion. The randomness is given by a symmetric unimodal beta distribution for $x_\alpha(\omega)b$ in the domain $x_\alpha(\omega)b \in [0.2; 0.4]$ with parameters $\beta_1 = \beta_2 = 2$. The free stream Mach number is chosen to correspond to the flutter speed for the mean center of mass location $x_\alpha b = 0.3$. The parameter values $\bar{\omega} = 0.2$, $r_\alpha = 0.5$, $\mu = 100$, and $a_{\mathrm{h}} = -0.5$ are taken from [49]. Initially the airfoil is at rest at a deflection of $\alpha(0) = 5^{\mathrm{o}}$ and $\xi(0) = -0.026$ from its equilibrium position, which corresponds to a zero ξ-deflection of the center of mass for its mean location $x_\alpha b = 0.3$ at $t = 0$. The static pressure field of the flow around the airfoil at τ_{stop} is shown in Figure 6.22b for $x_\alpha = \mu_{\mathrm{x}_\alpha}$ and free stream pressure $p_\infty = 1.0 \cdot 10^5$ Pa. The output of interest is the effect of the random $x_\alpha(\omega)b$ on the time evolution of the energy of the system. The potential energy, the kinetic energy, and the combination of both are considered as measures for the amount of positive or negative aerodynamic damping of practical importance. Results for the single-frequency motion in the pitch degree of freedom are presented.

The nondimensional potential energy $E_{\mathrm{p}}(\tau, \omega)$, kinetic energy $E_{\mathrm{k}}(\tau, \omega)$, and total energy $E_{\mathrm{tot}}(\tau, \omega)$ at τ_{stop} are given in Figure 6.23 as function of random parameter $x_\alpha(\omega)b$ for $N_{\mathrm{e}} = 3$ elements and $N_{\mathrm{s}} = 7$ samples. Both $E_{\mathrm{p}}(\tau_{\mathrm{stop}}, \omega)$ and $E_{\mathrm{k}}(\tau_{\mathrm{stop}}, \omega)$ show an oscillatory dependence on $x_\alpha(\omega)b$. The potential energy $E_{\mathrm{p}}(\tau_{\mathrm{stop}}, \omega)$ vanishes at $x_\alpha(\omega)$ values at which the kinetic energy $E_{\mathrm{k}}(\tau_{\mathrm{stop}}, \omega)$ reaches a maximum, and vise versa. The total energy of the system $E_{\mathrm{tot}}(\tau_{\mathrm{stop}}, \omega)$ is continuously transferred between $E_{\mathrm{p}}(\tau_{\mathrm{stop}}, \omega)$ and $E_{\mathrm{k}}(\tau_{\mathrm{stop}}, \omega)$. The oscillations in the response surface of $E_{\mathrm{tot}}(\tau_{\mathrm{stop}}, \omega)$ are caused by the transfer of energy between the flow and the structure within one oscillation and between the pitch and plunge degree of freedom of the structure.

Overall, the energies $E_{\mathrm{p}}(\tau_{\mathrm{stop}}, \omega)$, $E_{\mathrm{k}}(\tau_{\mathrm{stop}}, \omega)$, and $E_{\mathrm{tot}}(\tau_{\mathrm{stop}}, \omega)$ have an increasing trend with increasing $x_\alpha(\omega)b$. This trend is caused by a decreasing aerodynamic damping with increasing $x_\alpha(\omega)b$. For $x_\alpha(\omega)b = 0.3$ the total energy $E_{\mathrm{tot}}(\tau_{\mathrm{stop}}, \omega)$ at t_{stop} is equal to the initial total energy of $E_{\mathrm{tot}}(0, \omega) = 0.123$, since the free stream Mach number corresponds to the flutter speed for $x_\alpha(\omega)b = 0.3$. Total energy $E_{\mathrm{tot}}(\tau_{\mathrm{stop}}, \omega)$ has decreased at τ_{stop} for $x_\alpha(\omega)b < 0.3$ and has increased for $x_\alpha(\omega)b > 0.3$. The aeroelastic system is, therefore, subject to a 50% probability of flutter.

Both the time evolutions of the nondimensional mean $\mu_{\mathrm{E}}(\tau)$ and standard devia-

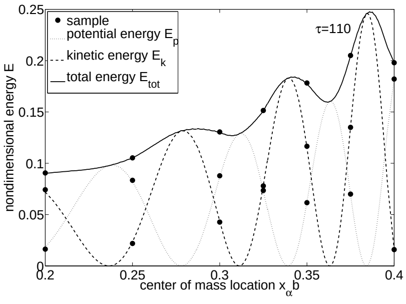

Figure 6.23: Nondimensional potential energy $E_{\mathrm{p}}(\tau,\omega)$, kinetic energy $E_{\mathrm{k}}(\tau,\omega)$, and total energy $E_{\mathrm{tot}}(\tau,\omega)$ as function of random parameter $x_\alpha(\omega)$ at τ_{stop} by Unsteady Adaptive Stochastic Finite Elements (UASFE) with $N_{\mathrm{e}} = 3$ ($N_{\mathrm{s}} = 7$) for the rigid-airfoil fluid-structure interaction.

tion $\sigma_{\mathrm{E}}(\tau)$ of $E_{\mathrm{p}}(\tau,\omega)$, $E_{\mathrm{k}}(\tau,\omega)$, and $E_{\mathrm{tot}}(\tau,\omega)$ show an increasing behavior in Figure 6.24. Until $\tau = 50$ the mean values are oscillations with decreasing amplitude. For $\tau > 50$ the mean values show a slight increase in time due to the asymmetric effect of positive and negative damping. The mean value of non-negative energy $E_{\mathrm{tot}}(\tau)$ does not decay to zero like the mean of the pitch angle $\alpha(\tau,\omega)$, which attains both positive and negative values as it oscillates around its equilibrium angle $\alpha = 0^{\mathrm{o}}$. System energy is, therefore, a more intuitive measure to illustrate the effect of randomness on the system response than deflection.

The standard deviation of $E_{\mathrm{p}}(\tau,\omega)$, $E_{\mathrm{k}}(\tau,\omega)$, and $E_{\mathrm{tot}}(\tau,\omega)$, shown in Figure 6.24b, have an initial transient until $\tau = 30 - 60$ due to the deterministic initial conditions. In the asymptotic range for $\tau > 60$ the standard deviations show an increasing trend in time due to the nonzero probability of negative aerodynamic damping. The standard deviation of the total energy $E_{\mathrm{tot}}(\tau,\omega)$ is smaller than those of $E_{\mathrm{p}}(\tau,\omega)$ and $E_{\mathrm{k}}(\tau,\omega)$, since its value varies less with variations of $x_\alpha(\omega)$, see Figure 6.23.

The convergence of UASFE is illustrated for the mean and standard deviation of the total energy, $\mu_{\mathrm{E_{tot}}}(\tau)$ and $\sigma_{\mathrm{E_{tot}}}(\tau)$ in Figure 6.25. Results are shown for $N_{\mathrm{e}} = \{1,2,3\}$ elements and $N_{\mathrm{s}} = \{3,5,7\}$ samples. The approximations with $N_{\mathrm{e_{ini}}} = 2$ and $N_{\mathrm{e_{ini}}} = 3$ almost coincide. It can be seen that the solution on the initial grid with $N_{\mathrm{e_{ini}}} = 1$ gives already a good approximation.

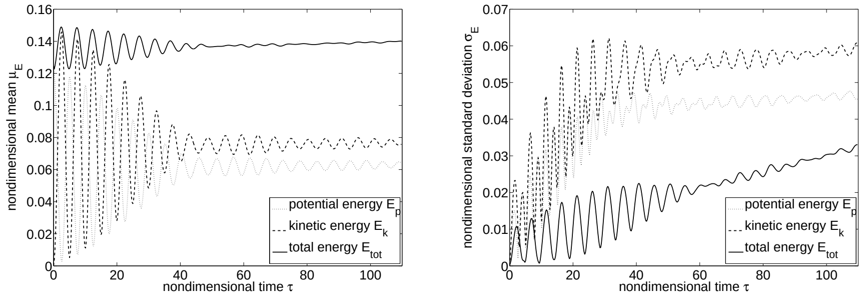

(a) mean $\mu_{\mathrm{E}}(\tau)$ (b) standard deviation $\sigma_{\mathrm{E}}(\tau)$

Figure 6.24: Nondimensional mean $\mu_{\mathrm{E}}(\tau)$ and standard deviation $\sigma_{\mathrm{E}}(\tau)$ of potential energy $E_{\mathrm{p}}(\tau,\omega)$, kinetic energy $E_{\mathrm{k}}(\tau,\omega)$, and total energy $E_{\mathrm{tot}}(\tau,\omega)$ as function of nondimensional time τ by Unsteady Adaptive Stochastic Finite Elements (UASFE) with $N_{\mathrm{e}} = 3$ ($N_{\mathrm{s}} = 7$) for the rigid-airfoil fluid-structure interaction.

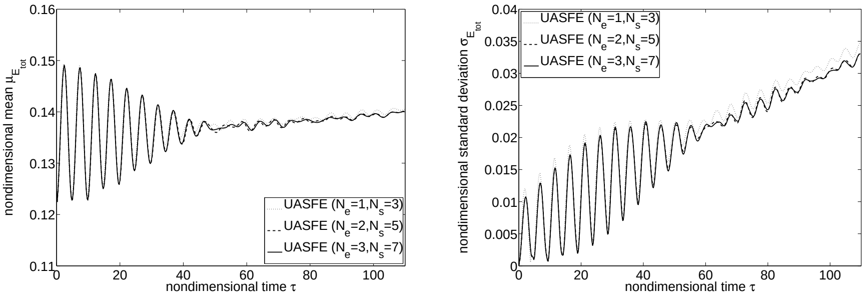

(a) mean $\mu_{\mathrm{E_{tot}}}(\tau)$ (b) standard deviation $\sigma_{\mathrm{E_{tot}}}(\tau)$

Figure 6.25: Convergence of Unsteady Adaptive Stochastic Finite Elements (UASFE) with $N_{\mathrm{e}} = \{1, 2, 3\}$ ($N_{\mathrm{s}} = \{3, 5, 7\}$) for nondimensional mean $\mu_{\mathrm{E_{tot}}}(\tau)$ and standard deviation $\sigma_{\mathrm{E_{tot}}}(\tau)$ as function of nondimensional time τ for the rigid-airfoil fluid-structure interaction.

6.4 Summary

An Unsteady Adaptive Stochastic Finite Elements (UASFE) formulation for unsteady problems is developed based on a time-independent parameterization of sampled deterministic time series. Stochastic Finite Elements methods usually require an impractically high number of samples for resolving the asymptotic stochastic behavior of dynamical systems. Due to the time-independent parameterization, UASFE maintain a constant interpolation accuracy in time with a constant number of elements. The parameterization of the samples consists of the frequency, phase, amplitude, reference value, damping, and period shape. The parameters are interpolated using a robust Adaptive Stochastic Finite Element (ASFE) method based on Newton-Cotes quadrature in simplex elements. This approach requires a relatively low number of deterministic solves and preserves monotonicity and optima of the samples. In order to ensure the robustness of the method, (1) the elements are refined adaptively until L_∞-convergence criterion $\bar{\delta}$ is reached, and (2) parameterization error $\varepsilon_{\mathrm{u}_k}(t)$ is computed to determine the time interval in which the UASFE approximation is valid.

The robustness of the ASFE interpolation enables the application of the proposed approach to problems with bifurcations, in which the time-independent functionals are non-smooth. The effect of positive and negative damping is resolved using a damping parameter in the time-independent parameterization. The proposed UASFE formulation includes an algorithm for parameterizing multi-period oscillations. The application of the proposed approach is limited to the asymptotic range of single-frequency rigid-body motions in which the time-independent parameterization is well-defined.

UASFE is successfully applied to a mass-spring-damper system, the Duffing equation, and a rigid-airfoil fluid-structure interaction simulation with multiple random input parameters. For the mass-spring-damper system the effect of positive and negative damping on the stochastic results is studied. Input randomness assumed in the spring stiffness parameter, the damping parameter, and a combination of both, shows that a non-zero probability of negative damping results asymptotically in a diverging output standard deviation. In case of two random parameters, the required number of samples for UASFE has shown to be up to a factor $2.6 \cdot 10^3$ smaller than for Monte Carlo simulation. The study of one and two random initial conditions for the Duffing equation illustrates that nonlinear dynamical systems with discontinuous solutions can be extremely sensitive to random initial conditions. An amplification factor of 52.0 has been observed for the standard deviation. The application to the rigid-airfoil fluid-structure interaction problem shows in the asymptotic range a diverging mean and standard deviation of the system energy in case of a non-zero probability of flutter.

Chapter 7

Unsteady Adaptive Stochastic Finite Elements with interpolation at constant phase

The Unsteady Adaptive Stochastic Finite Elements method based on time-independent parameterization developed in the previous chapter resolves the effect of random parameters in unsteady simulations efficiently. In this chapter an alternative Unsteady Adaptive Stochastic Finite Elements formulation based on interpolation at constant phase is developed to further improve the accuracy and extend the applicability compared to time-independent parameterization. In order to emphasize the difference between the two methods, in this chapter Unsteady Adaptive Stochastic Finite Elements based on time-independent parameterization is referred to as UASFE-ti and UASFE-cp refers to Unsteady Adaptive Stochastic Finite Elements based on interpolation at constant phase. In addition to achieving a constant number of samples in time, interpolation at constant phase: (1) eliminates the parameterization error of the time-independent parameterization; (2) resolves time-dependent functionals, which cannot be modeled by the parameterization; and (3) captures transient behavior of the samples, which is an important special case of time-dependent functionals. These three points are illustrated by the comparison of UASFE-cp results to those of UASFE-ti for random parameters in a mass-spring-damper system, the damped nonlinear Duffing oscillator, and an elastically mounted airfoil with nonlinearity in the flow and the structure.

Based on: J.A.S. Witteveen, H. Bijl, An alternative Unsteady Adaptive Stochastic Finite Elements formulation based on interpolation at constant phase, Comput. Method Appl. M. 198 (2008) 578–591.

7.1 Introduction

In this chapter, an alternative Unsteady Adaptive Stochastic Finite Elements formulation based on interpolation at constant phase (UASFE-cp) is developed to further improve the accuracy and extend the applicability of the UASFE-ti formulation based on time-independent parameterization. The usual increase of the number of samples with time is caused by increasing phase differences between the realizations. Scaling the samples with their phase and performing the uncertainty quantification interpolation of the samples at constant phase instead of at constant time, eliminates the effect of the phase differences. The increase of the number of samples with time due to an increasingly oscillatory response surface is, therefore, avoided by interpolation at constant phase. In addition to the constant number of samples in time, the proposed UASFE-cp formulation has the following three advantages over UASFE-ti:

1. **Parameterization error is eliminated**
   The time-independent parameterization of the samples in UASFE-ti is subject to numerical discretization and interpolation errors. UASFE-cp uses an exact representation of the samples, which improves the convergence behavior of the method.

2. **Time-dependent functionals can be resolved**
   The application of UASFE-ti is limited to time series which can be represented by time-independent functionals such as frequency and damping. UASFE-cp is applicable to time series in which these functionals change in time. Time-dependent functionals are encountered in practice in, for example, damped nonlinear systems.

3. **Transient behavior can be captured**
   Deterministic transient behavior is an important special case of time-dependent functionals that cannot be captured by the time-independent parameterization of UASFE-ti. The UASFE-cp formulation is capable of resolving the effect of random parameters in both the asymptotic and transient regime of the samples. Transient behavior is seen in virtually all nonlinear practical applications.

UASFE-cp can be applied to problems in which the phase of the oscillatory samples is well-defined.

The Unsteady Adaptive Stochastic Finite Elements formulation based on interpolation at constant phase is introduced in section 7.2. The effect of the elimination of the parameterization error on the convergence of UASFE-cp is studied for a mass-spring-damper system in section 7.3.1. In section 7.3.2 UASFE-cp is employed to resolve the effect of multiple random parameters on a response with time-dependent functionals of the damped nonlinear Duffing oscillator. The stochastic bifurcation behavior of the fluid-structure interaction system of nonlinear flow around an elastically mounted airfoil with nonlinear structural stiffness is analyzed in section 7.3.3. This application involves transient behavior in the post-bifurcation region. Results for various probability distributions are compared to those of UASFE-ti and Monte Carlo simulations. The chapter is concluded in section 7.4.

7.2 Unsteady Adaptive Stochastic Finite Elements based on interpolation at constant phase

The procedure for interpolation at constant phase in the Unsteady Adaptive Stochastic Finite Elements framework is developed in section 7.2.1. The Adaptive Stochastic Finite Elements formulation employed for the interpolation is briefly reviewed in section 7.2.2. In section 7.2.3 the resulting UASFE-cp algorithm is summarized.

7.2.1 Interpolation at constant phase

Consider dynamical system (1.1) subject to random input parameters, which governs an oscillatory response $u(\mathbf{x}, t, \omega)$

$$\mathcal{L}(\mathbf{x}, t; u(\mathbf{x}, t, \omega)) = S(\mathbf{x}, t). \tag{7.1}$$

Assume that the phase of the oscillatory samples $u_k(t) \equiv u(t, \omega_k)$ for realizations of the random parameters $\mathbf{a}_k \equiv \mathbf{a}(\omega_k)$ is well defined for $k = 1, \dots, N_\mathrm{s}$. The argument $\mathbf{x}$ has been dropped here for convenience in the notation. In order to interpolate the samples $u_k(t)$ at constant phase, first, their phase as function of time $\phi_k(t)$ is extracted from the deterministic solves $u_k(t)$. Second, the time series for the phase $\phi_k(t)$ are used to transform the samples $u_k(t)$ to functions of their phase $u_k^*(\phi_k)$ instead of time, see Figure 7.1. The initial $N_{\mathrm{s}_\mathrm{ini}} = 3$ samples of UASFE-cp with $N_{\mathrm{e}_\mathrm{ini}} = 1$ element for the mass-spring-damper system. For discrete time histories the vectors u_k and u_k^* are identical. Third, the transformed samples $u_k^*(\phi_k)$ are interpolated to the function $u^*(\phi, \omega)$ using Adaptive Stochastic Finite Elements interpolation. This step involves both the interpolation of the sampled phases $\phi_k(t)$ to the function $\phi(t, \omega)$ and the interpolation of the samples $u_k^*(\tilde{\phi})$ to the function $u^*(\tilde{\phi}, \omega)$ at constant phase $\tilde{\phi}$. Repeating the latter interpolation for all phases $\tilde{\phi}$ results in the function $u^*(\phi, \omega)$. Finally, transforming $u^*(\phi, \omega)$ back to $u(t, \omega)$ using $\phi(t, \omega)$ yields the unknown response surface of

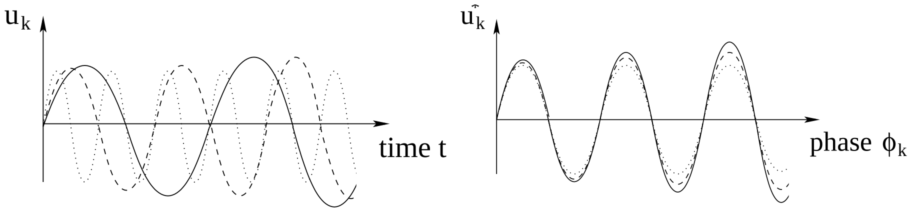

(a) samples $u_k(t)$ (b) samples $u_k^*(\phi_k)$

Figure 7.1: Oscillatory samples as function of time and phase.

the system response as function of the random parameters $\mathbf{a}(\omega)$ and time t. Integrating this response surface approximation results in an approximation of the statistical moments of the response.

The phase $\phi_k(t)$ is extracted from the samples based on the local extrema of the time series $u_k(t)$. A trial and error procedure identifies a cycle of oscillation based on two or more successive local maxima. The selected cycle is accepted if the maximal error of its extrapolation in time with respect to the actual sample is smaller than a threshold value $\bar{\varepsilon}_k$ for at least one additional cycle length. The function for the phase $\phi_k(t)$ in the whole time domain $t \in T$ is constructed by identifying all successive cycles of $u_k(t)$ and extrapolation to $t = 0$ and $t = t_{\max}$ before and after the first and last complete cycle, respectively. The phase is normalized to zero at the start of the first cycle and a user defined parameter determines whether the sample is assumed to attain a local extremum at $t = 0$. If the phase $\phi_k(t)$ cannot be extracted from one of the samples $k = 1, \ldots, N_\mathrm{s}$, Adaptive Stochastic Finite Elements interpolation can directly be applied to the time-dependent samples $u_k(t)$.

7.2.2 Adaptive Stochastic Finite Elements interpolation

The interpolation of the samples at constant phase is performed in parameter space A using the non-intrusive Adaptive Stochastic Finite Elements (ASHE) interpolation based on Newton-Cotes quadrature points in simplex elements developed in Chapter 4. The ASFE formulation employs a piecewise quadratic approximation of the response surface by dividing parameter space A into N_e simplex elements A_i with $i = 1, \ldots, N_\mathrm{e}$. The quadratic approximation in the elements is constructed by performing deterministic solves for the values of the random parameters $\mathbf{a}(\omega)$ that correspond to the $\binom{n+2}{2}$ second-degree Newton-Cotes quadrature points in the elements shown in

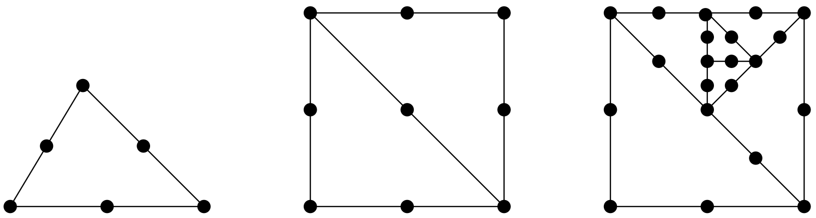

(a) Element (b) Initial grid (c) Adapted grid

Figure 7.2: Discretization of two-dimensional parameter space A using 2-simplex elements and second-degree Newton-Cotes quadrature points given by the dots.

Figure 7.2.

7.2.3 UASFE-cp algorithm summary

The Unsteady Adaptive Stochastic Finite Elements algorithm based on interpolation at constant phase can be summarized as follows:

1. Solve (7.1) for the parameter values $\mathbf{a}_k$ corresponding to the quadrature points in the initial stochastic grid to obtain the deterministic time series $u_k(t)$ with $k = 1, \dots, N_{\mathrm{s_{ini}}}$;
2. Extract the phase $\phi_k(t)$ from the time histories $u_k(t)$;
3. Transform the samples $u_k(t)$ to functions of their phase $u_k^*(\phi_k)$;
4. Use ASFE to interpolate the sampled phases $\phi_k(t)$ to the function $\phi(\omega, t)$ and the samples $u_k^*(\tilde{\phi})$ to the function $u^*(\tilde{\phi}, \omega)$ for all phases $\tilde{\phi}$;
5. Transform $u^*(\phi, \omega)$ back to the unknown response surface as function of time $u(t, \omega)$;
6. Determine the refinement measure ρ_i in the elements for $i = 1, \dots, N_{\mathrm{e_{ini}}}$ and refine the element with the highest value for refinement measure ρ_i;
7. The ASFE interpolation is performed for both the sampled phases from $\phi_k(t)$ to $\phi(t, \omega)$ and the samples at constant phase from $u_k^*(\tilde{\phi})$ to $u^*(\tilde{\phi}, \omega)$. Repeat steps

1 to 6 for the parameter values $\mathbf{a}_k$ corresponding to the new quadrature points in the refined element with $k = N_{\mathrm{s}_{\mathrm{old}}} + 1, \ldots, N_{\mathrm{s}_{\mathrm{new}}}$;

8. Stop the adaptive stochastic grid refinement based on a threshold for convergence $\bar{\delta}$ or the maximum number of samples $\bar{N}_{\mathrm{s}}$.

Since each sample reaches a different minimum and maximum phase in the time domain $t \in T$, the ASFE interpolation at constant phase is restricted to the range of phases that is reached by all samples in an element. The UASFE-cp interpolation is then limited to the time domain which corresponds to $\tilde{\phi} \in [\max_k \phi_k(0), \min_k \phi_k(t_{\max})]$ in the elements. The time domain of approximation approaches $[0, t_{\max}]$ as the number of elements N_{e} increases. Outside this domain, ASFE can directly be applied to the time-dependent samples $u_k(t)$.

7.3 Results

The results of the Unsteady Adaptive Stochastic Finite Elements method based on interpolation at constant phase (UASFE-cp) and time-independent parameterization (UASFE-ti) are compared with those of converged Monte Carlo simulations with evenly spaced realizations in sample space $\omega \in [0, 1]$. The methods are applied to a linear mass-spring-damper system in section 7.3.1, the damped nonlinear Duffing oscillator in section 7.3.2, and the flow around an elastically mounted airfoil with nonlinear structural stiffness in section 7.3.3.

7.3.1 Mass-spring-damper system

Consider a mass attached to a spring and a damper as shown in Figure 7.3. The governing equation for the motion of the mass is given in section 7.3.1.1. Randomness is here assumed in the spring stiffness parameter $K(\omega)$, since the frequency of the response is sensitive to variations in $K(\omega)$. The effect of the elimination of the parameterization error $\varepsilon_k(t)$ on the error convergence of UASFE-cp is studied in section 7.3.1.2.

7.3.1.1 Governing mass-spring-damper equation

The mass-spring-damper system is governed by

$$M \frac{\partial^2 x}{\partial t^2} + C \frac{\partial x}{\partial t} + K(\omega) x = 0, \qquad t \in [0, \infty), \tag{7.2}$$

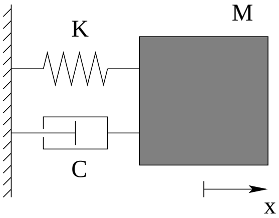

Figure 7.3: The mass-spring-damper system.

with mass $M = 1$, damping parameter $C = 0.03$, position of the mass $x(t, \omega)$, and initial conditions $x(0) = 1$ and $\partial x/\partial t(0) = 1$. This can be a model for a more complex structure with internal damping and stiffness. The randomness in the positive spring stiffness $K(\omega)$ is given by a lognormal distribution with mean $\mu_{\mathrm{K}} = 1$ and coefficient of variation $\mathrm{cv}_{\mathrm{K}} = 10\%$. As is common in multi-element methods, the tails of the probability distribution are truncated such that the resolved parameter domain accounts for 99.8% of the realizations. The resulting 0.2% truncation error is small compared to the usual discretization and time integration errors in engineering simulations. The results below are based on the analytical solution of (7.2) evaluated at discrete time levels $t_l = l\Delta t$, with $l = 0, \ldots, N_{\mathrm{t}}$, $N_{\mathrm{t}} = t_{\max}/\Delta t$, $t_{\max} = 100$, and $\Delta t = 0.01$, to be able to analyze the parameterization error $\varepsilon_k(t)$ as for problems solved by numerical time integration. The considered time interval corresponds to approximately 16 cycles of the decaying oscillation for the deterministic case with $K = \mu_{\mathrm{K}}$.

7.3.1.2 Parameterization error eliminated

The initial UASFE-cp approximation of the effect of random spring stiffness $K(\omega)$ on the position of the mass $x(t, \omega)$ is constructed on a coarse grid in probability space with $N_{\mathrm{e_{ini}}} = 1$ element and $N_{\mathrm{s_{ini}}} = 3$ samples. The $N_{\mathrm{s_{ini}}} = 3$ initial samples for varying spring stiffness are shown as function of time in Figure 7.4a. The realizations $x_k(t)$ for $k = 1, \ldots, N_{\mathrm{s_{ini}}}$ are decaying oscillations due to the moderate positive value of damping parameter C. The random $K(\omega)$ affects the frequency and the amplitude of the samples. The differences in frequency result in increasing phase differences in time starting from the deterministic initial condition as shown in Figure 7.4b for the phase of the samples $\phi_k(t)$ in radians. Plotting the samples $x_k^*(\phi_k)$ as function of their phase $\phi_k(t)$ as in Figure 7.4c reveals that the effect of $K(\omega)$ on the samples is much more regular as function of their phase ϕ_k than as function of time t. This illustrates the effectiveness of interpolating the samples at constant phase to eliminate the effect

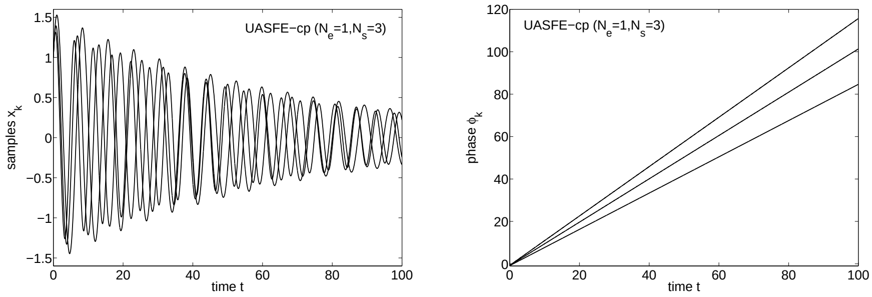

(a) samples $x_k(t)$ (b) phase $\phi_k(t)$

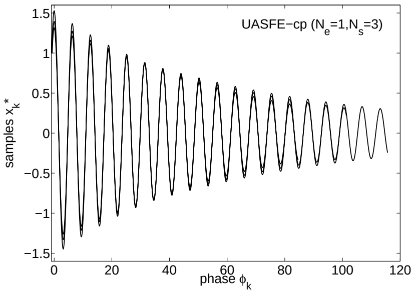

(c) samples $x_k^*(\phi_k)$

Figure 7.4: The initial $N_{\mathrm{s_{ini}}} = 3$ samples of UASFE-cp with $N_{\mathrm{e_{ini}}} = 1$ element for the mass-spring-damper system.

of increasing phase differences.

The UASFE interpolation at constant phase is constructed by first interpolating the phase of the samples $\phi_k(t)$ to the function $\phi(t, \omega)$ in terms of $K(\omega)$ at a certain time t. Consider, for example, the phase of the $N_{\mathrm{s_{ini}}} = 3$ samples at $t = 70$ given by the dots in Figure 7.5a. The ASFE interpolation of the sample values $\phi_k(t)$ gives then at, for example, $K = 0.9$ a phase of $\tilde{\phi} = 65.5$. The corresponding position of the mass x at $\tilde{\phi} = 65.5$ is found by using ASFE interpolation of the samples $x_k^*(\tilde{\phi})$ at constant phase $\tilde{\phi} = 65.5$. Figure 7.5b shows that for $K = 0.9$ this interpolation predicts a position of $x = -0.461$. Repeating these two interpolations for all $K(\omega) \in A$ results in an approximation of the response surface of the position $x(t, \omega)$ as function of $K(\omega)$ at $t = 70$, see Figure 7.5c. The highly oscillatory response surface which is resolved using only $N_{\mathrm{s}_{\mathrm{ini}}} = 3$ samples matches the one predicted by a Monte Carlo simulation with $N_{\mathrm{s}} = 1000$ samples. Applying the quadratic ASFE interpolation at constant time directly in Figure 7.5c would obviously give a much larger interpolation error. The mean, standard deviation, and higher statistical moments of $x(t, \omega)$ can be determined by integrating over the approximation of the response surface. By repeating this procedure for all $t \in [0, t_{\max}]$ the time evolution of the mean $\mu_{\mathrm{x}}(t)$ and standard deviation $\sigma_{\mathrm{x}}(t)$ can be determined.

The results for the mean $\mu_{\mathrm{x}}(t)$ and the standard deviation $\sigma_{\mathrm{x}}(t)$ for $N_{\mathrm{e}} = 4$ elements and $N_{\mathrm{s}} = 9$ samples shown in Figure 7.6 are converged up to $\delta_{N_{\mathrm{e}}} = 1 \cdot 10^{-3}$. The mean $\mu_{\mathrm{x}}(t)$ is a decaying oscillation to zero due to damping C and the effect of the random $K(\omega)$ on the increasing phase differences with time. The importance of taking the random parameter into account is illustrated by the standard deviation $\sigma_{\mathrm{x}}(t)$, which shows a fast oscillatory increase from the deterministic initial condition to a maximum of $\sigma_{\mathrm{x}} = 0.70$ after which it decays due to damping C.

Since each sample reaches a different minimum and maximum phase in $t \in [0, 100]$, the interpolation at constant phase is for $N_{\mathrm{e}} = 4$ limited to the time domain $t \in [0, 90.7]$. The UASFE-cp results match those of the Monte Carlo simulation up to a maximum error of $\varepsilon = 2.0 \cdot 10^{-4}$ for the discretization with $N_{\mathrm{s}} = 9$ samples compared to $N_{\mathrm{s}} = 1000$ samples in the Monte Carlo simulation.

In contrast with UASFE-cp, the accuracy of UASFE-ti is limited by parameterization error $\varepsilon_k(t)$ in constructing the time-independent parameterization of the samples $x_k(t)$. The error $\varepsilon_k(t)$ of UASFE-ti reaches for this problem a maximum of 0.091 as shown in Figure 7.7a for the $N_{\mathrm{s}_{\mathrm{ini}}} = 3$ samples of the initial grid of $N_{\mathrm{e}_{\mathrm{ini}}} = 1$ element. The parameterization error is small near $t = t_{\max}$, since the time-independent parameterization is extracted from the last completed cycle to minimize the influence of transient behavior. The parameterization error is caused by numerical inaccuracies in retrieving the time-independent functionals such as frequency and amplitude from the discrete time series solutions $x_k(t)$. These errors amplify with decreasing time. The effect of the parameterization error can be recognized in the increasing error in the mean $\mu_{\mathrm{x}}(t)$ and $\sigma_{\mathrm{x}}(t)$ with decreasing time in Figures 7.7b and 7.7c. The error reaches a maximum of $\varepsilon = 4.5 \cdot 10^{-2}$ for UASFE-ti with $N_{\mathrm{e}} = 4$ elements, which is 2 orders of magnitude larger than for UASFE-cp with the same number of elements.

The effect of the elimination of the parameterization error on the error convergence of UASFE-cp compared to UASFE-ti is illustrated in Figure 7.8 for $c = 0$ and $\partial x / \partial t(0) = 0$. UASFE-cp shows a linear error convergence rate of order 4, which is in line with the Adaptive Stochastic Finite Elements discretization based on second-degree Newton-Cotes quadrature in simplex elements developed in Chapter 4. The error convergence of UASFE-ti is limited by the parameterization error $\varepsilon_k = 0.091$.

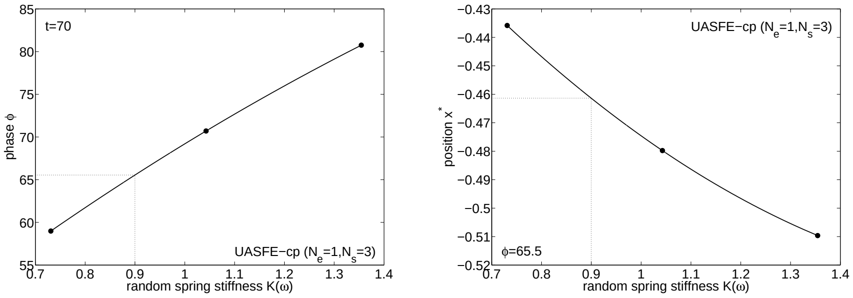

(a) phase ϕ-K at $t = 70$ (b) position x^*-K at $\phi = 65.5$

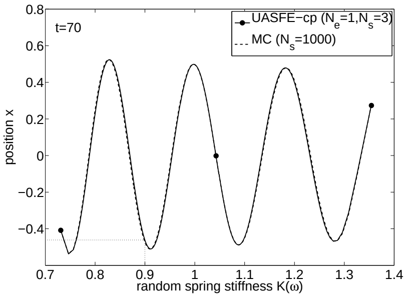

(c) position x-K at $t = 70$

Figure 7.5: UASFE-cp interpolation with $N_{\mathrm{e}_{\mathrm{ini}}} = 1$ element and $N_{\mathrm{s}_{\mathrm{ini}}} = 3$ samples compared to Monte Carlo simulation results with $N_{\mathrm{s}} = 1000$ for the mass-spring-damper system.

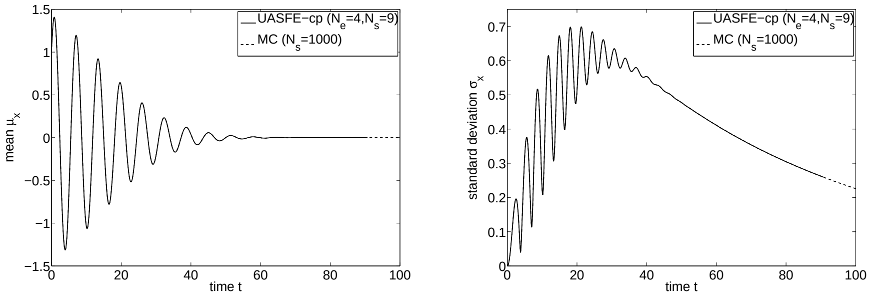

(a) mean $\mu_{\mathrm{x}}(t)$ (b) standard deviation $\sigma_{\mathrm{x}}(t)$

Figure 7.6: Results of UASFE-cp with $N_{\mathrm{e}} = 4$ elements and $N_{\mathrm{s}} = 9$ samples compared to those of Monte Carlo simulation with $N_{\mathrm{s}} = 1000$ for the mass-spring-damper system.

The elimination of the parameterization error has, therefore, a significant effect on the accuracy of the UASFE-cp formulation.

The correspondence between the maximal error ε of UASFE-cp and the convergence measure $\delta_{N_{\mathrm{e}}}$ is given in Table 7.1. The results illustrate that the definition of the convergence measure is sufficiently robust to control the error in this example, since ε is for all refinements smaller than $\delta_{N_{\mathrm{e}}}$. Our experience is that, in general, the maximal error ε is of the same order or smaller than convergence criterion $\delta_{N_{\mathrm{e}}}$. The table also contains the time interval in which the UASFE-cp approximation can be constructed. This time interval approaches $[0, t_{\max}]$ as the number of elements N_{e} increases.

7.3.2 Damped nonlinear Duffing oscillator

A model for a damped oscillator with nonlinear structural stiffness is the damped Duffing equation given in section 7.3.2.1. The response of the damped nonlinear Duffing oscillator cannot be represented by the time-independent parameterization of UASFE-ti. In section 7.3.2.2 it is studied how this affects the comparison of the results of UASFE-cp and UASFE-ti for random initial condition $x_0(\omega)$. The effect of randomness in both initial condition $x_0(\omega)$ and damping parameter $\delta(\omega)$ is considered is section 7.3.2.3.

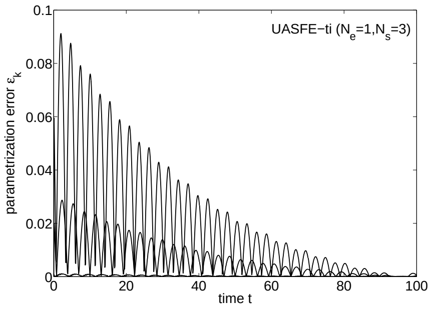

(a) UASFE-ti parameterization error $\varepsilon_k(t)$

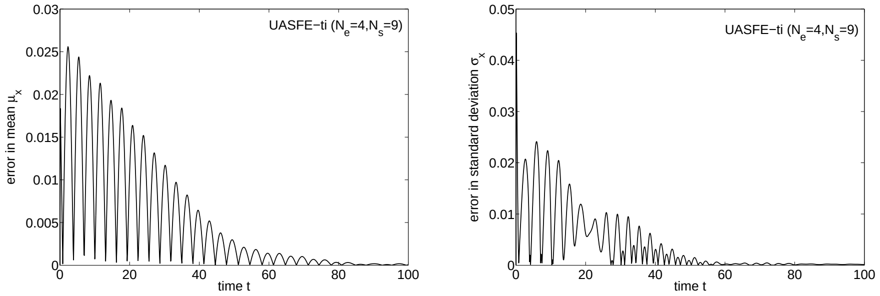

(b) error in mean $\mu_{\mathrm{x}}(t)$

(c) error in standard deviation $\sigma_{\mathrm{x}}(t)$

Figure 7.7: Results of UASFE-ti with $N_{\mathrm{e_{ini}}} = 1$ elements and $N_{\mathrm{s_{ini}}} = 3$ samples, and $N_{\mathrm{e}} = 4$ and $N_{\mathrm{s}} = 9$ for the mass-spring-damper system.

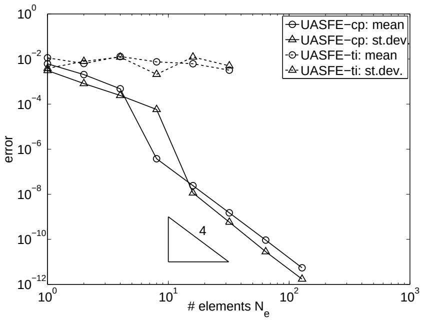

Figure 7.8: Error convergence of UASFE-cp and UASFE-ti for the mass-spring-damper system.

Table 7.1: Convergence measure δ_{N_e}, maximal error ε in the approximation of the mean $\mu_\mathrm{x}(t)$ and standard deviation $\sigma_\mathrm{x}(t)$, and approximation time interval of UASFE-cp as function of the number of elements N_e and number of samples N_s for the mass-spring-damper system.

N_e	N_s	μ_x		σ_x		time interval
		δ_{N_e}	ε	δ_{N_e}	ε	
1	3	-	$5.70 \cdot 10^{-3}$	-	$6.43 \cdot 10^{-3}$	$[0.2; 73.3]$
2	5	$6.43 \cdot 10^{-3}$	$1.17 \cdot 10^{-3}$	$6.59 \cdot 10^{-3}$	$9.52 \cdot 10^{-4}$	$[0; 83.6]$
4	9	$1.18 \cdot 10^{-3}$	$1.53 \cdot 10^{-4}$	$9.55 \cdot 10^{-4}$	$1.99 \cdot 10^{-4}$	$[0; 90.7]$
8	17	$1.53 \cdot 10^{-4}$	$1.20 \cdot 10^{-5}$	$1.99 \cdot 10^{-4}$	$3.34 \cdot 10^{-5}$	$[0; 95.0]$

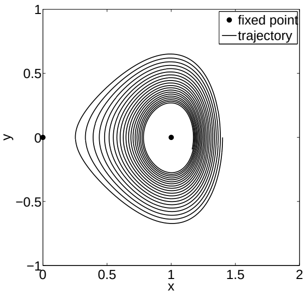

Figure 7.9: Phase diagram of the damped Duffing oscillator with the trajectory for initial condition $x_0 = 1.4$.

7.3.2.1 Duffing equation

The nonlinear Duffing oscillator is governed by the following system of differential equations:

$$\frac{\partial x}{\partial t} = y, \tag{7.3}$$

$$\frac{\partial y}{\partial t} = \omega_0^2 x - \beta x^3 - \delta y + \gamma \cos(\omega_\gamma t + \phi), \tag{7.4}$$

for $t \in [0, \infty)$ with linear natural frequency $\omega_0 = 1$, damping $\delta = 0.02$, forcing amplitude $\gamma = 0$, and initial conditions $x(0) = x_0(\omega)$ and $y(0) = 0$. The structural nonlinearity is modeled as a hard spring by a cubic nonlinear spring stiffness parameter $\beta = 1$. Structural stiffness behaves as a cubic hard spring in, for example, the torsional direction of wing structures [113]. Initial condition $x_0(\omega)$ is assumed to be random with a uniform distribution $U(1.3; 1.4)$, which corresponds to a standard deviation of $\sigma_{\mathrm{x}_0} = 0.029$. For this parameter setting the trajectories are damped oscillations around the fixed point $(x, y) = (1, 0)$, see Figure 7.9 for part of the trajectory for initial condition $x_0 = 1.4$. Due to the nonlinearity of the system, the shape of the trajectory changes as it approaches the fixed point. This change of shape is not captured by the time-independent parameterization of UASFE-ti. The system (7.3) and (7.4) is solved numerically up to $t_{\max} = 100$ using fourth-order explicit Runge-Kutta time integration with a time step of $t = 0.01$. Only the results for $x(t, \omega)$ are shown as those for $y(t, \omega)$ lead to the same observations.

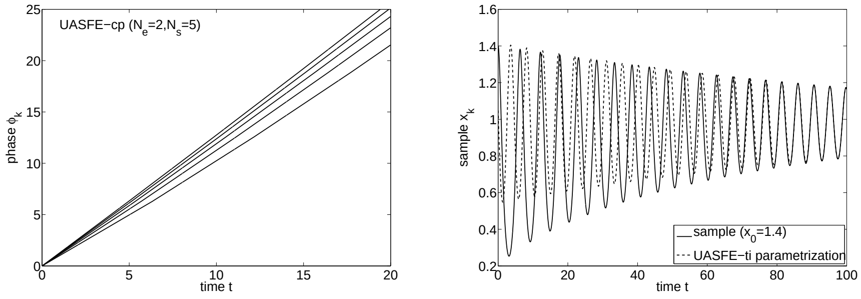

(a) phase $\phi_k(t)$

(b) sample $x_k(t)$

Figure 7.10: Results of UASFE-cp with $N_\mathrm{e} = 2$ elements and $N_\mathrm{s} = 5$ samples, and UASFE-ti parameterization of the sample for $x_0 = 1.4$ for the damped Duffing oscillator with random initial condition $x_0(\omega)$.

7.3.2.2 Time-dependent functionals resolved

When the phase $\phi_k(t)$ of the samples $x_k(t)$ is plotted against time for $t \in [0, 20]$ the result of Figure 7.10a is obtained for UASFE-cp with $N_\mathrm{e} = 2$ elements and $N_\mathrm{s} = 5$ samples. The phase $\phi_k(t)$ is a slightly curved function of time, which indicates that the frequency of the response is a function of time. The time-independent description of the samples of UASFE-ti in terms of a constant frequency and shape function is not able to parameterize the samples $x_k(t)$ as shown in Figure 7.10b for $x_0 = 1.4$. The UASFE-ti parameterization captures the sample close to $t = t_\mathrm{max}$, since the time-independent parameterization is based on the last complete cycle, but it is unable to match the sample in the whole time domain.

Since the UASFE-ti parameterization is unable to model the samples $x_k(t)$, one cannot expect UASFE-ti to resolve the correct behavior of the mean $\mu_\mathrm{x}(t)$ and standard deviation $\sigma_\mathrm{x}(t)$ as demonstrated in Figure 7.11. The UASFE-cp solution for $N_\mathrm{e} = 4$ elements and $N_\mathrm{s} = 9$ samples has converged up to $\delta_{N_\mathrm{e}} = 1 \cdot 10^{-2}$ and matches the Monte Carlo results with $N_\mathrm{s} = 1000$ samples up to a maximum error of $\varepsilon = 7.3 \cdot 10^{-4}$. The mean $\mu_\mathrm{x}(t)$ is initially a fast decaying oscillation for $t \in [0, 40]$ and later a slower decaying oscillation towards the fixed point $x = 1$. The standard deviation $\sigma_\mathrm{x}(t)$ shows a more irregular oscillatory behavior from the random initial condition $x_0(\omega)$ with standard deviation $\sigma_{\mathrm{x}_0} = 0.029$ at $t = 0$ to a maximum of $\sigma_\mathrm{x} = 0.31$ at $t = 14.8$, after which it decays due to damping δ. This corresponds to a maximal amplification

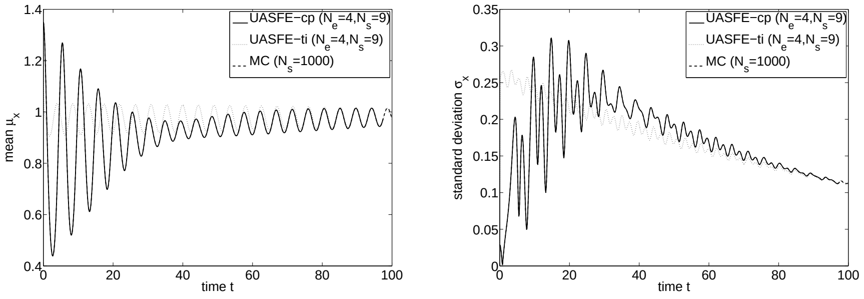

(a) mean $\mu_\mathrm{x}(t)$ (b) standard deviation $\sigma_\mathrm{x}(t)$

Figure 7.11: Results of UASFE-cp and UASFE-ti with $N_\mathrm{e} = 4$ elements and $N_\mathrm{s} = 9$ samples compared to those of Monte Carlo simulation with $N_\mathrm{s} = 1000$ for the damped Duffing oscillator with random initial condition $x_0(\omega)$.

of the initial standard deviation σ_{x_0} by a factor 10.7.

7.3.2.3 Combined randomness in initial condition $x_0(\omega)$ and damping $\delta(\omega)$

Considering next to random initial condition $x_0(\omega)$ also randomness in damping parameter $\delta(\omega)$ results in a two-dimensional probability space. The two-dimensional UASFE-cp response surface approximation of $x(\omega, t)$ as function of random parameters $x_0(\omega)$ and $\delta(\omega)$ at $t = 50$ is shown in Figure 7.12a for a UASFE-cp grid $N_\mathrm{e} = 16$ elements and $N_\mathrm{s} = 45$ samples, see Figure 7.13. The approximation is compared to that of Monte Carlo simulation based on $N_\mathrm{s} = 10^4$ samples in Figure 7.12b. The UASFE-cp results are converged up to $\delta_{N_\mathrm{e}} = 2 \cdot 10^{-2}$ and have a maximum error with respect to the Monte Carlo results of $\varepsilon = 3.1 \cdot 10^{-3}$. The response surface shows an oscillatory behavior which is not aligned with one of the axes. For low values of damping $\delta(\omega)$ the response is sensitive to variations in initial condition $x_0(\omega)$ as $x(\omega)$ alternately reaches values below 0.4 and above 1.2. As damping $\delta(\omega)$ increases the response surface gets less oscillatory and $x(\omega)$ approaches fixed point $x = 1$. UASFE-cp captures this behavior accurately while the number of samples has been reduced with two orders of magnitude compared to Monte Carlo simulation.

The resulting time histories for the mean $\mu_\mathrm{x}(t)$ and standard deviation $\sigma_\mathrm{x}(t)$ by UASFE-cp match those of Monte Carlo simulation as well, see Figure 7.14. Compared to the results of Figure 7.11 for random initial condition $x_0(\omega)$ in combination with

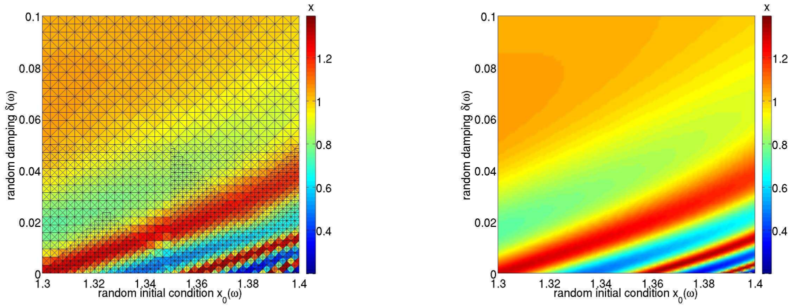

(a) UASFE-cp (b) MC

Figure 7.12: Response surface $x(\omega, t)$ at $t = 50$ as function of random initial condition $x_0(\omega)$ and damping $\delta(\omega)$ by UASFE-cp with $N_\mathrm{e} = 16$ elements, $N_\mathrm{s} = 45$ samples, and $N_{\mathrm{e}_\mathrm{sub}} = 4^4$ post-processing subelements compared to Monte Carlo simulation with $N_\mathrm{s} = 10^4$ for the damped Duffing oscillator.

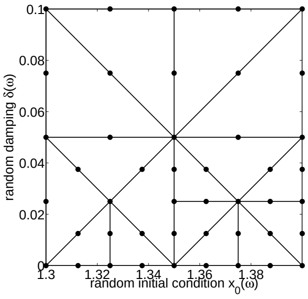
0.1
0.08
0.06
0.04
0.02
0
random damping δ(ω)
1.3
1.32
1.34
1.36
1.38
random initial condition x0(ω)

Figure 7.13: UASFE-cp grid in two-dimensional parameter space $x_0(\omega)$–$\delta(\omega)$ with $N_\mathrm{e} = 16$ elements and $N_\mathrm{s} = 45$ samples given by the dots for the damped Duffing oscillator.

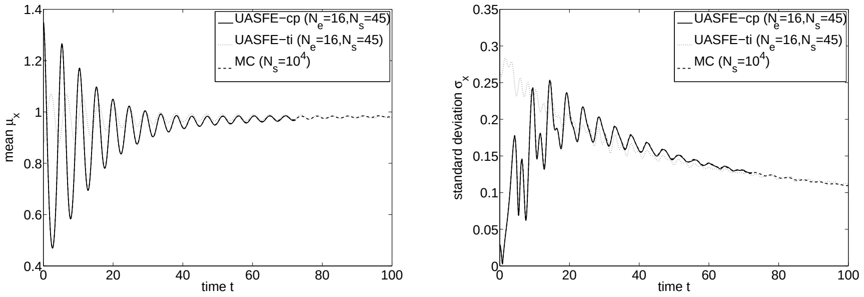

(a) mean $\mu_\mathrm{x}(t)$ (b) standard deviation $\sigma_\mathrm{x}(t)$

Figure 7.14: Results of UASFE-cp and UASFE-ti with $N_\mathrm{e} = 16$ elements and $N_\mathrm{s} = 45$ samples compared to those of Monte Carlo simulation with $N_\mathrm{s} = 10^4$ for the damped Duffing oscillator with random initial condition $x_0(\omega)$ and damping $\delta(\omega)$.

deterministic damping parameter $\delta = 0.02$, the oscillations in the mean $\mu_\mathrm{x}(t)$ decay faster with time, see Figure 7.14a. This is caused by the higher mean value of the random damping parameter $\mu_\delta = 0.05$ than its deterministic value. A similar effect can be observed in the time history of the standard deviation $\sigma_\mathrm{x}(t)$, which reaches a maximum of $\sigma_\mathrm{x} = 0.25$ at $t = 14.5$ compared to $\sigma_\mathrm{x} = 0.31$ for case with deterministic damping. This illustrates that the combined effect of multiple random parameters is not necessarily larger than that of a single parameter, especially when the mean of one of the parameters does not correspond to its deterministic value. The samples up to $t_\mathrm{max} = 100$ result in a smaller UASFE-cp approximation interval of $t \in [0; 72.4]$ than $t \in [0; 97.5]$ in the one-dimensional case due to larger phase differences between the larger number of samples in the elements. In order to obtain an approximation of the stochastic solution in a larger time domain, longer deterministic simulations can be performed up to a later t_max.

7.3.3 Stochastic bifurcation behavior of an elastically mounted airfoil

A special class of responses that cannot be represented by time-independent parameterization consists of responses with a transient part. An application of practical interest with transient behavior is the (post-)bifurcation analysis of an elastically mounted airfoil with nonlinear structural stiffness. The governing equations for a two-degree-of-freedom airfoil in an inviscid flow are outlined in section 7.3.3.1. In section 7.3.3.2 the effect of randomness in the ratio of natural frequencies $\overline{\omega}(\omega)$ at the deterministic bifurcation point is studied. The P-bifurcation behavior of the probability distribution of the system response is analyzed in section 7.3.3.3.

7.3.3.1 Governing equations

The nonlinear structural stiffness is modeled by a cubic spring stiffness term in the following two-degree-of-freedom model for coupled pitch and plunge motion of the airfoil [25]:

$$\xi'' + x_\alpha \alpha'' + \left(\frac{\bar{\omega}}{U^*}\right)^2 (\xi + \beta_\xi \xi^3) = -\frac{1}{\pi\mu} C_\mathrm{l}(\tau), \tag{7.5}$$

$$\frac{x_\alpha}{r_\alpha^2}\xi'' + \alpha'' + \frac{1}{U^{*2}}(\alpha + \beta_\alpha \alpha^3) = \frac{2}{\pi\mu r_\alpha^2} C_\mathrm{m}(\tau), \tag{7.6}$$

where $\beta_\xi = 0\text{m}^{-2}$ and $\beta_\alpha = 3\text{rad}^{-2}$ are nonlinear spring constants, $\xi(\tau) = h/b$ is the nondimensional plunge displacement of the elastic axis, see Figure 7.15a, $\alpha(\tau)$ is the pitch angle, and $(')$ denotes differentiation with respect to nondimensional time $\tau = Ut/b$, with half-chord length $b = c/2 = 0.5$m and free stream velocity $U = 103.6$m/s, which corresponds to a Mach number of $M_\infty = 0.3$ for free stream density $\rho_\infty = 0.12\text{kg/m}^3$ and pressure $p_\infty = 1.0 \cdot 10^5$Pa. The radius of gyration around the elastic axis is $r_\alpha b = 0.25$m, bifurcation parameter U^* is defined as $U^* = U/(b\omega_\alpha)$, and the airfoil-air mass ratio is $\mu = m/\pi\rho_\infty b^2 = 100$, with m the airfoil mass. The elastic axis is located at a distance $a_\mathrm{h} b = -0.25$m from the mid-chord position and the mass center is located at a distance $x_\alpha b = 0.125$m from the elastic axis. These values for the structural parameters are taken from [49]. Randomness is introduced in the ratio of natural frequencies $\overline{\omega}(\omega) = \omega_\xi/\omega_\alpha$, with ω_ξ and ω_α the natural frequencies of the airfoil in pitch and plunge, respectively. The randomness is described by a symmetric unimodal beta distribution with parameters $\beta_1 = \beta_2 = 2$ around a mean of $\mu_{\overline{\omega}} = 0.2$ in the domain $\overline{\omega}(\omega) \in [0.15; 0.25]$.

The nondimensional aerodynamic lift and moment coefficients, $C_\mathrm{l}(\tau)$ and $C_\mathrm{m}(\tau)$, are determined by solving the nonlinear Euler equations for inviscid flow [15] using a second-order finite volume scheme on an unstructured hexahedral mesh with $7.5 \cdot 10^3$ volumes in spatial domain D with dimensions $30c \times 20c$. An Arbitrary Lagrangian-Eulerian formulation is employed to couple the fluid mesh with the movement of the structure. The fluid mesh is deformed using radial basis function interpolation of the boundary displacements [9]. Time integration is performed using the BDF-2 method with stepsize $\Delta\tau = 0.4$ until $\tau_\mathrm{max} = 1000$. Initially the airfoil is at rest at a deflection of $\alpha(0) = 0.1$deg and $\xi(0) = 0$ from its equilibrium position. The initial condition

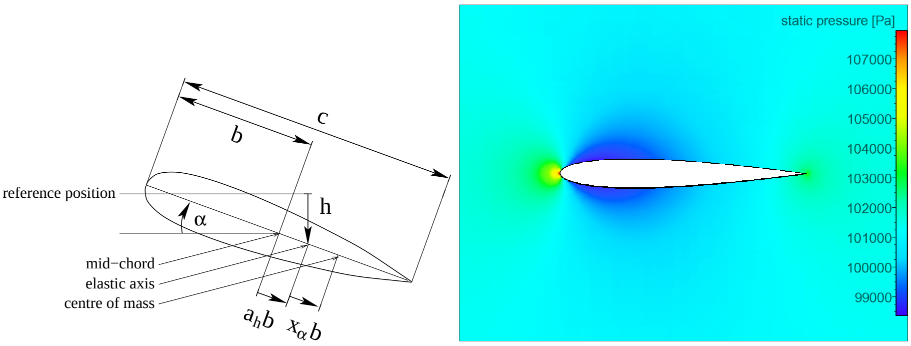

(a) structural model (b) initial flow conditions

Figure 7.15: The elastically mounted airfoil in uniform Euler flow.

of the flow field is given by the steady state solution for the initial deflection shown in Figure 7.15b in terms of the static pressure p. The output of interest is the angle of attack $\alpha(\tau, \omega)$. The plunge deflection $\xi(\tau, \omega)$ gives equivalent results.

In the deterministic case, the airfoil exhibits an oscillation which either decays to zero or diverges until it reaches a limit cycle oscillation after a transient, depending on the value of bifurcation parameter U^*. The deterministic bifurcation behavior of the system for the mean frequency ratio $\mu_{\overline{\omega}}$ is given in Figure 7.16 in terms of the amplitude A_α of pitch angle $\alpha(\tau)$ as function of normalized bifurcation parameter U^*/U_L^*. The linear flutter point U_L^* is determined numerically by a trial and error procedure for the linear system with $\beta_\alpha = 0$. The location of the flutter point $U^*/U_L^* = 1$ is not affected by the nonlinear term, since the onset of flutter is a linear phenomenon. For $U^*/U_L^* = 1$ the response is a linearly stable periodic motion of which the amplitude A_α is approximately equal to the initial condition $\alpha(0)$. The system shows a supercritical Hopf-bifurcation with zero amplitudes A_α below the flutter point for $U^*/U_L^* < 1$ and finite amplitudes A_α increasing with U^*/U_L^* for $U^*/U_L^* > 1$. In the next section the effect of randomness in $\overline{\omega}(\omega)$ on the response at the deterministic bifurcation point $U^*/U_L^* = 1$ is resolved. The stochastic system bifurcation as function of bifurcation parameter U^*/U_L^* is analyzed in section 7.3.3.3.

7.3.3.2 Transient behavior captured

The large effect of randomness in the frequency ratio $\overline{\omega}(\omega)$ on the linearly stable response in the deterministic bifurcation point is illustrated by the $N_{\mathrm{s}_{\mathrm{ini}}} = 3$ initial sam-

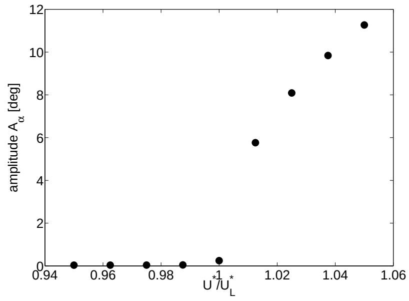

Figure 7.16: Deterministic bifurcation diagram of the elastically mounted airfoil.

ples for $\overline{\omega}_k \in \{0.15; 0.2; 0.25\}$ in Figure 7.17. Sample $\alpha_k(\tau)$ for the mean value of the frequency ratio $\mu_{\overline{\omega}} = 0.2$ is periodic with amplitude $A_\alpha \approx \alpha(0)$ as expected. Decreasing the frequency ratio to $\overline{\omega} = 0.15$ results in a qualitative change to a damped response. On the other hand, increasing $\overline{\omega}$ to 0.25 leads to the onset of unstable behavior, which a single deterministic simulation for the mean value $\mu_{\overline{\omega}}$ would have missed. The corresponding realization shows a transient diverging oscillation until $\tau = 400$ where it reaches a periodic limit cycle oscillation with a constant amplitude of $A_\alpha = 8.0$deg due the hard spring structural nonlinearity. The system, therefore, shows a supercritical Hopf bifurcation as function of $\overline{\omega}(\omega)$ as well.

The effect of the transient behavior of part of the realizations on the time histories of the mean $\mu_\alpha(\tau)$ and standard deviation $\sigma_\alpha(\tau)$ is shown in Figure 7.18 for UASFE-cp with $N_\mathrm{e} = 5$ and $N_\mathrm{e} = 10$ elements. The results are compared to those of UASFE-ti with $N_\mathrm{e} = 10$. In contrast to the other examples, in this case the mean $\mu_\alpha(\tau)$ is initially a diverging oscillation due to diverging transient oscillation of part of the realizations. For $\tau > 600$ the mean shows a decaying oscillation due to the effect of $\overline{\omega}(\omega)$ on the frequency of the response in combination with the constant limit cycle oscillation amplitude of the post-flutter realizations beyond their transient. The transient contributes also to the fast initial increase of the standard deviation $\sigma_\alpha(\tau)$ to 2.3deg at $\tau \approx 1000$, which is more than a factor 20 larger than the deterministic amplitude $A_\alpha \approx 0.1$deg of the periodic oscillation for $\mu_{\overline{\omega}}$. The successive UASFE-cp approximations for $N_\mathrm{e} = 5$ and $N_\mathrm{e} = 10$ elements display the convergence of the adaptive refinement. It has been verified that it requires $N_\mathrm{e} = 16$ elements to obtain a comparable degree of convergence using uniform grid refinement. The adaptive refinement, therefore, results here in a 36% reduction of the required number of samples from $N_\mathrm{s} = 33$ to $N_\mathrm{s} = 21$. The

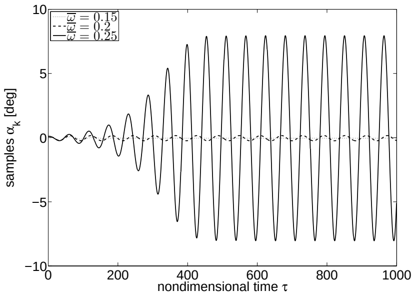

Figure 7.17: The initial $N_{\mathrm{s_{ini}}} = 3$ samples of UASFE-cp with $N_{\mathrm{e_{ini}}} = 1$ element for the elastically mounted airfoil.

UASFE-ti formulation does not predict the initial increase of $\mu_\alpha(\tau)$ and $\sigma_\alpha(\tau)$, since it is unable to model the transient behavior of the samples $\alpha_k(\tau)$. The large errors in the UASFE-ti approximation compared to the UASFE-cp results demonstrate the importance of capturing transient behavior.

7.3.3.3 Stochastic bifurcation behavior

By repeating the preceding analysis for a range of values of bifurcation parameter U^*/U_L^*, the stochastic bifurcation behavior of the system can be explored. Due to the random frequency ratio $\overline{\omega}(\omega)$, the system bifurcation can no longer be described by a single deterministic flutter point, but rather by a P-bifurcation region for the probability distribution. The response surface approximation of $\alpha(\omega)$ at $\tau = 800$ as function of $\overline{\omega}(\omega)$ for $U^*/U_L^* \in [0.95; 1.05]$ is shown in Figure 7.19. The bifurcation of the probability distribution as function of U^*/U_L^* is here the primary output of interest. The two-dimensional surface of Figure 7.19 is, therefore, constructed using one-dimensional approximations as function of $\overline{\omega}(\omega)$ at discrete steps $\Delta U^*/U_L^* = 0.0125$ given by the black lines instead of a full two-dimensional response surface approximation. A bifurcation line in the $\overline{\omega}$-U^*/U_L^* plane can clearly be identified between $(\overline{\omega}, U^*/U_L^*) = (0.25; 0.975)$ and $(\overline{\omega}, U^*/U_L^*) = (0.15; 1.025)$. For lower values of $\overline{\omega}(\omega)$ and U^*/U_L^* the response is a pre-bifurcation decaying oscillation which results at $\tau = 800$ in a pitch angle $\alpha(\omega)$ close to zero. The bifurcation region starts at $U^*/U_L^* = 0.975$ for $\overline{\omega} = 0.25$ and extends to $U^*/U_L^* = 1.025$, after which the system develops a fully oscillatory response. In the post-bifurcation domain for

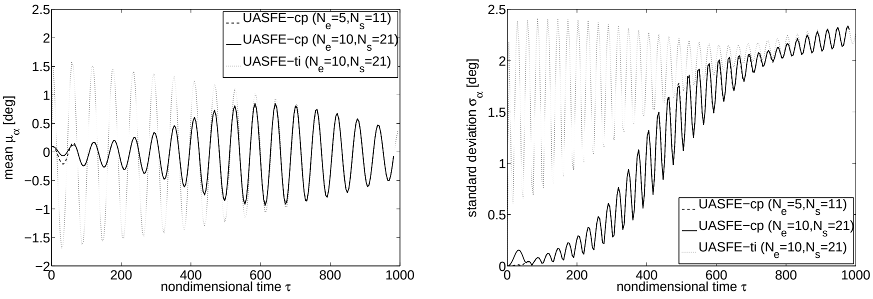

(a) mean $\mu_\alpha(\tau)$ (b) standard deviation $\sigma_\alpha(\tau)$

Figure 7.18: Results of UASFE-cp with $N_{\mathrm{e}} = 5$ elements and $N_{\mathrm{s}} = 11$ samples, and $N_{\mathrm{e}} = 10$ and $N_{\mathrm{s}} = 21$ compared to those of UASFE-ti with $N_{\mathrm{e}} = 10$ and $N_{\mathrm{s}} = 21$ for the elastically mounted airfoil with $U^*/U^*_L = 1$.

$U^*/U^*_L > 1.025$ the maximum deflection $|\alpha(\omega)|$ continues to increase with increasing U^*/U^*_L.

These results are reflected in the P-bifurcation behavior of the cumulative probability distribution function of $|\alpha(\omega)|$ at the discrete values of U^*/U^*_L and $\tau = 800$ in Figure 7.20. The cumulative distribution is shown here since it enables quantitative observations about the probability of flutter. The solutions based on two different grids with N_{e} and $\lfloor N_{\mathrm{e}}/2 \rfloor$ elements as used in the convergence criterion are shown to display the convergence of the approximations. In order to capture the stochastic bifurcation the required number of elements N_{e} is in the bifurcation region of $U^*/U^*_L \in [0.975; 1.025]$ up to 5 times larger than in the pre- or post-bifurcation domain. In the pre- as well as the post-bifurcation range a discretization with a single element is actually already sufficient.

When we define the bifurcation point as the absolute pitch angle $|\alpha(\omega)|$ which corresponds to a 50% probability of flutter at the deterministic flutter point $U^*/U^*_L = 1$ in Figure 7.20e, then we can determine the probability of flutter as function of bifurcation parameter U^*/U^*_L. The pre-bifurcation domain of $U^*/U^*_L < 0.975$ shows a 100% probability of a damped response in Figures 7.20a and 7.20b. The 3.8% probability of post-flutter behavior at $U^*/U^*_L = 0.975$ indicates the start of the P-bifurcation. The probability of flutter increases further with increasing U^*/U^*_L to 24.2% and 94.5% at $U^*/U^*_L = 0.9875$ and $U^*/U^*_L = 1.0125$, respectively. The maximal possible pitch angle $|\alpha(\omega)|$ continues to increase with U^*/U^*_L in the post-bifurcation domain for

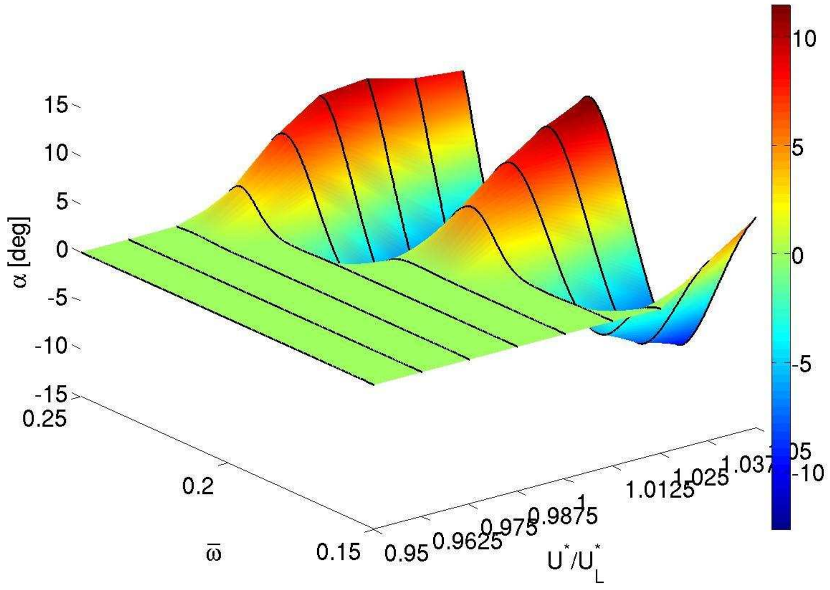

Figure 7.19: Response surface approximation of $\alpha(\omega)$ at $\tau = 800$ as function of random $\overline{\omega}(\omega)$ and bifurcation parameter U^*/U_L^* by UASFE-cp for the elastically mounted airfoil.

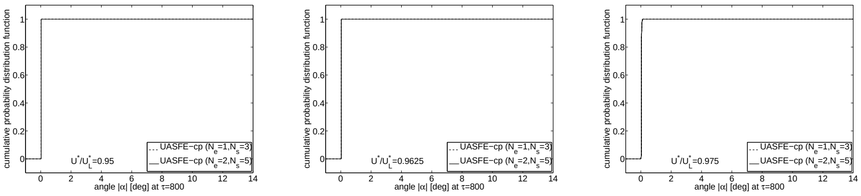

(a) $U^*/U_L^* = 0.95$ (b) $U^*/U_L^* = 0.9625$ (c) $U^*/U_L^* = 0.975$

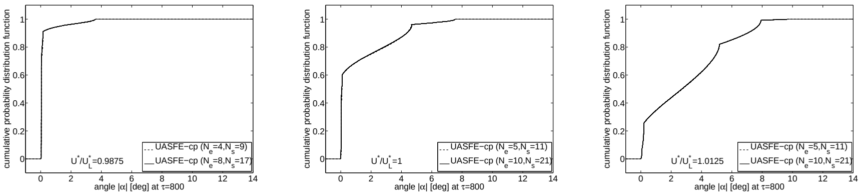

(d) $U^*/U_L^* = 0.9875$ (e) $U^*/U_L^* = 1$ (f) $U^*/U_L^* = 1.0125$

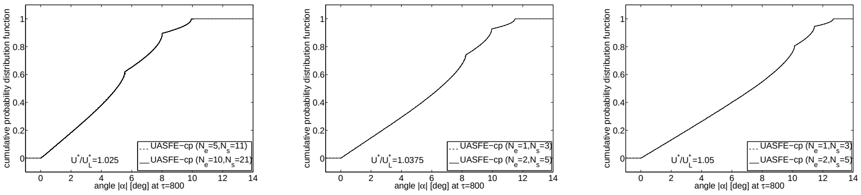

(g) $U^*/U_L^* = 1.025$ (h) $U^*/U_L^* = 1.0375$ (i) $U^*/U_L^* = 1.05$

Figure 7.20: Cumulative probability distribution of absolute pitch angle $|\alpha(\omega)|$ for $U^*/U_L^* \in [0.95; 1.05]$ at $\tau = 800$ for the elastically mounted airfoil.

$U^*/U_L^* \geq 1.025$, in which the probability of flutter is larger than 99.5%. These results indicate that based on the assumed input probability distribution the acceptance of 24.2%, 3.8%, or 0% probability of flutter would reduce the location of the stochastic bifurcation point by 1.25%, 2.5%, or 3.75% compared to its deterministic position, respectively. The availability of this quantitative probabilistic information can be utilized in practice in reducing the safety factors in actual designs.

A typical P-bifurcation can also be recognized in the evolution of the probability density of amplitude $A_\alpha(\omega)$ for increasing U^*/U_L^* at $\tau = 800$ in Figure 7.21. In the pre-bifurcation domain of $U^*/U_L^* < 0.975$ the probability density resembles a Dirac delta function at $A_\alpha = 0$. At $U^*/U_L^* = 0.9875$ the probability still has a maximum at $A_\alpha = 0$ and decays monotonically to zero for positive values of A_α. The probability density develops a local maximum at a positive amplitude $A_\alpha = 5.7$deg for $U^*/U_L^* = 1$. The local maximum increases and occurs at increasing values of A_α until it turns into the global most probable point at $U^*/U_L^* = 1.025$. In the post-bifurcation domain of $U^*/U_L^* \geq 1.025$ the unimodal probability density function allows for positive A_α values only. The increased insight into the bifurcation behavior of the elastically mounted airfoil through these detailed stochastic results demonstrates the additional value of a stochastic analysis compared to a deterministic simulation for complex physical systems.

7.4 Summary

An Unsteady Adaptive Stochastic Finite Elements formulation based on interpolation at constant phase (UASFE-cp) is developed to further improve the accuracy and extend the applicability of UASFE based on time-independent parameterization (UASFE-ti). UASFE-ti already achieves a constant accuracy in time with a constant number of samples for resolving the effect of random parameters in unsteady simulations. In addition to the constant number of samples, interpolation at constant phase (1) eliminates the parameterization error of the time-independent parameterization, which improves the convergence behavior; (2) resolves time-dependent functionals, which cannot be modeled by the parameterization; and (3) captures transient behavior of the samples, which is an important special case of time-dependent functionals. The proposed UASFE-cp approach is based on scaling sampled oscillatory time series with their phase and performing the uncertainty quantification interpolation of the samples at constant phase instead of at constant time. This eliminates the effect of increasing phase differences with time, which results for other methods usually in a fast increasing number of samples with time. UASFE-cp can be applied to problems in which the phase of the oscillatory samples is well-defined.

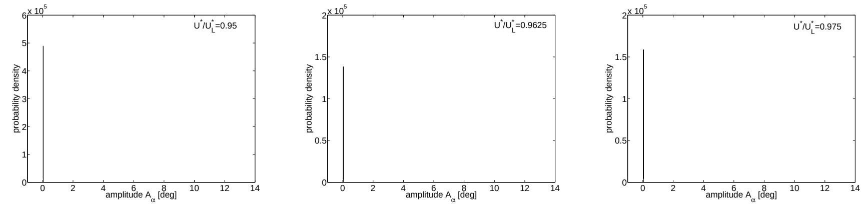

(a) $U^*/U_L^* = 0.95$ (b) $U^*/U_L^* = 0.9625$ (c) $U^*/U_L^* = 0.975$

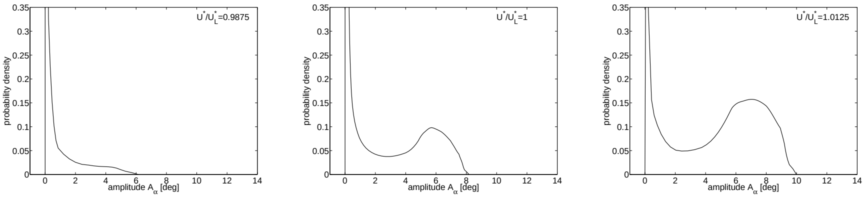

(d) $U^*/U_L^* = 0.9875$ (e) $U^*/U_L^* = 1$ (f) $U^*/U_L^* = 1.0125$

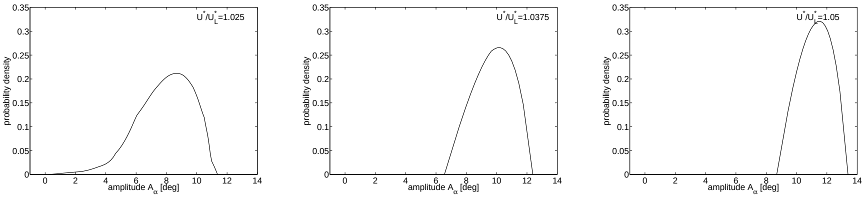

(g) $U^*/U_L^* = 1.025$ (h) $U^*/U_L^* = 1.0375$ (i) $U^*/U_L^* = 1.05$

Figure 7.21: Probability density of amplitude $A_\alpha(\omega)$ for $U^*/U_L^* \in [0.95; 1.05]$ at $\tau = 800$ for the elastically mounted airfoil.

The three points mentioned above are illustrated in applications of UASFE-cp to a mass-spring-damper system, the damped nonlinear Duffing oscillator, and an elastically mounted airfoil with nonlinear structural stiffness subject to random input parameters. Results for different types of probability distributions are compared to those of UASFE-ti and Monte Carlo simulations. For the mass-spring-damper system, UASFE-cp shows a fourth-order linear error convergence rate, while the error convergence of UASFE-ti is limited by the parameterization error. The importance of resolving the effect of random parameters in unsteady problems is illustrated by the maximum amplification of the input standard deviation by a factor 10.7 in the damped nonlinear Duffing oscillator. UASFE-cp results match those of Monte Carlo for two random input parameters in the Duffing system, while reducing the number of samples by two orders of magnitude to $N_\mathrm{s} = 45$. UASFE-ti is in this problem unable to resolve the time-independent functionals of the response of the damped nonlinear system.

The results for the elastically mounted airfoil demonstrate that randomness in the frequency ratio $\overline{\omega}(\omega)$ can leads to the onset of unstable behavior, which a single deterministic simulation for mean value $\mu_{\overline{\omega}}$ would have missed. The UASFE-ti formulation does not capture the fast initial amplification of the standard deviation $\sigma_\alpha(\tau)$ of the pitch angle $\alpha(\omega)$ caused by the transient behavior of the samples to more than a 20 times its deterministic amplitude. The adaptive refinement of UASFE-cp results, for this problem, in a 36% reduction of the required number of samples to $N_\mathrm{s} = 21$ compared to uniform grid refinement. The bifurcation of the cumulative probability distribution of the absolute pitch angle $|\alpha(\omega)|$ shows that due to the random $\overline{\omega}(\omega)$ a 2.5% reduction of the flutter boundary compared to its deterministic location still results in a 3.8% probability of flutter. A stochastic bifurcation analysis of the probability density of pitch amplitude $A_\alpha(\omega)$ reveals a typical P-bifurcation behavior from a Dirac delta function at zero amplitude to a unimodal probability density function for positive amplitudes.

Chapter 8

Unsteady Adaptive Stochastic Finite Elements for multi-frequency aeroelastic responses

The interpolation of the samples at constant phase limits the application of the UASFE formulation developed in the previous chapter to single-frequency responses of which the phase is well-defined. The fluid-structure interaction of continuous structures, however, naturally contains multiple frequencies. In this chapter, the UASFE method based on interpolation at constant phase is extended to multi-frequency responses and continuous structures by employing a wavelet decomposition pre-processing step. The effect of randomness on the multi-mode signal is then resolved by applying UASFE interpolation to the single-frequency components obtained by the wavelet decomposition. Results for multi-frequency responses and continuous structures show a 3 orders of magnitude reduction of computational costs compared to Monte Carlo simulations in a harmonically forced oscillator, a flutter panel problem, and the three-dimensional transonic AGARD 445.6 wing aeroelastic benchmark subject to random fields and random parameters with various probability distributions.

Based on: J.A.S. Witteveen, H. Bijl, Effect of randomness on multi-frequency aeroelastic responses resolved by Unsteady Adaptive Stochastic Finite Elements, J. Comput. Phys. (2009) submitted.

8.1 Introduction

In this chapter the Unsteady Adaptive Stochastic Finite Elements framework is further extended to resolve the effect of randomness on multi-frequency aeroelastic responses by employing a wavelet decomposition. The multi-frequency samples are first converted into their single-frequency components in a standard wavelet decomposition pre-processing step. The effect of the physical variations on the different frequency components is then resolved using UASFE interpolation of the single-frequency signals at constant phase. The final effect of the randomness on the multi-frequency response is obtained by summing the contributions of the single-frequency components. The multi-frequency response of a continuous structure is first projected onto either the nodal basis of a finite elements discretization or the modal basis of the natural modes of the structure in vacuum, before the wavelet decomposition is performed.

The proposed UASFE formulation for multi-frequency responses is developed in section 8.2. The effect of randomness on the multi-frequency response of a single-degree-of-freedom mass-spring system with harmonic external forcing is resolved and the error convergence is assessed in section 8.3.1. In section 8.3.2 the stochastic multi-frequency response of a continuous panel structure in supersonic flow is analyzed using a modal projection of the structural response. The three-dimensional transonic AGARD 445.6 wing subject to random free stream flow conditions is studied in section 8.3.3. A nodal representation of the continuous structure shows based on the tip-node displacement that the randomness causes a non-zero probability of flutter. The results for input random fields and random parameters with various probability distributions are compared to those of Monte Carlo simulations. This chapter is concluded in section 8.4.

8.2 Unsteady Adaptive Stochastic Finite Elements for multi-frequency responses

The wavelet decomposition of multi-frequency time series is briefly reviewed in section 8.2.1. In section 8.2.2 the procedure for multi-frequency responses of continuous structures is detailed. The UASFE interpolation of the single-frequency components is developed in section 8.2.3. The resulting UASFE algorithm for multi-frequency responses is summarized in section 8.2.4.

8.2.1 Wavelet decomposition of multi-frequency signals

Assume that dynamical system (1.1)

$$\mathcal{L}(\mathbf{x},t;u(\mathbf{x},t,\omega))=S(\mathbf{x},t), \tag{8.1}$$

results in an oscillatory response $u(\mathbf{x},t,\omega)$, which consists of multiple frequency components. The stochastic behavior of multi-frequency response $u(\mathbf{x},t,\omega)$ is resolved using UASFE by computing N_s deterministic samples $u_i(\mathbf{x},t)$ for varying parameter values $\mathbf{a}_i$, with $i=1,\dots,N_\mathrm{s}$. The multi-frequency samples $u_i(\mathbf{x},t)$ are first decomposed into their different modes using wavelets [18, 102]. The discrete wavelet transform of a signal $f(t)$ is given by

$$f(t)=\sum_a\sum_b\gamma_{a,b}\psi_{a,b}(t), \tag{8.2}$$

with wavelet transform coefficients $\gamma_{a,b}$ and wavelet

$$\psi_{a,b}(t)=\frac{1}{\sqrt{a}}\Psi\left(\frac{t-b}{a}\right), \tag{8.3}$$

scaled and translated versions of the mother wavelet $\Psi(t)$, with positive scale parameter a and real shift parameter b. The discrete wavelet transform is used here to divide the multi-frequency samples $u_i(t)$ into N_f single-frequency components $\tilde{u}_{i,k}(t)$

$$u_i(t)=\sum_{k=1}^{N_\mathrm{f}}\tilde{u}_{i,k}(t), \tag{8.4}$$

see Figure 8.1. The argument $\mathbf{x}$ has been dropped here for convenience in the notation. UASFE interpolation of the single-frequency signals $\tilde{u}_{i,k}(t)$ is then performed to resolve the effect of the randomness on the different frequency components given by the functions $\tilde{u}_k(t,\omega)$. In order to obtain an approximation of the stochastic behavior of the multi-frequency response $u(t,\omega)$ the contributions of the different frequency components are summed

$$u(t,\omega)=\sum_{k=1}^{N_\mathrm{f}}\tilde{u}_k(t,\omega), \tag{8.5}$$

from which the probability distribution and statistical moments of the output, e.g. mean $\mu_\mathrm{u}(t)$ and standard deviation $\sigma_\mathrm{u}(t)$, can be determined using sorting and numerical integration. In order to effectively decompose a multi-mode signal using wavelet

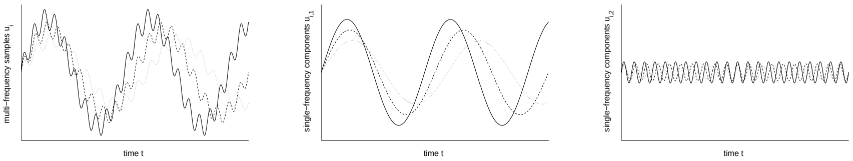

(a) samples $u_i(t)$ (b) components $\tilde{u}_{i,1}(t)$ (c) components $\tilde{u}_{i,2}(t)$

Figure 8.1: Decomposition of multi-frequency samples $u_i(t)$ into single-frequency components.

transformation, the different frequencies need to be sufficiently distinct. The wavelet decomposition is performed using the *Matlab* Wavelet Toolbox. In the applications Coifman's wavelets [16] are employed, which give the best results for the considered examples.

8.2.2 Treatment of continuous structures

Continuous structures in vacuum exhibit in general a multi-frequency response in terms of their natural modes and natural frequencies. The coupling of the structure with a flow field in a fluid-structure interaction alters the eigenmodes of the complete system. Usually the natural modes and frequencies of the coupled system are unknown due to the nonlinearity of the flow. Therefore, both a nodal and a modal description of the structural response in terms of, respectively, the degrees-of-freedom of a finite element discretization or the natural modes of the structure in vacuum result in multi-frequency signals. The nodal description results in multi-frequency responses due to the multiple natural frequencies of the system. The modal description gives rise to multi-frequency signals due to the change of the natural modes and frequencies of the system caused by the coupling with the flow.

The stochastic response of a continuous structure is analyzed by, firstly, projecting the sampled responses $u_i(t)$ onto either a nodal or modal basis, resulting in multi-frequency signals $u_{i,j}(t)$ with $j = 1, \dots, N_{\mathrm{DOF}}$ and N_{DOF} the number of degrees-of-freedom of the discretized structure. Secondly, the multi-frequency nodal or modal response signals $u_{i,j}(t)$ are decomposed into their single-frequency components $\tilde{u}_{i,j,k}(t)$, with $k = 1, \dots, N_{\mathrm{f}}$, using the wavelet analysis based on (8.2) and (8.3). UASFE interpolation is then, thirdly, performed for the single-frequency components $\tilde{u}_{i,j,k}(t)$ of the nodal or modal response to obtain $\tilde{u}_{j,k}(t,\omega)$. Finally, the UASFE results for the components $\tilde{u}_{j,k}(t,\omega)$ are summed together

$$u(t,\omega) = \sum_{j=1}^{N_{\mathrm{DOF}}} \sum_{k=1}^{N_{\mathrm{f}}} \tilde{u}_{j,k}(t,\omega), \tag{8.6}$$

to determine the stochastic response surface $u(t,\omega)$.

8.2.3 Unsteady Adaptive Stochastic Finite Elements sampling interpolation

The single-frequency signals $\tilde{u}_{i,j,k}(t)$ which result from the wavelet decomposition of multi-frequency signals $u_{i,j}(t)$ are interpolated using Unsteady Adaptive Stochastic Finite Elements (UASFE) with interpolation of the samples at constant phase developed in chapter 7. The values of the n random parameters $\mathbf{a}(\omega)$ for the N_{s} deterministic computations are selected using a non-intrusive Adaptive Stochastic Finite Elements (ASFE) method based on Newton-Cotes quadrature points in simplex elements developed in chapter 4. The ASFE formulation employs a piecewise quadratic approximation of the response surface by dividing parameter space A into N_{e} simplex elements A_l with $l = 1, \dots, N_{\mathrm{e}}$. The quadratic approximation in the elements is constructed by performing deterministic solves for the values of the random parameters $\mathbf{a}(\omega)$ that correspond to the $\binom{n+2}{2}$ second-degree Newton-Cotes quadrature points in the elements shown in the two-dimensional example of Figure 7.2a. The formulation can geometrically be extended to arbitrarily higher-dimensional parameter spaces A.

The single-frequency signals $\tilde{u}_{i,j,k}(t)$ are interpolated at constant phase by scaling them with their phase $\phi_{i,j,k}(t)$ to $\tilde{u}^*_{i,j,k}(\phi_{i,j,k}(t))$. The time series of the phases $\phi_{i,j,k}(t)$ and the scaled signals $\tilde{u}^*_{i,j,k}(\phi_{i,j,k}(t))$ are interpolated using the piecewise quadratic interpolation of ASFE to the functions $\phi_{j,k}(t,\omega)$ and $\tilde{u}^*_{j,k}(\phi_{j,k}(t,\omega),\omega)$, respectively. The result of the ASFE interpolation $\tilde{u}^*_{j,k}(\phi_{j,k}(t,\omega),\omega)$ is scaled back to a function of time $\tilde{u}_{j,k}(t,\omega)$ using $\phi_{j,k}(t,\omega)$. The approximation of the stochastic response surface $u(t,\omega)$ is finally obtained by summing the contributions of the single-frequency components $\tilde{u}_{j,k}(t,\omega)$ according to (8.6).

The phase $\phi_{i,j,k}(t)$ is extracted from the single-frequency signals using a trial-and-error procedure based on the local extrema of the time series $\tilde{u}_{i,j,k}(t)$ detailed in Chapter 7. The UASFE interpolation is restricted to the time domain that corresponds to the range of phases that is reached by all samples in each of the elements. UASFE can be applied to problems in which the phase of the single-frequency signals $\tilde{u}_{i,j,k}(t)$ is well-defined. In other cases the ASFE interpolation is applied directly to the samples $u_i(t)$.

The initial discretization of parameter space A consisting of the minimum of $N_{\mathrm{e}_{\mathrm{ini}}} = n!$ simplex elements and $N_{\mathrm{s}_{\mathrm{ini}}} = 3^n$ samples, see Figure 7.2b, is adaptively refined as illustrated in Figure 7.2c. The refinement measure ρ_l in element A_l is the total of the absolute eigenvalues of the Hessians of the quadratic approximations of $\phi_{j,k}(t,\omega)$ and $\tilde{u}^*_{j,k}(\phi_{j,k}(t,\omega),\omega)$ for $j = 1,\ldots,N_{\mathrm{DOF}}$ and $k = 1,\ldots,N_{\mathrm{f}}$ weighted by the probability contained by element A_l. The stochastic grid refinement is terminated when a convergence criterion for the approximation $\delta_{N_{\mathrm{e}}}$ of the mean $\mu_{\mathrm{u}}(t)$ and standard deviation $\sigma_{\mathrm{u}}(t)$ defined in chapter 6 is reached or when a threshold for the maximum number of samples $\bar{N}_{\mathrm{s}}$ is exceeded.

8.2.4 Algorithm summary

The resulting Unsteady Adaptive Stochastic Finite Elements algorithm for resolving the effect of random parameters on fluid-structure interaction systems with multi-frequency responses and continuous structures is listed below:

1. Compute the deterministic system responses $u_i(t)$ by solving (8.1) for the parameter values $\mathbf{a}_i$ corresponding to the quadrature points in the initial stochastic grid for $i = 1,\ldots,N_{\mathrm{s}_{\mathrm{ini}}}$;
2. Project the deterministic responses of the continuous structure onto a nodal finite element representation or onto the natural modes of the structure in vacuum, which results in the time series $u_{i,j}(t)$ with $j = 1,\ldots,N_{\mathrm{DOF}}$;
3. Decompose the multi-frequency signals $u_{i,j}(t)$ into single-frequency components $\tilde{u}_{i,j,k}(t)$ using wavelet decomposition based on Equations (8.2) and (8.3);
4. Interpolate the single-frequency time series $\tilde{u}_{i,j,k}(t)$ to the functions $\tilde{u}_{j,k}(t,\omega)$ using UASFE interpolation of the signals $\tilde{u}_{i,j,k}(t)$ at constant phase;
5. Determine the stochastic response surface $u(t,\omega)$ by summing the contributions of the single frequency components $\tilde{u}_{j,k}(t,\omega)$ according to Equation (8.6);
6. Refine the element of the stochastic grid with the largest value of refinement measure ρ_l with $l = 1,\ldots,N_{\mathrm{e}_{\mathrm{ini}}}$;
7. Repeat steps 1 to 6 for the parameter values $\mathbf{a}_i$ corresponding to the new quadrature points in the refined element with $i = N_{\mathrm{s}_{\mathrm{old}}} + 1,\ldots,N_{\mathrm{s}_{\mathrm{new}}}$;
8. Stop the adaptive stochastic grid refinement based on convergence of the mean $\mu_{\mathrm{u}}(t)$ and standard deviation $\sigma_{\mathrm{u}}(t)$, or threshold $\bar{N}_{\mathrm{s}}$ for the maximum number of samples.

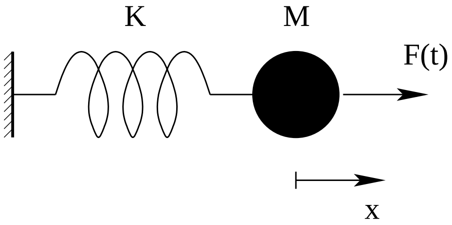

Figure 8.2: Forced mass-spring system.

For single-degree-of-freedom structural systems step 2 can obviously be omitted.

8.3 Results

The UASFE method is applied to multi-frequency signals and continuous structures in a harmonically forced oscillator in section 8.3.1, a flutter panel in section 8.3.2, and the transonic three-dimensional AGARD 445.6 wing in section 8.3.3. The results are compared to those of converged Monte Carlo simulations with evenly spaced realizations in sample space $\omega \in [0, 1]$.

8.3.1 Harmonically forced oscillator

The mass-spring system with a harmonic forcing as described in section 8.3.1.1 is a simple model problem for a structural system with aerodynamic forcing. The resulting multi-frequency response contains the forcing frequency and the natural frequency of the structure. The effect of a random spring stiffness on the multi-frequency response is resolved in section 8.3.1.2. In section 8.3.1.3 the effect of independent randomness in a combination of spring stiffness and forcing frequency is studied.

8.3.1.1 Forced mass-spring system

The forced mass-spring system of Figure 8.2 is governed by

$$M\frac{\partial^2 x}{\partial t^2} + K(\omega)x = A_{\mathrm{F}} \sin \omega_{\mathrm{F}}(\omega)t, \qquad t \in [0, \infty), \tag{8.7}$$

with initial conditions $x(0) = 0$ and $\partial x/\partial t(0) = 0$ for the position and velocity of mass $M = 1$, and forcing amplitude $A_{\mathrm{F}} = 1$. Randomness is assumed in the positive parameters spring stiffness $K(\omega)$ and forcing frequency $\omega_\mathrm{F}(\omega)$ given by truncated lognormal distributions with mean values $\mu_\mathrm{K} = 1$ and $\mu_{\omega_\mathrm{F}} = 5$ and coefficients of variation of 10%. The forcing frequency ω_F has been chosen here to differ sufficiently from the structural eigenfrequency for the mean structural stiffness $\sqrt{\mu_\mathrm{K}/M} = 1$ for the wavelet decomposition to be effective. The tails of the probability distribution are truncated such that the resolved parameter domain accounts for 99.8% of the realizations as is common for multi-element methods. The resulting 0.2% truncation error is small compared to the usual discretization and time integration errors in engineering simulations. The $N_\mathrm{f} = 2$ frequencies in the time evolution of $x(t,\omega)$ can clearly be recognized in the analytical solution of (8.7)

$$x(t,\omega) = \frac{A_\mathrm{F}}{K(\omega) - M\omega_\mathrm{F}(\omega)^2}\left(\sin \omega_\mathrm{F}(\omega)t - \frac{\omega_\mathrm{F}(\omega)}{\sqrt{K(\omega)/M}} \sin \sqrt{\frac{K(\omega)}{M}}t\right). \quad (8.8)$$

The frequency of the first sinusoidal term equals the forcing frequency ω_F and the second term is governed by the natural frequency of the structure $\sqrt{K(\omega)/M}$. Analytical solution (8.8) is evaluated at discrete time levels $t_m = m\Delta t$, with $m = 0,\ldots,N_\mathrm{t}$, $N_\mathrm{t} = t_\mathrm{max}/\Delta t$, and $\Delta t = 0.01$ for the results to be comparable with those of problems solved by numerical time integration. The samples are computed until $t_\mathrm{max} = 100$ to determine the stochastic solution until $t = 50$. The considered time interval corresponds to approximately 80 and 16 periods for the mean harmonic forcing frequency μ_{ω_F} and the structural eigenfrequency for the mean value of the stiffness μ_K, respectively.

8.3.1.2 Multi-frequency response resolved

First randomness is assumed in the spring-stiffness $K(\omega)$ in combination with the mean value of the forcing frequency μ_{ω_F}. According to analytical solution (8.8), $K(\omega)$ influences the frequency and amplitude of the second sinusoidal term originating from the eigenmotion of the structure. The randomness has no effect on the frequency and only a small effect on the amplitude of the term induced by the forcing. These observations are illustrated by the $N_\mathrm{s} = 3$ samples of the initial UASFE discretization of probability space with $N_\mathrm{e} = 1$ element for $t = [0, 20]$ in Figure 8.3a. The multi-frequency responses consist of a varying large amplitude and low frequency eigenmotion superimposed with a small amplitude and constant forcing frequency signal. It is essential to decompose these multi-frequency signals into single-frequency components, since the phase of the samples is determined by the UASFE algorithm by identifying periods of oscillation based on the continuation of the signal after a local maximum.

The separate frequency components can be recognized in the level 7 wavelet decomposition of the samples $x_i(t)$ into two single-frequency signals $\tilde{x}_{i,k}(t)$ shown in

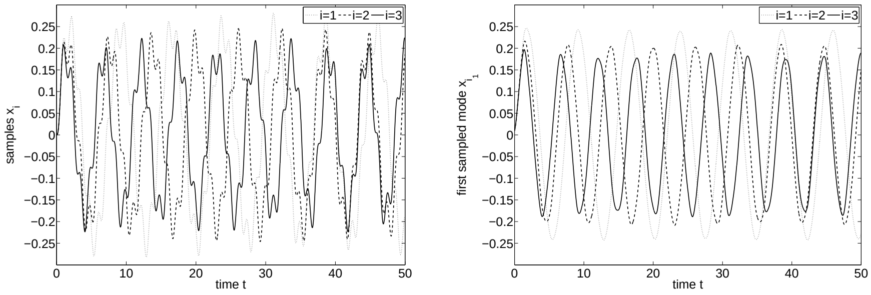

(a) samples $x_i(t)$ (b) decomposed samples $\tilde{x}_{i,1}(t)$

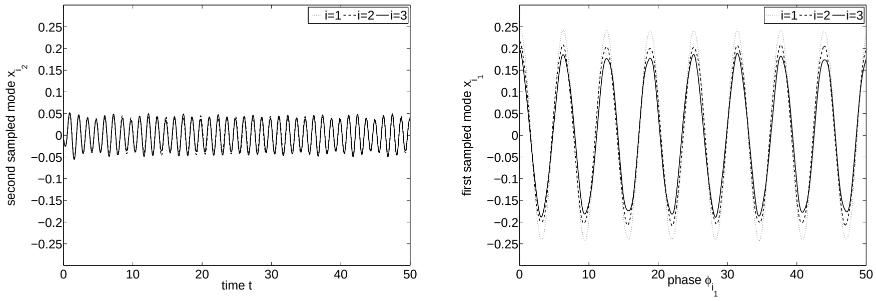

(c) decomposed samples $\tilde{x}_{i,2}(t)$ (d) decomposed samples $\tilde{x}^*_{i,1}(\phi_{i,1})$

Figure 8.3: The $N_\mathrm{s} = 3$ samples of UASFE with $N_\mathrm{e} = 1$ element for the harmonically forced oscillator with random $K(\omega)$.

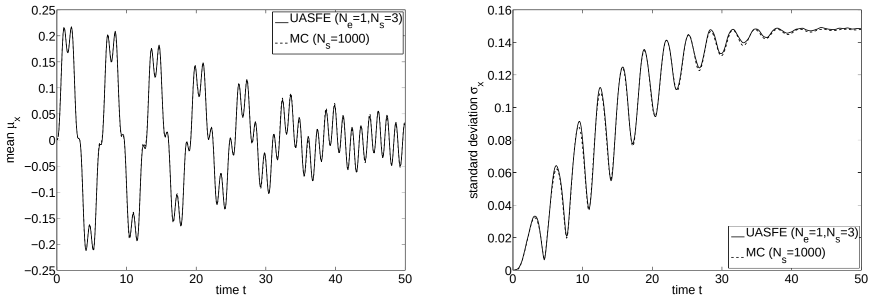

(a) mean $\mu_{\mathrm{x}}(t)$ (b) standard deviation $\sigma_{\mathrm{x}}(t)$

Figure 8.4: Results for the harmonically forced oscillator with random $K(\omega)$.

Figures 8.3b and 8.3c. It can be seen that the wavelet decomposition does not exactly reconstruct the single-frequency components as periodic sinusoidal functions. This results in a slightly different decomposition of each sample, which can affect the convergence behavior of the method. These effects decrease as the difference between the frequencies increases. The UASFE interpolation of the samples is performed at constant phase ϕ after extracting the phase as function of time $\phi_{i,k}(t)$ from the single-frequency signals $\tilde{x}_{i,k}(t)$. In Figure 8.3d the single-frequency signals as function of their phase $\tilde{x}^*_{i,k}(\phi_{i,1})$ are shown for $j = 1$. It can be observed that scaling the signals $\tilde{x}_{i,k}(t)$ with their phase $\phi_{i,k}(t)$ eliminates the effect of the increasing phase differences with time, which results in the time-independent accuracy of UASFE. For $j = 2$ the plot of the single-frequency signals in terms of their phase $\tilde{x}^*_{i,2}(\phi_{i,2})$ resembles that of the time histories $\tilde{x}_{i,2}(t)$ of Figure 8.3c, since their frequency is not affected by the randomness in $K(\omega)$.

Combining the UASFE interpolations of the decomposed single-frequency components $\tilde{x}_k(t,\omega)$ according to (8.5) results in the approximation of the mean $\mu_{\mathrm{x}}(t)$ and standard deviation $\sigma_{\mathrm{x}}(t)$ given in Figure 8.4 for $N_{\mathrm{e}} = 1$ and $N_{\mathrm{s}} = 3$. The results match those of a converged Monte Carlo simulation with $N_{\mathrm{s}} = 1000$ samples up to a maximum error of $\varepsilon = 3.4 \cdot 10^{-2}$, while reducing the computational costs in terms of the number of deterministic solves by 3 orders of magnitude.

In the time history of the mean $\mu_{\mathrm{x}}(t)$ the two frequency components are clearly present in terms of a decaying low frequency oscillation superimposed by a high frequency periodic oscillation. The low-frequency component with approximately the natural frequency of the structure decays due the effect of $K(\omega)$ on the frequency and

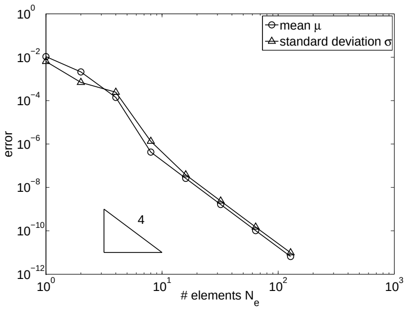

Figure 8.5: UASFE error convergence for the harmonically forced oscillator with random $K(\omega)$.

the increasing phase differences between the low-frequency components of the samples $\tilde{x}_{i,1}(t)$. The high-frequency forcing component of $\mu_{\mathrm{x}}(t)$ does not decay with time, since the forcing frequency is unaffected by $K(\omega)$. The mean of this stochastic multi-frequency response does, therefore, not reach an asymptotically steady value, in contrast with single-frequency periodic responses subject to a random frequency.

The standard deviation $\sigma_{\mathrm{x}}(t)$ shows, on the other hand, the typical behavior of single-frequency signal with a random frequency and deterministic initial condition. The initially oscillatory increase to a steady asymptotic value of $\sigma_{\mathrm{x}} = 0.148$ originates from the effect of $K(\omega)$ on the frequency and amplitude of the eigenmotion component of the response $\tilde{x}_{i,1}(t)$. The forcing component $\tilde{x}_{i,1}(t)$ does not significantly contribute to $\sigma_{\mathrm{x}}(t)$, since $K(\omega)$ has only a small effect on the amplitude on the forcing mode.

In Figure 8.5 the error convergence of UASFE based on the components of analytical solution (8.8) is given. The relative maximum error in the mean $\mu_{\mathrm{x}}(t)$ and standard deviation $\sigma_{\mathrm{x}}(t)$ with respect to the Monte Carlo reference solution are shown. The UASFE discretization maintains asymptotically a fourth-order error convergence also for multi-frequency responses, which is in accordance with the underlying Adaptive Stochastic Finite Elements method based on second-degree Newton-Cotes quadrature of Chapter 4.

8.3.1.3 Combination of randomness in structure and forcing

Randomness in an independent combination of spring stiffness $K(\omega)$ and forcing frequency $\omega_{\mathrm{F}}(\omega)$ results in a qualitatively different stochastic solution. The UASFE ap-

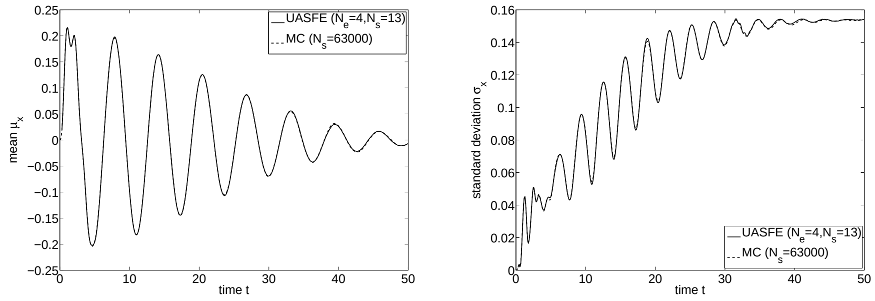

(a) mean $\mu_{\mathrm{x}}(t)$ (b) standard deviation $\sigma_{\mathrm{x}}(t)$

Figure 8.6: Results for the harmonically forced oscillator with random $K(\omega)$ and $\omega_{\mathrm{F}}(\omega)$.

proximation of the mean $\mu_{\mathrm{x}}(t)$ and standard deviation $\sigma_{\mathrm{x}}(t)$ for $N_{\mathrm{e}} = 4$ elements and $N_{\mathrm{s}} = 13$ given in Figure 8.6 is converged up to $\delta_{N_{\mathrm{e}}} = 5 \cdot 10^{-2}$. The comparison with a converged Monte Carlo result based on $N_{\mathrm{s}} = 6.3 \cdot 10^4$ samples shows that UASFE leads to a maximum error of $\varepsilon = 1.5 \cdot 10^{-2}$ while achieving a reduction of samples by 3 orders of magnitude. The large sample size required by the Monte Carlo method to converge illustrates the complexity of this multi-scale stochastic example. The mean $\mu_{\mathrm{x}}(t)$ shows for this case a decaying oscillation to zero due to the effect of $K(\omega)$ and $\omega_{\mathrm{F}}(\omega)$ on the frequency of both modes $\tilde{x}_{i,1}(t)$ and $\tilde{x}_{i,2}(t)$. The contribution of the high frequency component $\tilde{x}_{i,2}(t)$ to $\mu_{\mathrm{x}}(t)$ decays fast and can only be identified for $t < 5$. The standard deviation $\sigma_{\mathrm{x}}(t)$ shows a more complex initial behavior due to the additional randomness in $\omega_{\mathrm{F}}(\omega)$. For $t > 5$ the standard deviation $\sigma_{\mathrm{x}}(t)$ is slightly higher compared to the results for deterministic forcing with an asymptotic value of $\sigma_{\mathrm{x}} = 0.154$.

8.3.2 Flutter panel

The two-dimensional panel problem is a relatively simple example of a continuous structure which exhibits a multi-frequency response as a result of aerodynamic loads [51]. A modal representation of the response of the panel problem described in section 8.3.2.1 is used here in terms of the eigenmodes of the structure. The effect of randomness in the panel density on the energy of the structure is analyzed in section 8.3.2.2. In section 8.3.2.3 a random field for the modulus of elasticity of the plate

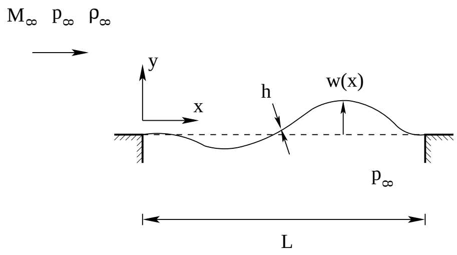

Figure 8.7: Two-dimensional flutter panel problem.

is considered.

8.3.2.1 Panel problem

The dynamical behavior of a fully clamped plate subject to a supersonic flow sketched in Figure 8.7 is a standard test problem in aeroelasticity [21, 100]. The material of the plate with length $L = 1\text{m}$ has a Poisson ratio of $\nu_\mathrm{p} = 0.35$. The air flow with unperturbed density $\rho_\infty = 1.225\text{kg/m}^3$ and pressure $p_\infty = 1.0 \cdot 10^5\text{Pa}$ has a free stream Mach number of $M_\infty = 2.5$ and ratio of specific heats $\gamma = 1.4$. The effect of randomness in the density ρ_p and the modulus of elasticity $E_\mathrm{p}(x,\omega)$ of the plate is considered. Parametric randomness is assumed in the plate density ρ_p given by a uniform distribution around mean $\mu_{\rho_\mathrm{p}} = 2700\text{kg/m}^3$ with coefficient of variation $\mathrm{cv}_{\rho_\mathrm{p}}$ of 10%. The randomness in the modulus of elasticity of the plate $E_\mathrm{p}(x,\omega)$ is described in terms of a random field with local mean $\mu_\mathrm{E} = 70 \cdot 10^9\text{Pa}$ and local coefficient of variation of 0.1% for the linear physical modeling to remain valid. The spatial correlation is given by the exponential covariance function

$$C(x_1, x_2) = \mathrm{e}^{-\frac{|x_1 - x_2|}{L_\mathrm{c}}}, \tag{8.9}$$

with correlation length $L_\mathrm{c} = L$. The thickness of the plate $h = 4.38 \cdot 10^{-3}\text{m}$ is chosen such that it corresponds to the deterministic flutter point.

The equations of motion of the plate are discretized by a finite element discretization with 3 spatial elements with Hermitian basis functions for the nodal displacements and rotations. Piston theory is used to determine the aerodynamic pressure $p_\mathrm{u}(x,t)$ on the upper side of the panel

$$p_\mathrm{u}(x,t) = \rho_\infty c_\infty \left(\frac{\partial w}{\partial t} + V_\infty \frac{\partial w}{\partial x} \right), \tag{8.10}$$

with vertical plate displacement $w(x, t, \omega)$, and free stream speed of sound c_∞ and velocity V_∞. First-order relation (8.10) is a valid approximation for supersonic flow with Mach numbers from 2 to 5 [21]. The discretization of the flow and the structure results in a matrix equation governing the coupled aeroelastic system

$$M\frac{\partial^2 u}{\partial t^2} + D\frac{\partial u}{\partial t} + Ku = 0, \tag{8.11}$$

with $u(t, \omega)$ the nodal degrees of freedom of the structure, structural mass matrix M, aerodynamic damping matrix D, and stiffness matrix K with a symmetric and asymmetric contribution of the structure and the flow, respectively. The random field for the modulus of elasticity $E_\mathrm{p}(x, \omega)$ is discretized in terms of a finite number of random parameters using a Karhunen-Loève (KL) expansion [52] truncated after the second term. Time marching is performed until $t = 0.5$ using a second-order implicit time integration scheme with a time step of $\Delta t = 1 \cdot 10^{-4}$.

Since the aerodynamic forces are modeled here using linear piston theory, the eigenfrequencies and eigenmodes of the coupled fluid-structure system can, in principle, be determined. However, this example is used here as a test problem for an aeroelastic system with, in general, nonlinear aerodynamics. It is, therefore, assumed in the stochastic analysis that only the eigenmodes of the linear structure in vacuum are known. The motion of the structure is here described in terms of the structural eigenmodes. The initial condition is given by the first eigenmode of the plate with a maximum deflection of 0.01m.

8.3.2.2 Continuous structure analyzed

The difference between the eigenmodes of the structure and those of the coupled fluid-structure interaction system for the mean values of the random parameters are shown in Figure 8.8. Due to these differences the initial deflection of the first structural eigenmode excites all eigenmodes of the coupled system. In the resulting dynamical response the coupled eigenmodes oscillate at their coupled eigenfrequencies, which differ from the structural natural frequencies as given in Table 8.1. Projecting the plate motion back onto the structural eigenmodes results in multi-frequency signals for the dynamical behavior of the plate described in terms of its structural eigenmodes. Also a nodal description of the structure in terms of the degrees-of-freedom of the finite element discretization gives rise to multi-frequency signals.

The multi-frequency response of the structural eigenmodes is illustrated in Figure 8.9 for the example of the velocity component of the fourth eigenmode $v_4(t)$ for randomness in the plate density $\rho_\mathrm{p}(\omega)$ and a deterministic modulus of elasticity $E_\mathrm{p} = \mu_{\mathrm{E}_\mathrm{p}}$. The $N_\mathrm{s} = 3$ UASFE samples $v_{4_i}(t)$ for $N_\mathrm{e} = 1$ element show the effect of

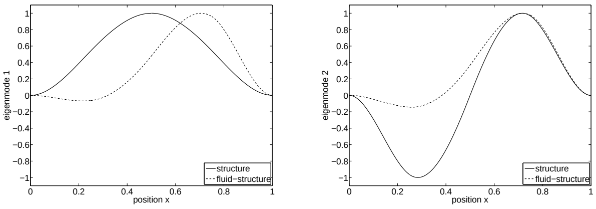

(a) eigenmode 1 (b) eigenmode 2

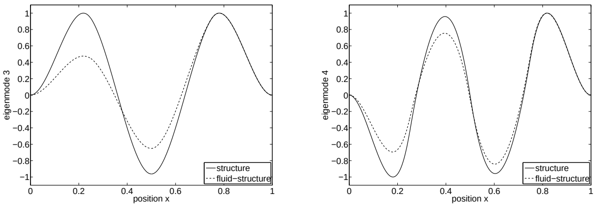

(c) eigenmode 3 (d) eigenmode 4

Figure 8.8: Deterministic eigenmodes of the structure and the coupled fluid-structure interaction system for the panel problem.

Table 8.1: Deterministic eigenfrequencies of the structure and the coupled fluid-structure interaction system for the panel problem.

eigenmode	eigenfrequency [Hz]	
	structure	fluid-structure
1	24.49	53.81
2	68.05	59.78
3	135.0	133.3
4	255.4	254.8

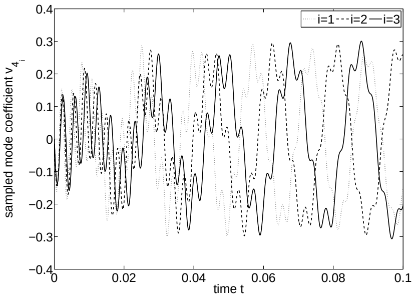

Figure 8.9: The $N_{\mathrm{s}} = 3$ sampled velocity components of the fourth eigenmode $v_{4_i}(t)$ of UASFE with $N_{\mathrm{e}} = 1$ element for the panel problem with random plate density $\rho_p(\omega)$.

the randomness on the multi-frequency response up to $t = 0.1$s. The multi-frequency signals for the eigenmode deflections and velocities are here decomposed into single-frequency signals using a level 5 wavelet decomposition.

The influence of the random $\rho_p(\omega)$ on the mean $\mu(t)$ and standard deviation $\sigma(t)$ of the total energy of the structure is shown in Figure 8.10. Results for the potential and kinetic energy, $U(t,\omega)$ and $T(t,\omega)$, of the plate are also given. The UASFE results for $N_{\mathrm{e}} = 1$ element and $N_{\mathrm{s}} = 3$ samples agree up to a maximum error of $\varepsilon = 7.7 \cdot 10^{-3}$ with converged Monte Carlo results based on $N_{\mathrm{s}} = 500$ samples, while reducing the computational costs by 2 orders of magnitude. In Figure 8.10a also the deterministic total structural energy is shown, which exhibits initially a fast increase due to transport of energy from the flow to the structure. The asymptotically periodic oscillation for the total structural energy illustrates that the deterministic parameter settings correspond to the deterministic flutter point. The mean total energy is initially close to the deterministic result for $t < 0.05$. However, for larger t the random $\rho_{\mathrm{p}}(\omega)$ results in an asymptotically diverging mean total energy. This observation is in correspondence with the well know fact that randomness can trigger the onset of unstable behavior of aeroelastic systems. The mean total energy is approximately equally divided between mean potential and kinetic energy.

Random $\rho_{\mathrm{p}}(\omega)$ results also in an increasing standard deviation for the total, potential, and kinetic energy of the plate as shown in Figure 8.10b. Initially the variation of the potential and kinetic energy partially cancel each other, which results in a smaller standard deviation for the total energy. For $t > 0.3$ the standard deviation of the total

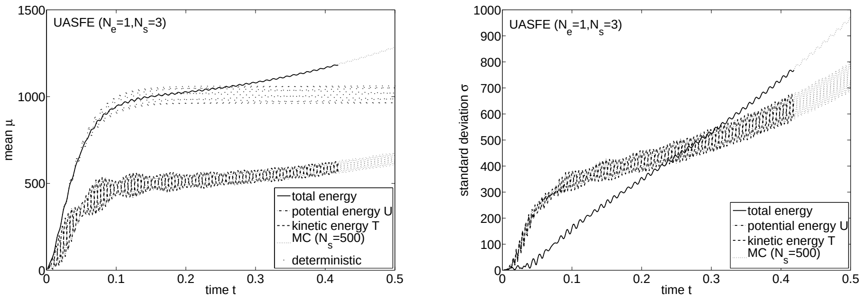

(a) mean $\mu(t)$ (b) standard deviation $\sigma(t)$

Figure 8.10: Results for the panel problem with random plate density $\rho_p(\omega)$.

energy is larger than those of the potential and kinetic energy. The coefficient of variation of the total energy increases to a value of 62.5% at $t = 0.4$, which corresponds to an amplification factor of the input randomness of 6.25.

8.3.2.3 Random field for modulus of elasticity

The random field for the modulus of elasticity $E_{\rm p}(x, \omega)$ results in a different behavior of the mean and standard deviation of the potential and kinetic energy, $U(t, \omega)$ and $T(t, \omega)$, of the plate than random $\rho_{\rm p}(\omega)$, see Figure 8.11. The mean and the standard deviation of $U(t, \omega)$ and $T(t, \omega)$ oscillate alternately between zero and the value of the mean and standard deviation of the total energy, respectively. This indicates that the randomness in $E_{\rm p}(x, \omega)$ does not significantly affect the frequency of oscillation of the plate. The 0.1% variation in the modulus of elasticity has, however, a similar quantitative influence on the mean and standard deviation of the total energy of the plate as the 10% variation of $\rho_{\rm p}(\omega)$. The total energy of the plate is, therefore, 2 orders of magnitude more sensitive to variation in $E(x, \omega)$ than in $\rho_{\rm p}(\omega)$. The mean and standard deviation increase in time to a coefficient of variation of 48.5% at $t = 0.4$, which corresponds to an amplification factor for the coefficient of variation of 485.

The UASFE results shown for $N_{\rm e} = 8$ elements and $N_{\rm s} = 25$ samples are converged up to $1 \cdot 10^{-3}$. In Figure 8.12 the mean and standard deviation of the total energy approximation of UASFE are compared to those of Monte Carlo simulation based on the same Karhunen-Loève expansion as used for UASFE to eliminate the Karhunen-Loève discretization error. The Monte Carlo results for 10^3, 10^4, and 10^5

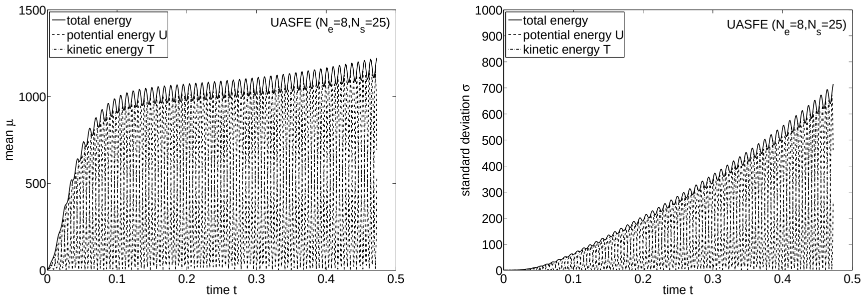

(a) mean $\mu(t)$ (b) standard deviation $\sigma(t)$

Figure 8.11: Results for the panel problem with random modulus of elasticity field $E(x, \omega)$.

samples converge to the UASFE results, although Monte Carlo simulation with 10^5 samples has not yet reached the accuracy of UASFE based on $N_\mathrm{s} = 25$ samples. The comparison for the potential and kinetic energy results in the same observations.

8.3.3 Three-dimensional transonic wing

The transonic AGARD 445.6 wing [120] is a standard benchmark case for the fluid-structure interaction of a three-dimensional continuous structure. The discretization of the aeroelastic configuration is described in section 8.3.3.1. In section 8.3.3.2 randomness is introduced in the free stream velocity. The stochastic response of the system and the flutter probability are determined.

8.3.3.1 AGARD 445.6 wing benchmark problem

The AGARD aeroelastic wing configuration number 3 [120] known as the weakened model is considered here with a NACA 65A004 symmetric airfoil, taper ratio of 0.66, 45$^\mathrm{o}$ quarter-chord sweep angle, and a 2.5-foot semi-span subject to an inviscid flow. The structure is described by a nodal discretization using an undamped linear finite element model in the *Matlab* finite element toolbox *OpenFEM* [73]. The discretization contains in the chordal and spanwise direction 6×6 brick-elements with 20 nodes and 60 degrees-of-freedom, and at the leading and trailing edge 2×6 pentahedral elements with 15 nodes and 45 degrees-of-freedom as in [125]. The orthotropic material proper-

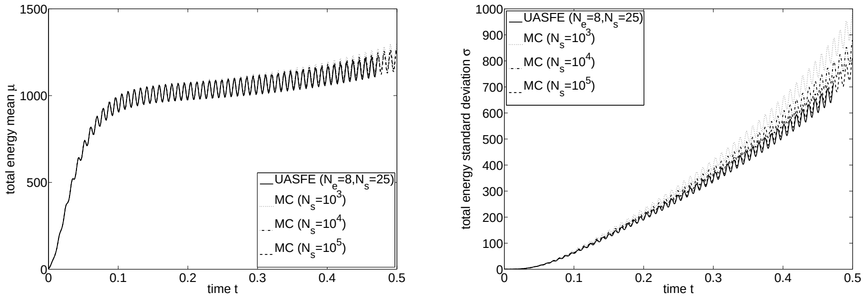

(a) mean $\mu(t)$

(b) standard deviation $\sigma(t)$

Figure 8.12: Results for the panel problem with random modulus of elasticity field $E(x,\omega)$.

ties are obtained from [6] and the fiber orientation is taken parallel to the quarter-chord line.

The Euler equations for inviscid flow [15] are solved using a second-order central finite volume discretization on a $60 \times 15 \times 30$m domain using an unstructured hexahedral mesh. The free stream conditions for the density $\rho_\infty = 0.099468$kg/m^3 and pressure $p_\infty = 7704.05$Pa are taken from [120]. Time integration of the samples is performed using a third-order implicit Runge-Kutta scheme [44] until $t = 1.25$s to determine the stochastic solution until $t = 1$s. The first bending mode with a vertical tip displacement of $y_{\mathrm{tip}} = 0.01$m is used as initial condition for the structure, see Figure 8.13.

The coupled fluid-structure interaction system is solved using a partitioned IMEX scheme [123, 124] with explicit treatment of the coupling terms without sub-iterations. An Arbitrary Lagrangian-Eulerian formulation is employed to couple the fluid mesh with the movement of the structure. The flow forces and the structural displacements are imposed on the structure and the flow using nearest neighbor and radial basis function interpolation [125], respectively. The fluid mesh is also deformed using radial basis function interpolation of the boundary displacements [9]. A convergence study has been performed to determine a suitable flow mesh discretization and time step size. Deterministic results for the selected flow mesh with $3.1 \cdot 10^4$ volumes and time step of $\Delta t = 2.5 \cdot 10^{-3}$s agree well with experimental and computational results in the literature [46, 120, 125]. The deterministic flutter velocity is found to be $U_{\mathrm{flut}} = 313$m/s, which corresponds to a Mach number of $M_\infty = 0.951$.

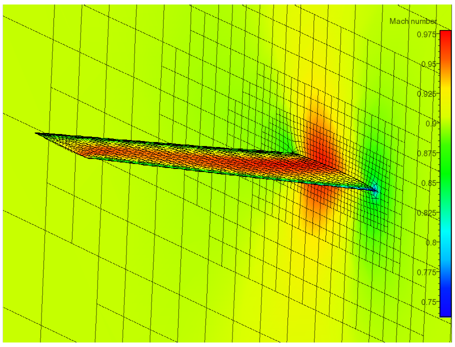

Figure 8.13: Initial condition and grid for the AGARD 445.6 wing for mean free stream velocity μ_{U_∞}.

8.3.3.2 Randomness causes non-zero flutter probability

In the following, the effect of randomness in the free stream velocity $U_\infty(\omega)$ is studied. The mean free stream velocity is chosen 5% below the actual deterministic flutter velocity, $\mu_{\mathrm{U}_\infty} = 0.95 U_{\mathrm{flut}}$, to assess the effectiveness of a realistic design safety factor. The coefficient of variation of the assumed unimodal beta distribution is set to $\mathrm{cv}_{\mathrm{U}_\infty} = 3.5\%$. The outputs of interest are the lift $L(t,\omega)$ and the vertical tip displacement of the tip-node $y_{\mathrm{tip}}(t,\omega)$.

The first $N_{\mathrm{s}} = 3$ sampled time series of the lift $L_i(t,\omega)$ of the UASFE discretization with $N_{\mathrm{e}} = 1$ element show in Figure 8.14a that the first bending mode is the dominant mode in the system response. A second mode which is initially present in the response, damps out quickly, such that a wavelet decomposition pre-processing step is in this case not necessary to obtain the stochastic solution using UASFE. The samples illustrate that the free stream velocity has a significant effect on the frequency and the damping of the system response, which results in a diverging oscillation for $i = 3$, and decaying oscillations for $i = 1$ and mean value μ_{U_∞} at $i = 2$. The same conclusions can be drawn from Figure 8.14b in which the response surface approximation of the lift $L(t,\omega)$ at $t = 1$ is given for $N_{\mathrm{e}} = 5$ elements and $N_{\mathrm{s}} = 11$ samples. The response surface has an oscillatory character due to the effect of the random $U_\infty(\omega)$ on the frequency of the lift oscillation and consequently on the phase differences in $L(t,\omega)$ at $t = 1$. The adaptive UASFE grid refinement results automatically in a gradually finer mesh in the region of large lift amplitudes at large values of $U_\infty(\omega)$.

Results for the time evolution of the mean $\mu_{\mathrm{L}}(t)$ and the standard deviation $\sigma_{\mathrm{L}}(t)$

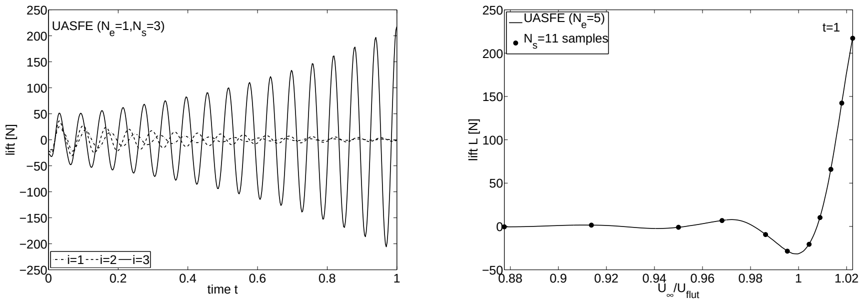

(a) lift samples $L_i(t)$

(b) lift response surface $L(t, \omega)$ at $t = 1$

Figure 8.14: Results for the AGARD 445.6 wing with random free stream velocity $U_\infty(\omega)$.

of the lift are given in Figure 8.15 for $N_\mathrm{e} = 4$ and $N_\mathrm{e} = 5$ elements. The two approximations are converged with respect to each other up to $5 \cdot 10^{-3}$. The time history for the mean lift $\mu_\mathrm{L}(t)$ shows a decaying oscillation up to $t = 0.4$s from the initial value of $\mu_\mathrm{L} = -23.9$N. This behavior can be explained by the decaying lift oscillation for a large range of $U_\infty(\omega)$ values and the effect of $U_\infty(\omega)$ on the increasing phase differences with time. For $t > 0.4$ the decay is approximately balanced by the exponentially increasing amplitude of the unstable part of the $U_\infty(\omega)$ parameter domain. In contrast, the standard deviation shows an oscillatory increase from the initial $\sigma_\mathrm{L} = 2.46$N up to a local maximum of $\sigma_\mathrm{L} = 18.3$N at $t = 0.31$s due to the increasing phase differences with time. For $t > 0.31$ the standard deviation slightly decreases due to the decreasing lift amplitude in part of the parameter domain. Eventually, the unstable realizations result in an increasing standard deviation which reaches at $t = 1$ values between $\sigma_\mathrm{L} = 14$ and $\sigma_\mathrm{L} = 19$, which corresponds to an amplification of the initial standard deviation with a factor 6 to 8.

The nodal description of the structure directly returns the vertical tip-node displacement $y_\mathrm{tip}(t, \omega)$. The approximations of the mean $\mu_{\mathrm{y}_\mathrm{tip}}(t)$ and standard deviation $\sigma_{\mathrm{y}_\mathrm{tip}}(t)$ of $y_\mathrm{tip}(t, \omega)$ show in Figure 8.16 a qualitatively similar behavior as the lift $L(t, \omega)$. The standard deviation $\sigma_{\mathrm{y}_\mathrm{tip}}(t)$ vanishes, however, initially due to the deterministic initial condition for the structure in contrast with the non-zero $\sigma_\mathrm{L}(t)$ at $t = 0$. The standard deviation reaches values between $\sigma_{\mathrm{y}_\mathrm{tip}} = 4.2 \cdot 10^{-3}$m and $\sigma_{\mathrm{y}_\mathrm{tip}} = 5.6 \cdot 10^{-3}$m at $t = 1$, which corresponds to a standard deviation equal to 42% and 56% of the deterministic initial vertical tip deflection.

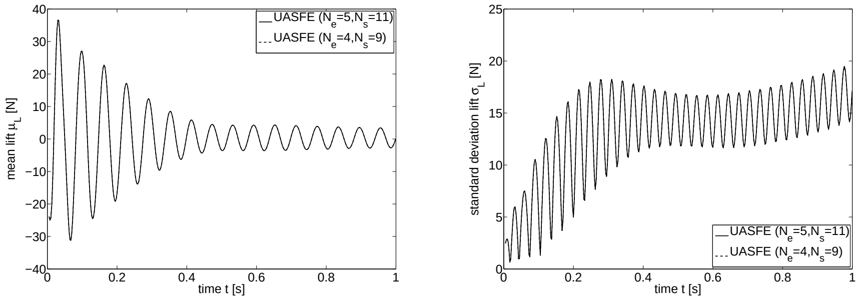

(a) mean μ_{L} (b) standard deviation σ_{L}

Figure 8.15: Results for the AGARD 445.6 wing with random free stream velocity $U_\infty(\omega)$.

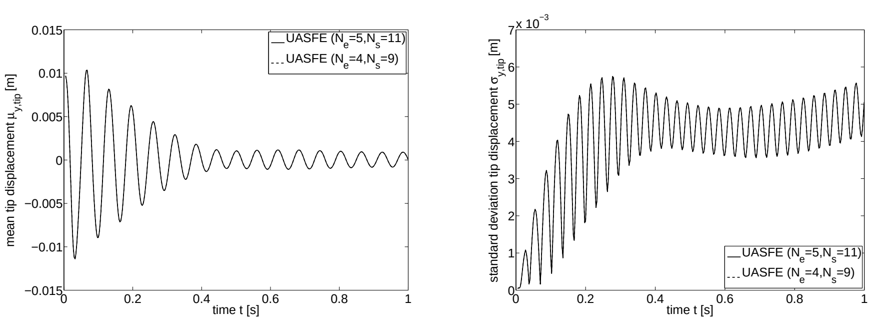

(a) mean $\mu_{\mathrm{y_{tip}}}$ (b) standard deviation $\sigma_{\mathrm{y_{tip}}}$

Figure 8.16: Results for the AGARD 445.6 wing with random free stream velocity $U_\infty(\omega)$.

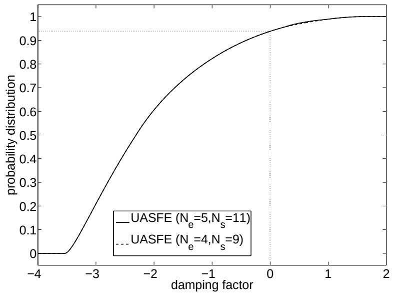

Figure 8.17: Results for the AGARD 445.6 wing with random free stream velocity $U_\infty(\omega)$.

The probability of flutter can be determined by constructing the probability distribution of the damping factor of the system given in Figure 8.17. The damping factor is here extracted from the last period of oscillation of the sampled vertical tip node displacements. Positive and negative damping factors denote unstable and damped oscillatory responses, respectively. Even though the mean free stream velocity μ_{U_∞} is fixed at a safety margin of 5% below the deterministic flutter velocity U_{flut}, the non-zero probability of positive damping indicates a non-zero flutter probability. The 3.5% variation in $U_\infty(\omega)$ results actually in a probability of flutter of 6.19%. Taking physical uncertainties into account in numerical predictions is, therefore, a more reliable approach than using safety margins in combination with deterministic simulation results.

8.4 Summary

The Unsteady Adaptive Stochastic Finite Elements (UASFE) method based on interpolation at constant phase is extended to resolve the effect of randomness in aeroelastic simulations with multi-frequency responses and continuous structures by employing a wavelet decomposition pre-processing step. The sampled multi-frequency signals are decomposed into their single-frequency components in the wavelet analysis. The effect of the randomness on the single-mode components is determined by employing UASFE interpolation of the single-frequency signals at constant phase. This eliminates the effect of the increasing phase differences between the samples and consequently the increasing number of samples with time usually required by uncertainty quantification methods in time-dependent problems. The stochastic behavior of the multi-frequency response is, finally, obtained by summing the separate effects of the single-mode components. The actual interpolation is performed using a non-intrusive higher-order total variation diminishing Adaptive Stochastic Finite Elements (ASFE) approach based on Newton-Cotes quadrature in simplex elements. The resulting UASFE method is an efficient and robust approach for resolving the stochastic response of multi-frequency systems and continuous structures.

The application of UASFE to the multi-frequency response of a harmonically forced oscillator with randomness in the spring stiffness and the forcing frequency illustrates the effectiveness of the approach for this complex multi-scale stochastic problem by reducing the required number of samples by 3 orders of magnitude compared to Monte Carlo simulations. The UASFE discretization achieves a fourth-order error convergence with respect to the Monte Carlo reference solution for random spring stiffness. The study of a multi-mode response of a continuous plate structure in supersonic flow with a random plate density and a random field modulus of elasticity shows a qualitatively different stochastic behavior of the potential and kinetic energy of the plate for the two sources of randomness. The diverging mean and standard deviation of the total structural energy are 2 orders of magnitude more sensitive to variations in the modulus of elasticity than the plate density, which results in an amplification of the input coefficient of variation by a factor 485 at $t = 0.4$. The results for the aeroelastic simulation of the three-dimensional transonic AGARD 445.6 wing with random free stream velocity illustrate that, although the mean free stream velocity is a safety margin of 5% below the deterministic flutter velocity, a 3.5% variation still results in a non-zero flutter probability of 6.19%.

Chapter 9

Derivation of total variation diminishing, extrema diminishing, and bounded error properties

In Chapters 5 to 8 an efficient Unsteady Adaptive Stochastic Finite Elements (UASFE) method is developed for uncertainty quantification in time-dependent simulations based on interpolation at constant phase. The underlying Adaptive Stochastic Finite Elements (ASFE) method based on Newton-Cotes quadrature in simplex elements is introduced in Chapter 4 for robust uncertainty quantification in steady problems. In this chapter the total variation diminishing (TVD), extrema diminishing (ED), and bounded error properties of the presented methods are derived. These properties are demonstrated in application to a steady transonic airfoil flow and a transonic airfoil flutter problem.

9.1 Introduction

Global polynomial approximations of discontinuities in probability space can result in oscillatory predictions and unphysical realizations. Since the main motivation for

---

Based on: J.A.S. Witteveen, H. Bijl, A TVD uncertainty quantification method with bounded error applied to transonic airfoil flutter, Commun. Comput. Phys. 6 (2009) 406–432.

performing uncertainty analysis is to obtain reliable computational predictions, it is important to assure the robustness of uncertainty quantification methods. In the deterministic finite volume community the total variation diminishing (TVD) and extrema diminishing (ED) properties [33, 42] of finite volume methods ascertain that no unphysical solutions are predicted due to overshoots and undershoots near discontinuities. It is, therefore, useful to extend these concepts to uncertainty quantification methods in probability space.

In unsteady problems, uncertainty quantification methods usually require a fast increasing number of samples with time to maintain a constant accuracy. This effect is especially profound in problems with oscillatory solutions in which the frequency of the response is affected by the random parameters. As a consequence, the error in an approximation based on a constant number of samples increases rapidly with time. The derivation of an error bound for an uncertainty quantification method for unsteady problems is, therefore, important to establish its reliability.

It is shown that the Adaptive Stochastic Finite Elements method with Newton-Cotes quadrature in simplex elements is an extrema diminishing uncertainty quantification method in section 9.2. It is also shown that the method is total variation diminishing for one random parameter and for multiple random parameters for first degree Newton-Cotes quadrature. It is proven in section 9.3 that the Unsteady Adaptive Stochastic Finite Elements method with interpolation at constant phase results in a bounded error as function of the phase for periodic responses and under certain conditions also in a bounded error in time. The two methods are applied to a steady transonic airfoil flow and a transonic airfoil flutter problem in section 9.4. The conclusions are summarized in section 9.5.

9.2 Adaptive Stochastic Finite Elements

The Adaptive Stochastic Finite Elements method based on Newton-Cotes quadrature in simplex elements is presented in section 9.2.1. It is shown under which conditions the approach is total variation diminishing in probability space in section 9.2.2. In section 9.2.3 it is proven that the method is extrema diminishing in probability space.

9.2.1 Newton-Cotes quadrature in simplex elements

Adaptive Stochastic Finite Elements with Newton-Cotes quadrature and simplex elements evaluate integral (1.3) by dividing parameter space A in n_{e} non-overlapping simplex elements A_j

$$\mu_{\mathrm{u}_i}(\mathbf{x},t) = \sum_{j=1}^{n_\mathrm{e}} \int_{A_j} u^*(\mathbf{x},t,\mathbf{a})^i f_\mathbf{a}(\mathbf{a})\mathrm{d}\mathbf{a}. \tag{9.1}$$

A piecewise polynomial approximation $w^*(\mathbf{x},t,\mathbf{a})$ of the response $u^*(\mathbf{x},t,\mathbf{a})$ is constructed based on n_s deterministic solutions $v_{j,k}(\mathbf{x},t) = u^*(\mathbf{x},t,\mathbf{a}_{j,k})$ for the values of the random parameters $\mathbf{a}_{j,k}$ that correspond to the $\tilde{n}_\mathrm{s}$ Newton-Cotes quadrature points of degree d in the element A_j

$$\mu_{\mathrm{u}_i}(\mathbf{x},t) \approx \mu_{\mathrm{w}_i}(\mathbf{x},t) = \sum_{j=1}^{n_\mathrm{e}} \sum_{k=1}^{\tilde{n}_\mathrm{s}} c_{j,k} v_{j,k}(\mathbf{x},t)^i, \tag{9.2}$$

where $c_{j,k}$ is the weighted integral of the Lagrange interpolation polynomial $L_{j,k}(\mathbf{a})$ through Newton-Cotes quadrature point k in element A_j

$$c_{j,k} = \int_{A_j} L_{j,k}(\mathbf{a}) f_\mathbf{a}(\mathbf{a})\mathrm{d}\mathbf{a}, \tag{9.3}$$

for $j = 1,\dots,n_\mathrm{e}$ and $k = 1,\dots,\tilde{n}_\mathrm{s}$.

Here, first and second degree Newton-Cotes quadrature is considered, $d = 1$ and $d = 2$. The second degree Newton-Cotes formulation is combined with adaptive mesh refinement in probability space. The initial discretization of parameter space A for the second degree adaptive scheme consists of the minimum of $n_{\mathrm{e}_\mathrm{ini}} = n_\mathrm{a}!$ simplex elements and $n_{\mathrm{s}_\mathrm{ini}} = 3^{n_\mathrm{a}}$ samples, see Figure 7.2. The example of Figure 7.2 for two random input parameters can geometrically be extended to higher dimensional probability spaces. The elements A_j are adaptively refined using a refinement measure ρ_j based on the largest absolute eigenvalue of the Hessian H_j, as measure of the curvature of the response surface approximation in the elements, weighted by the probability f_j contained by the elements

$$f_j = \int_{A_j} f_\mathbf{a}(\mathbf{a})\mathrm{d}\mathbf{a}, \tag{9.4}$$

with $\sum_{j=1}^{n_\mathrm{e}} f_j = 1$. The stochastic grid refinement is terminated when $\delta_{n_\mathrm{e}} < \bar{\delta}$, where convergence measure δ_{n_e} is defined as

$$\begin{aligned}\delta_{n_\mathrm{e}} = \max\Bigg(& \frac{|\mu_{\mathrm{u}_{\lfloor n_\mathrm{e}/2 \rfloor}}(\mathbf{x},t) - \mu_{\mathrm{u}_{n_\mathrm{e}}}(\mathbf{x},t)|_\infty}{|\mu_{\mathrm{u}_{n_\mathrm{e}}}(\mathbf{x},t)|_\infty}, \\ & \frac{|\sigma_{\mathrm{u}_{\lfloor n_\mathrm{e}/2 \rfloor}}(\mathbf{x},t) - \sigma_{\mathrm{u}_{n_\mathrm{e}}}(\mathbf{x},t)|_\infty}{|\sigma_{\mathrm{u}_{n_\mathrm{e}}}(\mathbf{x},t)|_\infty}\Bigg),\end{aligned} \tag{9.5}$$

with $\mu_{\mathrm{u}}(\mathbf{x},t)$ and $\sigma_{\mathrm{u}}(\mathbf{x},t)$ the mean and standard deviation of $u(\mathbf{x},t,\omega)$, or when a threshold for the maximum number of samples $\bar{n}_{\mathrm{s}}$ is reached. Convergence measure $\delta_{n_{\mathrm{e}}}$ can be extended to include higher statistical moments of the output.

Due to the location of the Newton-Cotes quadrature points the deterministic samples are reused in successive refinements and the samples are used in approximating the response in multiple elements. In elements where the quadratic second degree interpolation results in an extremum other than in a quadrature point, the element is subdivided into $\tilde{n}_{\mathrm{e}} = 2^{n_{\mathrm{a}}}$ subelements with a linear first degree Newton-Cotes approximation of the response without performing additional deterministic solves.

As is common in multi-element methods, the probability of the random parameters $\mathbf{a}(\omega)$ is assumed to be zero outside a finite domain. Probability distributions on infinite domains are truncated at a small enough threshold value for the probability, such that the truncation error is small compared to other numerical errors that occur in practical applications.

9.2.2 Total variation diminishing

It is shown that Adaptive Stochastic Finite Elements based on Newton-Cotes quadrature in simplex elements is total variation diminishing for one random parameter in section 9.2.2.1. In section 9.2.2.2 it is argued that the method is also total variation diminishing in higher dimensional probability spaces up to first degree Newton-Cotes quadrature.

9.2.2.1 One-dimensional probability space

Consider uncertainty quantification problem (1.1) with one random input parameter $a(\omega)$, $n_{\mathrm{a}} = 1$, on a bounded connected domain $a \in A$, with one-dimensional parameter space $A = [\min(a), \max(a)]$. Let response surface $u^*(\mathbf{x},t,a)$ be a continuously differentiable function. The arguments $\mathbf{x}$ and t, and the index $*$ are omitted in the following for simplicity of the notation. Let sampling method g result in a discrete set of n_{s} samples $\mathbf{v} = \{v_1,\dots,v_{n_{\mathrm{s}}}\} = g(u(a))$ of response surface $u(a)$, with $v_k = g_k(u(a)) = u(a_k)$, $a_k = a(\omega_k)$, $k = 1,\dots,n_{\mathrm{s}}$, and

$$a_1 \le a_2 \le \cdots \le a_{n_{\mathrm{s}}}, \tag{9.6}$$

with $a_1 = \min(a)$ and $a_{n_{\mathrm{s}}} = \max(a)$. Let interpolation method h of the samples $\mathbf{v}$ result in a piecewise continuously differentiable interpolation function $w(a) = h(\mathbf{v})$ with $w(a_k) = v_k$, which is continuously differentiable on subdomains A_j of A and continuous on the subdomain boundaries ∂A_j with $j = 1,\dots,n_{\mathrm{e}}$. Let uncertainty quantification method l evaluate (1.3) by approximating response surface $u(a)$ with interpolation $w(a) = l(u(a)) = h(g(u(a)))$ of the samples $\mathbf{v}$. Then the concepts total variation, total variation diminishing, and total variation conserving are defined in probability space as follows in correspondence to their definitions for finite volume methods in physical space in [33].

Definition 1. (Total variation) The total variation TV of response surface $u(a)$ in the space A of random parameter $a(\omega)$ is

$$\mathrm{TV}(u) = \int_A \left| \frac{\partial u}{\partial a} \right| \mathrm{d}a. \tag{9.7}$$

The total variation of the continuous and piecewise continuously differentiable approximation $w(a)$ is

$$\mathrm{TV}(w) = \sum_{j=1}^{n_\mathrm{e}} \mathrm{TV}(w_j) = \sum_{j=1}^{n_\mathrm{e}} \int_{A_j} \left| \frac{\partial w_j}{\partial a} \right| \mathrm{d}a. \tag{9.8}$$

The total variation of the discrete set of samples $\mathbf{v}$ is

$$\mathrm{TV}(\mathbf{v}) = \sum_{k=1}^{n_\mathrm{s}-1} \left| v_{k+1} - v_k \right|. \tag{9.9}$$

Definition 2. (Total variation diminishing) A set of samples $\mathbf{v}$ is total variation diminishing (TVD) with respect to response surface $u(a)$ if

$$\mathrm{TV}(\mathbf{v}) \leq \mathrm{TV}(u). \tag{9.10}$$

Sampling method g is TVD if the resulting set of samples $\mathbf{v}$ is TVD for all $u(a)$. Approximation $w(a)$ of response surface $u(a)$ is TVD if

$$\mathrm{TV}(w) \leq \mathrm{TV}(u). \tag{9.11}$$

Uncertainty quantification method l is TVD if the resulting approximation $w(a)$ is TVD for all $u(a)$.

Definition 3. (Total variation conserving) Interpolation $w(a)$ of samples $\mathbf{v}$ is total variation conserving (TVC) if

$$\mathrm{TV}(w) = \mathrm{TV}(\mathbf{v}). \tag{9.12}$$

Interpolation method h is TVC if the resulting interpolation $w(a)$ is TVC for all $\mathbf{v}$.

Based on these definitions it is proven below that Stochastic Finite Elements with Newton-Cotes quadrature in simplex elements is a TVD uncertainty quantification method for random parameter $a(\omega)$.

Lemma 1. *Sampling method g is TVD for random parameter $a(\omega)$.*

Proof. For the total variation of the samples $\mathbf{v} = g(u(a))$ holds according to Definition 1

$$\begin{aligned} \mathrm{TV}(\mathbf{v}) &= \sum_{k=1}^{n_\mathrm{s}-1} |v_{k+1} - v_k| = \sum_{k=1}^{n_\mathrm{s}-1} |u(a_{k+1}) - u(a_k)| \\ &\leq \sum_{k=1}^{n_\mathrm{s}-1} \int_{a_k}^{a_{k+1}} \left|\frac{\partial u}{\partial a}\right| \mathrm{d}a = \int_A \left|\frac{\partial u}{\partial a}\right| \mathrm{d}a = \mathrm{TV}(u). \end{aligned} \tag{9.13}$$

Since (9.13) holds for all $u(a)$, sampling method g is TVD according to Definition 2. □

Consider Stochastic Finite Elements uncertainty quantification method l^1 with first degree Newton-Cotes quadrature in simplex elements. Sampling method g^1 then results in n_s samples $\mathbf{v}^1$ in the vertices of the n_e simplex elements. Interpolation method h^1 results in a linear interpolation $w_j^1(a)$ of the samples $\mathbf{v}_j^1$ in the elements A_j. For one random parameter $a(\omega)$ sampling method g^1 results in $n_\mathrm{s} = n_\mathrm{e} + 1$ samples $\mathbf{v}^1$. Interpolation method h^1 then results in the piecewise linear interpolation $w^1(a)$

$$w^1(a) = w_j^1(a) = \frac{v_j^1(a_{j+1} - a) + v_{j+1}^1(a - a_j)}{a_{j+1} - a_j}, \tag{9.14}$$

for $a \in A_j = [a_j, a_{j+1}]$ and $j = 1, \dots, n_\mathrm{e}$.

Theorem 1. *Uncertainty quantification method l^1 based on first degree Newton-Cotes quadrature in simplex elements is TVD for random parameter $a(\omega)$.*

Proof. The total variation of $w^1(a)$ is according to Definition 1 and (9.14)

$$\begin{aligned} \mathrm{TV}(w^1) &= \sum_{j=1}^{n_\mathrm{e}} \int_{A_j} \left|\frac{\partial w_j^1}{\partial a}\right| \mathrm{d}a = \sum_{j=1}^{n_\mathrm{e}} \left|\frac{v_{j+1}^1 - v_j^1}{a_{j+1} - a_j}\right| (a_{j+1} - a_j) \\ &= \sum_{k=1}^{n_\mathrm{s}-1} \left|v_{k+1}^1 - v_k^1\right| = \mathrm{TV}(\mathbf{v}^1). \end{aligned} \tag{9.15}$$

Since (9.15) holds for all $\mathbf{v}^1$, interpolation method h^1 is TVC according to Definition 3. Lemma 1 gives

$$\mathrm{TV}(w^1) = \mathrm{TV}(\mathbf{v}^1) \leq \mathrm{TV}(u). \tag{9.16}$$

Since (9.16) holds for all $u(a)$, uncertainty quantification method l^1 is TVD according to Definition 2. ☐

Consider Stochastic Finite Elements uncertainty quantification method l^2 with second degree Newton-Cotes quadrature in simplex elements. Sampling method g^2 then results in n_s samples $\mathbf{v}^2$ in the middle of the edges and in the vertices of the n_e simplex elements. Interpolation method h^2 results in a quadratic interpolation $w_j^2(a)$ of the samples $\mathbf{v}_j^2$ in the elements A_j. For one random parameter $a(\omega)$ sampling method g^2 results in $n_\mathrm{s} = 2n_\mathrm{e} + 1$ samples. Interpolation method h^2 then results in quadratic approximation $w_j^2(a)$ in the element A_j through the samples v_k^2 for $k = \{2j-1, 2j, 2j+1\}$, $j = 1, \ldots, n_\mathrm{e}$. If the quadratic approximation $w_j^2(a)$ in an element A_j has an extremum other than in a quadrature point a_k, i.e.,

$$\begin{aligned}\min_{A_j}(w_j^2(a)) &< \min(v_{2j-1}^2, v_{2j}^2, v_{2j+1}^2) \;\vee \\ \max_{A_j}(w_j^2(a)) &> \max(v_{2j-1}^2, v_{2j}^2, v_{2j+1}^2),\end{aligned} \tag{9.17}$$

then element A_j is subdivided into $\tilde{n}_\mathrm{e} = 2$ subelements with a linear first degree Newton-Cotes approximation based on the samples v_k with $k = \{2j-1, 2j, 2j+1\}$

$$w_j^2(a) = \begin{cases} \frac{v_{2j-1}^2(a_{2j}-a)+v_{2j}^2(a-a_{2j-1})}{a_{2j}-a_{2j-1}}, & a \in [a_{2j-1}, a_{2j}], \\ \frac{v_{2j}^2(a_{2j+1}-a)+v_{2j+1}^2(a-a_{2j})}{a_{2j+1}-a_{2j}}, & a \in [a_{2j}, a_{2j+1}], \end{cases} \tag{9.18}$$

Theorem 2. *Uncertainty quantification method l^2 based on second degree Newton-Cotes quadrature in simplex elements is TVD for random parameter $a(\omega)$.*

Proof. Two cases have to be considered to prove Theorem 2. In case (i) the quadratic approximation $w_j^2(a)$ in element A_j has an extremum other than in a quadrature point a_k (9.17)

$$\min_{A_j}(w_j^2(a)) < \min(v_{2j-1}^2, v_{2j}^2, v_{2j+1}^2) \;\vee\; \max_{A_j}(w_j^2(a)) > \max(v_{2j-1}^2, v_{2j}^2, v_{2j+1}^2).$$

The approximation $w_j^2(a)$ in element A_j is then given by the piecewise linear function

(9.18). The total variation of $w_j^2(a)$ in element A_j is then according to Definition 1

$$\begin{aligned} \mathrm{TV}(w_j^2(a)) &= \int_{A_j} \left| \frac{\partial w_j^2}{\partial a} \right| \mathrm{d}a = \left| v_{2j}^2 - v_{2j-1}^2 \right| + \left| v_{2j+1}^2 - v_{2j}^2 \right| \\ &= \mathrm{TV}(v_{2j-1}^2, v_{2j}^2, v_{2j+1}^2). \end{aligned} \tag{9.19}$$

In case (ii) the quadratic approximation $w_j^2(a)$ has its extrema in element A_j in quadrature points

$$\min_{A_j}(w_j^2(a)) = \min(v_{2j-1}^2, v_{2j}^2, v_{2j+1}^2) \ \wedge \tag{9.20}$$

$$\max_{A_j}(w_j^2(a)) = \max(v_{2j-1}^2, v_{2j}^2, v_{2j+1}^2). \tag{9.21}$$

The total variation of $w_j^2(a)$ in element A_j is then

$$\begin{aligned} \mathrm{TV}(w_j^2(a)) &= \int_{A_j} \left| \frac{\partial w_j^2}{\partial a} \right| \mathrm{d}a = \left| v_{2j}^2 - v_{2j-1}^2 \right| + \left| v_{2j+1}^2 - v_{2j}^2 \right| \\ &= \mathrm{TV}(v_{2j-1}^2, v_{2j}^2, v_{2j+1}^2), \end{aligned} \tag{9.22}$$

which is equal to the result of case (i). For the interpolation $w^2(a)$ of the samples $\mathbf{v}^2$ over all n_e elements then holds

$$\mathrm{TV}(w^2) = \sum_{j=1}^{n_\mathrm{e}} \mathrm{TV}(w_j^2) = \sum_{j=1}^{n_\mathrm{e}} \mathrm{TV}(v_{2j-1}^2, v_{2j}^2, v_{2j+1}^2) = \mathrm{TV}(\mathbf{v}^2). \tag{9.23}$$

Since (9.23) holds for all $\mathbf{v}^2$, interpolation method h^2 is TVC according to Definition 3. Lemma 1 gives

$$\mathrm{TV}(w^2) = \mathrm{TV}(\mathbf{v}^2) \leq \mathrm{TV}(u). \tag{9.24}$$

Since (9.24) holds for all $u(a)$, uncertainty quantification method l^2 is TVD according to Definition 2. ☐

Similarly, it can be proven that zero degree Newton-Cotes quadrature in simplex elements is also a TVD uncertainty quantification method for random parameter $a(\omega)$.

9.2.2.2 Multi-dimensional probability space

Consider an uncertainty quantification problem with an arbitrary number of n_a random input parameters $\mathbf{a}(\omega) = \{a_1(\omega), \ldots, a_{n_\mathrm{a}}(\omega)\}$ on a bounded connected domain

$\mathbf{a} \in A$. In this section it is argued that Stochastic Finite Elements with Newton-Cotes quadrature in simplex elements is also a TVD uncertainty quantification method in the resulting multi-dimensional probability space for first degree Newton-Cotes.

Also for an arbitrary number of random parameters $\mathbf{a}(\omega)$ holds that a sampling method g is TVD, since the resulting set of samples $\mathbf{v}$ cannot result in larger total variation than response surface $u(\mathbf{a})$.

Uncertainty quantification method l^1 based on first degree Newton-Cotes quadrature in simplex elements is also TVD in multi-dimensional probability spaces. The linear interpolation $w_j^1(\mathbf{a})$ of the samples $\mathbf{v}_j^1$ in the vertices of simplex element A_j conserves the total variation of the samples $\mathbf{v}_j$ in element A_j. Since the piecewise linear interpolation $w^1(a)$ of the samples $\mathbf{v}^1$ is continuous over the element boundaries ∂A_j, interpolation $w^1(a)$ is TVC with respect to the TVD samples $\mathbf{v}$.

Uncertainty quantification method l^2 based on second degree Newton-Cotes quadrature in simplex elements results for multi-dimensional probability spaces in an approximation $w^2(\mathbf{a})$, which is not everywhere continuous on the element boundaries ∂A_j. Uncertainty quantification method l^2 is, therefore, not TVD for multi-dimensional probability spaces.

Zero degree Newton-Cotes quadrature in simplex elements also results in an approximation which is discontinuous at the element boundaries ∂A_j.

9.2.3 Extrema diminishing

Another important property for uncertainty quantification methods is the extrema diminishing concept. This property eliminates the possibility of predicting non-zero probabilities for unphysical outcomes due to overshoots and undershoots near discontinuities. Consider again an uncertainty quantification problem with an arbitrary number of n_a random input parameters $\mathbf{a}(\omega) = \{a_1(\omega), \ldots, a_{n_\mathrm{a}}(\omega)\} \in A$. The concepts extrema diminishing and extrema conserving are defined for probability space below in accordance with their definitions in the context of finite volume methods for physical space [42].

Definition 4. (Extrema diminishing) A set of samples $\mathbf{v}$ is extrema diminishing (ED) with respect to response surface $u(\mathbf{a})$ if

$$\min(\mathbf{v}) \geq \min_A(u(\mathbf{a})) \ \wedge \ \max(\mathbf{v}) \leq \max_A(u(\mathbf{a})). \tag{9.25}$$

Sampling method g is ED if the resulting set of samples $\mathbf{v}$ is ED for all $u(\mathbf{a})$. Approximation $w(\mathbf{a})$ of response surface $u(\mathbf{a})$ is ED if

$$\min_A(w(\mathbf{a})) \geq \min_A(u(\mathbf{a})) \ \wedge \ \max_A(w(\mathbf{a})) \leq \max_A(u(\mathbf{a})). \tag{9.26}$$

Uncertainty quantification method l is ED if the resulting approximation $w(\mathbf{a})$ is ED for all $u(\mathbf{a})$.

Definition 5. (Extrema conserving) Interpolation $w(\mathbf{a})$ of samples $\mathbf{v}$ is extrema conserving (EC) if

$$\min_A(w(\mathbf{a})) = \min(\mathbf{v}) \;\wedge\; \max_A(w(\mathbf{a})) = \max(\mathbf{v}). \tag{9.27}$$

Interpolation method h is EC if the resulting interpolation $w(\mathbf{a})$ is EC for all $\mathbf{v}$.

It is proven below that the Stochastic Finite Elements method with Newton-Cotes quadrature in simplex elements satisfies the definition of an ED uncertainty quantification method.

Lemma 2. *Sampling method g is ED.*

Proof. For the minimum of the samples $\mathbf{v}$ holds

$$\min(\mathbf{v}) = \min_k(v_k) = \min_k(u(\mathbf{a}_k)) \geq \min_A(u(\mathbf{a})), \tag{9.28}$$

and equivalently for the maximum

$$\max(\mathbf{v}) \leq \max_A(u(\mathbf{a})). \tag{9.29}$$

Since (9.28) and (9.29) hold for all $u(\mathbf{a})$, sampling method g is ED according to Definition 4. ☐

Theorem 3. *Uncertainty quantification method l^1 based on first degree Newton-Cotes quadrature in simplex elements is ED.*

Proof. For the minimum of the linear interpolation $w_j^1(\mathbf{a})$ of the samples $\mathbf{v}_j^1$ in the vertices of simplex element A_j holds

$$\min_{A_j}(w_j^1(\mathbf{a})) = \min(\mathbf{v}_j^1). \tag{9.30}$$

For the minimum of the piecewise linear interpolation $w^1(\mathbf{a})$ of the samples $\mathbf{v}^1$ then holds

$$\min_A(w^1(\mathbf{a})) = \min_j\left(\min_{A_j}(w_j^1(\mathbf{a}))\right) = \min_j(\min(\mathbf{v}_j^1)) = \min(\mathbf{v}^1), \tag{9.31}$$

and equivalently for the maximum

$$\max_A(w^1(\mathbf{a})) = \max(\mathbf{v}^1). \tag{9.32}$$

Since (9.31) and (9.32) hold for all $\mathbf{v}^1$, interpolation method h^1 is EC according to Definition 5. Lemma 2 gives

$$\min_A(w^1(\mathbf{a})) = \min(\mathbf{v}^1) \geq \min_A(u(\mathbf{a})), \tag{9.33}$$

$$\max_A(w^1(\mathbf{a})) = \max(\mathbf{v}^1) \leq \max_A(u(\mathbf{a})). \tag{9.34}$$

Since (9.33) and (9.34) hold for all $u(\mathbf{a})$, uncertainty quantification method l^1 is ED according to Definition 4. ☐

Theorem 4. *Uncertainty quantification method l^2 based on second degree Newton-Cotes quadrature in simplex elements is ED.*

Proof. The two cases (i) and (ii) again have to be considered to prove Theorem 4. In case (i) the quadratic approximation $w_j^2(\mathbf{a})$ in element A_j has an extremum other than in a quadrature point $\mathbf{a}_k$ (9.17)

$$\min_{A_j}(w_j^2(\mathbf{a})) < \min(\mathbf{v}_j^2) \ \vee \ \max_{A_j}(w_j^2(\mathbf{a})) > \max(\mathbf{v}_j^2). \tag{9.35}$$

The approximation $w_j^2(\mathbf{a})$ in element A_j is then given by a piecewise linear interpolation of the samples $\mathbf{v}_j^2$, for which holds according to (9.31) and (9.32)

$$\min_{A_j}(w_j^2(\mathbf{a})) = \min(\mathbf{v}_j^2), \quad \max_{A_j}(w_j^2(\mathbf{a})) = \max(\mathbf{v}_j^2). \tag{9.36}$$

In case (ii) the quadratic approximation $w^2(\mathbf{a})$ in element A_j has its extrema in quadrature points

$$\min_{A_j}(w_j^2(\mathbf{a})) = \min(\mathbf{v}_j^2) \ \wedge \ \max_{A_j}(w_j^2(\mathbf{a})) = \max(\mathbf{v}_j^2), \tag{9.37}$$

which is equivalent to the result of case (i). For the minimum and maximum of interpolation $w^2(\mathbf{a})$ of samples $\mathbf{v}^2$ on A then holds

$$\min_A(w^2(\mathbf{a})) = \min(\mathbf{v}^2), \quad \max_A(w^2(\mathbf{a})) = \max(\mathbf{v}^2). \tag{9.38}$$

Since (9.38) holds for all $\mathbf{v}^2$, interpolation h^2 is EC according to Definition 5. Lemma 2 gives

$$\min_A(w^2(\mathbf{a})) = \min(\mathbf{v}^2) \geq \min_A(u(\mathbf{a})), \tag{9.39}$$

$$\max_A(w^2(\mathbf{a})) = \max(\mathbf{v}^2) \leq \max_A(u(\mathbf{a})). \tag{9.40}$$

Since (9.39) and (9.40) hold for all $u(\mathbf{a})$, uncertainty quantification method l^2 is ED according to Definition 4. □

Similarly, it can be shown that zero degree Newton-Cotes quadrature in simplex elements is also ED.

9.3 Unsteady Adaptive Stochastic Finite Elements

The Unsteady Adaptive Stochastic Finite Elements method based on interpolation of oscillatory samples at constant phase ϕ is introduced in section 9.3.1. In section 9.3.2 it is proven that the method results in a bounded error as function of the phase for periodic responses. It is also shown under which conditions the error is bounded in time.

9.3.1 Interpolation at constant phase

Assume that solving equation (1.1) for realizations of the random parameters $\mathbf{a}_k$ results in oscillatory samples $v_k(t) = u(\mathbf{a}_k)$, of which the phase $v_{\phi_k}(t) = \phi(t, \mathbf{a}_k)$ is a well-defined function of time t. In order to interpolate the samples $\mathbf{v}(t) = \{v_1(t), \dots, v_{n_\mathrm{a}}(t)\}$ at constant phase, first, their phase as function of time $\mathbf{v}_\phi(t) = \{v_{\phi_1}(t), \dots, v_{\phi_{n_\mathrm{a}}}(t)\}$ is extracted from the deterministic solves $\mathbf{v}(t)$. Second, the time series for the phase $\mathbf{v}_\phi(t)$ are used to transform the samples $\mathbf{v}(t)$ to functions of their phase $\hat{\mathbf{v}}(\mathbf{v}_\phi(t)) = \{\hat{v}_1(v_{\phi_1}(t)), \dots, \hat{v}_{n_\mathrm{a}}(v_{\phi_{n_\mathrm{a}}}(t))\}$ instead of time, see Figure 7.1. Third, the transformed samples $\hat{\mathbf{v}}(\mathbf{v}_\phi(t))$ are interpolated to the function $\hat{w}(w_\phi(t, \mathbf{a}), \mathbf{a})$. This step involves both the interpolation of the sampled phases $\mathbf{v}_\phi(t)$ to the function $w_\phi(t, \mathbf{a}) = h(\mathbf{v}_\phi(t))$ and the interpolation of the samples $\hat{\mathbf{v}}(\varphi)$ to the function $\hat{w}(\varphi, \mathbf{a}) = h(\hat{\mathbf{v}}(\varphi))$ at constant phase $\phi = \varphi$. Repeating the latter interpolation for all phases φ results in the function $\hat{w}(\varphi, \mathbf{a})$. Finally, transforming $\hat{w}(\varphi, \mathbf{a})$ back to $w(t, \mathbf{a})$ using $w_\phi(t, \mathbf{a})$ yields an approximation the unknown response surface $u(t, \mathbf{a})$ of the system response as function of time t and the random parameters $\mathbf{a}(\omega)$. The actual sampling and interpolation is performed using the Adaptive Stochastic Finite Elements uncertainty quantification method l based on Newton-Cotes quadrature in simplex elements.

The phases $\mathbf{v}_\phi(t)$ are extracted from the samples based on the local extrema of the time series $\mathbf{v}(t)$. A trial and error procedure identifies a cycle of oscillation based on two or more successive local maxima. The selected cycle is accepted if the maximal error of its extrapolation in time with respect to the actual sample is smaller than a threshold value $\bar{\varepsilon}_k$ for at least one additional cycle length. The functions for the phases

$\mathbf{v}_\phi(t)$ in the whole time domain T are constructed by identifying all successive cycles of $\mathbf{v}(t)$ and extrapolation to $t = 0$ and $t = t_{\max}$ before and after the first and last complete cycle, respectively. The phase is normalized to zero at the start of the first cycle and a user defined parameter determines whether the sample is assumed to attain a local extremum at $t = 0$. If the phase $\mathbf{v}_\phi(t)$ cannot be extracted from one of the samples $v_k(t)$ for $k = 1, \ldots, n_\mathrm{s}$, uncertainty quantification method l is directly applied to the time-dependent samples $\mathbf{v}(t)$.

9.3.2 Bounded error

It is shown below that the uncertainty quantification interpolation of periodic samples at constant phase results in a bounded error. Let $u(t, \mathbf{a})$ be a periodic response as function of time t for $t \in \mathbb{R}$

$$u(t + zT(\mathbf{a}), \mathbf{a}) = u(t, \mathbf{a}), \qquad \text{for all } z \in \mathbb{Z} \text{ and } \mathbf{a} \in A, \tag{9.41}$$

with $T(\mathbf{a}) = 1/f(\mathbf{a}) > 0$ the period length and $f(\mathbf{a})$ the frequency affected by the random input $\mathbf{a}(\omega)$. The phase $\phi(t, \mathbf{a})$ of the response $u(t, \mathbf{a})$ is given by

$$\phi(t, \mathbf{a}) = \phi_0(\mathbf{a}) + \frac{t}{T(\mathbf{a})}, \tag{9.42}$$

with $\phi_0(\mathbf{a}) = \phi(0, \mathbf{a})$. Consider uncertainty quantification method l which results in an approximation $w(t, \mathbf{a})$ of $u(t, \mathbf{a})$ based on applying interpolation method h at constant phase to n_s samples $\mathbf{v}(t) = \{v_1(t), \ldots, v_{n_\mathrm{s}}\}$ for parameter values $\mathbf{a}_k$ for $k = 1, \ldots, n_\mathrm{s}$ resulted from sampling method g.

Theorem 5. *The error $\hat{\varepsilon}(\varphi, \mathbf{a}) = \hat{w}(\varphi, \mathbf{a}) - \hat{u}(\varphi, \mathbf{a})$ in approximation $\hat{w}(\varphi, \mathbf{a})$ with respect to periodic response surface $\hat{u}(\varphi, \mathbf{a})$ as resulted from uncertainty quantification method l applied at constant phase φ is bounded for all $\varphi \in \mathbb{R}$ and $\mathbf{a} \in A$ by δ for which holds*

$$\hat{\varepsilon}(\varphi, \mathbf{a}) < \delta, \qquad \text{for all } \varphi \in [0, 1] \text{ and } \mathbf{a} \in A. \tag{9.43}$$

Proof. Sampling method g results in samples

$$v_k(t) = g_k(u(t, \mathbf{a})) = u(t, \mathbf{a}_k), \tag{9.44}$$

for $k = 1, \ldots, n_\mathrm{s}$. The samples $v_k(t)$ are periodic signals with period length $v_{T_k} = T(\mathbf{a}_k)$, since using (9.41)

$$v_k(t + z v_{T_k}) = u(t + zT(\mathbf{a}_k), \mathbf{a}_k) = u(t, \mathbf{a}_k) = v_k(t) \qquad \text{for all } z \in \mathbb{Z}, \tag{9.45}$$

for $k = 1, \ldots, n_\mathrm{s}$. The phase $v_{\phi_k}(t) = \phi(t, \mathbf{a}_k)$ of the samples $v_k(t)$ is then in correspondence with (9.42) given by

$$v_{\phi_k}(t) = v_{\phi_{0_k}} + \frac{t}{v_{T_k}}, \tag{9.46}$$

for $k = 1, \ldots, n_\mathrm{s}$, with $v_{\phi_{0_k}} = v_{\phi_k}(0)$. Scaling the samples $v_k(t)$ with their phase $v_{\phi_k}(t)$ results in

$$v_k(t) = \hat{v}_k(v_{\phi_k}(t)) = \hat{v}_k\left(v_{\phi_{0_k}} + \frac{t}{v_{T_k}}\right), \tag{9.47}$$

for $k = 1, \ldots, n_\mathrm{s}$. Periodicity of $v_k(t)$ gives

$$\begin{aligned} \hat{v}_k(v_{\phi_k}(t) + z) &= \hat{v}_k\left(v_{\phi_{0_k}} + \frac{t}{v_{T_k}} + z\right) = \hat{v}_k\left(v_{\phi_{0_k}} + \frac{t + z v_{T_k}}{v_{T_k}}\right) \\ &= v_k(t + z v_{T_k}) = v_k(t) = \hat{v}_k(v_{\phi_k}(t)), \text{ for all } z \in \mathbb{Z}, \end{aligned} \tag{9.48}$$

for $k = 1, \ldots, n_\mathrm{s}$. Uncertainty quantification method l results in approximation $\hat{w}(\varphi, \mathbf{a})$ by applying interpolation method h of the samples $\mathbf{v}(t)$ at a constant phase φ

$$\hat{w}(\varphi, \mathbf{a}) = h(\hat{\mathbf{v}}(\varphi)) = h(\hat{v}_1(\varphi), \ldots, \hat{v}_{n_\mathrm{s}}(\varphi)). \tag{9.49}$$

The error $\hat{\varepsilon}(\varphi, \mathbf{a})$ as function of phase φ in approximation $\hat{w}(\varphi, \mathbf{a})$ with respect to $\hat{u}(\varphi, \mathbf{a})$ is defined as

$$\hat{\varepsilon}(\varphi, \mathbf{a}) = \hat{w}(\varphi, \mathbf{a}) - \hat{u}(\varphi, \mathbf{a}), \tag{9.50}$$

with

$$u(t, \mathbf{a}) = \hat{u}(\phi(t, \mathbf{a}), \mathbf{a}), \tag{9.51}$$

and

$$\begin{aligned} \hat{u}(\phi + z, \mathbf{a}) &= \hat{u}\left(\phi_0(\mathbf{a}) + \frac{t + zT(\mathbf{a})}{T(\mathbf{a})}, \mathbf{a}\right) = u(t + zT(\mathbf{a}), \mathbf{a}) \\ &= u(t, \mathbf{a}) = \hat{u}(\phi, \mathbf{a}), \qquad \text{for all } z \in \mathbb{Z} \text{ and } \mathbf{a} \in A. \end{aligned} \tag{9.52}$$

For error $\hat{\varepsilon}(\varphi, \mathbf{a})$ then holds using (9.48), (9.49), and (9.52)

$$\begin{aligned} \hat{\varepsilon}(\varphi + z, \mathbf{a}) &= \hat{w}(\varphi + z, \mathbf{a}) - \hat{u}(\varphi + z, \mathbf{a}) \\ &= h(\hat{v}_1(\varphi + z), \ldots, \hat{v}_{n_\mathrm{s}}(\varphi + z)) - \hat{u}(\varphi + z, \mathbf{a}) \\ &= h(\hat{v}_1(\varphi), \ldots, \hat{v}_{n_\mathrm{s}}(\varphi)) - \hat{u}(\varphi, \mathbf{a}) \\ &= \hat{w}(\varphi, \mathbf{a}) - \hat{u}(\varphi, \mathbf{a}) \\ &= \hat{\varepsilon}(\varphi, \mathbf{a}), \qquad \text{for all } z \in \mathbb{Z} \text{ and } \varphi \in \mathbb{R} \text{ and } \mathbf{a} \in A. \end{aligned} \tag{9.53}$$

Error $\hat{\varepsilon}(\varphi, \mathbf{a})$ is, therefore, a periodic function of φ. Define δ for which holds (9.43)

$$\hat{\varepsilon}(\varphi, \mathbf{a}) < \delta \qquad \text{for all } \varphi \in [0,1] \text{ and } \mathbf{a} \in A,$$

then holds

$$\hat{\varepsilon}(\varphi + z, \mathbf{a}) = \hat{\varepsilon}(\varphi, \mathbf{a}) < \delta \qquad \text{for all } z \in \mathbb{Z} \text{ and } \varphi \in [0,1] \text{ and } \mathbf{a} \in A, \tag{9.54}$$

and

$$\hat{\varepsilon}(\varphi, \mathbf{a}) < \delta \qquad \text{for all } \varphi \in \mathbb{R} \text{ and } \mathbf{a} \in A, \tag{9.55}$$

Error $\hat{\varepsilon}(\varphi, \mathbf{a})$ in approximation $\hat{w}(\varphi, \mathbf{a})$ is, therefore, bounded by δ for all $\varphi \in \mathbb{R}$ and $\mathbf{a} \in A$. ☐

Notice that the proof of Theorem 5 is independent of uncertainty quantification method l, sampling method g, and interpolation method h.

The bounded error $\hat{\varepsilon}(\varphi, \mathbf{a})$ as function of phase φ also results in a bounded error $\varepsilon(t, \mathbf{a})$ in time for the Unsteady Adaptive Stochastic Finite Elements method l^1 based on first degree Newton-Cotes quadrature, if initial phase $\phi_0(\mathbf{a})$ and frequency $f(\mathbf{a})$ depend linearly on $\mathbf{a}$. Let initial phase $\phi_0(\mathbf{a})$, therefore, depend linearly on the random parameters $\mathbf{a}$

$$\phi_0(\mathbf{a}) = c_{\phi_0,0} + \mathbf{c}_{\phi_0,1} \cdot \mathbf{a}. \tag{9.56}$$

where $\cdot$ denotes the vector inner product, with $c_{\phi_0,0}$ constant and $\mathbf{c}_{\phi_0,1}$ a vector containing n_a constants. And let frequency $f(\mathbf{a})$ also depend linearly on $\mathbf{a}(\omega)$

$$f(\mathbf{a}) = c_{\mathrm{f},0} + \mathbf{c}_{\mathrm{f},1} \cdot \mathbf{a}, \tag{9.57}$$

with $c_{\mathrm{f},0}$ constant and $\mathbf{c}_{\mathrm{f},1}$ an n_a-dimensional constant vector. Consider uncertainty quantification method l^1 based on piecewise linear interpolation method h^1 of samples in the first degree Newton-Cotes quadrature points in the vertices of simplex elements of sampling method g^1.

Theorem 6. *The error $\varepsilon(t, \mathbf{a}) = w(t, \mathbf{a}) - u(t, \mathbf{a})$ in approximation $w(t, \mathbf{a})$ with respect to periodic response surface $u(t, \mathbf{a})$ as resulted from uncertainty quantification method l^1 applied at constant phase φ is bounded for all $t \in \mathbb{R}$ and $\mathbf{a} \in A$ by δ for which holds (9.43)*

$$\hat{\varepsilon}(\varphi, \mathbf{a}) < \delta, \qquad \text{for all } \varphi \in [0,1] \text{ and } \mathbf{a} \in A,$$

if initial phase $\phi_0(\mathbf{a})$ and frequency $f(\mathbf{a})$ depend linearly on $\mathbf{a}$.

Proof. The phase $\phi(t, \mathbf{a})$ of the periodic response $u(t, \mathbf{a})$ is given by (9.42)

$$\phi(t, \mathbf{a}) = \phi_0(\mathbf{a}) + \frac{t}{T(\mathbf{a})} = \phi_0(\mathbf{a}) + f(\mathbf{a})t.$$

The linear dependence of $\phi_0(\mathbf{a})$ and $f(\mathbf{a})$ on $\mathbf{a}$ given by (9.56) and (9.57) results in

$$\phi(t, \mathbf{a}) = c_{\phi_0,0} + c_{\mathrm{f},0}t + (\mathbf{c}_{\phi_0,1} + \mathbf{c}_{\mathrm{f},1}t) \cdot \mathbf{a} \tag{9.58}$$

The n_s sampled phases $\mathbf{v}_\phi^1(t) = \{v_{\phi_1}(t), \ldots, v_{\phi_{n_\mathrm{s}}}(t)\}$ resulting from sampling method g^1 are, therefore,

$$v_{\phi_k}^1(t) = c_{\phi_0,0} + c_{\mathrm{f},0}t + (\mathbf{c}_{\phi_0,1} + \mathbf{c}_{\mathrm{f},1}t) \cdot \mathbf{a}_k, \tag{9.59}$$

for $k = 1, \ldots, n_\mathrm{s}$. The resulting $w_\phi^1(t, \mathbf{a})$ of piecewise linear interpolation h^1 of the samples $\mathbf{v}_\phi^1(t)$ then exactly reconstructs the function $\phi(t, \mathbf{a})$

$$w_\phi^1(t, \mathbf{a}) = h^1(\mathbf{v}_\phi^1(t)) = c_{\phi_0,0} + c_{\mathrm{f},0}t + (\mathbf{c}_{\phi_0,1} + \mathbf{c}_{\mathrm{f},1}t) \cdot \mathbf{a} = \phi(t, \mathbf{a}). \tag{9.60}$$

Therefore, error $\hat{\varepsilon}(\phi(t, \mathbf{a}), \mathbf{a})$ in the approximation $\hat{w}^1(w_\phi^1(t, \mathbf{a}), \mathbf{a})$ of response $\hat{u}(\phi(t, \mathbf{a}), \mathbf{a})$ becomes

$$\begin{aligned}
\hat{\varepsilon}(\phi(t, \mathbf{a}), \mathbf{a}) &= \hat{w}^1(w_\phi^1(t, \mathbf{a}), \mathbf{a}) - \hat{u}(\phi(t, \mathbf{a}), \mathbf{a}) \\
&= \hat{w}^1(\phi(t, \mathbf{a}), \mathbf{a}) - \hat{u}(\phi(t, \mathbf{a}), \mathbf{a}) \\
&= w^1(t, \mathbf{a}) - u(t, \mathbf{a}) \\
&= \varepsilon(t, \mathbf{a}) < \delta \quad \text{for all } \phi \in \mathbb{R} \text{ and } \mathbf{a} \in A,
\end{aligned} \tag{9.61}$$

according to Theorem 5. Using (9.42) gives

$$\varepsilon(t, \mathbf{a}) < \delta \quad \text{for all } t \in \mathbb{R} \text{ and } \mathbf{a} \in A. \tag{9.62}$$

□

Unsteady Adaptive Stochastic Finite Elements method l^2 based on a piecewise quadratic interpolation method h^2 of samples in the second degree Newton-Cotes quadrature points in simplex elements of sampling method g^2 consequently gives $\varepsilon(t, \mathbf{a}) < \delta$ for all $t \in \mathbb{R}$ and $\mathbf{a} \in A$ up to quadratic dependence of $\phi_0(\mathbf{a})$ and $f(\mathbf{a})$ on $\mathbf{a}$.

For periodic responses the interpolation of the samples at constant phase eliminates the effect of the increasing phase differences in time, which usually causes the fast increase of the number of required samples. The error is even bounded in time for periodic problems with an up to quadratic dependence of initial phase $\phi_0(\mathbf{a})$ and

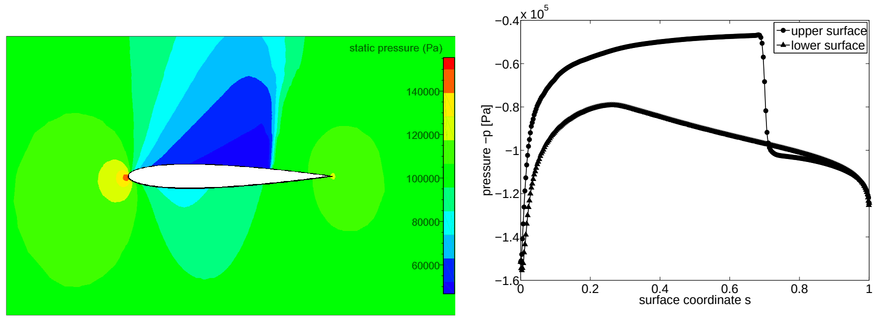

(a) Pressure field

(b) Surface distribution

Figure 9.1: Deterministic pressure for mean angle of attack $\mu_\alpha = 2^o$ for the steady transonic airfoil flow.

frequency $f(\mathbf{a})$ on random parameters $\mathbf{a}$. For non-periodic responses the interpolation at constant phase also eliminates the effect of the increasing phase differences on the increase of the number of required samples. The error is for non-periodic responses not bounded in time due to, for example, increasing amplitudes with time. In practice, interpolation of oscillatory samples in time results, however, in an approximately constant accuracy in time with a constant number of samples for periodic and non-periodic responses of which the phase is well-defined.

9.4 Numerical results

The developed uncertainty quantification methods are applied to transonic airfoil flows. Adaptive Stochastic Finite Elements with Newton-Cotes quadrature in simplex elements is applied to a steady transonic airfoil flow in section 9.4.1. A transonic airfoil flutter problem is analyzed in section 9.4.2 using Unsteady Adaptive Stochastic Finite Elements with interpolation at constant phase.

9.4.1 Steady transonic airfoil flow

The steady transonic flow over a NACA0012 airfoil is considered with randomness in the angle of attack $\alpha(\omega)$. The randomness around the mean angle of attack $\mu_\alpha = 2^o$ is given by a symmetrical beta distribution with $\beta_1 = \beta_2 = 2$ in domain $\alpha \in [1^o, 3^o]$, which corresponds to an input coefficient of variation of $\mathrm{cv}_\alpha = 22.4\%$. Standard atmospheric free stream pressure $p_\infty = 101300$Pa and temperature $T_\infty = 293$K results for free stream velocity $V_\infty = 276.27$m/s in a Mach number of $M_\infty = 0.8$. The flow is modeled here by the compressible Euler equations [15] mainly to demonstrate the properties of the uncertainty quantification method. The two-dimensional flow domain is discretized by an unstructured hexahedral mesh of $12 \cdot 10^3$ cells, which was selected based on a grid convergence study. The Euler equations are discretized using a second order central finite volume discretization stabilized with artificial dissipation [35]. The steady state solution is obtained by time integration with a CFL number of 1.5.

The deterministic flow for the mean angle of attack $\mu_\alpha = 2^\mathrm{o}$ is transonic with a shock wave at 70.2% of the upper surface, as can be identified in the pressure field and the pressure distribution over the airfoil surface in Figure 9.1. This shock wave in physical space results in a discontinuity in probability space. On the lower surface there is also a small supersonic region present.

Adaptive Stochastic Finite Elements with first and second degree Newton-Cotes (NC) quadrature in simplex elements are employed to resolve the response surfaces and probability distributions of the functionals lift, drag, pitching moment, and shock location in Figures 9.2 and 9.3. The first and second degree Newton-Cotes approximations of the response surfaces based on $n_\mathrm{s} = 17$ samples are in close agreement in Figure 9.2. Both discretizations result in an interpolation that preserves the extrema of the samples. The response surface of the shock location is less smooth than that of the other functionals, because the shock location attains discrete values of the locations of the volume faces on the airfoil surface. Since the multi-element approximations are piecewise continuously differentiable, it is more appropriate to study the variation in the functionals in terms of the resulting cumulative probability distributions in Figure 9.3 than in terms of their probability densities. The convergence for the mean and standard deviation of the lift, drag, pitching moment, and shock location given in Tables 9.1 to 9.4 shows a higher accuracy for second degree Newton-Cotes quadrature compared to first degree Newton-Cotes especially for the mean. The standard deviation ranges from 4.6% of the mean for the shock location to 27.4% for the pitching moment.

The effect of the random $\alpha(\omega)$ on the surface pressure distribution in terms of the mean and the 99% uncertainty interval is given in Figure 9.4 for the more accurate second degree Newton-Cotes quadrature. The discretization based on $n_\mathrm{s} = 17$ samples and $n_\mathrm{e} = 8$ elements in Figure 9.4a shows that the shock wave on the upper surface is smeared out in the mean sense compared to the deterministic case of Figure 9.1b. The uncertainty interval in the shock region indicates that $\alpha(\omega)$ has more effect on the shock wave location than on the shock wave strength. This Euler computation also indicates a significantly larger uncertainty interval upstream of the shock than down-

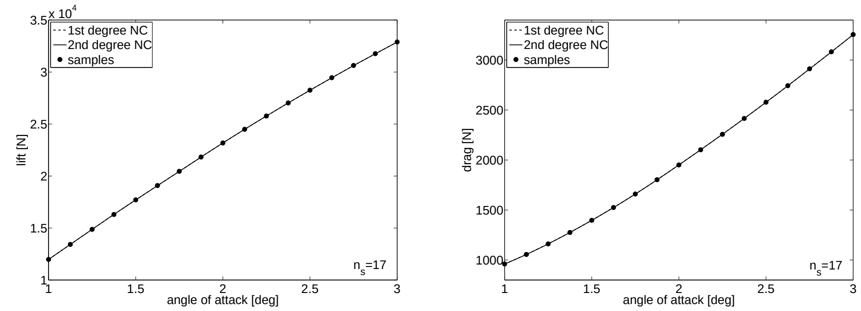

(a) Lift (b) Drag

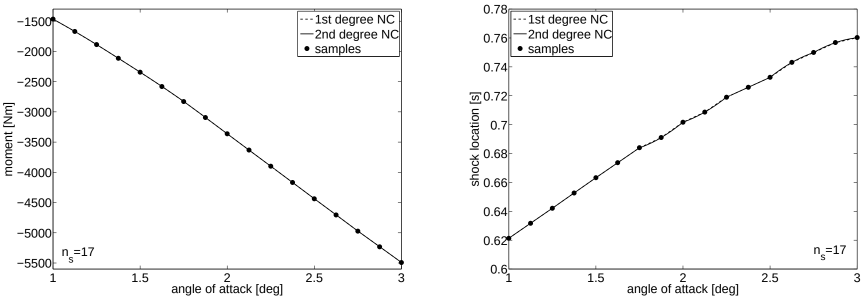

(c) Moment (d) Shock location

Figure 9.2: Response surfaces of lift, drag, pitching moment, and shock location for the steady transonic airfoil flow with random angle of attack $\alpha(\omega)$.

Table 9.1: Mean and standard deviation of lift $L(\omega)$ for the steady transonic airfoil flow with random angle of attack $\alpha(\omega)$.

	1st degree NC			2nd degree NC		
n_{s}	n_{e}	mean μ_{L}	st.dev. σ_{L}	n_{e}	mean μ_{L}	st.dev. σ_{L}
2	1	$2.244 \cdot 10^4$	$4.676 \cdot 10^3$	-	-	-
3	2	$2.290 \cdot 10^4$	$4.679 \cdot 10^3$	1	$2.303 \cdot 10^4$	$4.679 \cdot 10^3$
5	4	$2.299 \cdot 10^4$	$4.703 \cdot 10^3$	2	$2.302 \cdot 10^4$	$4.710 \cdot 10^3$
9	8	$2.301 \cdot 10^4$	$4.711 \cdot 10^3$	4	$2.302 \cdot 10^4$	$4.714 \cdot 10^3$
17	16	$2.302 \cdot 10^4$	$4.712 \cdot 10^3$	8	$2.302 \cdot 10^4$	$4.712 \cdot 10^3$

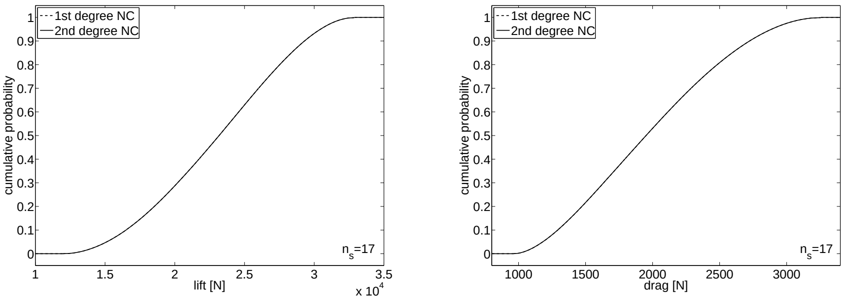

(a) Lift
(b) Drag

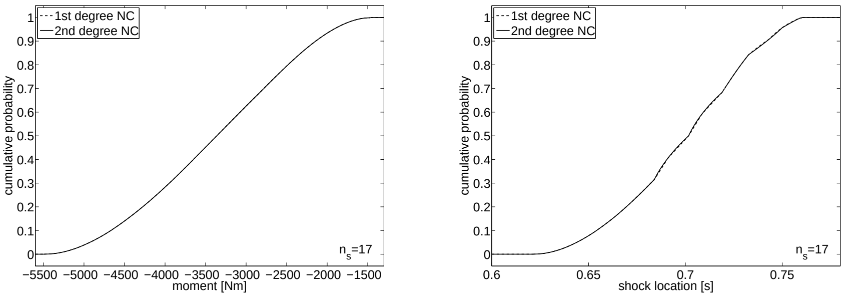

(c) Moment
(d) Shock location

Figure 9.3: Cumulative probability distributions of lift, drag, pitching moment, and shock location for the steady transonic airfoil flow with random angle of attack $\alpha(\omega)$.

Table 9.2: Mean and standard deviation of drag $D(\omega)$ for the steady transonic airfoil flow with random angle of attack $\alpha(\omega)$.

	1st degree NC			2nd degree NC		
n_s	n_e	mean μ_D	st.dev. σ_D	n_e	mean μ_D	st.dev. σ_D
2	1	$2.108 \cdot 10^3$	$5.132 \cdot 10^2$	-	-	-
3	2	$2.010 \cdot 10^3$	$5.146 \cdot 10^2$	1	$1.982 \cdot 10^3$	$5.143 \cdot 10^2$
5	4	$1.988 \cdot 10^3$	$5.231 \cdot 10^2$	2	$1.981 \cdot 10^3$	$5.256 \cdot 10^2$
9	8	$1.982 \cdot 10^3$	$5.254 \cdot 10^2$	4	$1.981 \cdot 10^3$	$5.261 \cdot 10^2$
17	16	$1.981 \cdot 10^3$	$5.258 \cdot 10^2$	8	$1.981 \cdot 10^3$	$5.259 \cdot 10^2$

Table 9.3: Mean and standard deviation of pitching moment $M(\omega)$ for the steady transonic airfoil flow with random angle of attack $\alpha(\omega)$.

	1st degree NC			2nd degree NC		
n_s	n_e	mean μ_M	st.dev. σ_M	n_e	mean μ_M	st.dev. σ_M
2	1	$-3.479 \cdot 10^3$	$9.003 \cdot 10^2$	-	-	-
3	2	$-3.406 \cdot 10^3$	$9.008 \cdot 10^2$	1	$-3.386 \cdot 10^3$	$9.007 \cdot 10^2$
5	4	$-3.390 \cdot 10^3$	$9.219 \cdot 10^2$	2	$-3.385 \cdot 10^3$	$9.279 \cdot 10^2$
9	8	$-3.385 \cdot 10^3$	$9.275 \cdot 10^2$	4	$-3.383 \cdot 10^3$	$9.292 \cdot 10^2$
17	16	$-3.384 \cdot 10^3$	$9.282 \cdot 10^2$	8	$-3.384 \cdot 10^3$	$9.285 \cdot 10^2$

Table 9.4: Mean and standard deviation of shock location $s_\mathrm{shock}(\omega)$ for the steady transonic airfoil flow with random angle of attack $\alpha(\omega)$.

	1st degree NC			2nd degree NC		
n_s	n_e	mean μ_s	st.dev. σ_s	n_e	mean μ_s	st.dev. σ_s
2	1	$6.908 \cdot 10^{-1}$	$3.108 \cdot 10^{-2}$	-	-	-
3	2	$6.976 \cdot 10^{-1}$	$3.120 \cdot 10^{-2}$	1	$6.995 \cdot 10^{-1}$	$3.117 \cdot 10^{-2}$
5	4	$6.985 \cdot 10^{-1}$	$3.118 \cdot 10^{-2}$	2	$6.988 \cdot 10^{-1}$	$3.118 \cdot 10^{-2}$
9	8	$6.994 \cdot 10^{-1}$	$3.166 \cdot 10^{-2}$	4	$6.997 \cdot 10^{-1}$	$3.181 \cdot 10^{-2}$
17	16	$6.992 \cdot 10^{-1}$	$3.184 \cdot 10^{-2}$	8	$6.991 \cdot 10^{-1}$	$3.190 \cdot 10^{-2}$

stream of the shock. The 99% uncertainty interval falls within the range of the sampled minimum and maximum given by the dotted line in Figure 9.4a, which demonstrates the extrema diminishing property of the method. The result for the pressure distribution on the lower surface of Figure 9.4b predicts a shock wave only for a fraction of the realizations. Discretizations with $n_{\mathrm{s}} = \{3, 5, 9\}$ show in Figure 9.4c convergence of a staircase approximation of the mean and the uncertainty interval to a smooth behavior. Uniform stochastic grid refinement is used here in the examples.

Figure 9.5 shows an approximation of the mean and standard deviation of the pressure field relative to the airfoil. In the mean pressure field the smearing of the shock wave can again be identified. The standard deviation field shows that standard deviation is produced in the shock region with a maximum coefficient of variation of $\mathrm{cv}_{\mathrm{p}} = 37.1\%$ at 68.9% of the upper surface. This corresponds to a maximum amplification of input randomness $\alpha(\omega)$ by 65.6%.

9.4.2 Transonic airfoil flutter

The combined effect of independent randomness in the ratio of natural frequencies $\bar{\omega}(\omega)$ and the free stream velocity $U_\infty(\omega)$ on the post-flutter behavior of an elastically mounted airfoil is analyzed. The structural model of the pitch-plunge airfoil with cubic nonlinear spring stiffness is given (7.5) and (7.6), see Figure 7.15a. The nonlinear spring constant for the pitch degree of freedom is here $\beta_\alpha = 3\mathrm{rad}^{-}2$. The randomness in $\bar{\omega}(\omega)$ is described by a uniform distribution around mean value $\mu_{\bar{\omega}} = 0.25$ with a coefficient of variation of 10%. The free stream velocity $U_\infty(\omega)$ is subject to a symmetric unimodal beta distribution with $\beta_1 = \beta_2 = 2$ with a coefficient of variation of 1% around mean $\mu_{\mathrm{U}_\infty} = 276.27$m/s, which corresponds to $M_\infty = 0.8$.

The non-dimensional aerodynamic lift and moment coefficients, $C_{\mathrm{l}}(\tau)$ and $C_{\mathrm{m}}(\tau)$, are determined by solving the Euler equations as for the steady transonic airfoil flow. An Arbitrary Lagrangian-Eulerian formulation is employed to couple the fluid mesh with the movement of the structure. The fluid mesh is deformed using radial basis function interpolation of the boundary displacements [9]. Time integration is performed using the second order BDF-2 method until $t = 3$ with time step $\Delta t = 0.002$, which was established after a time step refinement study. Initially the airfoil is at rest at a deflection of $\alpha(0) = 0.1$deg and $\xi(0) = 0$ from its equilibrium position. In order to study the post-bifurcation behavior, the bifurcation parameter U^* is fixed at 130% of the deterministic linear bifurcation point for the mean values of the random parameters. The stochastic behavior of the angle of attack $\alpha(t, \omega)$ is resolved as indicator for the post-flutter airfoil behavior.

The Unsteady Adaptive Stochastic Finite Elements response surface approximation of the angle of attack $\alpha(t, \omega)$ as function of the random parameters $\bar{\omega}(\omega)$ and $U_\infty(\omega)$

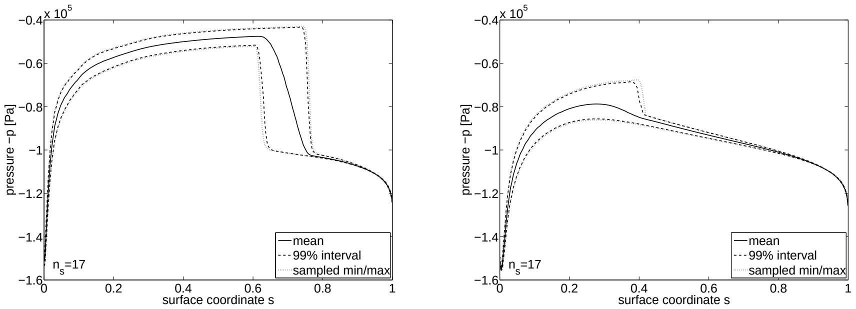

(a) Upper surface (b) Lower surface

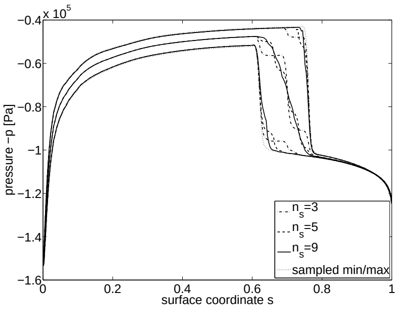

(c) Convergence

Figure 9.4: Mean surface pressure and 99% uncertainty interval of second degree Newton-Cotes quadrature for the steady transonic airfoil flow with random angle of attack $\alpha(\omega)$.

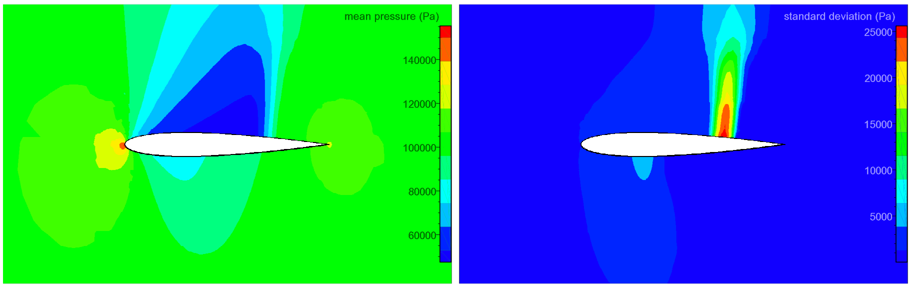

(a) Mean (b) Standard deviation

Figure 9.5: Mean and standard deviation of the pressure field for second degree Newton-Cotes quadrature with $n_{\mathrm{s}} = 17$ for the steady transonic airfoil flow with random angle of attack $\alpha(\omega)$.

at $t = \{0.5; 1.5; 2.5\}$ given in Figure 9.6 shows an increasingly oscillatory response surface with time. The 10% variation in $\bar{\omega}(\omega)$ has a larger effect on the frequency of the response than $U_\infty(\omega)$ with 1% variation. Both parameters have a small effect on the amplitude of the oscillation of $\alpha(t,\omega)$ of approximately 3^{o}. At $t = 0.5$ the airfoil exhibits transient behavior from its initial perturbation of $\alpha(0) = 0.1^{\mathrm{o}}$, which is indicated by the smaller amplitude of the response surface variations of approximately 2^{o}. These results are obtained using the time-independent grid in probability space shown in Figure 9.6d with $n_{\mathrm{s}} = 9$ samples, $n_{\mathrm{e}} = 2$ elements, and $n_{\mathrm{e_{sub}}} = 4096$ post-processing subelements.

The resulting UASFE approximation of the mean $\mu_\alpha(t)$ and standard deviation $\sigma_\alpha(t)$ of the angle of attack $\alpha(t,\omega)$ in Figure 9.7 shows two frequency signals due to the effect of the two random parameters on the frequency of the response. The mean $\mu_\alpha(t)$ exhibits initially an increasing oscillation caused by the deterministic transient of the samples, after which it develops a decaying oscillation due to the effect of the random parameters on the frequency of the response. The large effect of the random parameters on the dynamical system is illustrated by the fast initial increase of the standard deviation $\sigma_\alpha(t)$ from its deterministic initial condition. Although the deterministic post-flutter behavior is highly unsteady, the stochastic response reaches a steady asymptotic behavior with a standard deviation of $\sigma_\alpha = 1.6^{\mathrm{o}}$, which is a factor 16 larger than the initial angle of attack $\alpha(0) = 0.1^{\mathrm{o}}$. The discretizations with $n_{\mathrm{s}} = \{9, 13, 25\}$ samples and $n_{\mathrm{e}} = \{2, 4, 8\}$ uniformly refined elements, respectively, indicate that the results are uniformly converged in time. The approximation with $n_{\mathrm{s}} = 25$ is converged

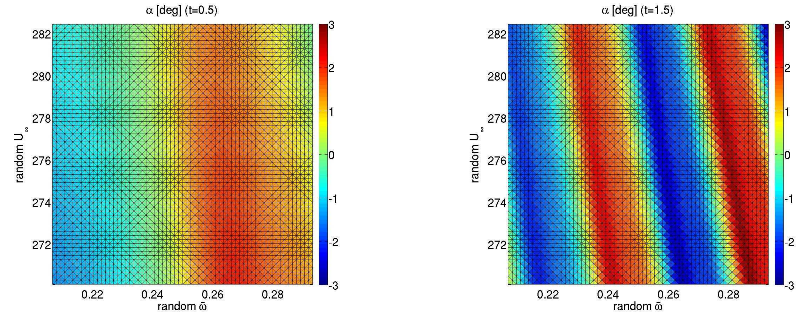

(a) $t = 0.5$

(b) $t = 1.5$

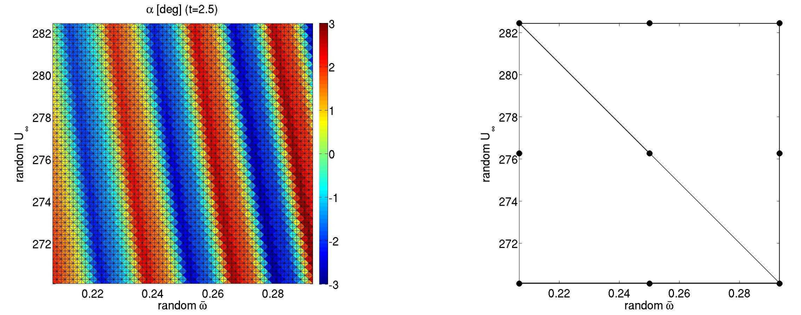

(c) $t = 2.5$

(d) Stochastic grid

Figure 9.6: Response surface of angle of attack $\alpha(\omega)$ as function of random natural frequency ratio $\bar{\omega}(\omega)$ and free stream velocity $U_\infty(\omega)$ for transonic airfoil flutter.

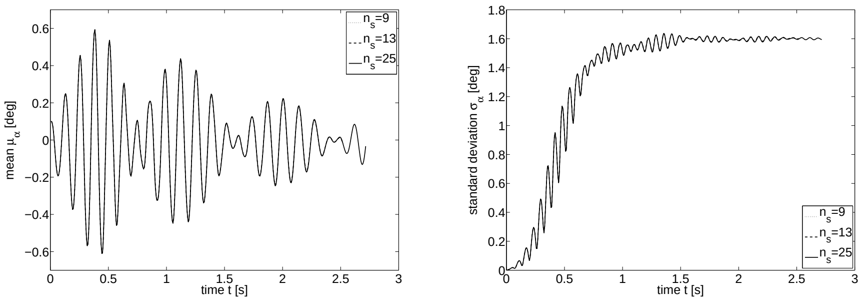

(a) Mean

(b) Standard deviation

Figure 9.7: Mean and standard deviation of angle of attack $\alpha(\omega)$ for transonic airfoil flutter with random natural frequency ratio $\bar{\omega}(\omega)$ and free stream velocity $U_\infty(\omega)$.

Table 9.5: Convergence measure δ_{n_e} for mean angle of attack $\alpha(t,\omega)$ for transonic airfoil flutter with random natural frequency ratio $\bar{\omega}(\omega)$ and free stream velocity $U_\infty(\omega)$.

n_s	n_e	$t = 0.5$	$t = 1.0$	$t = 1.5$	$t = 2.0$	$t = 2.5$
13	4	$0.64 \cdot 10^{-3}$	$3.71 \cdot 10^{-3}$	$4.43 \cdot 10^{-3}$	$7.21 \cdot 10^{-3}$	$4.33 \cdot 10^{-3}$
25	8	$0.27 \cdot 10^{-3}$	$2.46 \cdot 10^{-3}$	$3.14 \cdot 10^{-3}$	$4.42 \cdot 10^{-3}$	$2.68 \cdot 10^{-3}$

up to $\delta_{n_\mathrm{e}} = 6.2 \cdot 10^{-3}$, where δ_{n_e} is defined by (9.5). The local convergence for $\mu_\alpha(t)$ and $\sigma_\alpha(t)$ at $t = \{0.5; 1.0; 1.5; 2.0; 2.5\}$ given in Tables 9.5 and 9.6 for $n_\mathrm{s} = \{13, 25\}$ shows no clear increase of convergence measure δ with time. This illustrates that the convergence and the accuracy of the UASFE approximation are in practice constant in time.

9.5 Summary

A robust and efficient Unsteady Adaptive Stochastic Finite Elements (UASFE) method is developed for uncertainty quantification in time-dependent simulations. The underlying Adaptive Stochastic Finite Elements (ASFE) discretization based on Newton-Cotes quadrature in simplex elements is extrema diminishing (ED) in probability space. The method is also total variation diminishing (TVD) in probability space for one

Table 9.6: Convergence measure δ_{n_e} for the standard deviation of angle of attack $\alpha(t,\omega)$ for transonic airfoil flutter with random natural frequency ratio $\bar{\omega}(\omega)$ and free stream velocity $U_\infty(\omega)$.

n_s	n_e	$t = 0.5$	$t = 1.0$	$t = 1.5$	$t = 2.0$	$t = 2.5$
13	4	$2.94 \cdot 10^{-3}$	$3.28 \cdot 10^{-3}$	$7.50 \cdot 10^{-3}$	$5.38 \cdot 10^{-3}$	$3.90 \cdot 10^{-3}$
25	8	$0.97 \cdot 10^{-3}$	$4.39 \cdot 10^{-3}$	$0.86 \cdot 10^{-3}$	$2.19 \cdot 10^{-3}$	$3.34 \cdot 10^{-3}$

random parameter and for multiple random parameters for first degree Newton-Cotes quadrature. These properties eliminate the possibility of predicting non-zero probabilities for unphysical outcomes due to overshoots and undershoots at discontinuities. The interpolation of the oscillatory samples at constant phase in the UASFE method results in a bounded error as function of the phase for periodic responses. The UASFE method also results in a bounded error in time, if the initial phase and the frequency of the response depends linearly or quadratically on the random parameters. In practice this results in a constant uncertainty quantification accuracy in time with a constant number of samples for both periodic and non-periodic responses.

The applications to a transonic airfoil flow and a transonic airfoil flutter problem show a significant effect of input randomness. In the steady transonic airfoil flow randomness in the angle of attack results in production of standard deviation in the shock region with a maximum coefficient of variation $\mathrm{cv}_\mathrm{p} = 37.1\%$ at 68.9% of the upper surface, which corresponds to an amplification of input randomness by 65.6%. The unsteady transonic airfoil flutter problem shows a steady asymptotic stochastic behavior with a standard deviation of 1.6^o, which is a factor 16 larger than the deterministic initial condition.

Chapter 10

Conclusions and recommendations

Efficient and robust uncertainty quantification methods are presented for resolving the effect of physical randomness in computationally intensive flow and fluid-structure simulations including discontinuities and unsteadiness. The main conclusions of this thesis are summarized in section 10.1. In section 10.2 recommendations for future work are given.

10.1 Conclusions

The properties of the developed uncertainty quantification methods are summarized in section 10.1.1. The physical observations that result from the application of these methods are resumed in section 10.1.2.

10.1.1 Developed uncertainty quantification methods

A number of uncertainty quantification methods are derived that result in a significant improvement over existing methods in terms of efficiency and robustness. These developments show the potential to advance uncertainty quantification for computationally intensive unsteady problems with discontinuities from practically impossible to a routine analysis. The proposed Gram-Schmidt Polynomial Chaos method improves the efficiency of the Galerkin Polynomial Chaos method by contributing to the extension of the spectral convergence to arbitrary distributions. The introduced Monomial Chaos method leads to an efficient construction of the Polynomial Chaos expansion using an uncoupled set of linear equations for problems with polynomial nonlinearities. Discontinuities can robustly be resolved by the developed non-intrusive Adaptive Stochastic Finite Elements method based on Newton-Cotes quadrature in simplex elements, which is total variation diminishing and extrema diminishing in probability space. The efficient methods developed for oscillatory unsteady problems are Probabilistic Collocation for Limit Cycle Oscillations, and Unsteady Adaptive Stochastic Finite Elements with time-independent parameterization, with interpolation at constant phase, and with wavelet decomposition for multi-frequency responses. They result in a bounded uncertainty quantification error for periodic responses, which results in practice in a constant accuracy in time with a constant number of samples. Three strategies for resolving the effect of multiple random inputs efficiently are studied in the context of Gram-Schmidt Polynomial Chaos.

10.1.1.1 Gram-Schmidt Polynomial Chaos

A Gram-Schmidt Polynomial Chaos method is proposed to contribute to the extension of the spectral convergence of Galerkin Polynomial Chaos to arbitrary input probability distributions. Gram-Schmidt orthogonalization is employed to analytically construct a set of suitable orthogonal basis polynomials using the statistical moments of random input with an arbitrary distribution. Three strategies for reducing the computational costs in case of many random input parameters are also studied in this context: (i) select only the most important parameters; (ii) combine multiple parameters into fewer ones; and (iii) estimate their first-order combined effect. The second approach can be used effectively due to the extension of the Polynomial Chaos formulation to arbitrary input distributions. A combination of the three strategies approximates the effect of six random parameters in a channel flow heat transfer problem using a two-dimensional probability space.

10.1.1.2 Monomial Chaos

A Monomial Chaos approach is developed which results in an uncoupled set of linear equations for constructing the Polynomial Chaos expansion in problems involving polynomial nonlinearities. This reduces the computational work per additional Polynomial Chaos order to the equivalence of a single linear Newton iteration. The proposed approach employs a Polynomial Chaos expansion with monomials as basis functions. The equations for the Monomial Chaos coefficients are obtained by differentiating the governing deterministic equations. Results for the Burgers equation with small input variation lead to a 2 to 3 times faster error convergence as function of computational work compared to other Polynomial Chaos methods. It is illustrated for a boundary layer flow problem that the additional computational costs for a Monomial Chaos uncertainty quantification can be smaller than that of a single deterministic solve.

10.1.1.3 Adaptive Stochastic Finite Elements with Newton-Cotes quadrature in simplex elements

An Adaptive Stochastic Finite Elements (ASFE) method is presented based on Newton-Cotes quadrature in simplex elements. The method is an extrema diminishing (ED) uncertainty quantification method in probability space. It is also shown that the method is total variation diminishing (TVD) for one random parameter and for multiple random parameters for first degree Newton-Cotes quadrature. These properties assure that no non-zero probabilities of unphysical realizations can be predicted due to overshoots and undershoots near discontinuities. The error convergence rate for one random parameter is of second and fourth order for first and second degree Newton-Cotes, respectively. The second degree Newton-Cotes method is extended to an adaptive scheme in probability space. The stochastic grid is refined based on the largest absolute eigenvalue of the Hessian weighted by the probability contained in the elements until a robust convergence criterion is reached. The second degree Newton-Cotes quadrature points result for uniform refinement in approximately 2 samples per element by reusing samples in successive refinement steps and by using samples in approximating the response in multiple elements. If the quadratic interpolation in an element results in an extremum other than in a quadrature point, then the element is divided into subelements with a linear approximation of the response.

10.1.1.4 Probabilistic Collocation for Limit Cycle Oscillations

For unsteady problems the concept of interpolating a time-independent parameterization of periodic samples instead of the time-dependent samples themselves is introduced. This results in a time-independent uncertainty quantification interpolation accuracy of the time-independent parameters for a constant number of samples. The approach is applicable to the asymptotic range of period-1 limit cycle oscillations (LCO), for which a suitable parameterization consists of the time-independent functionals frequency, relative phase, amplitude, a reference value, and the normalized period. In the developed Probabilistic Collocation for Limit Cycle Oscillations (PCLCO) approach the global polynomial approximation and the Gauss quadrature sampling of Probabilistic Collocation are employed for the actual interpolation. A number of 3 deterministic samples is found to be already sufficient for PCLCO to resolve the asymptotic effect of random free stream velocity on an elastically mounted cylinder.

10.1.1.5 Unsteady Adaptive Stochastic Finite Elements

The applicability of the uncertainty quantification interpolation of a time-independent parameterization is extended in the Unsteady Adaptive Stochastic Finite Elements (UASFE) method. Stochastic bifurcations of dynamical systems are resolved by the ASFE interpolation with Newton-Cotes quadrature in simplex elements of non-smooth time-independent functionals. Asymptotically non-periodic responses are parameterized by the inclusion of a damping parameter. Higher-period oscillations are resolved by an algorithm for parameterizing more complex shape functions. The parameterization error is used to determine the time interval in which the UASFE approximation is valid. Results for the Duffing oscillator show a reduction of computational costs by 3 orders of magnitude compared to Monte Carlo simulation.

10.1.1.6 Unsteady Adaptive Stochastic Finite Elements with interpolation at constant phase

A second UASFE concept for uncertainty quantification of oscillatory responses is developed based on interpolation of the samples at constant phase. The scaling of the samples with their phase eliminates the effect of the increasing phase differences in the response. It is shown that this formulation results in a bounded error as function of the phase for periodic responses. The UASFE method also results in a bounded error in time, if the initial phase and the frequency of the response depend linearly or quadratically on the random parameters. In practice this results in a constant uncertainty quantification accuracy in time with a constant number of samples. The resulting formulation is not subject to a parameterization error, which improves the convergence behavior of the method, and it can resolve time-dependent functionals such as in transient behavior. The method is applicable to responses of which the phase is well-defined. Results show a fourth-order convergence, in line with the underlying second degree Newton-Cotes ASFE interpolation.

10.1.1.7 Unsteady Adaptive Stochastic Finite Elements for multi-frequency aeroelastic responses

The Unsteady Adaptive Stochastic Finite Elements framework is further extended to fluid-structure interactions with multi-frequency responses and continuous structures by employing a wavelet decomposition preprocessing step. The effect of the input randomness on the single-frequency components obtained by the wavelet decomposition is determined by employing UASFE interpolation at constant phase. The stochastic behavior of the multi-frequency response is finally determined by summing the separate effects of the single-mode components. The multi-frequency response of a continuous structure is first projected onto either the nodal basis of a finite elements discretization or the modal basis of the natural modes of the structure in vacuum. Fourth-order convergence leads also for multi-frequency responses and continuous structures to a 3 orders of magnitude reduction of computational costs compared to Monte Carlo simulation.

10.1.2 Physical observations

The developed methods are applied to steady problems in channel flow heat transfer, boundary layer flow, and transonic flow around a NACA0012 airfoil. Unsteady applications include a piston problem, airfoil flutter models, the Duffing oscillator, and fluid-structure interaction of an elastically mounted cylinder and airfoil, a flutter panel, and the three-dimensional transonic AGARD 445.6 wing aeroelastic benchmark. Random fields and random input parameters with various probability distributions in physical parameters, geometrical parameters, and boundary and initial conditions are considered. Their effect on the probability distribution and statistical moments of an output of practical interest is resolved. The main physical observations resulting from these applications are summarized below:

- The various random parameters in the channel flow heat transfer problem have significantly different qualitative and quantitative effects on the standard deviation temperature field. The combined effect of the parameters is larger than their separate effects.

- Nonlinear advection-diffusion problems with discontinuities can be highly sensitive to input variation with amplification of the input coefficient of variation up to a factor 18.4 for the piston problem. The transonic airfoil flow shows a variation of the shock wave location from 50% to 80% of the chord due to a 1% variation in free stream Mach number.

- A random parameter that affects the frequency of a periodic oscillation results in steady asymptotic stochastic behavior. The mean structural displacement exhibits a decaying oscillation to its equilibrium position. The standard deviation shows an initially oscillatory increase from a deterministic initial condition to a steady asymptotic value.

- Oscillatory linear problems with a non-zero probability of negative damping result asymptotically in a diverging output standard deviation. The mean system energy also diverges asymptotically in that case in contrast with the mean displacement. In that respect, system energy is a more intuitive measure to illustrate the effect of randomness on the system response.

- Dynamical systems with bifurcations can be extremely sensitive to random initial conditions with an amplification of input randomness by a factor 52.0 for the standard deviation in the Duffing oscillator.

- Randomness leads to the onset of unstable behavior in the elastically mounted airfoil problem, which a single deterministic simulation for the mean value would have missed. The probability density of the pitch amplitude exhibits a typical P-bifurcation behavior from a Dirac delta function at zero amplitude to a unimodal probability density function for positive amplitudes. The bifurcation of the probability distribution of the absolute pitch angle shows that a 2.5% reduction of the flutter boundary compared to its deterministic location still results in a 3.8% probability of flutter.

- The potential and kinetic energy of the flutter panel show a qualitatively different stochastic behavior as a result of random plate density and random field modulus of elasticity. The diverging mean and standard deviation of the total structural energy are 2 orders of magnitude more sensitive to variations in the modulus of elasticity than the plate density, which results in an amplification of the input coefficient of variation by a factor 485.

- Even though the mean free stream velocity in the AGARD 445.6 wing problem is fixed at a realistic safety margin of 5% below the deterministic flutter velocity, a 3.5% velocity variation results in a non-zero flutter probability of 6.19%. Taking physical uncertainties into account in numerical predictions is, therefore, a more reliable approach than using safety margins in combination with deterministic simulation results.

10.2 Recommendations

Based on this thesis a number of recommendations for future work are formulated for the further development of the proposed methods in section 10.2.1 and for additional applications to interesting physical problems in section 10.2.2.

10.2.1 Uncertainty quantification methods

Directions of further improvement of the robustness, efficiency, and applicability of the proposed Monomial Chaos, Adaptive Stochastic Finite Elements, and Unsteady Adaptive Stochastic Finite Elements methods are suggested below.

10.2.1.1 Monomial Chaos

The robustness of the Monomial Chaos approach can be improved by extending it to a multi-elements framework. Since the elements would represent only a fraction of the total input variation, a multi-element Monomial Chaos formulation would be applicable to larger input variations. A non-intrusive Monomial Chaos formulation can also be developed for a more straightforward implementation by computing the Monomial Chaos coefficients using finite differences in probability space. This would, however, result in performing a series of deterministic solves, which would compromise the efficiency of the approach.

10.2.1.2 Adaptive Stochastic Finite Elements

The convergence of the Adaptive Stochastic Finite Elements method with Newton-Cotes quadrature in simplex elements can be further improved by implementing higher-order Newton-Cotes quadrature rules than second-degree quadrature used in this thesis. The adaptive grid refinement can also be improved by using the eigenvectors of the Hessian to determine in which direction refinement is most important. Applications to more than 3 random parameters would be interesting to study the effectiveness of the adaptive scheme in high-dimensional probability spaces.

10.2.1.3 Unsteady Adaptive Stochastic Finite Elements

The applicability of Unsteady Adaptive Stochastic Finite Elements can be further extended by integrating it with steady Adaptive Stochastic Finite Elements. Oscillatory samples of which the phase can be determined can then be handled by UASFE and the other samples can be interpolated using steady ASFE. This method adaption can be applied in probability space, physical space, and the temporal dimension.

10.2.2 Applications

Further applications to challenging physical problems including chaotic systems, high-dimensional probability spaces, weakly correlated stochastic processes, geometric variations, validation studies, and model uncertainties are indicated below:

- Chaotic dynamical systems are an interesting application for uncertainty quantification due to their high sensitivity to input variations [93]. At this moment, Monte Carlo simulation seems the most suitable method for this application due to the lack of sufficient regularity in chaotic responses.

- The application of uncertainty quantification to high-dimensional probability spaces forms an important challenge due to the curse-of-dimensionality for most methods. The scalability of methods with the number of random parameters is essential in that respect [20, 70]. More specifically a constant order of convergence independent of the dimensionality of probability space is required.

- For weakly correlated stochastic processes Markov chain Monte Carlo is a more suitable approach than the Karhunen-Loève expansion. It would be interesting to develop more efficient alternatives for Markov chain Monte Carlo of stochastic processes in analogy to the more efficient methods developed as alternatives for Monte Carlo simulation of random parameters. This problem appears to have similarities to the problem of high-dimensional probability spaces.

- In this thesis a number of relatively simple random geometric parameters is considered. More complex geometric variations pose a particular challenge for intrusive Polynomial Chaos formulations in terms of domain definition [75, 118] and the computational mesh [79]. For non-intrusive methods, geometric variations lead to practical issues of generating the different computational domains for the deterministic solves [74] and presenting the results on stochastic domains.

- Validating numerical uncertainty quantification results based on measured physical input variability and the resulting output variations would increase the awareness of the additional value of uncertainty quantification in numerical simulations [82]. This is obviously not a straightforward exercise due to difficulties in, for example, measuring the input variations, quantifying the degree of match between the numerical and experimental results [72, 76], and accounting for experimental and numerical errors.

- Next to the well-established quantification of numerical errors and the quantification of the effect of physical randomness also other sources of uncertainty should be incorporated in a complete analysis. Model uncertainties are an important third factor which affects the reliability of computational predictions. For example, the model uncertainty in RANS turbulence models results in significant variation in the prediction of flow phenomena. Model uncertainty can be taken into account using non-parametric uncertainties [94] or in a multimodel approach based on evidence theory [81].

Appendix A

Standard uncertainty quantification methods

Below, four widely used uncertainty quantification methods are briefly reviewed for comparison with the methods developed here: the Monte Carlo method, the perturbation method [45], the Galerkin Polynomial Chaos method [27], and a non-intrusive Polynomial Chaos method [36]. For simplicity, the methods are reviewed for the case of a single uncertain parameter $\alpha(\omega)$. They all have extensions to higher dimensions.

A.1 The Monte Carlo method

A robust approach to solving (3.1) is the Monte Carlo method. It is based on solving the deterministic problem multiple times for a set of N realizations of the uncertain parameter $\{\alpha_k\}_{k=1}^N$ with $\alpha_k \equiv \alpha(\omega_k)$,

$$\mathcal{L}(\mathbf{x}, t, \alpha_k; u_k(\mathbf{x}, t)) = S(\mathbf{x}, t, \alpha_k), \qquad k = 1, \dots, N, \tag{A.1}$$

with $u_k(\mathbf{x}, t) \equiv u(\mathbf{x}, t, \omega_k)$. The stochastic properties of the output can be obtained from the set of N realizations of the uncertain variable $\{u_k(\mathbf{x}, t)\}_{k=1}^N$. Due to the slow convergence rate, the standard Monte Carlo approach can be impractical when solving a single deterministic problem already involving a large amount of computational work. Methods exist to improve the convergence rate of standard Monte Carlo, such as Latin-hypercube sampling and variance reduction techniques; see, for example, [32].

A.2 The perturbation method

A fast method for determining low-order statistics is the perturbation method (also called the moment method) [34, 45, 95]. It has recently been applied to problems in computational fluid dynamics [57, 99]. In the perturbation method the statistical moments of the output are expanded around the expected value of the uncertain parameter using Taylor series expansions. These expansions are usually truncated at second order, since for higher orders the equations become extremely complicated [27, 45]. The second-order estimate of the mean value is given by [45] as

$$\mathbb{E}[u(\mathbf{x},t,\omega)] \approx u(\mathbf{x},t,\omega)\bigg|_{\alpha=\mu_\alpha} + \frac{1}{2}\mathrm{Var}(\alpha(\omega))\frac{\partial^2 u}{\partial \alpha^2}\bigg|_{\alpha=\mu_\alpha}, \tag{A.2}$$

with $\mu_\alpha \equiv \mathbb{E}[\alpha(\omega)]$. For the first-order approximation, this relation reduces to $\mathbb{E}[u(\mathbf{x},t,\omega)] \approx u(\mathbf{x},t,\omega)|_{\mu_\alpha}$. The first-order estimate of the variance is given as

$$\mathrm{Var}[u(\mathbf{x},t,\omega)] \approx \left(\frac{\partial u}{\partial \alpha}\bigg|_{\alpha=\mu_\alpha}\right)^2 \mathrm{Var}[\alpha(\omega)]. \tag{A.3}$$

The moment approximations require the computation of the first and second sensitivity derivatives of the solution $u(\mathbf{x},t,\omega)$ with respect to the uncertain parameter $\alpha(\omega)$ for $\alpha(\omega) = \mu_\alpha$. A method for evaluating these sensitivity derivatives is the continuous sensitivity equation method [34, 95]. In the continuous sensitivity equation method a differential equation for the $i\mathrm{th}$ sensitivity derivative $\frac{\partial^i u}{\partial \alpha^i}|_{\mu_\alpha}$ is obtained by implicit differentiation of the governing equation (3.1) with respect to α for $\alpha(\omega) = \mu_\alpha$. The resulting equation is called the $i\mathrm{th}$ continuous sensitivity equation

$$\frac{\partial^i}{\partial \alpha^i}\mathcal{L}(\mathbf{x},t,\alpha(\omega);u(\mathbf{x},t,\omega))\bigg|_{\mu_\alpha} = \frac{\partial^i}{\partial \alpha^i}S(\mathbf{x},t,\alpha(\omega))\bigg|_{\mu_\alpha}. \tag{A.4}$$

The application of the perturbation method is limited to low-order approximations for small perturbations, i.e., inputs with a small variance. Furthermore, the method cannot readily be extended to compute the probability distribution function of the response process [27, 45].

A.3 The Galerkin Polynomial Chaos method

A method that is not limited to low-order statistics and small perturbations is the Polynomial Chaos expansion introduced by Ghanem and Spanos [27], which can approximate any functional in $L_2(C)$ and converges in the $L_2(C)$ sense [10]. The Polynomial

Chaos expansions of the uncertain input parameter $\alpha(\omega)$ and the uncertain solution $u(\mathbf{x}, t, \omega)$ are

$$\alpha(\omega) = \sum_{j=0}^{1} \alpha_j \Phi_j(\xi(\omega)), \qquad u(\mathbf{x}, t, \omega) = \sum_{i=0}^{\infty} u_i(\mathbf{x}, t) \Phi_i(\xi(\omega)), \tag{A.5}$$

where $\{\Phi_i(\xi)\}_{i=0}^{\infty}$ is a set of orthogonal polynomials and the random variable $\xi(\omega)$ is given by a linear transformation of $\alpha(\omega)$ to an appropriate standard domain, i.e. $[-1, 1]$, $[0, \infty)$, or $(-\infty, \infty)$. Due to this linear transformation the Polynomial Chaos expansion of $\alpha(\omega)$ in (A.5) is exact within the first two terms. For the numerical implementation the Polynomial Chaos expansion for $u(\mathbf{x}, t, \omega)$ in (A.5) is truncated to $(p+1)$ terms, where p is the Polynomial Chaos order of the approximation. Substituting the truncated expansions into (3.1) and performing a Galerkin projection onto each polynomial basis $\{\Phi_i(\xi)\}_{i=0}^{p}$ results in a coupled set of $(p+1)$ deterministic equations

$$\left\langle \mathcal{L}\left(\mathbf{x}, t, \sum_{j=0}^{1} \alpha_j \Phi_j; \sum_{i=0}^{p} u_i \Phi_i\right), \Phi_k \right\rangle = \left\langle S\left(\mathbf{x}, t, \sum_{j=0}^{1} \alpha_j \Phi_j\right), \Phi_k \right\rangle \tag{A.6}$$

for $k = 0, 1, \ldots, p$. This system of equations can be solved using standard iterative methods [31]. The Galerkin Polynomial Chaos method can be intrusive to implement and computationally intensive to solve, due to the coupled set of equations (A.6).

A.4 A non-intrusive Polynomial Chaos method

To avoid solving a coupled set of equations, a non-intrusive Polynomial Chaos method can be used. It approximates the Polynomial Chaos coefficients by solving a series of deterministic problems. An example of a non-intrusive Polynomial Chaos method is the method of Hosder and Walters (see [36, 104]). The Polynomial Chaos expansion coefficients $\{u_k(\mathbf{x}, t)\}_{k=0}^{p}$ in (A.5) are approximated by evaluating the deterministic problem at $(p+1)$ points in random space $\{\xi_k\}_{k=0}^{p}$, with $\xi_k \equiv \xi(\omega_k)$,

$$\mathcal{L}(\mathbf{x}, t, \alpha_k; u_k^*(\mathbf{x}, t)) = S(\mathbf{x}, t, \alpha_k), \qquad k = 0, 1, \ldots, p, \tag{A.7}$$

where $u_k^*(\mathbf{x}, t)$ is the realization of $u(\mathbf{x}, t, \omega)$ for $\alpha(\omega) = \alpha_k$. The Polynomial Chaos coefficients $\{u_k(\mathbf{x}, t)\}_{k=0}^{p}$ are then approximated by the following relatively small linear system:

$$\begin{pmatrix} \Phi_0(\xi_0) & \Phi_1(\xi_0) & \cdots & \Phi_p(\xi_0) \\ \Phi_0(\xi_1) & \Phi_1(\xi_1) & \cdots & \Phi_p(\xi_1) \\ \vdots & \vdots & \ddots & \vdots \\ \Phi_0(\xi_p) & \Phi_1(\xi_p) & \cdots & \Phi_p(\xi_p) \end{pmatrix} \begin{pmatrix} u_0(\mathbf{x},t) \\ u_1(\mathbf{x},t) \\ \vdots \\ u_p(\mathbf{x},t) \end{pmatrix} = \begin{pmatrix} u_0^*(\mathbf{x},t) \\ u_1^*(\mathbf{x},t) \\ \vdots \\ u_p^*(\mathbf{x},t) \end{pmatrix}, \qquad \text{(A.8)}$$

which can be solved using a single LU decomposition. This non-intrusive Polynomial Chaos method can be shown to converge to the Galerkin Polynomial Chaos expansion coefficients under certain conditions [36]. As for the Monte Carlo method (A.1), non-intrusive Polynomial Chaos results in a set of equations (A.7) which coincide with the deterministic problem for varying parameter values. However, the number of deterministic evaluations can be orders of magnitude smaller than for a standard Monte Carlo simulation due to the combination with the Polynomial Chaos expansion.

In non-intrusive Probabilistic Collocation or Stochastic Collocation approaches [5, 54, 62, 96] the sampling points $\{\xi_k\}_{k=0}^{p}$ are suitable Gauss quadrature points, which are the zeros of the polynomials orthogonal with respect to in input probability density. The interpolation through the quadrature points is then obtained by using Lagrange interpolation polynomials, which decouple system (A.8).

Bibliography

[1] D.A. Anderson, J.C. Tannehill, R.H. Pletcher, Computational fluid mechanics and heat transfer, Ser. Comput. Methods Mech. Thermal Sci., McGraw-Hill, New York (1997).

[2] J.D. Anderson, Fundamentals of aerodynamics, McGraw-Hill, New York (1991).

[3] S.T. Ariaratnam, Some illustrative examples of stochastic bifurcations, in Nonlinearity and chaos in engineering dynamics, J.M.T. Thompson, S.R. Bishop, Eds., Wiley, Chichester (1994) 267–274.

[4] I. Babuška, R. Tempone, G.E. Zouraris, Galerkin finite element approximations of stochastic elliptic partial differential equations, SIAM J. Numer. Anal. 42 (2004) 800–825.

[5] I. Babuška, F. Nobile, and R. Tempone, A stochastic collocation method for elliptic partial differential equations with random input data, SIAM J. Numer. Anal. 45 (2007) 1005–1034.

[6] R. Beaubien, F. Nitzsche, D. Feszty, Time and frequency domain solutions for the AGARD 445 wing, Proceedings of the International Forum on Aeroelasticity and Structural Dynamics (IFASD), Munich, Germany (2005).

[7] P.S. Beran, C.L. Pettit, D.R. Millman, Uncertainty quantification of limit cycle oscillations, J. Comput. Phys. 217 (2006) 217–247.

[8] B.F. Blackwell, K.J. Dowding, and R.J. Cochran, Development and implementation of sensitivity coefficient equations for heat conduction problems, Numer. Heat Tr. B-Fund. 36 (1999) 15–32.

[9] A. de Boer, M.S. van der Schoot, H. Bijl, Mesh deformation based on radial basis function interpolation, Comput. Struct. 85 (2007) 784–795.

[10] R.H. Cameron, W. T. Martin, The orthogonal development of nonlinear functionals in series of Fourier-Hermite functionals, Ann. Math. 48 (1947) 385–392.

[11] A. Carle, M. Fagan, L.L. Green, Preliminary results from the application of automated adjoint code generation to CFL3D, AIAA-1998-4807, 7th AIAA/USAF/NASA/ISSMO Symposium on Multidisciplinary Analysis and Optimization, St. Louis, Missouri (1998).

[12] F. Casciati, L. Faravelli, Fragility analysis of complex structural systems, Research Studies Press, Taunton (1990).

[13] F. Casciati, B. Roberts, Mathematical models for structural reliability analysis, CRC Press, Boca Raton (1996).

[14] A.J. Chorin, Gaussian fields and random flow, J. Fluid Mech. 63 (1974) 21–32.

[15] A.J. Chorin, J.E. Marsden, A mathematical introduction to fluid mechanics, Springer-Verlag, New York (1979).

[16] R. Coifman, M.V. Wickerhauser, Wavelets and adapted waveform analysis, Proceedings of Symposia in Applied Mathematics 47, American Mathematical Society, Providence, Rhode Island (1991) 119–154.

[17] E. Colin, S. Étienne, D. Pelletier, J. Borggaard, A general sensitivity equation formulation for turbulent heat transfer, Numer. Heat Tr. B-Fund. 49 (2006) 125–153.

[18] I. Daubechies, Ten lectures on wavelets, Society for Industrial and applied mathematics, Philadelphia (1992).

[19] M. Deb, I. Babuška, J. Oden, Solution of stochastic partial differential equations using Galerkin finite element techniques, Comput. Methods Appl. Mech. Eng. 190 (2001) 6359–6372.

[20] A. Doostan, G. Iaccarino, A least-squares approximation of high-dimensional uncertain systems, 5th European Congress on Computational Methods in Applied Sciences and Engineering ECCOMAS 2008, Venice, Italy (2008).

[21] E.H. Dowell, Aeroelasticity of plates and shells, Noordhoff International Publishing, Leiden (1975).

[22] E.H. Dowell, H.J. Curtiss, R. Scanlan, F. Sisto, A modern course in aeroelasticity, Kluwer Academic Publisher, Dordrecht (1989).

[23] P. Dunn, J. Dugundji, Nonlinear stall flutter and divergence analysis of cantilevered graphite/epoxy wings, AIAA J. 30 (1992) 153–162.

[24] R. Duvigneau, D. Pelletier, and J. Borggaard, An improved continuous sensitivity equation method for optimal shape design in mixed convection, Numer. Heat Tr. B-Fund. 50 (2006) 1–24.

[25] Y. Fung, An introduction to aeroelasticity, Dover Publications, New York (1969).

[26] W. Gautschi, Orthogonal polynomials; computation and approximation, Oxford University Press, Oxford (2004).

[27] R.G. Ghanem, P. Spanos, Stochastic finite elements: a spectral approach, Springer-Verlag, New York (1991).

[28] B. Ganapathysubramanian, N. Zabaras, Sparse grid collocation schemes for stochastic natural convection problems, J. Comput. Phys. 225 (2007) 652–685.

[29] L. Giraud, J. Langou, and M. Rozloznik, On the loss of orthogonality in the Gram-Schmidt orthogonalization process, Technical Report No. TR/PA/03/25, CERFACS, Toulouse, France (2002).

[30] G.H. Golub, C.F. van Loan. Matrix computations, 3rd ed., John Hopkins University Press, Baltimore (1996).

[31] A. Greenbaum, Iterative methods for solving linear systems, SIAM, Philadelphia (1997).

[32] J.M. Hammersley, D.C. Handscomb, Monte Carlo methods, Methuen's monographs on applied probability and statistics, Fletcher & Son Ltd., Norwich (1964).

[33] A. Harten, High resolution schemes for hyperbolic conservation laws, J. Comput. Phys 49 (1983) 357–393.

[34] E. J. Haug, K. Choi, and V. Komkov, Design sensitivity analysis of structural systems, Academic Press, Orlando (1986).

[35] C. Hirsch, Numerical computation of internal and external flows : fundamentals of computational fluid dynamics, Elsevier, Amsterdam (2007).

[36] S. Hosder, R.W. Walters, R. Perez, A non-intrusive polynomial chaos method for uncertainty propagation in CFD simulations, AIAA-2006-891, 44th AIAA Aerospace Sciences Meeting and Exhibit, Reno, Nevada (2006).

[37] S. Hosder, R.W. Walters, M. Balch, Efficient sampling for non-intrusive polynomial chaos applications with multiple uncertain input variables, AIAA-2007-1939, 48th AIAA/ASME/ASCE/AHS/ASC Structures, Structural Dynamics, and Materials Conference, Honolulu, Hawaii (2007).

[38] S. Hosder, R.W. Walters, M. Balch, Efficient uncertainty quantification applied to the aeroelastic analysis of a transonic wing, AIAA-2008-729, 46th AIAA Aerospace Sciences Meeting and Exhibit, Reno, Nevada (2008).

[39] R.L. Iman, J.C. Helton, J.E. Campbell, An approach to sensitivity analysis of computer models, Part 1. Introduction, input variable selection and preliminary variable assessment, J. Qual. Technol. 13 (1981) 174–183.

[40] K. Itō, Introduction to probability theory, Cambridge University Press, Cambridge (1984).

[41] F. James, Statistical methods in experimental physics, World Scientific, New Jersey (2006).

[42] A. Jameson, Positive schemes and shock modelling for compressible flows, Int. J. Num. Meth. Fluids 20 (1995) 743–776.

[43] R.T. Jones, The unsteady lift of a wing of finite aspect ratio, NACA Report 681 (1940).

[44] C. Kennedy, M. Carpenter, Additive Runge-Kutta schemes for convection-diffusion-reaction equations, Appl. Numer. Math. 44 (2003) 139–181.

[45] M. Kleiber, T.D. Hien, The stochastic finite element method, John Wiley and Sons, New York (1992).

[46] B. Koobus, C. Farhat, Second-order time-accurate and geometrically conservative implicit schemes for flow computations on unstructured dynamic meshes, Comput. Methods Appl. Mech. Engrg. 170 (1999) 103–129.

[47] U. Köylüoğlu, A. Çakmak, S. Nielsen, Interval algebra to deal with pattern loading and structural uncertainties, J. Engrg. Mech. 121 (1995) 1149–1157.

[48] B.H.K. Lee, P. LeBlanc, Flutter analysis of a two-dimensional airfoil with cubic nonlinear restoring force, NAE-AN-36, NRC 25438, National Research Council of Canada (1986).

[49] B.H.K. Lee, L.Y. Jiang, Y.S. Wong, Flutter of an airfoil with a cubic nonlinear restoring force, AIAA-1998-1725, 39th AIAA/ASME/ASCE/AHS/ASC Structures, Structural Dynamics, and Materials Conference, Long Beach, California (1998).

[50] G. Lin, C.H. Su, G.E. Karniadakis, The stochastic piston problem, P. Natl. Acad. Sci. USA 101 (2004) 15840–15845.

[51] N.J. Lindsley, P.S. Beran, C.L. Pettit, Effects of uncertainty on nonlinear plate aeroelastic response, AIAA-2002-1271, 43th AIAA/ASME/ASCE/AHS/ASC Structures, Structural Dynamics, and Materials Conference, Denver, Colorado (2002).

[52] M. Loève, Probability theory, 4th ed., Springer-Verlag, New York (1977).

[53] G.J.A. Loeven, J.A.S. Witteveen, H. Bijl, Efficient uncertainty quantification using a two-step approach with chaos collocation, European Conference on Computational Fluid Dynamics ECCOMAS CFD, Egmond aan Zee, The Netherlands (2006).

[54] G.J.A. Loeven, J.A.S. Witteveen, H. Bijl, Probabilistic collocation: an efficient non-intrusive approach for arbitrarily distributed parametric uncertainties, AIAA-2007-317, 45th AIAA Aerospace Sciences Meeting and Exhibit, Reno, Nevada (2007).

[55] G.J.A. Loeven, J.A.S. Witteveen, H. Bijl, A probabilistic radial basis function approach for uncertainty quantification, NATO RTO-MP-AVT-147 Computational Uncertainty in Military Vehicle Design Symposium, Athens, Greece (2007).

[56] D. Lucor, G.E. Karniadakis, Noisy inflows cause a shedding-mode switching in flow past an oscillating cylinder, Phys. Rev. Lett. 92 (2004) 4501.

[57] J.-N. Mahieu, S. Étienne, D. Pelletier, J. Borggaard, A second-order sensitivity equation method for laminar flow, Int. J. Comput. Fluid D 19 (2005) 143–157.

[58] O.P. Le Maître, O.M. Knio, H.N. Najm, R.G. Ghanem, A Stochastic Projection Method for Fluid Flow I. Basic Formulation, J. Comput. Phys. 173 (2001) 481–511.

[59] O.P. Le Maître, M.T. Reagan, H.N. Najm, R.G. Ghanem, O.M. Knio, A Stochastic Projection Method for Fluid Flow II. Random Process, J. Comput. Phys. 181 (2002) 9–44.

[60] O.P. Le Maître, O.M. Knio, H.N. Najm, R.G. Ghanem, Uncertainty propagation using Wiener-Haar expansions, J. Comput. Phys. 197 (2004) 28–57.

[61] O.P. Le Maître, H.N. Najm, R.G. Ghanem, O.M. Knio, Multi-resolution analysis of Wiener-type uncertainty propagation schemes, J. Comput. Phys. 197 (2004) 502–531.

[62] L. Mathelin, M.Y. Hussaini, Th.A. Zang, Stochastic approaches to uncertainty quantification in CFD simulations, Num. Alg. 38 (2005) 209–236.

[63] L. Mathelin, O.P. Le Maître, Dual-based a posteriori error estimate for stochastic finite element methods, Comm. App. Math. Comp. Sci. 2 (2007) 83–115.

[64] M.D. McKay, W.J. Conover, R.J. Beckman, A comparison of three methods for selecting values of input variables in the analysis of output from a computer code, Technometrics 21 (1979) 239–245.

[65] N. Metropolis, S. Ulam, The Monte Carlo method, J. Am. Stat. Assoc. 44 (1949) 335–341.

[66] D.R. Millman, P.I. King, Airfoil pitch-and-plunge bifurcation behavior with Fourier chaos expansions, J. Aircraft 42 (2005) 376–384.

[67] D. Moens, D. Vandepitte, Fuzzy finite element method for frequency response function analysis of uncertain structures, AIAA J. 40 (2002) 126–136.

[68] R.E. Moore, Interval Analysis, Prentice-Hall, Englewood Cliff (1966).

[69] H.N. Najm, Uncertainty quantification and polynomial chaos techniques in computationl fluid dynamics, Annu. Rev. Fluid Mech. 41 (2009) 35–52.

[70] F. Nobile, R. Tempone, C. Webster, An anisotropic sparse grid stochastic collocation method for partial differential equations with high-dimensional random input data, 5th European Congress on Computational Methods in Applied Sciences and Engineering ECCOMAS 2008, Venice, Italy (2008).

[71] W.L. Oberkampf, S.M. DeLand, B.M. Rutherford, K.V. Diegert, K.F. Alvin, Error and uncertainty in computational simulation, Reliab. Eng. Syst. Safe. 75 (2002) 333–357.

[72] W.L. Oberkampf, S. Ferson, Model validation under both aleatory and epistemic uncertainty, NATO RTO-MP-AVT-147 Computational Uncertainty in Military Vehicle Design Symposium, Athens, Greece (2007).

[73] Openfem, A finite element toolbox for Matlab and Scilab, release 2006a (2006): http://www-rocq.inria.fr/OpenFEM/.

[74] L. Parussini, V. Pediroda, Fictitious domain with least-squares spectral element method to explore geometric uncertainties by non-intrusive polynomial chaos method, CMES 22 (2007) 41–63.

[75] L. Parussini, V. Pediroda, Investigation of multi geometric uncertainties by different polynomial chaos methodologies using a fictitious domain solver, CMES 23 (2008) 29–51.

[76] J.E. Pepin, A.C. Rutherford and F.M. Hemez, Defining a practical QMU metric, AIAA-2008-1717, 49th AIAA/ASME/ASCE/AHS/ASC Structures, Structural Dynamics, and Materials Conference, Schaumburg, Illinois (2008).

[77] C.L. Pettit, P.S. Beran, Effects of parametric uncertainty on airfoil limit cycle oscillations, J. Aircraft 40 (2004) 1217–1229.

[78] C.L. Pettit, P.S. Beran, Spectral and multiresolution Wiener expansions of oscillatory stochastic processes, J. Sound Vib. 294 (2006) 752–779.

[79] C.L. Pettit, P.S. Beran, Convergence studies of Wiener expansions for computational nonlinear mechanics, AIAA-2006-1993, 8th AIAA Non-Deterministic Approaches Conference, Newport, Rhode Island (2006).

[80] D. Poirel, S.J. Price, Bifurcation characteristics of a two-dimensional structurally nonlinear airfoil in turbulent flow, Nonlinear Dynamics 48 (2007) 423–435.

[81] S.V. Poroseva, M.Y. Hussaini, S.L. Woodruff, On improving the predictive capability of turbulence models using evidence theory, AIAA J. 44 (2006) 1220–1228.

[82] P.D.A. Platteeuw, G.J.A. Loeven, H. Bijl, Uncertainty quantification applied to the k-epsilon model of turbulence using the probabilistic collocation method, AIAA-2008-2150, 49th AIAA/ASME/ASCE/AHS/ASC Structures, Structural Dynamics, and Materials Conference Schaumburg, Illinois (2008).

[83] M.M. Putko, P.A. Newman, A.C. Taylor III, L.L. Green, Approach for uncertainty propagation and robust design in CFD using sensitivity derivatives, AIAA-2001-2528, 15th AIAA Computational Fluid Dynamics Conference, Anaheim, California (2001).

[84] M.T. Reagan, H.N. Najm, R.G. Ghanem, O.M. Knio, Uncertainty quantification in reacting-flow simulations through non-intrusive spectral projection, Combust. Flame 132 (2003) 545–555.

[85] C.P. Robert, G. Casella, Monte Carlo statistical methods, Springer, New York (2004).

[86] R. Rubinstein, M. Choudhari, Uncertainty quantification for systems with random initial conditions using WienerHermite expansions, Stud. Appl. Math. 114 (2005) 167–188.

[87] A. Sarkar, R.G. Ghanem, Mid-frequency structural dynamics with parameter uncertainty, Comput. Method Appl. M. 191 (2002) 5499–5513.

[88] S. Sarkar, J.A.S. Witteveen, G.J.A. Loeven, H. Bijl, Effect of uncertainty on the bifurcation behavior of pitching airfoil stall flutter, J. Fluid. Struct. (2008) in press, DOI:10.1016/j.jfluidstructs.2008.06.006.

[89] H.T. Schlichting, K. Gersten, Boundary-layer theory, Springer, Berlin, (2000).

[90] W. Schoutens, Stochastic processes and orthogonal polynomials, Springer, New York, (2000).

[91] G.I. Schuëller, Ed., A state-of-the-art report on computational stochastic mechanics, Prob. Engrg. Mech. 12 (1997) 197–321.

[92] C. Schwab, R.A. Todor, Sparse finite elements for elliptic problems with stochastic loading, Numer. Math. 95 (2003) 707–734.

[93] C.Y. Shen, T.E. Evans, S. Finette, Polynomial-chaos applied to Lorenz's model for quantification of growth of initial uncertainties, 5th European Congress on Computational Methods in Applied Sciences and Engineering ECCOMAS 2008, Venice, Italy (2008).

[94] C. Soize, A nonparametric model of random uncertainties for reduced matrix models in structural dynamics, Probabilist. Eng. Mech. 15 (2000) 277–294.

[95] L.G. Stanley, D.L. Stewart, Design sensitivity analysis: Computational issues of sensitivity equation methods, Frontiers Appl. Math. 25, SIAM, Philadelphia (2002).

[96] M.A. Tatang, Direct incorporation of uncertainty in chemical and environmental engineering systems, PhD thesis, MIT, Cambridge (1995).

[97] J.M.T. Thompson, H.B. Stewart, Nonlinear dynamics and chaos, John Wiley, Chichester (1986).

[98] C. Tran, T. Petot, Semi-empirical model for the dynamic stall of airfoils in view of the application to the calculation of responses of a helicopter blade in forward flight, Vertica 5 (1981) 35–53.

[99] É Turgeon, D. Pelletier, J. Borggaard, A general continuous sensitivity equation formulation for complex flows, Numer. Heat Tr. B-Fund. 42 (2002) 485–508.

[100] C.V. Verhoosel, M.A. Gutirrez, S.J. Hulshoff, Iterative solution of the random eigenvalue problem with application to spectral stochastic finite element systems, Int. J. Numer. M. Eng. 68 (2006) 401-424.

[101] F. Verhulst, Nonlinear differential equations and dynamical systems, Springer, Berlin (2000).

[102] G.G. Walter, Wavelets and other orthogonal systems with applications, Chapman and Hall/CRC, Boca Raton (2001).

[103] R.W. Walters, L. Huyse, Uncertainty analysis for fluid mechanics with applications, NASA/CR-2002-21149, NASA Langley Research Center, Hampton, VA (2002), http://historical.ncstrl.org/tr/pdf/icase/TR-2002-1.pdf.

[104] R.W. Walters, Towards stochastic fluid mechanics via polynomial chaos, AIAA-2003-0413, 41st AIAA Aerospace Sciences Meeting and Exhibit, Reno, Nevada, (2003).

[105] X. Wan, G.E. Karniadakis, An adaptive multi-element generalized polynomial chaos method for stochastic differential equations, J. Comput. Phys. 209 (2005) 617–642.

[106] X. Wan, G.E. Karniadakis, Multi-element generalized polynomial chaos for arbitrary probability measures, SIAM J. Sci. Comput. 28 (2006) 901–928.

[107] X. Wan, G.E. Karniadakis, Long-term behavior of polynomial chaos in stochastic flow simulations, Comput. Method Appl. M. 195 (2006) 5582–5596.

[108] X. Wan and G.E. Karniadakis, Beyond Wiener-Askey expansions: Handling arbitrary PDFs, J. Sci. Comput. 27 (2006) 455–464.

[109] D.S. Watkins, Fundamentals of matrix computations, John Wiley & Sons, New York (1991).

[110] N. Wiener, Nonlinear problems in random theory, MIT Technology Press and John Wiley and Sons, New York (1958).

[111] J.A.S. Witteveen, H. Bijl, Modeling arbitrary uncertainties using Gram-Schmidt polynomial chaos, AIAA-2006-896, 44th AIAA Aerospace Sciences Meeting and Exhibit, Reno, Nevada (2006).

[112] J.A.S. Witteveen, H. Bijl, Using polynomial chaos for uncertainty quantification in problems with nonlinearities, AIAA-2006-2066, 47th AIAA/ASME/ASCE/AHS/ASC Structures, Structural Dynamics, and Materials Conference, Newport, Rhode Island (2006).

[113] J.A.S. Witteveen, S. Sarkar, H. Bijl, Modeling physical uncertainties in dynamic stall induced fluid-structure interaction of turbine blades using arbitrary polynomial chaos, Comput. Struct. 85 (2007) 866–878.

[114] D. Xiu, G.E. Karniadakis, The Wiener-Askey polynomial chaos for stochastic differential equations, SIAM J. Sci. Comput. 24 (2002) 619–644.

[115] D. Xiu, G.E. Karniadakis, Modeling uncertainty in flow simulations via generalized polynomial chaos, J. Comput. Phys. 187 (2003) 137–167.

[116] D. Xiu, G. E. Karniadakis, Uncertainty modeling of Burgers’ equation by generalized polynomial chaos, Computational Stochastic Mechanics, P.D. Spanos, G. Deodatis, Eds., 4th International Conference on Computational Stochastic Mechanics, Corfu, Greece (2002) 655–661.

[117] D. Xiu, J. Hesthaven, High-order collocation methods for differential equations with random inputs, SIAM J. Sci. Comput. 27 (2005) 1118–1139.

[118] D. Xiu, D.M. Tartakovsky, Numerical methods for differential equations in random domain, SIAM J. Sci. Comput. 28 (2006) 1167–1185.

[119] D. Xiu, Fast numerical methods for stochastic computations: A review, Commun. Comput. Phys. 5 (2009) 242–272.

[120] E. Yates Jr., AGARD standard aeroelastic configurations for dynamic response. Candidate configuration I.-Wing 445.6, Technical Memorandum 100492, NASA (1987).

[121] L.A. Zadeh, Fuzzy sets, Inform. Control 8 (1965) 338–353.

[122] O.C. Zienkiewicz, R.L. Taylor, The finite element method, 4th ed., McGraw-Hill, New York (1989).

[123] A.H. van Zuijlen, H. Bijl, Implicit and explicit higher-order time integration schemes for structural dynamics and fluid-structure interaction computations, Comput. Struct. 83 (2005) 93–105.

[124] A.H. van Zuijlen, H. Bijl, Implicit and explicit higher-order time integration schemes for fluid-structure interaction computations, Int. J. Multiscale Comput. Eng. 4 (2006) 255–263.

[125] A.H. van Zuijlen, A. de Boer, H. Bijl, Higher-order time integration through smooth mesh deformation for 3D fluid-structure interaction simulations, J. Comput. Phys. 224 (2007) 414–430.

List of publications

Journal articles

[1] J.A.S. Witteveen, S. Sarkar, H. Bijl, Modeling physical uncertainties in dynamic stall induced fluid-structure interaction of turbine blades using arbitrary polynomial chaos, Comput. Struct. 85 (2007) 866–878.

[2] J.A.S. Witteveen, H. Bijl, Efficient quantification of the effect of uncertainties in advection-diffusion problems using polynomial chaos, Numer. Heat Tr. B-Fund. 53 (2008) 437–465.

[3] J.A.S. Witteveen, H. Bijl, A monomial chaos approach for efficient uncertainty quantification in nonlinear problems, SIAM J. Sci. Comput. 30 (2008) 1296–1317.

[4] J.A.S. Witteveen, G.J.A. Loeven, S. Sarkar, H. Bijl, Probabilistic collocation for period-1 limit cycle oscillations, J. Sound Vib. 311 (2008) 421–439.

[5] J.A.S. Witteveen, H. Bijl, An unsteady adaptive stochastic finite elements formulation for rigid-body fluid-structure interaction, Comput. Struct. 86 (2008) 2123–2140.

[6] J.A.S. Witteveen, H. Bijl, An alternative unsteady adaptive stochastic finite elements formulation based on interpolation at constant phase, Comput. Method Appl. M. 198 (2008) 578–591.

[7] J.A.S. Witteveen, H. Bijl, A TVD uncertainty quantification method with bounded error applied to transonic airfoil flutter, Commun. Comput. Phys. 6 (2009) 406–432.

[8] J.A.S. Witteveen, G.J.A. Loeven, H. Bijl, An adaptive stochastic finite elements approach based on Newton-Cotes quadrature in simplex elements, Comput. Fluids (2009) in press, DOI:10.1016/j.compfluid.2008.12.002.

[9] S. Sarkar, J.A.S. Witteveen, G.J.A. Loeven, H. Bijl, Effect of uncertainty on the bifurcation behavior of pitching airfoil stall flutter, J. Fluid. Struct. (2009) in press, DOI:10.1016/j.jfluidstructs.2008.06.006.

[10] J.A.S. Witteveen, H. Bijl, Effect of randomness on multi-frequency aeroelastic responses resolved by unsteady adaptive stochastic finite elements, J. Comput. Phys. (2009) submitted.

Conference papers

[1] J.A.S. Witteveen, H. Bijl, Modeling arbitrary uncertainties using Gram-Schmidt polynomial chaos, AIAA-2006-896, 44th AIAA Aerospace Sciences Meeting and Exhibit, Reno, Nevada (2006).

[2] J.A.S. Witteveen, H. Bijl, Using polynomial chaos for uncertainty quantification in problems with nonlinearities, AIAA-2006-2066, 47th AIAA/ASME/ASCE/AHS/ASC Structures, Structural Dynamics, and Materials Conference, Newport, Rhode Island (2006).

[3] J.A.S. Witteveen, H. Bijl, An efficient monomial chaos approach for uncertainty quantification in nonlinear computational models, AIAA-2006-2071, 47th AIAA/ASME/ASCE/AHS/ASC Structures, Structural Dynamics, and Materials Conference, Newport, Rhode Island (2006).

[4] G.J.A. Loeven, J.A.S. Witteveen, H. Bijl, Efficient uncertainty quantification in computational fluid-structure interactions, AIAA-2006-1634, 47th AIAA/ASME/ASCE/AHS/ASC Structures, Structural Dynamics, and Materials Conference, Newport, Rhode Island (2006).

[5] J.A.S. Witteveen, H. Bijl, A monomial chaos approach for efficient uncertainty quantification in computational fluid dynamics, European Conference on Computational Fluid Dynamics ECCOMAS CFD, Egmond aan Zee, The Netherlands (2006).

[6] J.A.S. Witteveen, H. Bijl, Reliable computational predictions by modeling uncertainties using arbitrary polynomial chaos, European Conference on Compu-

tational Fluid Dynamics ECCOMAS CFD, Egmond aan Zee, The Netherlands (2006).

[7] G.J.A. Loeven, J.A.S. Witteveen, H. Bijl, Efficient uncertainty quantification using a two-step approach with chaos collocation, European Conference on Computational Fluid Dynamics ECCOMAS CFD, Egmond aan Zee, The Netherlands (2006).

[8] G.J.A. Loeven, J.A.S. Witteveen, H. Bijl, Probabilistic collocation: an efficient non-intrusive approach for arbitrarily distributed parametric uncertainties, AIAA-2007-317, 45th AIAA Aerospace Sciences Meeting and Exhibit, Reno, Nevada (2007).

[9] J.A.S. Witteveen, G.J.A. Loeven, H. Bijl, Quantifying the effect of physical uncertainties in unsteady fluid-structure interaction problems, AIAA-2007-1942, 48th AIAA/ASME/ASCE/AHS/ASC Structures, Structural Dynamics, and Materials Conference, Honolulu, Hawaii (2007).

[10] G.J.A. Loeven, S. Sarkar, J.A.S. Witteveen, H. Bijl, Dynamic stall flutter analysis with uncertainties using multi-element probabilistic collocation, AIAA-2007-1964, 48th AIAA/ASME/ASCE/AHS/ASC Structures, Structural Dynamics, and Materials Conference, Honolulu, Hawaii (2007).

[11] S. Sarkar, J.A.S. Witteveen, H. Bijl, Modeling physical uncertainties in stall induced oscillation of an airfoil using polynomial chaos approach, Asian Computational Fluid Dynamics Conference ACFD7, Bangalore, India (2007).

[12] G.J.A. Loeven, J.A.S. Witteveen, H. Bijl, Efficient uncertainty quantification in computational fluid-structure interactions: the probabilistic collocation method in a two step approach, International Workshop on Coupled Methods in Numerical Dynamics, Dubrovnik, Croatie (2007).

[13] J.A.S. Witteveen, G.J.A. Loeven, H. Bijl, Long-term stochastic behavior of aeroelastic systems, NATO RTO-MP-AVT-147 Computational Uncertainty in Military Vehicle Design Symposium, Athens, Greece (2007).

[14] G.J.A. Loeven, J.A.S. Witteveen, H. Bijl, A probabilistic radial basis function approach for uncertainty quantification, NATO RTO-MP-AVT-147 Computational Uncertainty in Military Vehicle Design Symposium, Athens, Greece (2007).

[15] J.A.S. Witteveen, H. Bijl, Unsteady adaptive stochastic finite elements for aeroelastic systems with randomness, AIAA-2008-2148, 49th AIAA/ASME/ASCE/

AHS/ASC Structures, Structural Dynamics, and Materials Conference, Schaumburg, Illinois (2008).

[16] J.A.S. Witteveen, H. Bijl, An unsteady adaptive stochastic finite elements uncertainty quantification method for fluid-structure interaction problems, 5th European Congress on Computational Methods in Applied Sciences and Engineering ECCOMAS 2008, Venice, Italy (2008).

[17] H. Bijl, J.A.S. Witteveen, G.J.A. Loeven, Uncertainty quantification in computational fluid dynamics and fluid-structure interaction, 13th International Conference on Computational and Applied Mathematics ICCAM 2008, Ghent, Belgium (2008).

[18] J.A.S. Witteveen, H. Bijl, Unsteady adaptive stochastic finite elements for quantification of uncertainty in time-dependent simulations, 6th International Conference on Engineering Computational Technology ECT2008, Athens, Greece (2008).

Summary

Robust and efficient methods are presented for resolving the effect of physical variations in computationally intensive flow and fluid-structure simulations including discontinuities and unsteadiness. The effect of inherent physical uncertainties due to, for example, varying atmospheric conditions and production tolerances can in sensitive engineering problems be larger than the numerical error in computational predictions. Detailed and quantitative probabilistic information on the effect of physical variability modeled by random parameters can be utilized in reducing design safety factors and robust design optimization, which eventually contributes to the development of aerodynamically more efficient and environmentally friendly transportation and renewable energy technologies.

In order to determine the effect of physical randomness reliably and at low computational costs a number of uncertainty quantification methods is developed. The introduced uncertainty quantification methods result in a significant improvement over existing methods in terms of efficiency and robustness. The proposed Gram-Schmidt Polynomial Chaos method contributes to the extension of the spectral convergence of Galerkin Polynomial Chaos to arbitrary input probability distributions. The developed Monomial Chaos approach results in an uncoupled set of linear equations for constructing the Polynomial Chaos expansion in problems involving polynomial nonlinearities. It is shown that the computational work per additional Monomial Chaos order of the equivalence of a linear Newton iteration can reduce the additional computational costs for a Monomial Chaos uncertainty quantification to less than that of a deterministic solve. The presented Adaptive Stochastic Finite Elements (ASFE) method based on Newton-Cotes quadrature in simplex elements is an extrema diminishing (ED) scheme in probability space. The method also satisfies the total variation diminishing (TVD) concept extended to probability space for first-degree Newton-Cotes quadrature.

For unsteady problems the concept of interpolating a time-independent parameterization of periodic samples instead of the time-dependent samples themselves is introduced in Probabilistic Collocation for Limit Cycle Oscillations (PCLCO). This results

in a time-independent uncertainty quantification interpolation accuracy for the time-independent parameters with a constant number of samples for period-1 limit cycle oscillations. The applicability of the time-independent parameterization is extended to non-smooth time-independent functionals, asymptotically non-periodic responses, and higher-period oscillations in the Unsteady Adaptive Stochastic Finite Elements (UASFE) method.

A second UASFE concept for uncertainty quantification of oscillatory responses is developed based on interpolation of the samples at constant phase. It is shown that this formulation results in a bounded error as function of the phase for periodic responses and under certain conditions also in a bounded error in time. In practice this leads to a constant uncertainty quantification accuracy in time with a constant number of samples. The resulting formulation is not subject to a parameterization error and it can resolve time-dependent functionals. The method is applicable to responses of which the phase is well-defined. The UASFE framework is further extended to fluid-structure interactions with multi-frequency responses and continuous structures by employing a wavelet decomposition preprocessing step. Fourth-order convergence results for one random parameter show a 3 orders of magnitude reduction of computational costs compared to Monte Carlo simulation.

The developed methods are applied to steady and unsteady problems with discontinuities subject to random fields and multiple random input parameters with various probability distributions in physical parameters, geometrical parameters, and boundary and initial conditions. Problems with discontinuities are found to be sensitive to input variations with an amplification factor of 18.4 for the coefficient of variation in a piston problem and a varying shock wave location from 50% to 80% of the chord in transonic airfoil flow due to a 1% variation in free stream Mach number.

The unsteady applications illustrate that the developed methods have the potential to advance uncertainty quantification for computationally intensive unsteady problems with discontinuities from practically impossible to a routine analysis. It is demonstrated that a random parameter which affects the frequency of a periodic oscillation results in steady asymptotic stochastic behavior. Oscillatory linear problems with a non-zero probability of negative damping are shown to result asymptotically in a diverging output standard deviation. Dynamical systems with bifurcations are found to be extremely sensitive to random initial conditions with an amplification of input randomness by a factor 52.0 for the standard deviation in the Duffing oscillator.

The fluid-structure interaction of a two-dimensional airfoil shows a typical P-bifurcation behavior for probability density of the pitch amplitude from a Dirac delta function at zero amplitude to a unimodal probability density function for positive amplitudes. A 2.5% reduction of the flutter boundary compared to its deterministic location still results in a 3.8% probability of flutter.

In the three-dimensional transonic AGARD 445.6 wing aeroelastic benchmark a mean free stream velocity fixed at a realistic safety margin of 5% below the deterministic flutter velocity in combination with a 3.5% velocity variation results in a non-zero flutter probability of 6.19%. This illustrates that randomness can lead to the onset of unstable behavior, which a single deterministic simulation for the mean value would have missed. Taking physical uncertainties into account in numerical predictions is, therefore, a more reliable design practice than using safety margins in combination with deterministic simulation results.

Samenvatting

Robuuste en efficiënte methoden worden gepresenteerd voor het bepalen van het effect van fysische variaties in reken-intensieve stroming en stroming-constructie simulaties met discontinuïteiten en tijdsafhankelijkheid. Het effect van inherente fysische onzekerheden ten gevolge van bijvoorbeeld variërende atmosferische condities en productietoleranties kunnen in gevoelige ingenieursproblemen groter zijn dan de numerieke fout in rekenkundige voorspellingen. Gedetailleerde en kwantitatieve probabilistische informatie over het effect van fysische variabiliteit gemodelleerd door stochastische parameters kan worden gebruikt in het reduceren van ontwerp veiligheidsfactoren en in robuuste ontwerp optimalisatie, wat uiteindelijk bijdraagt aan de ontwikkeling van aerodynamisch efficiëntere en milieuvriendelijk vervoer en duurzame energie technologie.

Ten einde het effect van fysische variaties betrouwbaar en met lage rekenkosten te bepalen, worden verscheidene onzekerheidskwantificeringsmethoden ontwikkeld. De geïntroduceerde methoden resulteren in een significante verbetering ten opzichte van bestaande methoden in termen van efficiëntie en robuustheid. De voorgestelde Gram-Schmidt Polynomische Chaos methode draagt bij aan de uitbreiding van de spectrale convergentie van Galerkin Polynomische Chaos naar willekeurige kansverdelingen. De ontwikkelde Monomische Chaos aanpak resulteert in een ontkoppelde set van lineaire vergelijkingen voor het construeren van de Polynomische Chaos expansie in problemen met polynomische niet-lineariteiten. Er is aangetoond dat het rekenwerk per additionele Monomische Chaos orde equivalent aan een lineaire Newton iteratie het additionele rekenwerk voor een Monomische Chaos onzekerheidskwantificering kan reduceren tot minder dan dat van een deterministische berekening. De gepresenteerde Adaptieve Stochastische Eindige Elementen (Adaptive Stochastic Finite Elements, ASFE) methode gebaseerd op Newton-Cotes kwadratuurpunten in simplex elementen is een extrema verlagend (extrema diminishing, ED) schema in de kansruimte. De methode voldoet ook aan de totale variatie verkleinende (total variation diminishing, TVD) conditie uitgebreid naar de kansruimte voor eerstegraads Newton-Cotes kwadratuurpunten.

Voor instationaire problemen wordt het concept van interpolatie van een tijdsafhankelijke parameterisatie van periodieke realisaties in plaats van de tijdsafhankelijke realisaties zelf geïntroduceerd in Probabilistische Collocatie voor Limietcykel Oscillaties (Probabilistic Collocation for Limit Cycle Oscillations, PCLCO). Dit resulteert in een tijdsonafhankelijke onzekerheidskwantificeringsinterpolatienauwkeurigheid voor de tijdsafhankelijke parameters met een constant aantal realisaties voor periode-1 limietcykel oscillaties. De toepasbaarheid van de tijdsafhankelijke parameterisatie wordt uitgebreid tot niet-gladde tijdsafhankelijke functionalen, asymptotisch niet-periodieke responsen en hogere-periode oscillaties in de Instationaire Adaptieve Stochastische Eindige Elementen (Unsteady Adaptive Stochastic Finite Elements, UASFE) methode.

Een tweede UASFE concept voor onzekerheidskwantificering van oscillatorische responsen wordt ontwikkeld gebaseerd op interpolatie van de realisaties bij constante fase. Het is aangetoond dat deze formulering resulteert in een begrensde fout als functie van de fase voor periodieke responsen en onder zekere condities ook in een begrensde fout in de tijd. In de praktijk leidt dit tot een constante onzekerheidskwantificeringsnauwkeurigheid in de tijd met een constant aantal realisaties. De resulterende formulering heeft geen parameterisatiefout en kan tijdsafhankelijke functionalen behandelen. De methode is toepasbaar op responsen waarvan de fase goed gedefiniëerd is. De UASFE methode wordt verder uitgebreid naar stroming-constructie interacties met meerdere-frequentie responsen en continue constructies door gebruik te maken van een wavelet ontbindingsstap. Vierde orde convergentie resultaten voor een stochastische parameter laten een 3 ordes van grootte reductie van de rekenkosten zien in vergelijking met Monte Carlo simulaties.

De ontwikkelde methoden zijn toegepast op stationaire en instationaire problemen met discontinuïteiten en met stochastische velden en meerdere stochastische parameters met verscheidene kansverdelingen in fysieke parameters, geometrische parameters, en rand- en beginvoorwaarden. Het is gevonden dat problemen met discontinuïteiten gevoelig zijn voor variaties met een versterkingsfactor van 18,4 voor de variatiecoëfficiënt in een zuiger probleem en een variërende schokgolf locatie van 50% tot 80% van de koorde in transsonische profielstroming ten gevolge van een 1% variatie in het ongestoorde Machgetal. De instationaire toepassingen laten zien dat de ontwikkelde methoden de potentie hebben om onzekerheidskwantificering voor rekenintensieve instationaire problemen met discontinuiteiten te transformeren van praktisch onmogelijk tot een routine analyse. Er is gedemonstreerd dat een stochastische parameter die effect heeft op de frequentie van een periodieke oscillatie resulteert in een stationair asymptotisch stochastisch gedrag. Er is aangetoond dat oscillerende lineaire problemen met een positieve kans op negatieve demping asymptotisch resulteren in een divergerende standard deviatie. Er is ook gevonden dat dynamische systemen met bifurcaties extreem gevoelig zijn voor stochastische begincondities met een amplificatie van variabiliteit met een factor 52,0 voor de standaard deviatie in de Duffing vergelijking.

De stroming-constructie interactie van een twee-dimensionaal profiel laat een typisch P-bifurcatiegedrag zien voor de kansdichtheid van de stamp amplitude vanuit een Dirac delta functie voor een amplitude van nul tot een mode-1 kansdichtheidsfunctie voor positieve amplitudes. Een 2,5% reductie van de fluttergrens ten opzichte van zijn deterministische locatie resulteert nog steeds in een 3,8% kans op flutter.

In het drie-dimensionale transsone AGARD vleugel 445.6 aero-elastisch standaardprobleem resulteert een gemiddelde ongestoorde snelheid op een realistische veiligheidsmarge van 5% beneden de deterministische fluttersnelheid in combinatie met een 3.5% snelheidsvariatie in een positieve kans of flutter van 6,19%. Dit illustreert dat variaties kunnen leiden tot het ontstaan van instabiel gedrag, dat een deterministische simulatie voor de gemiddelde waarde zou hebben gemist. Het meenemen van fysische onzekerheden in numerieke voorspellingen is daarom een betrouwbaardere ontwerpmethodologie dan het gebruiken van veiligheidsmarges in combinatie met deterministische simulatie resultaten.

Acknowledgments

First of all I would like to use this opportunity to thank my supervisor prof.dr.ir.drs. Hester Bijl for giving me the opportunity to perform my Ph.D. research in the exciting and dynamic field of uncertainty quantification for computational fluid dynamics and fluid-structure interaction. I am grateful for her continued support and all the things I learned from her also beyond uncertainty quantification on how to organize and present scientific research. I also thank prof.dr.ir. Barry Koren for notifying me of the vacancy for this Ph.D. research position.

Let me also take the opportunity to thank my other co-workers. I would like to thank ir. Alex Loeven for the collaboration first as supervisor of his Master's thesis project and later as a colleague. I am also grateful to dr. Sunetra Sarkar for the contribution of her expertise on dynamic stall flutter in our joint work. I thank my roommates dr.ir. Aukje Spruyt-de Boer and dr.ir. Sander van Zuijlen for their contributions to the development of the deterministic fluid-structure interaction code.

I thank also the other members of the Aerodynamics department for the pleasant working environment. I would like to thank the members of the STW user committee for the constructive meetings. I also would like to thank the members of my Ph.D. committee for proofreading the manuscript of this thesis. I am also grateful to the many researchers I met at conferences, workshops, and other meetings for their useful feedback.

Finally, I would like to thank my family and friends for their support during these years. This research was supported by the Technology Foundation STW, applied science division of NWO and the technology programme of the Ministry of Economic Affairs under grant 6583 “Uncertainties in unsteady flow and fluid-structure interaction simulations applied to wind turbines at sea”.

Jeroen A.S. Witteveen
Delft, September 2008
http://www.jeroenwitteveen.com

Curriculum Vitae

Jeroen Witteveen was born on September 3, 1980 in Tilburg, The Netherlands. He attended secondary school at the Theresia Lyceum in Tilburg from 1992 until he graduated the gymnasium with honors in 1998. In 1998 he started his study at the Aerospace Engineering faculty of the Delft University of Technology. He completed his Propedeuse year with honors in 1999.

At the end of his Bachelor phase in 2001 he participated in a Design Synthesis project for the European Space Agency (ESA) and the Dutch Organisation for Applied Scientific Research (TNO) on the feasibility of a hot plume wind tunnel facility for the Ariane 5 rocket. In his Master phase he did a three month internship in 2002 at the Von Karman Institute for Fluid Dynamics in Brussels, Belgium, on a Residual Distribution approach for two-phase flow simulations supervised by prof.dr.ir. Herman Deconinck and dr. Mario Ricchiuto. He obtained his Master of Science degree with honors at the Aerodynamics department in 2004. For his Master's thesis entitled "The simple wave shock wave approximation and a new numerical method for hyperbolic problems", supervised by prof.dr.ir Peter Bakker and prof.dr.ir. Barry Koren, he received the 2003/2004 best graduate award of the Aerospace Engineering faculty.

In October 2004 he started his Ph.D. research in the Computational Aerodynamics group supervised by prof.dr.ir.drs. Hester Bijl. The results of this work on efficient and robust uncertainty quantification methods for computational fluid dynamics and fluid-structure interaction are presented in this thesis. The research was funded by the Vidi-STW project entitled "Uncertainties in unsteady flow and fluid-structure interaction simulations applied to wind turbines at sea". In October 2008 he continued his work as a postdoctoral researcher in Computational Aerodynamics group funded by the European Commission's Sixth Framework Programme project entitled "Non-Deterministic Simulation for CFD-based design methodologies NODESIM-CFD". He is also a referee for international scientific journals.

Physical uncertainties due to atmospheric variations and production tolerances can nowadays have a larger effect on the accuracy of computational predictions than numerical errors. It is essential to quantify the effect of these uncertainties for reducing design safety factors and robust design optimization. This eventually contributes to the development of aerodynamically more efficient and environmentally friendly transportation and renewable energy technologies.

In this thesis, efficient and robust uncertainty quantification methods are developed for computationally intensive flow and fluid-structure interaction simulations including discontinuities and unsteadiness. The proposed methods satisfy the total variation diminishing and extrema diminishing concepts extended to probability space and result in practice in a constant error in time. The considered applications demonstrate that the developed methods have the potential to advance uncertainty quantification for computationally intensive unsteady problems with discontinuities from practically impossible to a routine analysis. The examples also illustrate that taking physical uncertainties into account is a more reliable design practice than using safety margins in combination with deterministic simulation results.

ISBN 978-90-9024167-8